EVALUATION OF THE SONICALLY INDUCED NARROWING OF NUCLEAR MAGNETIC RESONANCE SPECTRA OF SOLIDS

Mark James Howard

Doctor of Philosophy

THE UNIVERSITY OF ASTON IN BIRMINGHAM

September 1994.

The University of Aston in Birmingham

EVALUATION OF THE SONICALLY INDUCED NARROWING OF NUCLEAR MAGNETIC RESONANCE SPECTRA OF SOLIDS

MARK JAMES HOWARD

Doctor of Philosophy

1994

The Nuclear Magnetic Resonance (NMR) spectra of liquids contain a wealth of quantitative information that may be derived, for instance, from chemical shifts and spin-spin couplings. The available information depends on the incoherent rapid molecular motion that causes complicating effects present in the solid state to average to zero. Whereas liquid state NMR spectra show narrow lines, the corresponding NMR spectra from the solid state are normally composed of exceedingly broad resonance lines due to highly restricted molecular motion. It is, therefore, difficult to obtain directly as detailed information from the spectra of solids as from those derived from the liquid state.

Studies on a new technique (SINNMR, the sonically induced narrowing of the NMR spectra of solids) to remove line broadening effects in the NMR spectra of the solid state are reported within this thesis. SINNMR involves narrowing the NMR absorptions from solid particles by irradiating them with ultrasound when they are suspended in a support liquid. It is proposed that ultrasound induces incoherent motion of the suspended particles, producing motional characteristics of the particles similar to those of rather large molecules. The first report of apparently successful experiments involving SINNMR[1] emphasised both the irreproducibility of the technique and the uncertainty regarding its true origin. If SINNMR can be made reproducible and the effect definitively attributed to the sonically induced incoherent motional averaging of particles, the technique could offer a simple alternative to the now classical magic-angle spinning (MAS) NMR[2] and the recently reported dynamic angle spinning (DAS)[3] and double rotation (DOR)[4] techniques.

Evidence is presented in this thesis to support the proposal that ultrasound may be used to narrow the NMR spectral resonances from solids by inducing incoherent motion of particles suspended in support liquids and, additionally, for some solids, by inducing rotational motion of molecular constituents in the lattices of solids. Successful SINNMR line narrowing using 20 kHz ultrasound is reported for a variety of samples: including trisodium orthophosphate, polytetrafluoroethylene and aluminium alloys. Investigations of SINNMR line narrowing in trisodium phosphate have revealed the relationship between ultrasonic power, particle size and support liquid density for the production of optimum SINNMR conditions. It is also proposed that the incoherent motion of particles induced by 20 kHz ultrasound can originate from interactions between acoustically induced cavitation microjets and particles. This has enabled the prediction of a relationship between ultrasonic frequency and particle size for successful SINNMR experiments. Preliminary experiments using high frequency ultrasound, between 1 and 10 MHz, have produced successful SINNMR line narrowing of suspensions of silicon dioxide and sodium-boron-aluminium glasses.

Key Words: SINNMR, NMR, Ultrasound, Incoherent Motion, Solid-state.

This thesis is dedicated to my wife, Rachael whose interest and support throughout this and other ventures has enabled me to complete what originally appeared an impossible task.

Can I have some Remedy?
Remedy for me please.
'Cause if I had some remedy,
I'd take enough to please me.

- Chris and Rich Robinson
'The Black Crowes' © 1992.

ACKNOWLEDGEMENTS

I would like to express my gratitude to my supervisor Dr. John Homer for all the advice and assistance during the last three years.

I would also like to express my thanks to Dr. Mike Perry and Dr. Sunil Patel (while at Birbeck College, London) for between them running all the MAS NMR spectra refered to within this thesis and Mr. Roger Wheeler for producing specialist items from the workshop, including the high frequency ultrasound unit. My appreciation is also extended to Dr. Christian Jäger at the Max-Planck Institute for supplying the glasses used in the high frequency investigations for SINNMR.

I am also grateful for the support from other academic staff from within the department: Professor W.R. McWhinnie, Dr. Martin Beevers, Dr. Jack McCoubrey and Dr. Tony Kakhu.

My thanks are also due to my colleagues within the NMR spectroscopy research group: Mr. Gavin Tilstone, Mr. Stuart Palfreyman, Mr. Steven Reynolds Miss Anna Weekes and very briefly, Dr. John Robson.

Finally, this section would not be complete without thanks to my family. First and foremost, my wife, Rachael, to whom this thesis is dedicated. Second, my parents, Jean and Thomas Howard for their encouragement and support, both financially and emotionally, throughout my time at university. Third, my parents-in-law, Jenny and Matthew Chapman, for support, understanding and for putting up with the endless typing of this manuscript in their own home. Finally, my brother and sister-in-law, David and Sandra Howard, who have been shoulders to cry on, allowing me to get away from it all, and excellent friends beyond the call of duty. Without out you all, the production of the research within this thesis, and the manuscript itself, would not have been possible.

Mark James Howard, 1994.

TABLE OF CONTENTS

TITLE PAGE 1

SUMMARY 2

DEDICATION 3

ACKNOWLEDGEMENTS 4

TABLE OF CONTENTS 5

LIST OF TABLES 11

LIST OF FIGURES 16

CHAPTER ONE

INTRODUCTION TO NUCLEAR MAGNETIC RESONANCE SPECTROSCOPY 23

1.1 INTRODUCTION 24

1.2 MAGNETIC PROPERTIES OF NUCLEI 25
1.2.1 Nuclear Angular Momentum and Magnetic Moment 25
1.2.2 Nuclei in a Static Magnetic Field 27
1.2.3 Energy of the Nuclei in the Magnetic Field 28
1.2.4 Population of the Energy Levels 29
1.2.5 Macroscopic Magnetization 30

1.3 THE NMR EXPERIMENT 31

1.4 MAGNETIZATION 32
1.4.1 The Manipulation of Magnetization 32
1.4.2 The Bloch Equations 32
1.4.3 An Introduction to Relaxation 34
1.4.4 The Rotating Frame of Reference 35
1.4.5 The Intensity of NMR Absorptions 37

1.5 FACTORS AFFECTING THE APPEARANCE OF NMR SPECTRA 38
1.5.1 Line Widths - Transverse Relaxation and Inhomogeneity 38
1.5.2 Paramagnetic Species 39
1.5.3 Quadrupolar Effects 40
1.5.4 Digital Resolution 40

1.6 THE CHEMICAL SHIFT 40
1.6.1 Nuclear Screening 40
1.6.2 Spectral Referencing 41
1.6.3 The Use of Chemcial Shifts 43

1.7 SPIN-SPIN COUPLING 43
1.7.1 The Origin of Spin-Spin Coupling 44
1.7.2 The Use of Spin-Spin Coupling 46

1.8 NMR RELAXATION 45
1.8.1 The Effect of Motion on Relaxation 46
1.8.2 Relaxation Mechanisms 48
1.8.3 The Nuclear Overhauser Effect (nOe) 49

CHAPTER TWO

INTRODUCTION TO FOURIER TRANSFORM NUCLEAR MAGNETIC RESONANCE SPECTROSCOPY 51

2.1 THE FOURIER TRANSFORM 52
2.1.1 Introduction 52
2.1.2 Fourier Transformation 52

2.2 PULSED FOURIER TRANSFORM NMR 54
2.2.1 The Basic Pulse FT-NMR Experiment 54
2.2.2 The NMR Signal and Detection 55
2.2.3 The Parameters of a Basic 1D FT-NMR Experiment 55

2.3 SPECIAL CONSIDERATIONS 60
2.3.1 Acquisition Time and Digital Resolution 60
2.3.2 Convolution due to Truncation 60
2.3.3 Folding 61
2.3.4 Quadrature Detection 61
2.3.5 Obtaining Quantitative Information 61
2.3.6 Phase Corrections 62
2.3.7 Off Resonance Effects 62
2.3.8 The Observation of Solid State NMR Spectra using FT-NMR 64

CHAPTER THREE

INTRODUCTION TO SOLID STATE NUCLEAR MAGNETIC RESONANCE 65

3.1 INTRODUCTION 66

3.2 THE HAMILTONIANS WHICH DESCRIBE NMR 66
3.2.1 The Dipolar Interaction 67
3.2.2 The Chemical Shift Interaction 69
3.2.3 Quadrupolar Interaction 71

3.3 TECHNIQUES AVAILABLE TO REMOVE BROADENING INTERACTIONS 74
3.3.1 Magic Angle Spinning (MAS NMR) 75
3.3.2 Dynamic Angle Spinning (DAS NMR) and Double Rotation (DOR NMR) 77
3.3.3 Multiple Pulse Experiments 79
3.3.4 Other Averaging Techniques 80

CHAPTER FOUR

ULTRASONICS 81

4.1 INTRODUCTION 82
4.1.1 Vibrations and Waves 82
4.1.2 Attenuation of Plane Waves 86
4.1.3 Specific Acoustic Impedance 86

4.1.4 Reflection and Transmission at a Plane Boundary and the Quality of Resonance. ... 87
4.1.5 Stationary Waves ... 89

4.2 THE GENERATION OF ULTRASOUND ... 90
4.2.1 Piezoelectric Oscillators ... 90
4.2.1.1 Natural Piezoelectric Oscillators ... 90
4.2.1.2 Ceramic Transducers ... 92
4.2.1.3 Measurement of the Piezoelectric Effect ... 93
4.2.1.4 Practical Considerations when unsing Piezoelectric Transducers ... 94
4.2.3 Magnetostrictive Transducers ... 96
4.2.4 Mechanical Transducers ... 97
4.2.5 Miscellaneous Transducers ... 99
4.2.6 The Mechanical Amplification of Ultrasound ... 100

4.3 THE EFFECTS OF ULTRASOUND ON LIQUIDS AND SOLIDS ... 102
4.3.1 The Passage and Attenuation of Ultrasound Through Liquids and Solids. ... 102
4.3.2 Streaming ... 103
4.3.3 Chemical Reactivity ... 103
4.3.4 Cavitation ... 103
4.3.5 Emulsification, Agglomeration and Aggregate Dispersal ... 106

4.4 THE ACOUSTIC MANIPULATION OF OBJECTS ... 106
4.4.1 Interaction of a Sound Field with an Object ... 107

CHAPTER FIVE

INTRODUCTION TO THE SONICALLY INDUCED NARROWING OF THE NUCLEAR MAGNETIC RESONANCE SPECTRA OF SOLIDS ... 109

5.1 INTRODUCTION ... 110

5.2 THE UNDERLYING HYPOTHESIS AND PRINCIPLES OF SINNMR ... 110

CHAPTER SIX

EQUIPMENT AND EXPERIMENTAL METHODS ... 112

6.1 THE JEOL FX-90Q FT-NMR SPECTROMETER ... 113
6.1.1 The NMR Variable Temperature Apparatus ... 114
6.1.2 The NMR Probe ... 114
6.1.3 The Measurement of Spin-lattice Relaxation Times ... 115
6.1.4 The Operation of a High-resolution Spectrometer to Solid-State Detection. ... 117

6.2 THE KERRY ULTRASONICS 20 kHz ULTRASONIC APPARATUS ... 118

6.3 THE YAESU HIGH FREQUENCY ULTRASOUND APPARATUS ... 118
6.4 THE COUPLING OF THE NMR SPECTROMETER AND ULTRASOUND ... 119
6.4.1 NMR Tubes and Samples ... 119
6.4.2 NMR and 20 kHz Ultrasound ... 121
6.4.3 NMR and High Frequency Ultrasound ... 121

CHAPTER SEVEN

SINNMR EXPERIMENTS USING TRISODIUM PHOSPHATE ... 124

7.1 INTRODUCTION ... 125

7.2 INITIAL EXPERIMENTS 125

7.3 THE DEPENDENCE OF THE SIGNAL TO NOISE RATIO (S/N) OF 31P SINNMR WITH PARTICLE SIZE RANGE AND MASS OF SAMPLE USED. 126

7.4 THE DEPENDENCE OF THE SIGNAL TO NOISE RATIO (S/N) OF SINNMR EXPERIMENTS WITH VARYING DENSITY OF THE LIQUID SUPPORT MEDIUM. 128

7.5 THE REFINEMENT OF OPTIMUM CONDITIONS FOR SINNMR EXPERIMENTS 132

7.6 OBSERVATIONS MADE AFTER THE CONCLUSION OF SINNMR EXPERIMENTS 135

7.7 INVESTIGATIONS INTO THE ORIGIN OF SINNMR IN TSP 136
7.7.1 Possible Mechanisms for increasing Lattice Motion 136
7.7.2 Decay of SINNMR and Thermally Induced Narrow Resonances 137
7.7.3 Line Narrowing due to incoherent Particle Motion 140
7.7.4 Melting and Reaction 145

7.8 DISCUSSION 146

CHAPTER EIGHT

STUDIES OF ACOUSTICALLY INDUCED ROTATION OF SUSPENDED TRISODIUM PHOSPHATE PARTICLES 147

8.1 PARTICLE DISPLACEMENT 148
8.1.1 Introduction 148
8.1.2 Bench Observations 148
8.1.3 Using Bench Observation to Optimise Conditions for SINNMR 151

8.2 SINNMR MEASUREMENTS 151

8.3 PROPOSED MECHANISMS FOR SINNMR LINE NARROWING 157

8.4 DISCUSSION 164

CHAPTER NINE

SINNMR EXPERIMENTS ON POLYTETRAFLUOROETHYLENE (PTFE) 165

9.1 INTRODUCTION 166
9.2 ^{19}F SINNMR STUDIES OF PTFE 166

9.3 THE ORIGIN OF SINNMR LINE NARROWING IN PTFE 167

9.4 DISCUSSION 168

CHAPTER TEN

SINNMR INVESTIGATIONS OF KNIGHT SHIFTED NMR SIGNALS 170

10.1 INTRODUCTION 171

10.2 SINNMR INVESTIGATIONS INTO ALUMINIUM AND SOME OF ITS ALLOYS 171

10.3 SINNMR INVESTIGATIONS ON SINGLE CRYSTAL DOPED SILICON 175

10.4 DISCUSSION 176

CHAPTER ELEVEN

SINNMR EXPERIMENTS ON OTHER SYSTEMS 178

11.1 SINNMR INVESTIGATIONS OF AMBERLITE 179

11.2 SINNMR INVESTIGATIONS ON SILYLATED COAL 180

11.3 MATERIALS WHICH HAVE ELUDED SINNMR 182

11.4 DISCUSSION 183

CHAPTER TWELVE

PRELIMINARY SINNMR STUDIES USING HIGH FREQUENCY ULTRASOUND 184

12.1 INTRODUCTION 185

12.2 HIGH FREQUENCY SINNMR INVESTIGATIONS INTO SILICON DIOXIDE 187

12.3 HIGH FREQUENCY SINNMR INVESTIGATIONS INTO GLASSES 189

12.4 DISCUSSION 193

CHAPTER THIRTEEN

INVESTIGATIONS INTO OTHER SINNMR SYSTEM CONFIGURATIONS 194

13.1 INTRODUCTION 195
13.2 THE SIDE TRANSDUCER 195

13.3 BOTTOM TRANSDUCER 198

CHAPTER FOURTEEN

CONCLUSIONS AND SUGGESTIONS FOR FUTURE WORK 199

14.1 CONCLUSIONS 200

14.2 FUTURE WORK 201
14.2.1 Further Studies from experiments described in this thesis 202
14.2.2 Proposed Novel SINNMR Experiments 203

REFERENCES 204

BIBLOGRAPHY 228

APPENDIX ONE - INTRODUCTION TO HAMILTONIANS AND TENSOR MATHEMATICS 224

A1.1 A BRIEF INTRODUCTION TO HAMILTONIANS 225
A1.2 A BRIEF INTRODUCTION TO TENSOR MATHEMATICS 226

APPENDIX TWO - NMR PARAMETERS USED IN ALL EXPERIMENTS 228

APPENDIX THREE - THE CALCULATION OF GAUSSIAN DISTRIBUTION CURVES 238

LIST OF TABLES

CHAPTER ONE

TABLE 1.1 Magnetic Properties of Certain Nuclei of Interest to NMR Spectroscopists..... 26

CHAPTER TWO

TABLE 2.1 The time required of M_Z to recover to 99.5% M_0 for different values of M_{Zi}.. 58

CHAPTER THREE

TABLE 3.1 Approximate ranges of the different spin interactions and resultant of complete incoherent averaging (as in liquids)..... 67

TABLE 3.2. Summary of the angular dependence for selected solid state interactions. All angles are defined in figure 3.1..... 75

TABLE 3.3 Solution pairs to the angles required to solve the 4th order Legendre polynomial for $P_4(\cos \theta) = 0$..... 78

CHAPTER FOUR

TABLE 4.1 Compressional, Shear and General Properties for various Piezoelectric Materials..... 95

CHAPTER SIX

TABLE 6.1 General NMR Information for the nuclei observed during the course of SINNMR studies reported within this thesis..... 113

CHAPTER SEVEN

TABLE 7.1. The S/N ratio of the ^{31}P SINNMR resonance of TSP for varying particle size range and mass..... 127

TABLE 7.2. The variation in TSP ^{31}P SINNMR S/N ratio with liquid medium density..... 128

TABLE 7.3. ^{23}Na SINNMR S/N ratio and FWHM for different particle size ranges of TSP. All acquisition parameters were identical. The digital resolution was ± 7 Hz..... 131

Table 7.4. ^{23}Na S/N ratio and FWHM and ^{31}P FWHM for samples of TSP..... 139

Table 7.5. Spin-lattice relaxation times with experimental method used for different samples of 1000 - 500µm graded TSP..... 141

CHAPTER EIGHT

TABLE 8.1. Displacements of samples of TSP with varying density of support medium and 20kHz ultrasound tip displacement..... 149

TABLE 8.2. A and B values for the fitting equations to the data displayed in figure 8.2 for displacements of 10, 17 and 24 mm..... 151

TABLE 8.3. Prediction of TSP particle sizes to reach defined distances within a SINNMR experiment using 3µm 20kHz ultrasonic tip displacement and densities shown..... 152

TABLE 8.4. FWHM, estimated correlation time, τ_c and NMR spin-lattice relaxation times, T_1 for ^{31}P SINNMR spectra of 1000 - 210µm graded TSP in various support mixtures..... 153

TABLE 8.5. Specimen calculation data and M_0 obtained for the correction of NMR peak intensities using equation 8.6. The observed intensities I_{eq} are measured in arbitrary units from a SINNMR experiment with bromoform as the support liquid..... 154

TABLE 8.6. The calculated integrals of the mass distribution curve for different particle size limits present in the NMR detector coils. 156

TABLE 8.7. - SINNMR acquisition parameters and observed and corrected signal to noise ratio and relative peak areas for various support mixtures used..... 158

TABLE 8.8. Estimated percentage area of different size particle faces upon which microjet impact could facilitate incoherent particle motion. As the resonant bubble radius is dependant on the support liquid density, there will be a corresponding dependence of the percentage area to the mixture considerd..... 160

CHAPTER NINE

TABLE 9.1. The FWHM and final sample temperature measured for ^{19}F SINNMR spectra of PTFE. All acquisition parameters were identical..... 168

CHAPTER TEN

TABLE 10.1. ^{27}Al SINNMR Knight Shifts and line widths for a variety of metallic aluminium solids. *N.b.* Digital resolution throughout was set at 7 Hz (0.3 ppm)..... 172

TABLE 10.2 Some ^{27}Al Knight shift results for various experiments..... 174

CHAPTER ELEVEN

TABLE 11.1. List of compounds investigated by SINNMR which have failed to produce narrowing of resonances compared to the solid-state..... 182

CHAPTER TWELVE

TABLE 12.1. The required ultrasound frequency to produce certain cavitation bubble radii under isothermal conditions in a support liquid with a nominal density of 2.20 gcm^{-3}..... 185

TABLE 12.2. Visual observations using high frequency ultrasound on different compounds..... 186

TABLE 12.3. FWHM and chemical shift values (all relative and shielded to TMS) for the ^{29}Si NMR observation of SiO_2 in colloidal suspension and SINNMR experiments. The digital resolution in all experiments is 7.33 Hz (0.4 ppm)..... 188

TABLE 12.4. FWHM for the ^{11}B and ^{27}Al NMR observation of 20/70/10 glass in colloidal suspension and SINNMR experiments..... 190

APPENDIX TWO

TABLE A2.1. TSP ^{31}P SINNMR Initial Parameters as for figure 7.1..... 229

TABLE A2.2. TSP ^{31}P SINNMR parameters for measuremetns of the S/N ratio with varying particle size, mass of solid and density of support liquid..... 229

TABLE A2.3. TSP ^{23}Na SINNMR parameters for S/N ratio and FWHM with varying mass..... 230

TABLE A2.4. TSP ^{23}Na and ^{31}P solid and SINNMR Parameters for Optimum SINNMR Conditions. These parameters were used for all other TSP SINNMR experiements..... 230

TABLE A2.5. TSP ^{31}P solid Saturation Recovery Parameters..... 231

TABLE A2.6. TSP ^{31}P SINNMR Modified Saturation Recovery Parameters..... 231

TABLE A2.7. TSP ^{31}P solution DESPOT parameters (dummy pulses shown below)..... 232

TABLE A2.8. TSP ^{31}P solution DESPOT number of dummy pulses estimated for $t_i/T_1 = 0.1$..... 232

TABLE A2.9. PTFE ^{19}F SINNMR and solid parameters..... 233

TABLE A2.10. Aluminium and certain alloys, ^{27}Al NMR parameters for aqueous aluminium chloride reference..... 233

TABLE A2.11. Aluminium and its Alloys, ^{27}Al SINNMR parameters..... 234

TABLE A2.12. Doped Silicon ^{29}Si SINNMR Parameters..... 234

TABLE A2.13. Amberlite-MB3 ^{1}H SINNMR parameters..... 235

TABLE A2.14. Silylated coal ^{29}Si SINNMR Parameters..... 235

TABLE A2.15. Silicon dioxide ^{29}Si High frequency SINNMR parameters..... 236

TABLE A2.16. Sodium-boron-aluminium oxide glass ^{11}B SINNMR parameters for both 20/70/10 and 15/70/15 mole % samples..... 236

TABLE A2.17. Sodium-boron-aluminium oxide glass ^{27}Al SINNMR parameters for both 20/70/10 and 15/70/15 mole % samples..... 237

TABLE A2.18. ^{1}H NMR parameters for the investigation of $^{1}H_2O$ intensity with side transducer.....237

APPENDIX THREE

TABLE A3.1. Mean and standard deviation values calculated for the Gaussian distribution of 1000 - 500 μm and 1000 - 210 μm particle size ranges..... 240

TABLE A3.2. Calculated Gaussian distributions for 1000 - 500 μm and 1000 - 210 μm particle size ranges..... 240

TABLE A3.3. Data used in the calculation of the mass distribution 241

LIST OF FIGURES

CHAPTER ONE

FIGURE 1.1. Directional quantization of the angular momentum P in the magnetic field for nuclei with I = ½ and 1 27

FIGURE 1.2. Precession of Nuclear dipoles with spin I = ½ around a double cone 28

FIGURE 1.3. Energy level schemes for nuclei with I = ½ (a) and I = 1 (b). The energy difference ΔE between two adjacent energy levels as a function of the applied magnetic field is shown in (c) 29

FIGURE 1.4. Distribution of the precessing nuclear dipoles around the double cone As N_α is larger than N_β there is a resultant macroscopic magnetization M_0 30

FIGURE 1.5. Vectorial Representation of the Classical Larmor Precession 31

FIGURE 1.6. Manipulation of Magnetization by Nutation. When the system is allowed to relax $M_z \rightarrow M_0$ and $M_y \rightarrow 0$. The components and mechanisms of relaxation of themagnetization vector are introduced in the next section 32

FIGURE 1.7. The macroscopic magnetization shown resolved into three components M_x, M_y and M_z 33

FIGURE 1.8 The Behaviour of an Assembly of Identical Nuclear Magnetic Moments 35

FIGURE 1.9. Magnetic Fields in the Rotating Frame of Reference 36

FIGURE 1.10. Shapes of u and v Mode Signals from Bloch Equations 37

FIGURE 1.11. Bases for Referencing NMR Chemical Shifts 42

FIGURE 1.12. Motional frequency spectrum at high, medium and low correlation time. The vertical ordinate $J(\omega)$ represents the relative intensity of the motional frequency ω. The observation frequency being ω_0 47

FIGURE 1.13. Spin-lattice relaxation time T_1 and spin-spin relaxation time T_2 as a function of correlation time τ_c 47

CHAPTER TWO

FIGURE 2.1. Time and Frequencu Domain Responses of a monochromatic sine wave (a) and two superimposed sine waves with different frequencies and amplitudes (b)..... 53

FIGURE 2.2. Diagrams revealling how a narrow pulse has Fourier components over a relatively wide frequency range..... 54

FIGURE 2.3. Pictorial Example of a 1D Single Pulse Fourier Transform NMR Experiment..... 56

FIGURE 2.4. Chart of Jeol FX-90Q NMR Parameters and Gates for a Single Pulse Sequence..... 57

FIGURE 2.5. Lineshapes obtained by Fourier Transformation of Truncated Free Induction Decays where the ratio of the Acquisition Time to Transverse Relaxation T/T_2^* is *ca.* 1, 2 and 5 for (a), (b) and (c) respectively..... 60

FIGURE 2.6. Diagram showing the Tilted Effective Field in the Rotating Frame..... 63

CHAPTER THREE

FIGURE 3.1. The Description of angles for anisotropic rotation of the spin vector r_{ik}..... 67

FIGURE 3.2. Axial Symmetry CSA Powder Pattern..... 70

FIGURE 3.3. CSA Powder Pattern for No Axial Symmetry (a) and three different sets of $\sigma_{NN'}$ values producing the same isotropic shift (b)..... 71

FIGURE 3.4. Quadrupolar Powder Pattern for the case I = 3/2 showing the central transition -1/2, 1/2 superimposed on the broad pattern for the other two transitions: -3/2, -1/2 and 1/2, 3/2..... 74

FIGURE 3.5. The relationship of angles in Magic Angle Spinning NMR..... 76

CHAPTER FOUR

FIGURE 4.1. Variation of displacement y with time t for an ultrasonic source..... 83

FIGURE 4.2. Division into layers of a material through which ultrasound is propagated... 83

FIGURE 4.3. Appearance (exaggerated) of layers of a material in which longitudinal waves are propagated, showing compression at 'C' and expansion at 'E'..... .85

FIGURE 4.4. Reflection and Transmission for normal incidence at a plane boundary..... 87

FIGURE 4.5. Frequency response curves showing relationships between amplitude A and frequency f..... 89

FIGURE 4.6. Axes of a quartz crystal, indicating X-cut retangular and circular transducers..... 91

FIGURE 4.7. The Piezoelectric effect for compressional and shear wave transducers showing charges required on faces for oscillatory effects..... 91

FIGURE 4.8. Distribution of pressure and charge for a piezoelectric crystal oscillating at the fundamental frequency and at the second and third harmonics..... 92

FIGURE 4.9. A method of exciting a magnetostrictive transducer in the form of a rod.... 97

FIGURE 4.10. The Galton Whistle and Hartmann Generator..... 98

FIGURE 4.11. Side view arrangement for a wedge resonator..... 99

FIGURE 4.12. The profiles of horns for amplifying the output of transducers. The plots underneath each horn correspond to the velocity (top) and stress (bottom) profiles..... 101

FIGURE 4.13. A collapsing cavitation bubble showing a microjet directed at a solid surface..... 105

FIGURE 4.14. The balancing of ultrasonic and bouyancy forces on a single particle at different distances from an ultrasonic source. The supporting medium is considered to be more dense than the particle in this example..... 108

CHAPTER SIX

FIGURE 6.1. The Jeol FX-90Q Multinuclear NMR Probe showing air supplies, coils and seating within the permabody..... 115

FIGURE 6.2. Schematic of the High-Frequency Ultrasound Yaesu Apparatus..... 119

FIGURE 6.3. The relationship between the ratio of bromoform to chloroform and the density of support liquid produced..... 120

FIGURE 6.4. The position of the 20 kHz ultrasonic horn within a prepared sample tube for SINNMR experiments..... 121

FIGURE 6.5. High frequency ultrasound using a transducer directly bound to a glass rod by PTFE tape..... 122

FIGURE 6.6. Transducer unit, designed and built for SINNMR experiments. The main unit (a) is shown together with a cross-section of the transducer housing (b). All shaded areas are construced from brass..... 123

CHAPTER SEVEN

FIGURE 7.1. ^{31}P SINNMR spectrum of TSP under preliminary conditions..... 126

FIGURE 7.2. Hypothetical diagram of particle size distribution from the ultrasonic horn tip for a particular liquid density..... 129

FIGURE 7.3. Dependence of TSP particle displacement, from the tip of an ultrasonic horn operating at 20 kHz and 20 Wcm^{-2} (3 μm horn tip displacement), on support liquid density and particle size..... 131

FIGURE 7.4. ^{23}Na spectra (23.64 MHz) of TSP (a) static and (b) SINNMR with 20 kHz ultrasound and 3μm tip displacement: (c) and (d) are the corresponding ^{31}P spectra (36.20 MHz)..... 133

FIGURE 7.5. Effect of mass of solid TSP on (a) the S/N and (b) the FWHM of the ^{23}Na SINNMR spectra obtained using optimum particle size and support liquid. The error bars in (b) reflect the digital resolution..... 134

FIGURE 7.6. The proportions of 1000 - 500 μm fraction TSP recovered (w/w) after 5 minutes sonication with 20 kHz ultrasound at *ca.* 20 Wcm^{-2}. Different masses of TSP used are shown in the legend..... 135

FIGURE 7.7. The temperature dependence of (a) the S/N and (b) the FWHM of the thermally narrowed ^{23}Na resonance of a wetted solid sample of TSP. The error bars in (b) reflect the digital resolution..... 138

FIGURE 7.8. Decay of the ^{23}Na S/N from TSP with time after (a) thermal and (b) acoustic perturbations of approximately equal masses of solid..... 139

FIGURE 7.9. Theoretical dependence of relaxation times on correlation times, and T_1 values for the ^{31}P resonance (36.26 MHz) of TSP..... 142

FIGURE 7.10. Variation in Saturation Recovery of ^{31}P intensities of TSP under SINNMR conditions using the modified method with sonication time and (x) relaxation delay..... 143

FIGURE 7.11. Variation in Saturation Recovery of ^{31}P intensities of TSP heated to $50^{0}C$..... 143

FIGURE 7.12. Despot plot of $I_{eq} / \sin\theta$ against $I_{eq} \cos\theta / \sin\theta$ of ^{31}P TSP solution (0.05 M in water)..... 144

CHAPTER EIGHT

FIGURE 8.1. The displacement of the smallest TSP particles in each range with 20 kHz 3μ ultrasound and varying support medium..... 150

FIGURE 8.2. Support densities required for different TSP particle sizes to be displaced by 10, 17 and 24 mm from the ultrasonic horn by 20 kHz, 3μ ultrasound..... 152

FIGURE 8.3. Theoretically derived mass distribution curve for 1000 - 210 μm particle range of TSP. The equation of line for this distribution is given as equation (8.9)..... 156

FIGURE 8.4. Two dimensional slice through a hypothetical cubic particle used to discuss microjet interactions..... 159

FIGURE 8.5. Correlation time obtained from SINNMR experiments compared with a corrected (to obtain a comparable scale) inverse of microjet probability to facilitate incoherent motion..... 161

FIGURE 8.6. The interaction of an ultrasonic pressure wave with a particle showing the difference in pressure placed on faces A and B. The relative sizes of the particle and wavelength of ultrasound are exaggerated..... 163

CHAPTER NINE

FIGURE 9.1. The Static solid (a), and progressive narrowing by SINNMR (b) and (c), of the ^{19}F resonance in PTFE. Acquisition parameters were identical for all three experiments..... 167

FIGURE 9.2. Variation with temperature of the FWHM of the major ^{19}F resonance (84.26 MHz) of a static sample of PTFE..... 169

CHAPTER TEN

FIGURE 10.1. Superimposed ^{27}Al SINNMR spectra at 23.3 MHz of a metallic lithium (3%) / aluminium alloy and aqueous aluminium chloride (0.004 M) reference..... 173

FIGURE 10.2. Average ^{27}Al chemical shift positions (relative to aqueous aluminium chloride) obtained for (a) Li (3%) - Al alloy, (b) Dural®, (c) 99 % Al and (d) Al foil..... 173

CHAPTER ELEVEN

FIGURE 11.1. ^{1}H NMR spectra (89.56 MHz) of Amberlite showing narrowing from the static solid by 20 kHz SINNMR with 3μm tip displacement..... 180

FIGURE 11.2. ^{29}Si SINNMR resonances obtained using gated decoupling and 20 kHz ultrasound (3μm tip displacement) for silylated coal..... 181

CHAPTER TWELVE

FIGURE 12.1. ^{29}Si SINNMR spectrum of silicon dioxide obtained with 2 MHz ultrasound at 10 W power..... 188

FIGURE 12.2. ^{11}B NMR spectra of a $Na_2O/B_2O_3/Al_2O_3$ (15/70/15 mole %) glass with a density of 2.15 gcm^{-3}: (a) 96.3 MHz MAS NMR spectrum and (b) 28.75 MHz SINNMR resonance with FWHM 88 Hz in a suspension of bromoform with 2 MHz ultrasound from a PZT-5A transducer running at 10 W..... 191

FIGURE 12.3. ^{11}B SINNMR spectrum (28.75 MHz) of a $Na_2O/B_2O_3/Al_2O_3$ (20/70/10 mole %) glass from a suspension of bromoform irradiated with 2 MHz ultrasound at 10 W..... 191

FIGURE 12.4. Variation in the ^{11}B FWHM for the colloidal suspension of $Na_2O/B_2O_3/Al_2O_3$ (20/70/10 mole %) with electrical heating of the sample. The y axis error bars reflect the digital resolution..... 192

CHAPTER THIRTEEN

FIGURE 13.1. Prototype side transducer unit within a 10 mm o.d. glass NMR sample tube..... 195

FIGURE 13.2. The observed manipulation of 1 mm square PTFE particles in bromoform under (a) the action of only the 20 kHz ultrasound with 3 μm tip displacement and (b) with the addition of a 2 MHz side transducer driven at 10 W..... 196

FIGURE 13.3. Variation in intensity of ^{1}H NMR signal from water with orientation of a side transducer at the NMR probe region depth..... 197

APPENDIX ONE

FIGURE A1.1. The components of the magnetic moment μ in a magnetic field B_0..... 226

CHAPTER ONE

INTRODUCTION TO NUCLEAR MAGNETIC RESONANCE SPECTROSCOPY

1.1 INTRODUCTION

As the sonically induced narrowing of the nuclear magnetic resonance spectra of solids is principally of interest to the NMR community, the theoretical NMR chapters within this thesis have been simplified so that largely those areas relevant to the present research are discussed. This has enabled the inclusion of a substantial chapter on ultrasonics, which the author believes will be the area of least familiarity to the NMR spectroscopist. Further reading on any aspect of NMR can be gained from the texts listed in the bibliography.

Nuclear Magnetic Resonance (abbreviated to NMR) may be defined as a spectroscopic phenomenon exhibited by a large number of atomic nuclei, in which nuclei in a static magnetic field absorb energy from a (weaker) radio-frequency field at certain characteristic frequencies[5].

The existence of nuclear moments was first inferred from a study of the hyperfine structure observed in the electronic spectra of certain atoms[6]. This led Pauli[7] to suggest that certain nuclei possess spin angular momentum and thus a magnetic moment. In the presence of an applied magnetic field, magnetic moments take up specific orientations which can be perturbed by irradiation of the nuclei with energy of a suitable frequency. This absorption of energy by the nuclear moments forms the basis of the NMR technique. The first NMR signals were independently reported in 1945 by Bloch *et al*[8] and Purcell *et al*[9] through the observation of the proton (hydrogen - ^{1}H) nuclear resonance in water and paraffin wax respectively.

The first 25 years of NMR (up to *ca.*1970) saw the acquisition of spectra by the 'continuous-wave (CW)' technique in which either a polarizing field or rf field was swept with the other dependent experimental variable kept constant. In the course of the 1960's, the basic relation between measurement time and (poor) sensitivity[10] in NMR became common knowledge, and led to the use of signal averaging[11] instead of long-term single-scan measurements.

The 1970's heralded a revolution in NMR, firstly, with the development of pulse Fourier transform (FT) spectroscopy and secondly with the proposal and applications of two-dimensional spectroscopy[12]. These advancements have paved the way to modern spectrometers and the expansion of NMR into a much wider variety of applications.

1.2 MAGNETIC PROPERTIES OF NUCLEI

1.2.1 Nuclear Angular Momentum and Magnetic Moment

In addition to charge and mass, many nuclei possess intrinsic angular momentum, **P**. Quantum mechanical considerations show that, like many other atomic quantities, angular momentum is quantized:

$$\mathbf{P} = \sqrt{\mathbf{I}(\mathbf{I}+1)}\ \hbar \qquad \text{- (1.1)}$$

Here $\hbar = h/2\pi$, where h is Planck's constant, and I is the spin angular momentum quantum number, usually simply called the nuclear spin. Nuclei have one of the spin values I = 0, 1/2, 1, 3/2, 2 ....*etc* up to 6 and nuclei with I > 1/2 are said to be quadrupolar as the charge distribution on the nucleus is no longer spherical as in I = 1/2. The spin can be deduced theoretically using the quantum mechanical laws involving the shell model of nuclear structure with spins and parities[13]. However, there are useful empirical rules relating the mass number A and atomic number Z to the nuclear spin properties:

1. If both A and Z are even, then I = 0.

2. If A is odd and Z is odd or even, I will have a half-integral value.

3. If A is even and Z is odd, I will have a non-zero integral value.

The angular momentum **P** has associated with it a magnetic moment **μ**, both being vector quantities that are proportional to each other:

$$\boldsymbol{\mu} = \gamma \mathbf{P} \qquad \text{- (1.2)}$$

The proportionality factor γ is a constant for each nuclide (*i.e.* each isotope of each element), and is called the gyromagnetic ratio, or sometimes the magnetogyric ratio. The NMR detection sensitivity of a nuclide depends on γ; nuclides with large values of γ are said to be sensitive (*i.e.* easy to detect and observe), while those with small γ are insensitive. The magnetogyric ratio is defined for the maximum value of I as:

$$\gamma = \frac{2\pi\boldsymbol{\mu}}{\mathbf{I}h} \qquad \text{- (1.3)}$$

The combination of equations (1.1) and (1.2) defines the magnetic moment μ:

$$\boldsymbol{\mu} = \gamma\sqrt{I(I+1)}\hbar \qquad \text{- (1.4)}$$

It can be seen from equation (1.3) that nuclides with spin I = 0, such as ^{12}C, ^{16}O or ^{32}S, have no nuclear magnetic moment. Most nuclides have the angular momentum P and magnetic moment μ vectors (of the same sign) pointing in the same direction, *i.e.* they are parallel. However, in a few cases, for example ^{15}N and ^{29}Si, they are antiparallel. The nuclear magneton, which is analogous to the Bohr magneton for electron spin, can be used to specify observed nuclear moments by:

$$\mu = g\frac{ehI}{4\pi M_p c} \qquad \text{- (1.5)}$$

Table 1.1 shows the magnetic moments μ, gyromagnetic ratio γ, nuclear spin I and percentage abundance for a selection of nuclei.

Nucleus {Z}	Abundance (%)	Nuclear Spin I	Magnetic Moment μ *	Gyromagnetic Ratio γ #
^{1}H {1}	99.9844	1/2	2.7927	2.6752
^{2}H {1}	0.0156	1	0.8574	0.4107
^{13}C {6}	1.108	1/2	0.7022	0.6726
^{14}N {7}	99.635	1	0.4036	0.1933
^{19}F {9}	100	1/2	2.6273	2.5167
^{23}Na {11}	100	3/2	2.2161	0.7076
^{29}Si {14}	4.70	1/2	-0.5548	-0.5316
^{31}P {15}	100	1/2	1.1305	1.0829

TABLE 1.1 Magnetic Properties of Certain Nuclei of Interest to NMR Spectroscopists[14].

* - Magnetic moment in units of the nuclear magneton, $eh/(4\mu M_p c)$

\# - Gyromagnetic ratio in SI units, (x 10^8) rad T^{-1} s^{-1}.

1.2.2 Nuclei in a Static Magnetic Field

If a nucleus with angular momentum **P** and magnetic moment **μ** is placed in a static magnetic field B_0, the angular momentum is orientated such that its component P_Z along the direction of the field is an integral or half-integral multiple of $\hbar$:

$$\mathbf{P}_z = \mathbf{m}\hbar \qquad \text{- (1.5)}$$

where m is the magnetic or directional quantum number which can take any of the values m = I, I - 1,....., -I. It can be shown that there are (2I +1) different values of m, and consequently an equal number of possible orientations of the angular momentum and magnetic moment in the field B_0. This behaviour of the nuclei in a magnetic field is called directional quantization and is shown pictorially for nuclei with I = 1/2 and I = 1 in figure 1.1.

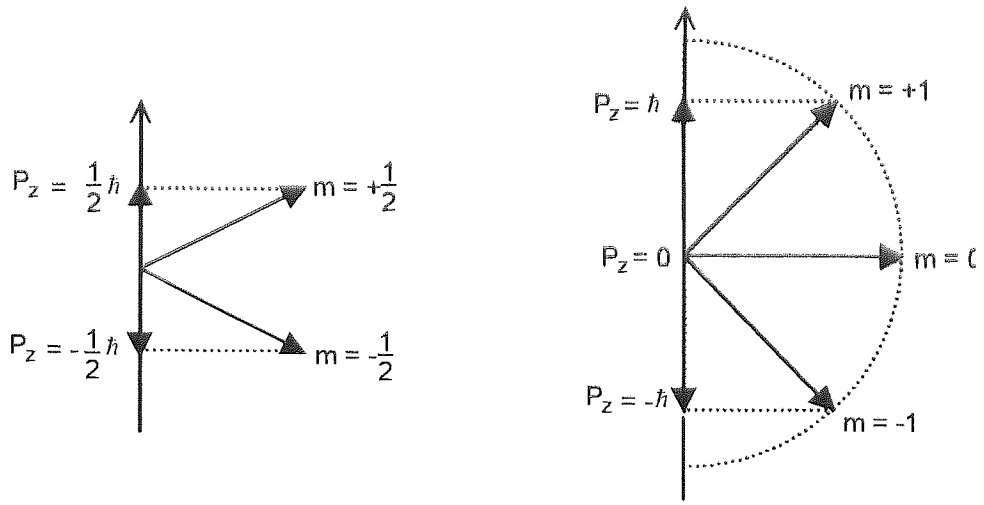

FIGURE 1.1. Directional quantization of the angular momentum P in the magnetic field for nuclei with I = ½ and 1.

The components of the magnetic moment along the polarizing field direction z can be obtained from equations (1.2) and (1.5):

$$\mu_z = m\gamma\hbar \qquad \text{- (1.6)}$$

In the classical representation the nuclear dipoles precess around the z-axis and their behaviour, shown in figure 1.2, resembles that of a spinning top.

The precessional frequency or Larmor frequency υ is proportional to B_0 through the well known relationship:

$$\nu = \frac{\gamma B_o}{2\pi} \qquad \text{- (1.7)}$$

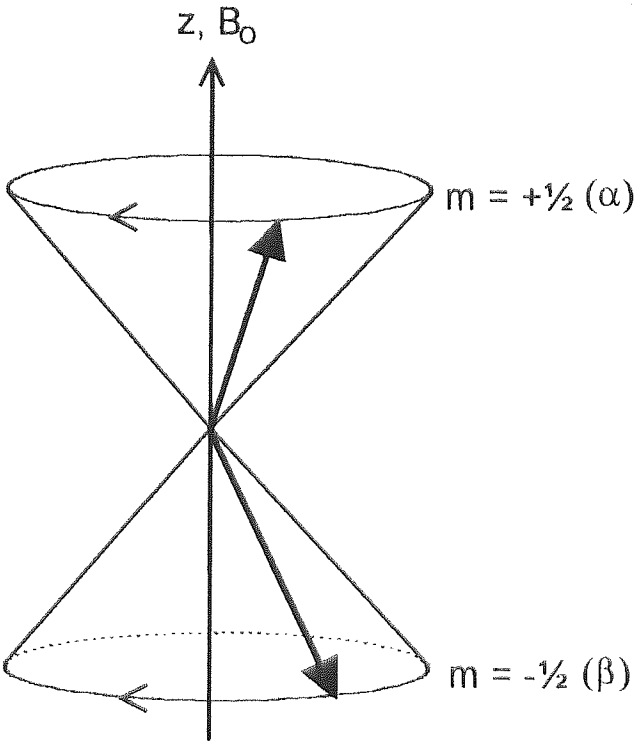

FIGURE 1.2. Precession of nuclear dipoles with spin I = ½ around a double cone.

or by incorporating equation (1.3):

$$\nu = \frac{\mu B_o}{Ih} \qquad \text{- (1.8)}$$

However, in contrast to the classical spinning top, a nuclear dipole can only precess at certain angles because of the directional quantization.

1.2.3 Energy of Nuclei in a Magnetic Field

The energy of a magnetic dipole in a magnetic field B_O (relative to that in zero field) is defined as:

$$E = -\mu_z B_o \qquad \text{- (1.9)}$$

A nucleus with (2I +1) possible orientations also has (2I +1) energy states, which are called the nuclear Zeeman levels, that may be obtained from the combination of equations (1.6) and (1.9):

$$E = -m\gamma\hbar B_o \qquad \text{- (1.10)}$$

The energy difference between adjacent levels is $\Delta E = \gamma\hbar B_0$. Figure 1.3 illustrates two energy level schemes using nuclei with I = 1/2 and I = 1 and the proportionality between ΔE and B_0 for an I = 1/2 nucleus.

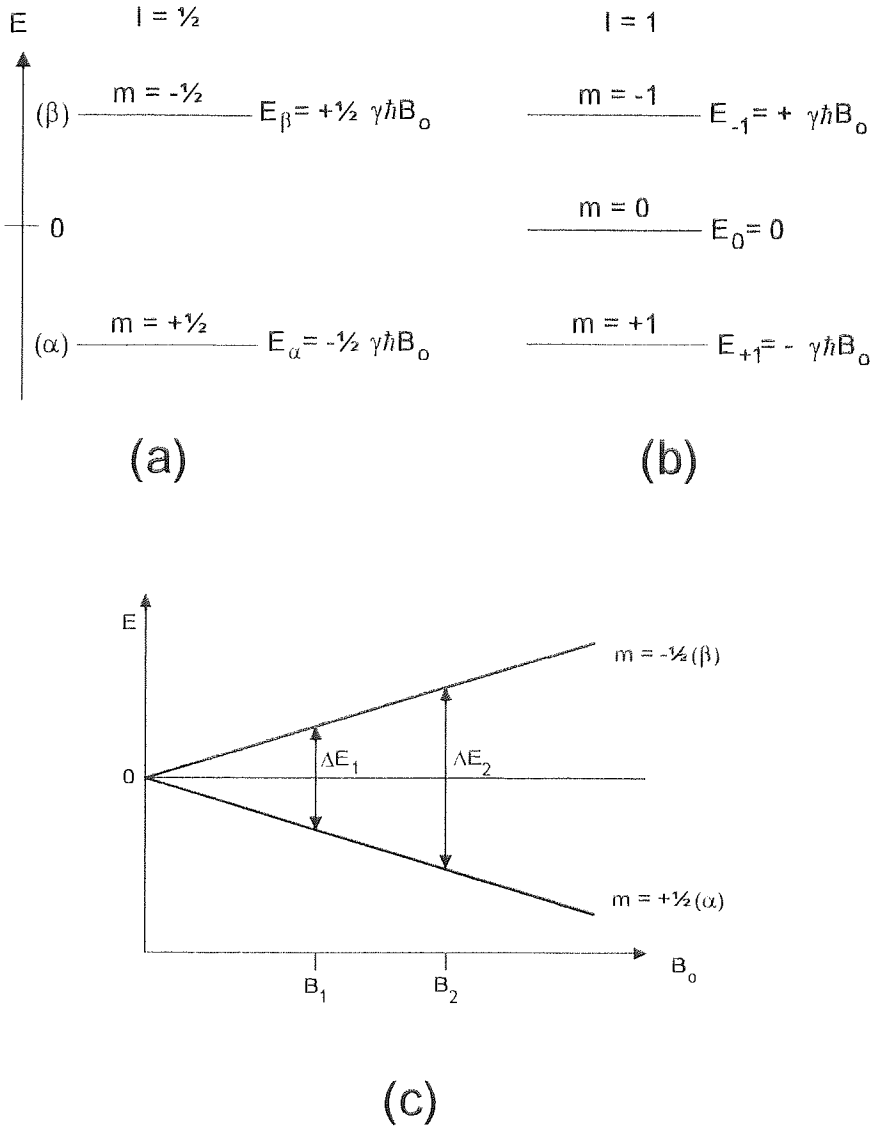

FIGURE 1.3. Energy level schemes for nuclei with I = ½ (a) and I = 1 (b). The energy difference ΔE between two adjacent energy levels as a function of the applied magnetic field is shown in (c).

1.2.4 Population of the Energy Levels

The nuclei within a macroscopic sample distribute themselves between the different allowed energy states according to Boltzmann statistics. For nuclei with I = 1/2, there are two energy levels as shown in figure 1.3 (a). If the number of nuclei in the upper energy level are N_β and the number in the lower energy level is N_α then:

$$\frac{N_\beta}{N_\alpha} = e^{-\frac{\Delta E}{k_b T}} \approx 1 - \frac{\Delta E}{k_b T} = 1 - \frac{\gamma \hbar B_o}{k_b T} \qquad \text{- (1.11)}$$

where k_b is the Boltzmann constant and T is absolute temperature in Kelvins (K).

It is found that the energy difference ΔE is very small compared with the average energy of thermal motions (K_bT), and consequently, the populations of the energy levels are almost equal. However there is an excess in the lower energy level α but this is only in the region of parts per million. Equation (1.11) gives the population's dependence on B_o and T; the population difference increases with increasing magnetic field strength and decreases with increasing temperature.

1.2.5 Macroscopic Magnetization

The classical description shows the magnetic moment of a nucleus with I = 1/2 precessing about a defined double cone as shown in figure 1.2. In a macroscopic sample there will be magnetic moments precessing in both cones, the numbers of which are governed by the Boltzmann statistics. If the sum of all the z components of the magnetic moments is taken, the resultant is the macroscopic magnetization (M) which at thermal equilibrium is referred to as M_o. This resultant lies along the field direction due to N_α being slightly larger than N_β (see figure 1.4) and the vector M is used extensively in the description of all types of pulsed NMR experiments.

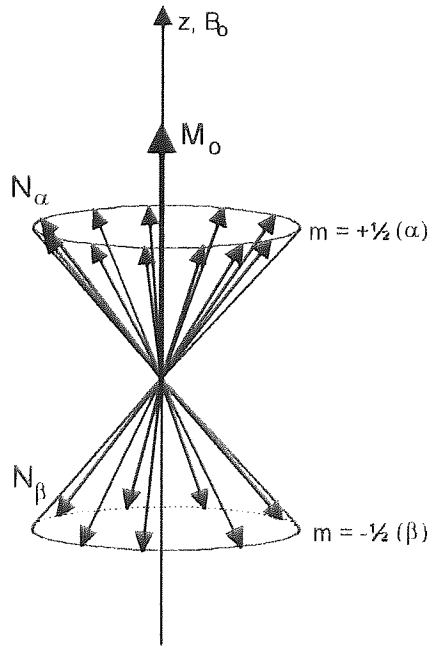

FIGURE 1.4. Distribution of the precessing nuclear dipoles around the double cone. As N_α is larger than N_β there is a resultant macroscopic magnetization M_o.

1.3 THE NMR EXPERIMENT

In the NMR experiment transitions are induced between different energy levels by irradiating the nuclei with a superimposed field B_1 of the correct quantum energy. The field B_1 is produced perpendicular to B_0 and rotates about the z axis with a frequency ω (equal to ω_0 only at exact resonance) and is produced by one of the two counter rotating magnetic vectors of a linearly polarised rf field. Consider for the moment only those nuclei with I = 1/2:

Transitions, from the lower to the upper energy levels correspond to an absorption of energy, and those in the reverse direction, an emission of energy. These transitions, of equal probability, are associated with a reversal of the spin orientation, but due to the population excess in the lower energy level, the absorption of energy from the radiating field is the dominant process. The term 'resonance' relates to the classical interpretation of the phenomenon, since transitions only occur when the rotating frequency of the electromagnetic superimposed field B_1 matches the Larmor frequency of the precessing nuclear moments. A pictorial classical representation of Larmor precession in relation to the fields B_0 and B_1 is shown in figure 1.5.

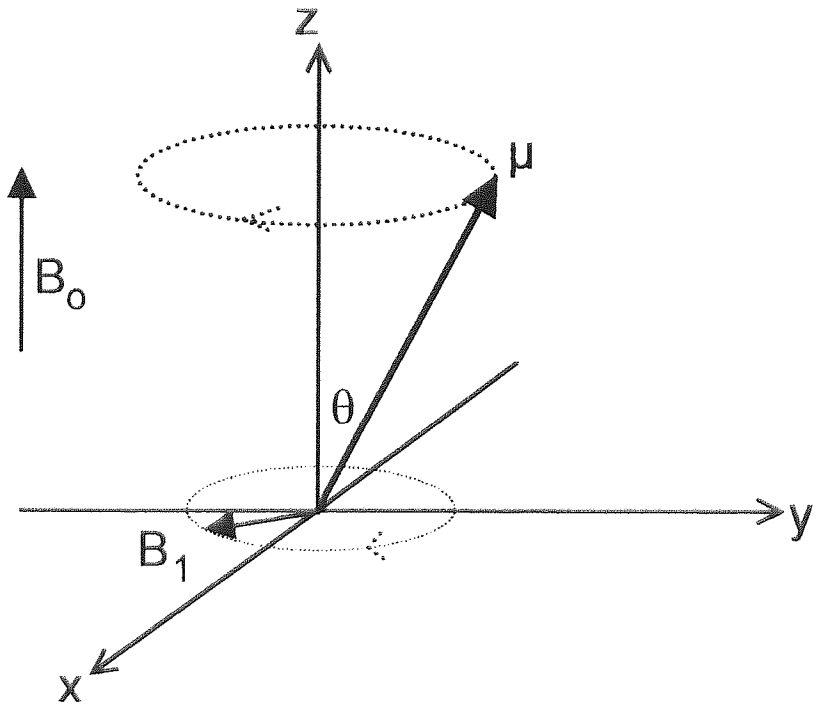

FIGURE 1.5. Vectorial Representation of the Classical Larmor Precession.

Nuclei with I > 1/2 have more than two energy levels and the understanding of the NMR experiment in such systems is enabled through quantum mechanics. Quantum mechanics states that only those transitions in which the magnetic quantum number m changes by 1, *i.e.* only single quantum transitions are allowed

so that $\Delta m = \pm 1$. According to this selection rule the transition from m = +1 to m = -1 for a ^{14}N nucleus, for example, is forbidden.

1.4 MAGNETIZATION

1.4.1 The Manipulation of Magnetization

Section 1.3 discusses the NMR experiment where a radio frequency field B_1 can produce resonance when the field rotates with the same frequency as the magnetic moment μ.

As the bulk magnetization M is a vector sum of the magnetic moments, the resonance condition also affects M. The application of the B_1 field causes the magnetization vector to tip (nutate) from its equilibrium position along the z axis towards the x,y plane as in figure 1.6. The time that B_1 is applied for determines the angle θ of the nutation (in radians) and is defined in equation (1.12):

$$\theta = \gamma B_1 \tau \qquad \text{- (1.12)}$$

It is this nutation which produces M_x, M_y (discussed later in section 1.4.3) and M_z vector components which govern the appearance of the NMR signal. Once the B_1 field is removed, the nutated magnetization components recover to their equilibrium values by relaxation processes (see section 1.4.3 and 1.8). The recovery of M_z shown in figure 1.6 is governed by spin-lattice (longitudinal) relaxation.

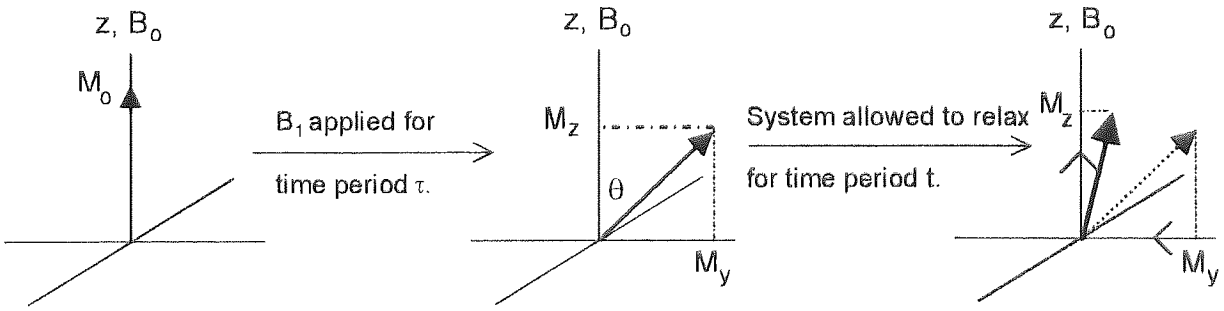

FIGURE 1.6. Manipulation of Magnetization by Nutation. When the system is allowed to relax $M_Z \rightarrow M_0$ and $M_y \rightarrow 0$. The components and mechanisms of relaxation of the magnetization vector are introduced in the next section.

1.4.2 The Bloch Equations

The experimental observations of NMR can be conveniently described by the approach of Bloch[15]. The macroscopic magnetization vector without

perturbation M can be resolved according to Bloch into three components M_x, M_y, and M_z. These components are shown conventionally in figure 1.7.

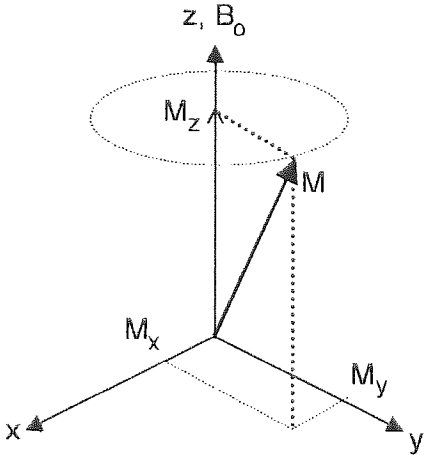

FIGURE 1.7. The macroscopic magnetization shown resolved into three components M_x, M_y and M_z.

The static B_O field is in the z direction, and M like the individual moments , will precess about the z axis. In the absence of relaxation effects and the rotating field B_1, M_Z would remain such that

$$\frac{dM_z}{dt} = 0 \qquad \text{- (1.13)}$$

The magnitudes of the x and y projections M_x and M_y however vary with time as M precesses about the z axis. The time dependence is expressed by:

$$\frac{dM_x}{dt} = \gamma M_y . B_o = \omega_o M_y \qquad \text{- (1.14)}$$

$$\frac{dM_y}{dt} = \gamma M_x . B_o = \omega_o M_x \qquad \text{- (1.15)}$$

In addition to the field B_O, the rotating field B_1 must also be considered. This field rotates in the x-y plane (see section 1.3) and its inclusion leads to the modification of equations (1.13 - 1.15) thus:

$$\frac{dM_x}{dt} = \gamma[M_y B_o - M_z (B_1)_y] \qquad \text{- (1.16)}$$

$$\frac{dM_y}{dt} = \gamma[M_x B_o - M_z (B_1)_x] \qquad \text{- (1.17)}$$

$$\frac{dM_z}{dt} = \gamma[M_x B_o - M_y (B_1)_x] \qquad \text{- (1.18)}$$

where $(B_1)_X$ and $(B_1)_Y$ are the components of B_1 along the x and y axes and are given by:

$$(B_1)_x = B_1 \cos\omega t \qquad \text{- (1.19)}$$

$$(B_1)_y = -B_1 \sin\omega t \qquad \text{- (1.20)}$$

The next step is to consider the relaxation of components of M in the x, y and z directions. The relaxation of the z component towards its equilibrium value M_O may be expressed:

$$\frac{dM_z}{dt} = -\frac{M_z - M_o}{T_1} \qquad \text{- (1.21)}$$

and similarly the relaxation of the x and y components have a different time constant T_2:

$$\frac{dM_x}{dt} = -\frac{M_x}{T_2} \qquad \text{- (1.22)}$$

$$\frac{dM_y}{dt} = -\frac{M_y}{T_2} \qquad \text{- (1.23)}$$

Addition of these terms to equations (1.16 - 1.20) results in the complete Bloch equations:

$$\frac{dM_x}{dt} = \gamma[M_y B_o - M_z (B_1)_y] - \frac{M_x}{T_2} \qquad \text{- (1.24)}$$

$$\frac{dM_y}{dt} = \gamma[M_x B_o - M_z (B_1)_x] - \frac{M_y}{T_2} \qquad \text{- (1.25)}$$

$$\frac{dM_z}{dt} = \gamma[M_x B_o - M_y (B_1)_x] - \frac{M_z - M_o}{T_1} \qquad \text{- (1.26)}$$

1.4.3 An Introduction to Relaxation

The final stage in the description of the Bloch equations involves the consideration of the relaxation of the components of the bulk magnetization. The relaxation of the magnetization enables a perturbed system, *e.g.* a system at the resonance condition, to return to its initial (equilibrium) state when for example the B_1 field is

removed. There are two main mechanistic types: longitudinal or spin-lattice relaxation and transverse or spin-spin relaxation. The relaxation of magetization to its equilibrium z axis value is governed by spin lattice relaxation with its characteristic time T_1. The latter has its mechanism for this kind of transition provided by the lattice, and because the probability of emmision transitions is greater than that of absorption, the process of spin-lattice relaxation is observed. Relaxation to the equilibrium y and z axes values is achieved by spin-spin relaxation with its characteristic time T_2.

Section 1.4.1 describes how the magnetization can be manipulated by applying the B_1 field which nutates the magnetization.

The nutation ceases when B_1 is removed and at this point the vector M as in figure 1.8 has three components M_x, M_y and M_z. These three components return to their respective equivalent equilibrium values of zero, zero and M_o respectively via the spin-spin relaxation mechanism for M_x and M_y and the spin-lattice relaxation mechanism for M_z. The relaxation processes are discussed further in section 1.8.

EQUILIBRIUM	RESONANCE	RETURN TO EQUILIBRIUM GOVERNED BY	
$\sum_i \mu_{z_i} = M_o$	M_z	$M_z\left(e^{-\frac{t}{T_1}} \longrightarrow\right) M_o$	Population Distribution
$\sum_i \mu_{y_i} = 0$	M_y	$M_y\left(e^{-\frac{t}{T_2}} \longrightarrow\right) 0$	Phase Incoherence
$\sum_i \mu_{x_i} = 0$	M_x	$M_x\left(e^{-\frac{t}{T_2}} \longrightarrow\right) 0$	Phase Incoherence

FIGURE 1.8 The Behaviour of an Assembly of Identical Nuclear Magnetic Moments.

1.4.4 The Rotating Frame of Reference

The resultant magnetization vector M, precessing in the laboratory frame with an angular frequency ω_o and in general B_1 rotating at ω is a complicated system to deal with. It simplifies matters if the manipulated magnetization in an NMR experiment can be considered stationary.

The picture can be simplified by not dealing with the situation in the laboratory frame as described above, but in a frame rotating with the same angular frequency as B_1. The rotating frame is assigned axes x', y' and z' to distinguish it from the laboratory frame which has axes x, y and z. However, as the frame rotates as B_1, the axes z and z' are identical. This means that B_1 is fixed in the rotating frame and M precesses at $(\omega_o - \omega)$.

This corresponds to precession in an apparent field defined as:

$$B_{app} = \frac{(\omega_o - \omega)}{\gamma} = B_o\left(1 - \frac{\omega}{\omega_o}\right) \qquad \text{- (1.27)}$$

The total field B_t experienced by M_z is the vector sum of B_o and B_1 which is essentially B_o. It can be of use to define an effective field B_{eff} as the sum of B_{app} and B_1; all these defined vectors (not to scale) can be seen in figure 1.9.

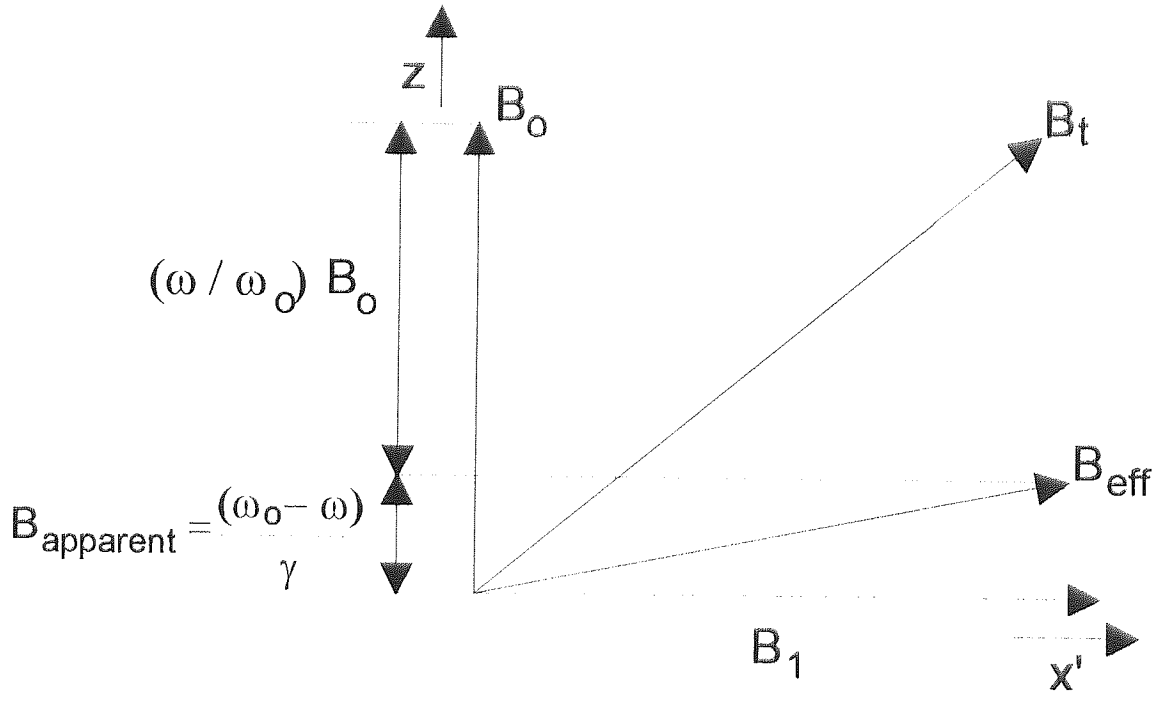

FIGURE 1.9. Magnetic Fields in the Rotating Frame of Reference.

In the rotating frame M will precess about B_{eff}. There are two limiting cases. Away from the resonance ($\omega \neq \omega_o$) precession about B_o occurs, while at resonance M precesses about B_1 at the rate γB_1 in the zy' plane so there is a y' component that can be detected as an NMR signal which is dependent on the rate of change of M_y.

The signal detected by the NMR spectrometer contains two components, u and v, that are along the x' and y' axes respectively. These give rise to absorption v mode and dispersion u mode signals, the form of which can be seen in figure 1.10.

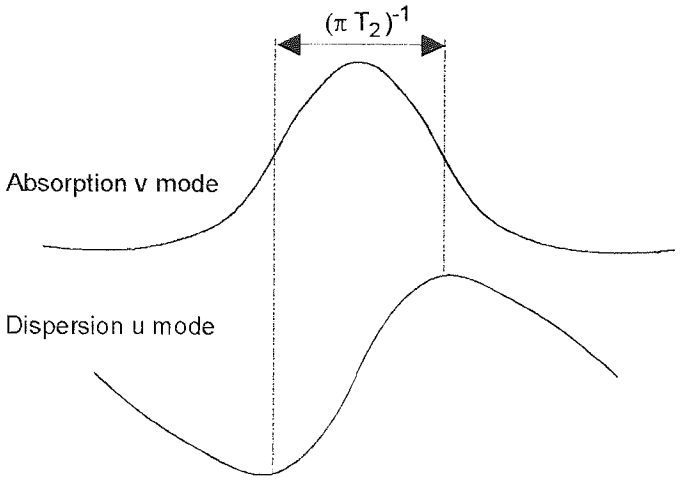

FIGURE 1.10. Shapes of u and v Mode Signals from Bloch Equations.

1.4.5 The Intensity of NMR Absorptions

The intensity of an I = ½ NMR signal is one of the five parameters which governs its appearance; the others being chemical shift, spin-lattice relaxation, spin-spin relaxation and scalar coupling.

As shown in section 1.3, the transitions of spins in the NMR experiment produce a signal. The intensity is proportional to the population difference N_α - N_β, and is, therefore, also proportional to the total number of spins in the sample, and thus to the concentration. However, if the populations are equal ($N_\alpha = N_\beta$) the absorption and emission processes cancel each other and no signal is observed. This condition is known as saturation.

The dependence of the NMR signal on the population difference and hence concentration indicates that the appearance of the signal will vary according to the sample under investigation and the parameters used for observation. Variations in signal intensity occur not only with the study of one NMR active nucleus in different samples, but also for different nuclei. This is due to two reasons. The population distribution described by equation (1.11) is proportional to the gyromagnetic ratio γ and, additionally, different NMR active isotopes are naturally abundant in different amounts. In order to place some classification of the ease of detection of nuclei, physical NMR data tables usually contain the relative receptivity and natural abundance of each NMR isotope.

The relative receptivity of an 'x' isotope to a standard 'y' nucleus is defined as:

$$R_x^y = \frac{a_x \gamma_x I_x (I_x + 1)}{a_y \gamma_y I_y (I_y + 1)} \qquad \text{- (1.28)}$$

where a_n is the number of nuclei of isotope 'n' as a percentage of the total number of nuclei. The standard 'y' nucleus is usually ^{13}C with an $R^{13C} = 1$. If an isotope of interest has an R value greater than 1, it can be considered easier to detect by NMR than ^{13}C; *vice versa* if R is less than 1. R values can also be given with ^{1}H as the standard but can be considered less useful due to ^{1}H being the most NMR receptive naturally occurring isotope.

The measurement of other parameters (such as T_1 and T_2) depends directly upon the measurement of signal intensities, which in modern spectrometers, usually involves software driven integration. The magnitudes of T_1 and T_2 affect the signal intensities in a way that is described in chapter 2, with direct relevance to Fourier transform NMR.

It must be remembered that under certain conditions anomalous intensities may be produced. The most obvious example is where partial saturation occurs. Another is the intensity modifications inherent in, for example, ^{13}C NMR spectra under conditions where the ^{1}H - ^{13}C nuclear Overhauser effect[16,17] is exploited to enhance sensitivity, *c.f.* section 1.8.3. It is important that in any NMR experiment in which the spin system is prepared in an arbitrary non-equilibrium state, the relevant theoretical considerations must be clearly understood before intensity measurements are used.

The spectroscopist can also unintentionally alter the signal intensity by the use of the many data manipulating functions available on modern spectrometers. Most commonly used are weighting functions on the raw data collected from the spectrometer coils which distort the line shape and hence intensities. However, a simple exponential weighting function will preserve the correct intensities for Lorentzian lines.

1.5 FACTORS AFFECTING THE APPEARANCE OF NMR SPECTRA

1.5.1 Line Widths - Transverse Relaxation and Inhomogeneity

The width of an NMR line is related to the spin-spin (transverse) relaxation time T_2 and the spin-dephasing caused by instrumental inhomogeneities; largely that is due to the inhomogeneity of the magnetic field. The full width at half maximum height (FWHM or $\Delta\upsilon_{1/2}$) of an NMR line is given by:

$$FWHM = \frac{1}{\pi T_2^*} \qquad \text{- (1.29)}$$

$$\text{where : } \frac{1}{T_2^*} = \frac{1}{T_{2s}} + \frac{1}{T_{2i}} \qquad \text{- (1.30)}$$

where T_{2s} is the spin-spin relaxation time of the spin system and T_{2i} characterises the spin-dephasing. It is because of field inhomogeneity that all NMR spectrometers have a maximum resolution (optimum FWHM) which for modern machines is approximately 0.1 Hz for ^1H observation in solution or liquids.

In section 1.8 it is shown how the motional characteristics of molecular species can affect the relaxation times and hence the line width. This knowledge can also be used in reverse; to deduce motional characteristics from line shapes.

The NMR line width for a molecular species also depend on whether that species is in chemical exchange with another chemically distinguishable site. The way chemical exchange affects the NMR spectrum depends very much on the rate of exchange. An excellent insight into how chemical exchange affects NMR has been written by Freeman[18].

1.5.2 Paramagnetic Species

Paramagnetic species, either unpaired electrons or other magnetic nuclei cause fluctuations in the static magnetic field at the observed NMR nucleus. These fluctuating fields are proportional to the magnetic moment μ_{para}, of the paramagnetic species and inversely proportional to the cubed distance (r^3), between the paramagnetic species and the observed nucleus.

The main effect is to cause an increase in the efficiency of nuclear relaxation and hence a subsequent increase in the width of the resonance line. In cases where μ_{para} is large, as for the unpaired electron, the line may be broadened to the extent that it might not be observed at all. Certain paramagnetic species (usually lanthanum or europium) can be used to produce a contact or pseudo-contact shift[19] without significant line broadening which greatly assists in the resolution of overlapping multiple resonances. There is an excellent review on Shift Reagents by Friebolin[20].

1.5.3 Quadrupolar Effects

Nuclei with spin quantum number I > 1/2 possess a nuclear quadrupole moment arising from a non spherical distribution of nuclear charge. Quadrupoles may precess in the presence of an electric field gradient enabling relaxation transitions to occur among the nuclear quadrupole energy levels. This process is often more efficient than the dipole relaxation processes (see section 1.8) exhibited by spin 1/2 nuclei. As before, the relaxation times become reduced and the resonance lines tend to be broad.

1.5.4 Digital Resolution

Fourier transform NMR relies on the digitisation of an analogue signal to eventually yield the spectrum (see chapter 2). If there are insufficient data points across the spectral width then the peak shape will be determined by the data point resolution.

1.6 THE CHEMICAL SHIFT

The power and utility of NMR spectroscopy is derived from the fact that the nuclear spins of the same isotope but in different chemical environments absorb energy at different radio frequencies for a given applied field. This discovery was made in 1949 while studying the NMR spectra of compounds containing phosphorus, nitrogen and fluorine[21]. It was also reported in 1950 that the ^1H NMR signal from water did not occur at that same frequency as for those in mineral oil[22,23].

1.6.1 Nuclear Screening

The absorption of energy by nuclei of the same isotope at different frequencies is due to the variation in magnetic field strength caused by local environment about each nucleus. Each group of magnetically equivalent nuclei in a sample experiences a modified magnetic field B_{loc} defined as:

$$B_{loc} = B_o(1-\sigma) \qquad -(1.31)$$

where σ is the screening constant (known as the shielding tensor[24]) for a particular environment. Incorporation of this equation into equation (1.8), gives the nuclear precessional frequency for each NMR environment as:

$$\upsilon = \frac{\mu B_o (1-\sigma)}{Ih} \qquad \text{- (1.32)}$$

Each NMR environment will have a unique value of σ and thus precessional frequency and so as long as resolution is favourable, the NMR spectrum should resolve resonances from each environment at their characteristic positions (chemical shifts) in the spectrum. The NMR spectrum is presented as NMR absorption (y-axis) with frequency (x-axis).

1.6.2 Spectral Referencing

Nuclei which resonate at different frequencies are separated by the chemical shift. The true definition of chemical shift between two nuclei i and j is:

$$\delta_{ij} = \sigma_i - \sigma_j \qquad \text{- (1.33)}$$

and by convention, NMR spectra are presented with the screening increasing from left to right. The implication of this in relation to equation (1.32) is shown in figure 1.11. In practice, chemical shifts, are calculated from experimentally measurable parameters such as magnetic field or frequency:

$$\delta_{ij} = \frac{(B_i - B_j)}{B_j} \text{ or } \delta_{ij} = \frac{(\upsilon_i - \upsilon_j)}{\upsilon_j} \qquad \text{- (1.34)}$$

In figure 1.11, j is taken as the reference and is more screened than i. This in magnetic field terms defines the chemical shift as negative. However, most spectrometer and chart manufacturers define the chemical shifts on their instruments using the frequencies. This is in accordance with the IUPAC convention[25] which states:

(a) $\delta > 0$ for any line detected at a higher frequency than that of the chosen reference (deshielded or downfield).

(b) $\delta < 0$ (*i.e.* negative) for any line detected at a lower frequency than that of the chosen reference (shielded or upfield).

The values obtained from equation (1.34) are usually presented as numbers of parts per million (ppm) by multiplying the result obtained from (1.34) by 1×10^6.

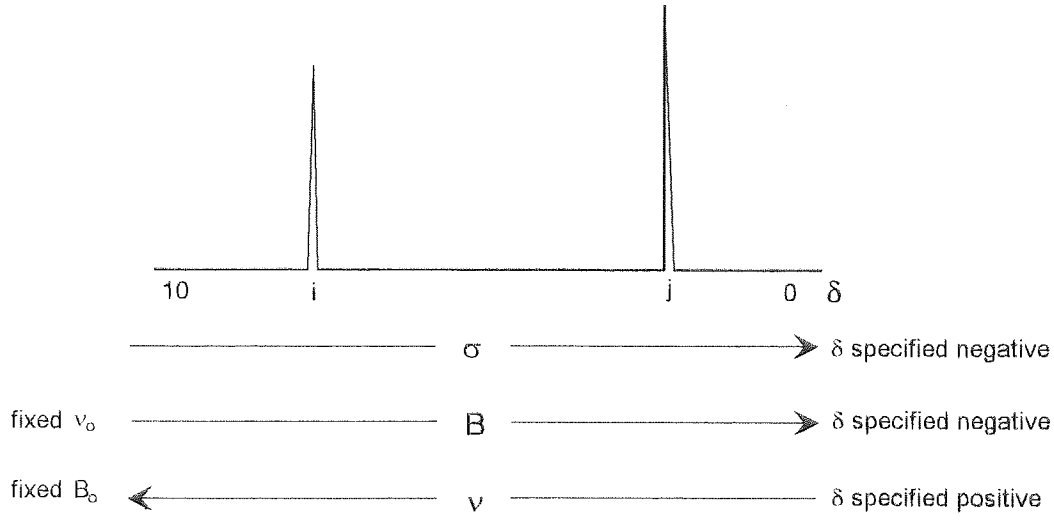

FIGURE 1.11. Bases for Referencing NMR Chemical Shifts. δ is specified according to equations (1.33) and (1.34).

Any signal can be used as reference as long as it is clearly stated, together with concentration and temperature of the experiment as there can severely affect the chemical shift in certain cases. There are recognised reference materials such as tetramethylsilane (TMS) - $(CH_3)_4Si$ which is used for ^1H and ^{13}C and ^{29}Si NMR. A comprehensive list of references for other NMR isotopes can be found in a guide by Brevard and Granger[26].

Chemical shifts are composed of intra and intermolecular shift differences relative to the reference and may be written simplistically as:

$$\Delta\sigma_{intra} = \Delta(\sigma_{elec} + \sigma_{E} + \sigma_{aniso} + \sigma_{deloc})_{sample-reference} \qquad \text{- (1.35)}$$

where the respective terms are due to the effects of neighbouring atom electronegativity, electric fields, magnetic fields produced by magnetic anisotropic species and delocalized ring currents. In addition there are terms arising from intermolecular interactions that may be characterized by:

$$\Delta\sigma_{inter} = \Delta(\sigma_{b} + \sigma_{w} + \sigma_{a} + \sigma_{e} + \sigma_{s})_{sample-reference} \qquad \text{- (1.36)}$$

Here the respective terms are due to bulk magnetic susceptibility, van der Waals forces, the neighbour anisotropy of molecules, electric fields and specific interactions such as hydrogen bonding.

1.6.3 The Use of Chemical Shifts

The use of ^{1}H and ^{13}C chemical shifts in the elucidation of the chemical environment and structure is well documented[27]. The chemical shifts obtained for other nuclei can also be of use in structural determination.

The range of chemical shifts varies with the NMR isotope under investigation, *e.g.* the chemical shift range for ^{1}H is *ca.* 10 ppm but for ^{13}C is *ca.* 200 ppm.

It was found by Knight[28] that the resonance frequency of copper - ^{63}Cu in metallic copper occurred at a frequency 0.23 percent higher than that of the diamagnetic CuCl salt in the same magnetic field. Since the shift was an order of magnitude greater than the chemical shifts of different diamagnetic compounds of Cu, he attributed the observations to an effect in the metal. This large deshielding, compared to the normal chemical shift range, (observed for most metallic elements and conducting species) is called the Knight shift. The large deshielding is thought to be due to the interactions of the Fermi electrons with the nucleus in each atom. A comprehensive treatment of the theoretical and practical details of Knight shifts has been made by Slichter[29] and Winter[30].

1.7 SPIN-SPIN COUPLING

The examination of spectra under high resolution conditions often reveals that the chemically shifted absorptions can be composed of several lines. The first observations of this nature were found for the antimony (^{121}Sb) resonance in $NaSbF_6$[31,32]. Purification ensured there was only one form of Sb present, but, the ^{121}Sb NMR spectrum had seven equally spaced lines intensity ratios 1:6:15:20:15:6:1.

A study of multiplet splitting by Gutowsky and McCall[32]showed that fine structure may arise for any molecule containing two or more chemically shifted nuclei. A molecule designated AX_n, where A and X are non-equivalent, would produce an NMR signal from nucleus A that is split into $2nI_X+1$ where I_X is the spin quantum number of X and the relative intensities given by the nth binomial coefficients. When the shifts between A and X are large, the multiplet lines are equally spaced with the magnitude of the spacing being known as the coupling or spin-spin coupling constant J (J_{AX} between nuclei A and X) in hertz. The case of $NaSbF_6$ is due to the ^{121}Sb NMR peak being split by the ^{19}F nuclei surrounding it. For brevity, second order spin-spin coupling and chemical and magnetic equivalence

are not discussed. The author directs the reader to any of the general NMR text books listed in the bibliography.

1.7.1 The Origin of Spin-Spin Coupling

Consider a two spin system AX, with the nuclei having different chemical shifted NMR signals, one at a frequency of υ_A and one at υ_X. If A and X are spin 1/2 and coupled to each other, two signals are observed for the A nuclei, and two for the X nuclei. Considering just A, the local magnetic field B_{loc} can be further perturbed by the neighbouring X nucleus. This is because X can be coupled to A while in the α or β spin energy state which each produce different magnetic fields at A. This interaction between A and X produces two additional field contributions at A, with the contributions of the two states of the X nucleus being equal in magnitude but opposite in sign. This produces two situations where υ_A is either shifted to higher frequency or lower frequency by an equal amount. In a macroscopic sample the number of X nuclei in the α state and β state is nearly identical and hence two lines of equal intensity occur. The splitting between the two lines is J_{AX} and the doublet lines are $\pm\frac{1}{2}J_{AX}$ from υ_A and υ_X respectively. The relative intensities are produced from the probabilities of producing the allowed spin state combinations. In an AX_2 system (all spin 1/2), the A resonance has three lines with relative intensities 1:2:1. If the two X nuclei are denoted X' and X'' then the spin state combinations are $\alpha'\alpha''$, $\alpha'\beta''$, $\beta'\alpha''$, $\beta'\beta''$.

The centre $\alpha\beta$ and $\beta\alpha$ combinations will produce an identical change in the magnetic field but as there are two combinations compared to one $\alpha\alpha$ and $\beta\beta$, then there is twice the probability of this state occurring. Thus the lines produce an intensity ratio seen as a reflection of the probability. The same argument can be taken to other spin 1/2 AX_n systems to show when n = 3, 4, 5.. then there are respectively 4, 5 and 6 lines with relative intensities 1:3:3:1, 1:4:6:4:1 and 1:5:10:10:5:1. Generalizing for a spin 1/2 nucleus with n equivalently coupled spin 1/2 neighbours, its resonance will be split into n+1 peaks corresponding to the n+1 spin states of the neighbouring groups with peak intensities determined by simple statistical considerations, or conveniently by use of Pascals triangle.

The coupling of nuclei with spins of one or greater is rarely dealt with, however, deuterium - ^2H and nitrogen - ^{14}N are the most frequently encountered. Nuclei such as these with a spin of one have three possible spin states. One such nucleus will split another nucleus (or equivalent nuclei), of whatever spin, into a 1:1:1 triplet; two will produce a 1:2:3:2:1 pentuplet and so on. A simple method of predicting multiplet intensities for $I>\frac{1}{2}$ has been given by Homer and Mohamaadi[33].

Spin-spin coupling can be either short range or long range, the former involving two nuclei directly bonded to each other with coupling constants ^1J. The number of bonds between the coupled nuclei is indicated by a superscript preceding the coupling constant symbol, *i.e.* ^nJ. Long range couplings are classed into three main groups and constants; geminal couplings - ^2J, vicinal couplings - ^3J and long range couplings - ^{3+n}J.

1.7.2 The Use of Spin-Spin Coupling

Much information can be gained from coupling patterns in spectra which can enable chemists and biochemists to understand the conformations and structure of compounds.

There have been extensive investigations into indirect spin-spin couplings (^1H-^1H) involving the dependence on bond angles, substituents and neighbouring π-electron groups. A dependence on the dihedral angle of vicinal (^3J) couplings in saturated systems was found by Karplus[34]. Karplus was able to state the form of the dependence of the vicinal coupling constant with the dihedral angle for appropriate compounds. This relationship was able to assist in the deduction of the energies of rotational isomers.

Recently, a new and convenient method of assignment and measurement of long-range ^{13}C - ^1H coupling constant using 2D-NMR has been established by Keeler *et al*[35].

1.8 NMR RELAXATION

In section 1.4.3, the concept of relaxation was discussed involving the two relaxation mechanisms important in NMR. Spin-lattice relaxation with its corresponding time T_1 is a process whereby a net non-radiative energy transfer takes place from an excited spin to the lattice degrees of freedom of the system. Spin-spin relaxation with its corresponding time T_2 is a process less easily understood in physical terms. T_2 relaxation does not involve the exchange of spin energy with the lattice, but is concerned with energy exchange between spins, via a flip-flop type mechanism.

1.8.1 The Effect of Motion on Relaxation

NMR relaxation can occur because each NMR nucleus is not entirely isolated from the assembly of molecules, commonly referred to as the lattice and hence 'spin-lattice relaxation' with the corresponding time T_1. The spins and the lattice can be considered as essentially separate coexisting systems with an inefficient but very important link by which thermal energy can be exchanged. This link may be provided by molecular motion.

Each nucleus will have encounters with other magnetic nuclei, both in the same molecule and in other molecules. These neighbouring nuclei may be moving with respect to the observed nucleus, and cause fluctuating magnetic fields. The observed nucleus will be precessing about the direction of the applied field B_0 but will also experience the fluctuating fields of its neighbours.

The magnitude of the fluctuating field component depends on molecular motion. The motion can involve both translation and rotation; and is best described by a correlation time τ_C. This can be defined as the time for a molecule to rotate through one radian or translate through one molecular spacing for rotational or translational motion respectively. Bloembergen, Purcell and Pound[36] extended Debye's theory and related the correlation time to the viscosity η of a solution by assuming that a molecule is a sphere of radius r that turns in a viscous fluid. In this way they showed that:

$$\tau_c = \frac{4\pi r^3 \eta}{3kT} \qquad \text{- (1.37)}$$

The intensity or concentration of fields fluctuating at a particular frequency is known as the spectral density $J(\omega)$, which can also be thought of as the fraction of time that the molecule is rotating at the rate ω. Figure 1.12 shows the dependence of $J(\omega)$ with frequency for different correlation times. The flat region of the $\omega\tau_C >> 1$ is known as the extreme narrowing condition. It is generally the case that T_1 values are identical to T_2 within this region, and sharp signals are observed.

The dependence of relaxation on $J(\omega)$ and its relation to the spin-lattice relaxation time T_1 and precessional frequency ω can be characterised *via* the following equations:

$$J(\omega) = \frac{2\tau_c}{1+\omega^2\tau_c} \qquad \text{- (1.38)}$$

$$\frac{1}{T_1} = 2\gamma^2[B_{ox1}]^2 \frac{\tau_c}{1+\omega^2\tau_c^2} \qquad \text{- (1.39)}$$

where B_{ox1} is the root mean square amplitude of the x component of the time varying magnetic field. The dependence of the relaxation times T_1 and T_2 on the correlation time can be seen in figure 1.13.

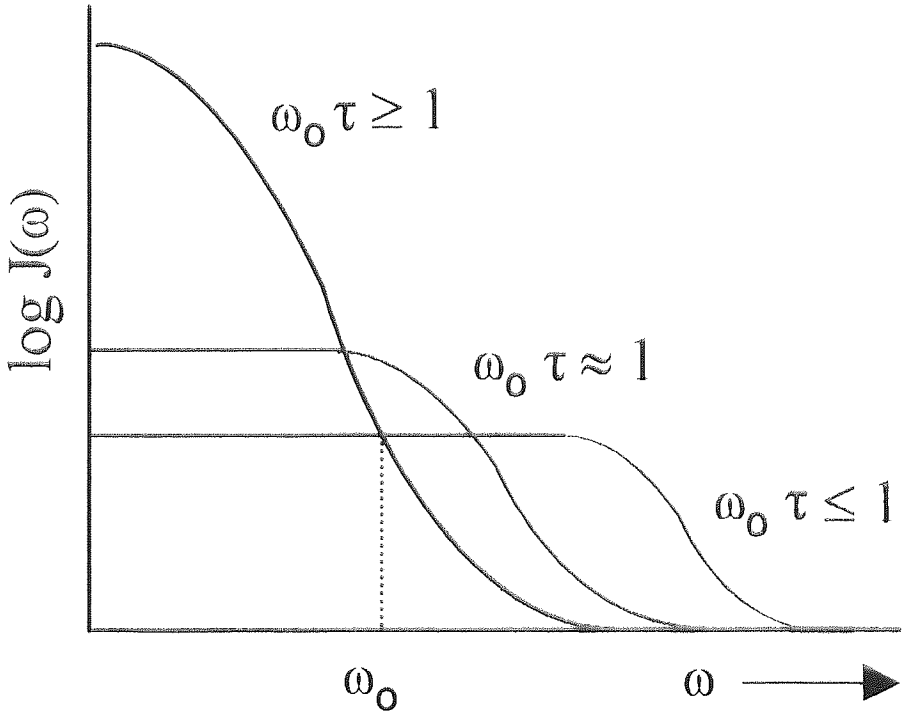

FIGURE 1.12. Motional frequency spectrum at high, medium and low correlation time. The vertical ordinate J(ω) represents the relative intensity of the motional frequency ω. The Larmor frequency being ω_0.

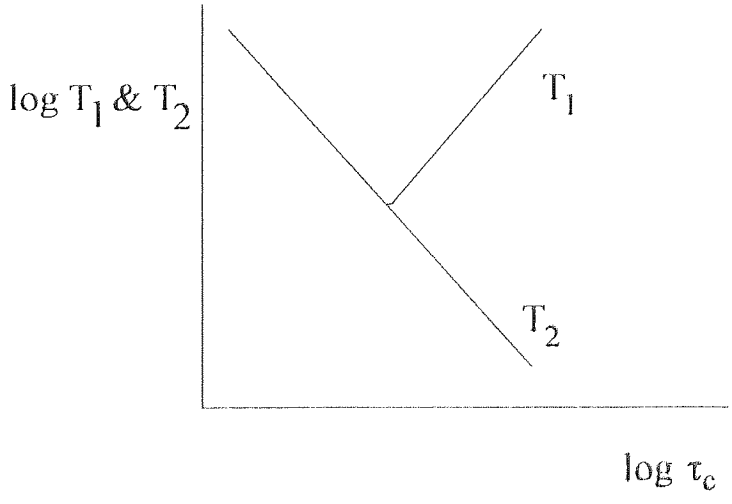

FIGURE 1.13. Spin-lattice relaxation time T_1 and spin-spin relaxation time T_2 as a function of correlation time τ_C.

The extreme narrowing condition can be observed when τ_c is short and the minimum in T_1 is defined as

$$\frac{1}{T_{1(min)}} = \frac{\gamma^2[B_{ox1}]^2}{\omega^2} \qquad \text{- (1.40)}$$

occurring at a correlation time of $1/\omega$. The definition of dipolar T_2 in contrast to T_1 in equation (1.39) is:

$$\frac{1}{T_2} = K\left(\frac{\gamma^4}{r^6}\right)\left\{3\tau_c + \frac{5\tau_c}{1+\omega^2\tau_c^2} + \frac{2\tau_c}{1+4\omega^2\tau_c^2}\right\} \qquad \text{- (1.41)}$$

K is defined as a spectrometer constant. The dependence of the line width on T_2 was discussed in section 1.5.1; and in conjunction with equation (1.41) shows its dependence on correlation time and hence molecular motion. A model for the influence of motion on the NMR lineshape has recently been published by Goldman *et al*[37].

1.8.2 Relaxation Mechanisms

Relaxation occurs as a contribution of both inter and intramolecular contributions and they can be added accordingly:

$$\frac{1}{T_{n(obs)}} = \frac{1}{T_{n(inter)}} + \frac{1}{T_{n(intra)}} \qquad \text{- (1.42)}$$

There are six relaxation mechanisms. The first two, dipole-dipole and electron-nuclear can operate through both inter- or intramolecular mechanisms. The remaining four, spin-rotation, chemical shift anisotropy, scalar and quadrupolar can only be intramolecular. Further details of these mechanisms can be found elsewhere[38,39,40].

It is usually the case for one mechanism such as dipole-dipole, electron-nuclear, or quadrupolar to dominate in the relaxation of a particular nucleus. The dominant mechanism tends to depend on the nucleus and local and global environments of the nucleus.

Dipole-dipole relaxation is caused by the magnetic field fluctuations of nearby dipoles and is a very common relaxation pathway for spin 1/2 nuclei. The relaxation rate depends strongly on the magnetogyric ratio and distance between

interacting spins and can be sufficiently inefficient to produce relaxation times which are very long. Quadrupolar relaxation is very frequently encountered in NMR because 87 of the 116 NMR active isotopes possess a quadrupole moment. The relaxation pathway can be very rapid unlike dipolar relaxation, and quadrupolar nuclei will tend to relax through the quadrupolar mechanism unless it is in a symmetrical environment when the dipolar mechanism becomes important. An example of this is ^{14}N relaxation in NH_4^+ where the symmetrical electric environment forces relaxation via the dipole-dipole mechanism and hence T_1 is long. If electron-nuclear relaxation is present, it generally dominates all other mechanisms and is due to paramagnetic species (generally as impurities, *e.g.* Mn^{2+}, Cr^{3+} and dissolved O_2).

Spin-rotation relaxation occurs due to electron distribution in a rotating molecule (or part thereof) causing fluctuating magnetic fields which affect magnetic moments. The spin-rotation T_1 is inversely proportional to temperature which is the opposite to all other T_1 mechanisms and so plotting T_1 with temperature will show if a spin-rotation mechanism is present.

Chemical shift anisotropy relaxation stems from the anisotropic nature of certain bonds causing field fluctuations as they tumble in solution. This mechanism is detected if the T_1 measured in the extreme narrowing region is found to be inversely proportional to the square of the applied field B_0, *i.e.* on two different spectrometers.

Scalar relaxation is related to spin-spin coupling. One nucleus coupled to another experiences a field component due to the orientation of the spin of the other nucleus with respect to the applied field. If this local field fluctuates at or close to the Larmor frequency, the first nucleus will relax. Most cases of scalar relaxation are of ^{13}C by ^{79}Br (a spin 1/2 nucleus coupled via a large J value to a quadrupolar nucleus), which is also assisted by the Larmor frequency of ^{79}Br being very close to that of ^{13}C.

1.8.3 The Nuclear Overhauser Effect (nOe)

Consider two nuclei A and X_i which are in close proximity and so can interact through space *via* a dipole-dipole mechanism. The irradiation of one of the X nuclei can lead to a modification of the energy level distribution of A and hence a modification of the intensity of the resonance line of the A nucleus. This phenomenon, known as the nuclear Overhauser effect (nOe)[16,17], depends on the applied field (because of the dependence on the Boltzmann distribution of spin

states). The nOe is categorised by the nOe enhancement factor η which is defined as:

$$\eta = \frac{I - I_o}{I_o} \qquad \text{- (1.43)}$$

where I_o and I are the intensity of the resonance line of A without and with perturbation of X respectively. In the extreme narrowing condition the maximum nOe enhancement is given by:

$$\eta_{max} = \frac{1}{2}\frac{\gamma_X}{\gamma_A} \qquad \text{- (1.44)}$$

where A and X are the respective observed and irradiated nuclei. If γ_A and γ_X are of the same sign then $\eta \geq 0$ but if they are of opposite sign then $\eta \leq 0$.

If η=-1 the resonance of A is nulled. This situation is over come by either employing a specific pulse sequence[41] or quenching the A-X dipole-dipole interaction with an inert paramagnetic reagent.

CHAPTER TWO

INTRODUCTION TO FOURIER TRANSFORM NUCLEAR MAGNETIC RESONANCE SPECTROSCOPY

2.1 THE FOURIER TRANSFORM

2.1.1 Introduction

Many of the modern NMR spectrometers collect data in the time domain. This is the process of storing spectral data in a computer as a function of the time of the acquisition of the data. However, it is evident from chapter one, that NMR spectroscopists are interested in the frequency domain response of a spin system since the characteristic resonance lines occur at different frequencies.

Time and frequency spectral domains are inextricably linked and conversion between the two is possible by a procedure known as Fourier transformation.

2.1.2 Fourier Transformation

The Fourier transformation relates the time domain data f(t) with the frequency domain data f(ω) by the following equation:

$$f(\omega) = \int_{-\infty}^{+\infty} f(t) \exp\{i\omega t\} dt \qquad \text{- (2.1)}$$

The form in equation (2.1) is known as the continuous transform, since the limits of integration extend to ±∞. Fourier transforms in NMR are achieved by digital computers using the Cooley-Tukey algorithm which defines a discrete Fourier transform:

$$f(\omega) = \int_{-t}^{+t} f(t) \exp\{i\omega t\} dt \qquad \text{- (2.2)}$$

This points to the fact that f(ω) is complex, but if the exponential part of (2.2) is represented in its alternative form as a combination of trigonometric functions:

$$\exp\{i\omega t\} = \cos\omega t + i \sin \omega t \qquad \text{- (2.3)}$$

The transform is then seen to have real and imaginary parts:

$$\mathrm{Re}[f(\omega)] = \int_{-t}^{+t} f(t) \cos\omega t dt \qquad \text{- (2.4)}$$

$$\mathrm{Im}[f(\omega)] = \int_{-t}^{+t} f(t) \sin \omega t dt \qquad \text{- (2.5)}$$

The real part of the transform contains the absorption mode lines and the imaginary part dispersion mode lines. This shows that there is a variable in the time domain as well as amplitude and frequency which is called the phase.

The Fourier transform is capable of two representations of a sinusoidal wave. One is amplitude vs. time and the other would be a spectrum of amplitude vs. frequency which amounts to a histogram of the frequencies of the sine wave. These two representations for a monochromatic sine wave (a) and two superimposed sine waves with different frequencies and amplitudes (b) is shown in figure 2.1.

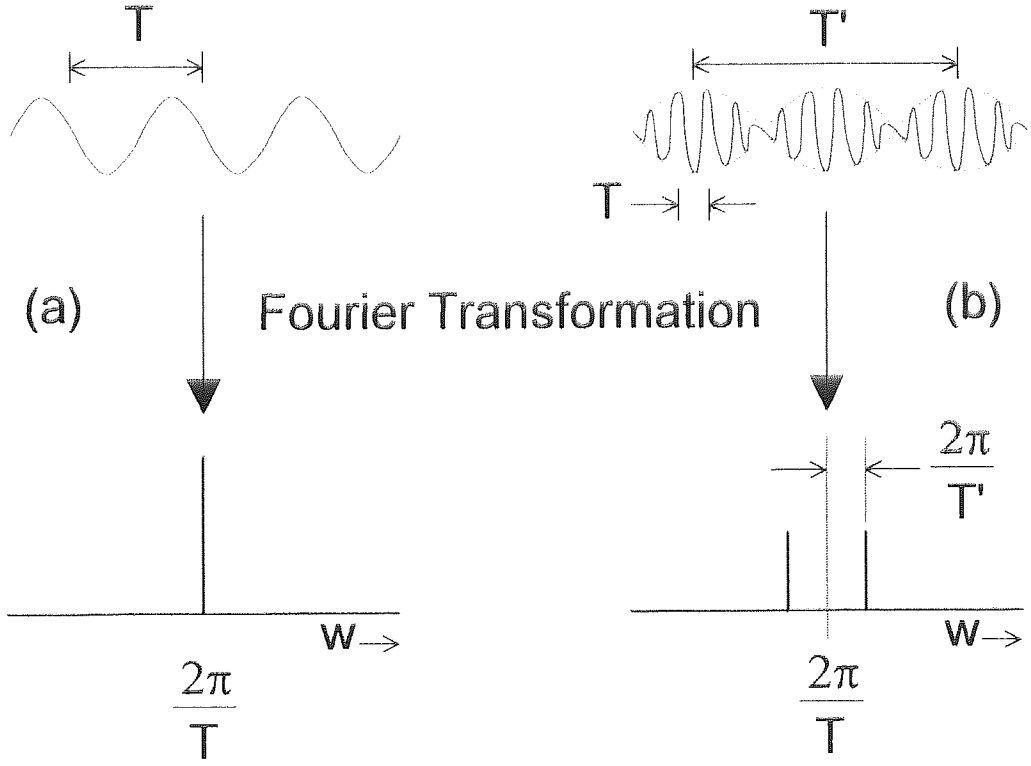

FIGURE 2.1. Time and Frequency Domain Responses of a monochromatic sine wave (a) and two superimposed sine waves with different frequencies and amplitudes (b).

In (a) the width of the peak is inversely proportional to the duration of the sine wave. In (b) the time domain response is an interference pattern with beats in it. The frequency domain response shows two peaks at their corresponding frequencies.

Further reading on the subject of Fourier Transformation is recommended *via* a book by Bracewell[42].

2.2 PULSED FOURIER TRANSFORM NMR

2.2.1 The Basic Pulse FT-NMR Experiment

The advantage of pulse FT-NMR is that NMR spectral data can be collected n times and the time domain response added which assists in the observation of nuclei with poor receptivity. Pulsed Fourier Transform (FT) NMR differs from the CW experiment not only in the storage of the signal with time, but also in the excitation of the nuclei under investigation. CW NMR relies on a slow frequency sweep at constant magnetic field (or vice versa) to individually pass through the resonance condition of each of the magnetically non-equivalent nuclei present. Pulse FT-NMR allows the irradiation of all non-equivalent nuclei simultaneously by the application of a short radio-frequency pulse as its source of B_1. The rf pulse is placed at a certain frequency known as the rf carrier frequency or pulse centre. Heisenberg's uncertainty principle[43] ensures that a short pulse is represented by a spread of frequencies about the carrier which can excite all nuclei within a region either side of the carrier. This can be visualised by the Fourier transform of an rf pulse as shown in figure 2.2. The rf pulse is represented by a 'spread' of frequencies centred about the rf carrier frequency. If the pulse length is reduced, it is found that the frequency spread increases.

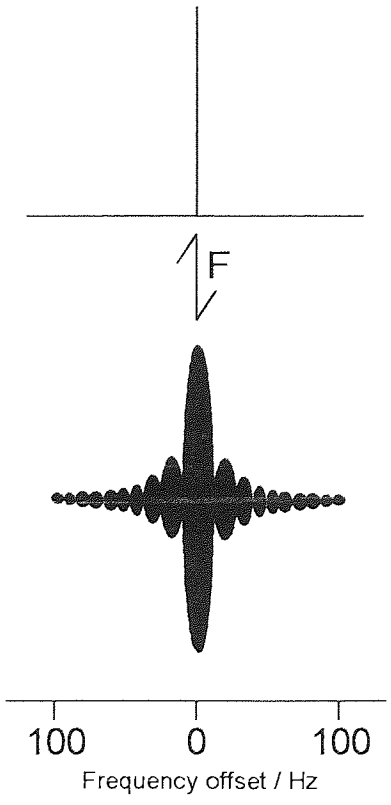

FIGURE 2.2. Diagrams revealling how a narrow pulse has Fourier components over a relatively wide frequency range.

Referring back to the manipulation of magnetization in chapter one, it can be seen that the time for which the pulse is applied is proportional to the angle through which the magnetization is rotated through. It is general policy to discuss the nutation of magnetization in terms of the nutation angle (*e.g.* a 90^{o} pulse) rather than the pulse length.

The pulsed FT-NMR experiment is thus performed in the following way. Consider a molecule with only chemically equivalent protons present (such as benzene). This will produce a large magnetization vector M_o when in equilibrium with the applied field B_o. Figure 2.3 shows the application of a 90^{o} pulse which nutates the magnetization completely into the x-y plane whereafter it precesses in time at the Larmor frequency and decays according to the time constant T_2^*.

2.2.2 The NMR Signal and Detection

The NMR pick up coils are mounted in the laboratory x-y plane and will have a voltage induced within them which decays exponentially. The coils send this exponentially decaying signal to a detector and then to an analogue-to-digital converter where the digitised sinusoidal wave is Fourier transformed, the output being the NMR spectrum of the sample.

The time domain response is usually encountered as a decaying sinusoid, and is known as a free induction decay (or FID). The FID is the signal response of the precessing transverse magnetization inducing e.m.fs in the receiver coils. Figure 2.3 shows that the FID decay is related to T_2^*.

As briefly discussed in chapter one, the pulse FT-NMR spectrum is composed of a number of data points and hence there is a data point resolution. The distance between two points is known as the digital resolution and close inspection of an FID or NMR spectrum shows it is composed of these data points. The FID and spectrum if plotted is just a line joining up these points.

2.2.3 The Parameters of a Basic 1D FT-NMR Experiment

The experiment outlined in the previous section was a single-shot 1D pulse FT-NMR experiment. This section involves the introduction of the parameters to be considered for a basic FT-NMR experiment, or basically, what the spectrometer must be 'told' in order to produce an NMR spectrum.

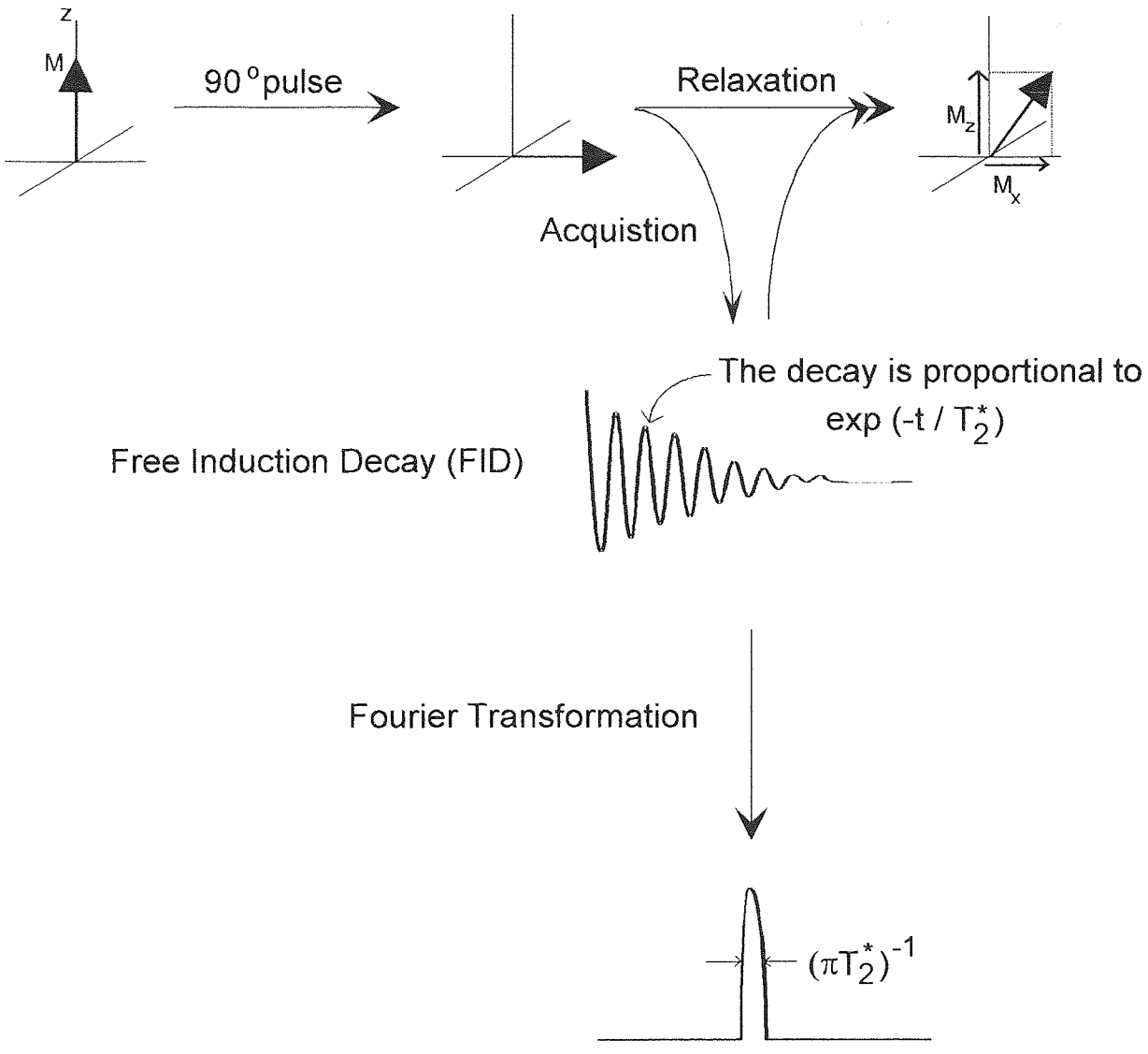

FIGURE 2.3. Pictorial Example of a 1D Single Pulse Fourier Transform NMR Experiment.

The most convenient starting point is the carrier frequency for the nucleus under investigation: this is obtained by addition of an observation frequency and offset frequency. These frequencies can be obtained from calculations using equations defined in chapter one, or more commonly by using the tables supplied by NMR manufacturers. The window (or spectral width) of observation also needs to be defined in hertz. If the carrier is at x MHz and a window of n Hz is set, then the spectrum recorded has the frequency limits of x MHz ± n/2 Hz; *i.e.* the carrier sits in the centre of a spectrum n Hz wide. All nuclei which precess at a resonance frequency within these limits will be detected.

The basic FT-NMR experiment involves three distinct parts known as pulse, acquisition and delay; these are shown in figure 2.4 together with the different gates of the NMR spectrometer.

The ability in pulse FT-NMR to repeat this sequence n times and the spectra added enables an improvement in signal to noise (S/N). This is useful for the observation of low receptivity nuclei where one scan or pulse would be insufficient to observe the signal. The object of adding FIDs before transformation is to enhance the signal. The efficiency can be assessed from the signal to rms noise ratio (S/N). The signal to noise ratio of an accumulation of spectra is the S/N from one spectrum multiplied by the square root of the number of scans added together. An example would be the signal to noise enhancement for 500 scans compared to one scan would be $\sqrt{500}$ or about 22.

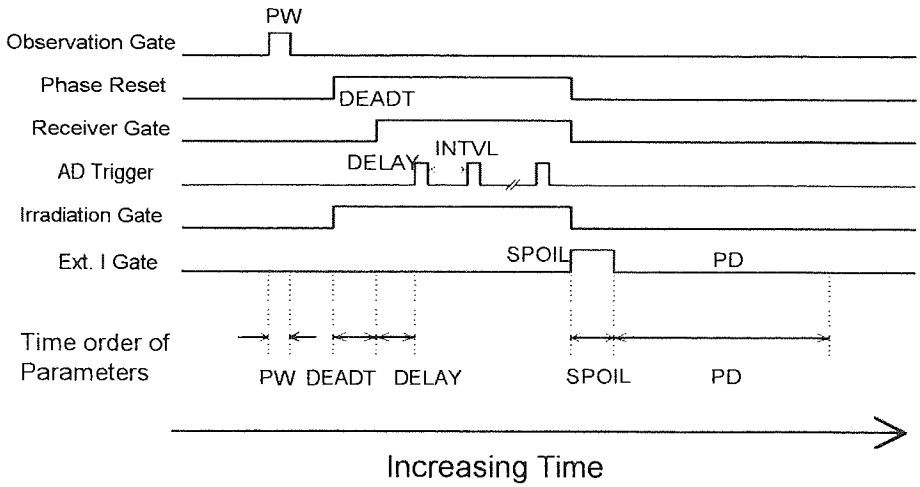

FIGURE 2.4. Chart of Jeol FX-90Q NMR Parameters and Gates for a Single Pulse Sequence.

Figure 2.4 shows the complexity of even the single pulse NMR experiment. The observation gate controls the pulse of rf, shown as PW which is followed by the acquisition sequence which is controlled by the phase reset gates, receiver gate, AD trigger and irradiation gate. The phase reset gate is opened and after the time period DEADT, the receiver gate is opened. Once the receiver is open, the first data sampling point is taken after a time period DELAY. This and successive sampling data points are detected and sent *via* the AD trigger and the detected signal is derived from sampling points spaced by the INTVL time period. The important point to note is that the time between the pulse and acquisition of the first data point is controlled by DEADT+DELAY. After acquisition, there is a SPOIL time period followed by the delay period PD. The SPOIL is an optional weak pulsed field gradient which destroys any residual transverse magnetization. If there are n scans, this cycle will be repeated n-1 times. The irradiation gate like the SPOIL can be switched on or off and is used to irradiate one nucleus or isotope whilst observing another.

The pulse width (PW) is entered in μs, but must be calibrated in order to nutate the magnetization though the required angle. Calibration is achieved by plotting the intensity of an NMR signal at carrier (the reason why will become apparent later) with increasing pulse width. It must be ensured that full relaxation of the magnetization to M_0 occurs between scans. As the signal intensity is proportional to the magnetization component in the x-y plane, the maximum signal intensity occurs for a 90^o pulse. An 180^o pulse will yield no x-y component and will result in zero signal, whereas a 270^o pulse will produce a signal of opposite phase to the 90^o pulse.

The intersequence or relaxation delay (PD) is a very important factor in pulse FT-NMR. When conducting an experiment over a number of scans, PD must be chosen so that adequate relaxation of the magnetization can occur before the next pulse. The integration of equation (1.21) produces a result which can be used to determine PD values:

$$\ln(M_o - M_z) = \frac{-t}{T_1} + \ln(M_o - M_{zi}) \qquad \text{- (2.3)}$$

Here t is the time period between pulses (*i.e.* acquisition+delay) and M_0, M_Z and M_{Zi} are the equilibrium, after perturbation and initial recovery values of the z magnetization vector respectively. One can use this equation to calculate the delay in terms of T_1 required to recover to 99.5% M_0. The modified equation and worked results are shown below.

$$\frac{\left(1 - \frac{99.5}{100}\right)M_o}{(M_o - M_{zi})} = \exp\left(\frac{-t}{T_1}\right) \qquad \text{- (2.4)}$$

M_{Zi} (as a fraction of M_0)	Time Required (factor of T_1)
0.05	5.3
0.5	4.6
0.75	3.9
0.90	3.0

TABLE 2.1 The time required of M_Z to recover to 99.5% M_0 for different values of M_{Zi}.

This information enables PD to be set so that (esentially) full recovery of the magnetization occurs if T_1 is known. If a 90^o pulse is used, PD should be set to at least $5T_1$ to allow essentially full relaxation of the z magnetization.

When a PD is set so that the magnetization is not given adequate time to return to equilibrium M_0 value, a driven equilibrium situation is set up. After the first scan, the z magnetization is not allowed to recover to the starting point and after the next scan, the z magnetization is even smaller. This continues after n scans to a point where an equilibrium is reached where the recovery during delay is just sufficient to return the vector to its previous value. If a system is driven to equilibrium using a fixed pulse delay value t, the measured intensity depends on the pulse width.

It is found that the intensity goes through a maximum value at a particular nutation angle which occurs at the Ernst condition[44]:

$$\cos\theta_E = \exp\left(\frac{-t}{T_1}\right) \qquad \text{- (2.5)}$$

This maximum will be different for different species and nuclei because of its dependence on T_1. The intensity at the Ernst condition is given by:

$$I_E = M_o \frac{(1-\cos\theta_E)}{\sin\theta_E} \qquad \text{- (2.6)}$$

The driven equilibrium experiment has been shown to produce a better S/N in the same time period as a classical (90^o - $5T_1$) experiment. The maximum theoretical enhancement over the classical experiment is 56%. This situation can be achieved using t/T_1 values between 0.1 and 0.5 and with the optimum nutation angle being deduced from equation (2.5). This technique has been referred to as rapid multipulsing but is still widely described as a steady state technique. If the nutation angle is θ, the expression for the NMR signal intensity I_{eq} produced as the result of steady state magnetization is given by:

$$\frac{I_{eq}}{M_o} \propto \frac{\left[\left(1-\exp\frac{-t}{T_1}\right)\sin\theta\right]}{\left[\left(1-\cos\theta\exp\frac{-t}{T_1}\right)\right]} \qquad \text{- (2.7)}$$

2.3 SPECIAL CONSIDERATIONS

The purpose of this section is to bring the readers attention to some of the effects and certain parameters which affect the resultant NMR spectra.

2.3.1 Acquisition Time and Digital Resolution

The acquisition time A_t, is related to the digital resolution R by:

$$R = \frac{1}{A_t} \qquad \text{- (2.8)}$$

so as the number of data points increases, the digital resolution gets smaller and the acquisition time increases. It is of importance to have enough data points to obtain the resolution required, but not so many as to increase the experimental time dramatically.

2.3.2 Convolution due to Truncation

A convoluted signal due to truncation is due to an accidental or deliberate mis-setting of the acquisition time. If the acquisition time is made short compared to T_2^* the FID appears truncated as in figure 2.5. The truncation is the result of terminating the acquisition of data before the FID has decayed to zero. The resulting Fourier transform bears a resemblance to a 'sinc x' function.

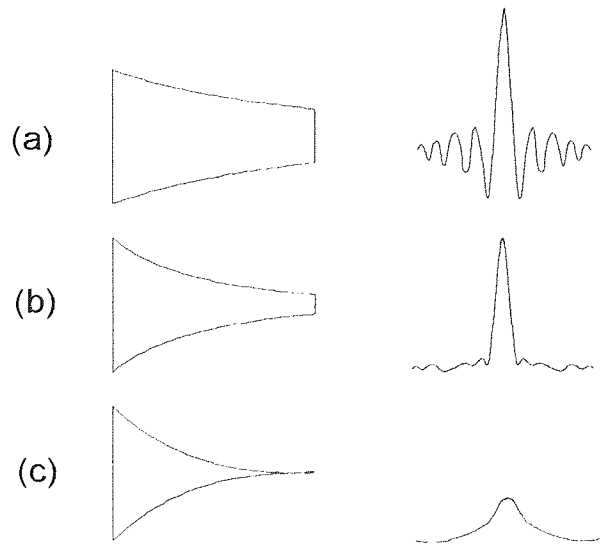

FIGURE 2.5. Lineshapes obtained by Fourier Transformation of Truncated Free Induction Decays where the ratio of the Acquisition Time to Transverse Relaxation t/T_2^* is *ca.* 1, 2 and 5 for (a), (b) and (c) respectively.

2.3.3 Folding

Folding (or aliasing) is the term given to a resonance line which appears on the spectrum but is actually at resonance outside the window of observation. Resonances outside the windows range appears to be reflected into the spectrum through the 'mirrors' formed by the window limit. Suspected peaks are identified by changing the frequency offset.

2.3.4 Quadrature Detection

In the rotating frame, the detectable magnetization is represented by a vector which precesses in the x'-y' axes of the frame. A detector aligned along the x' axis is insensitive to the direction of rotation of the vector, *.i.e.* the sign of the frequency with respect to the carrier offset is not determined. If there is a second detector arranged along the y' axis, it is now possible to discriminate between the signs of the frequencies. This is known as quadrature detection.

In reality, two detector coils are not necessary, but quadrature detection is derived by electronic means. The signal is split into two and fed into two phase sensitive detectors resulting in the determination of the precessional frequency direction and the absorption and dispersion components produce the respective real and imaginary parts of the spectrum.

2.3.5 Obtaining Quantitative Information

Quantitative NMR information includes signal intensity and relaxation time measurements. The measurement of T_1 and T_2 invariably utilises signal intensities, and it is indeed this area which has later relevance.

As outlined in chapter one, signal intensities depend on the concentration of sample and the relative numbers of equivalent nuclei present. In pulse FT-NMR this is only the case when the magnetization is allowed to return to M_0 between scans. In an NMR experiment using a 90^o pulse, the longest T_1 of all resonances present is used to dictate a delay of at least $5.3T_1$ between scans. It is also recommended that a field spoiling pulse is used to remove all transverse magnetization components after each scan. There can, however, be intensity anomalies caused by off resonance effects (see below).

If steady-state conditions are achieved, each resonance will produce a signal of intensity governed by its T_1 (see equation (2.7)). There are techniques[45,46]

which employ this theory to determine T_1 and relative intensities, however, an understanding of the underlying theory is paramount to obtaining the correct results.

2.3.6 Phase Corrections

In NMR spectroscopy, the spins are perturbed by the application of a phase coherent rf field and the phase of the detected magnetization can be expressed relative to this field. The phase of the resultant NMR spectrum is set to display the NMR signals in either absorption or dispersion mode.

The phase of NMR absorptions are found to depend on two effects, the distance from the carrier frequency and the changing pulse width. The reason for this is that the time taken as t=0 in the actual FID is not the correct time origin because of either the finite width of the pulse (the correct time origin being the middle of the pulse), the time required for the receiver to recover, or any other delays within the pulse sequence. This produces a frequency dependent phase shift for changing carrier frequency and a constant frequency phase error for changing pulse width. There is also a contribution to the phase error for changing pulse width from off resonance effects (see below). The phase error due to changing pulse width is not present if the NMR absorption occurs at the carrier frequency.

2.3.7 Off-Resonance Effects

The reason for undertaking a pulse width calibration with a resonance at the carrier frequency is because of off-resonance effects. Firstly, at the carrier frequency, there is no phase error or correction necessary with changing pulse width. This condition is, therefore, necessary for the detection of the null at 180^{o} or the antiphase maximum at 270^{o}. Secondly, it is assumed that the amplitude of the rf pulse is sufficient to excite uniformly all resonances within the range of interest, *i.e.* across the spectral width of the window. In some situations, it is necessary to have the spectral width comparable to the maximum available field strength γB_1, and the criterion for uniform excitation (equation (2.9)) does not hold.

$$|\gamma B_1| >> |\omega_o - \omega_{rf}| \qquad \text{- (2.9)}$$

Under these conditions the magnetization is rotated about a tilted effective field, which depends upon the resonance frequency $|\omega_O-\omega_{rf}|$ in the rotating frame. This results in intensity and phase anomalies. Figure 2.6 shows the tilted effective field in the rotating frame.

The tilted effective field about which rotation proceeds can be deduced from figure 2.5 . It is determined by the offset field ΔB_o:

$$\Delta B_o = B_o + \frac{\omega_{rf}}{\gamma} = \frac{-(\omega_o - \omega_{rf})}{\gamma} \qquad \text{- (2.10)}$$

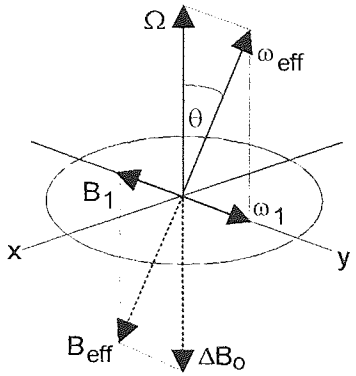

FIGURE 2.6. Diagram showing the Tilted Effective Field in the Rotating Frame. Ω is the related precession frequency vector and ω_{eff} is the tilted effective precession frequency vector as a resultant of Ω and ω_1.

which occurs along the z axis. The rf field B_1 in the transverse plane interacts with ΔB_o and therefore has its amplitude as the vector sum of B_1 and ΔB_o equal to:

$$B_{eff} = \{B_1^2 + (\Delta B_o)^2\}^{\frac{1}{2}} \qquad \text{- (2.11)}$$

and is tilted by an angle θ with respect to the z-axis with:

$$\tan\theta = \frac{B_1}{\Delta B_o} \qquad \text{- (2.12)}$$

The effective nutation angle β_{eff} during a pulse of duration τ is:

$$\beta_{eff} = -\gamma B_{eff} \tau \qquad \text{- (2.13)}$$

The off resonance effect equations show us that an on-resonance 90^o calibrated pulse angle does not nutate a magnetization vector through 90^o when the NMR absorption is away from the carrier frequency. It can be shown[47] that the pulse angle actually increases with increasing offset and it can be appreciated from the previous sections how this can affect quantitative measurements. The use of composite pulses can curb off resonance effects[48].

2.3.8 The Observation of Solid State NMR Spectra using FT-NMR

The NMR lines from solids can be particularly broad, due to T_2^* being very short. As the decay of the FID is proportional to $\exp(-t/T_2^*)$ then the time for the FID to decay to zero is very short. Section 2.2.3 shows there is a delay between pulsing and acquiring which is (DEADT+DELAY). If the FID is short, much of the available signal could decay before the acquisition is initiated.

One method to overcome such a problem is to shorten the DEADT and DELAY parameters. This can cause problems such as r.f. pulse breakthrough, where the pulse is picked up by the detector coils and in extreme cases can mask the true NMR signal. Another problem caused by such actions is the production of baseline roll. The second method is to employ a spin-echo sequence:

All NMR experiments depend upon the generation of phase coherence, which is, the manipulation of the magnetization vector M to the x-y plane by the application of an r.f. field at the Larmor frequency. The loss of phase coherence is due to T_2 relaxation and is detected as an NMR signal.

However, the magnetization can be manipulated by more than one pulse before detection, unlike the simple FT-NMR experiment described earlier. In some of these experiments, the phase coherence is refocussed at some time after the initial perturbation, resulting in the formation of spin echoes. The simplest experiment consists of the sequence[49] shown as equation (2.14).

$$90^{o}(+x) - \text{delay } \tau - 180^{o}(+x) - \text{delay } \tau - \text{acquire} \qquad -(2.14)$$

The transverse magnetization created by the initial $90^{o}(x)$ pulse decays during the time period τ due to the loss of phase coherence. The $180^{o}(x)$ pulse which is then applied flips the relative orientations of the individual spin vectors which then refocus along the -y axis after time τ. If the FID is acquired at this point the signal obtained will not be diminished by the DEADT and DELAY wait as in the single pulse experiment. In addition, the signal should not have any r.f. breakthrough due to the relatively long spin-echo time period after the pulse before acquisition.

The above spin-echo acquisition sequence is of great use in SINNMR experiments where the spin-spin relaxation times are quite long (due to substantial narrowing). Classically broad solid-state NMR spectra could not be acquired using such a sequence. The spin-spin relaxation rates for solid-state resonances are generally so rapid, that all magnetization in the x-y plane will have relaxed before the acquisition period of the spin-echo pulse sequence is initiated.

CHAPTER THREE

INTRODUCTION TO SOLID STATE NUCLEAR MAGNETIC RESONANCE

3.1 INTRODUCTION

The NMR spectra of solids typically consist of a number of relatively broad lines. However, the width of these is not due to any inherent lack of spectrometer resolution at a given field strength. The large linewidths of solid state NMR spectra reflect incomplete averaging of several components (interactions) of the spin Hamiltonian. In contrast, the NMR of liquids and solutions are usually sharp due to averaging out of all interactions except chemical shifts and scalar (spin-spin) couplings.

In order to assist with the understanding of the broadening interactions in solids, it is necessary to become familiar with the definitions of terms used in quantum mechanics. An introduction to Hamiltonians and tensor mathematics to assist in the understanding of this chapter can be found in appendix one although a more rigorous treatment is available in articles by Smith *et al*[50].

3.2 THE HAMILTONIANS WHICH DESCRIBE NMR

The Hamiltonians which describe the NMR spectra of a diamagnetic solid may be written as the sum of five terms.

$$\mathcal{H} = \mathcal{H}_Z + \mathcal{H}_{CS} + \mathcal{H}_D + \mathcal{H}_J + \mathcal{H}_Q \qquad \text{- (3.1)}$$

which are zeeman, chemical shift, dipolar, indirect J coupling and nuclear electric quadrupole moment interactions of the nuclei.

The Zeeman Hamiltonian is defined as:

$$\hbar\mathcal{H}_Z = -\gamma\,\hbar\,\mathbf{I}\,.\,\mathbf{B_0} \qquad \text{- (3.2)}$$

which is the energy of interaction between the nuclear magnetic moment and the magnetic field B_0.

If we ignore the Zeeman and J-coupling interactions; the three important interactions determining the appearance of solid state NMR spectra are chemical shift, dipolar and quadrupolar. These interactions are listed in table 3.1 together with their magnitudes which show how broad the NMR lines can be.

INTERACTION	MAGNITUDE OF INTERACTION (Hz)	RESULTANT OF COMPLETE AVERAGING
Dipolar	$0 - 10^5$	zero
Chemical Shift	$0 - 10^5$	isotropic shift
Quadrupolar	$0 - 10^9$	zero

TABLE 3.1 Approximate ranges of the different spin interactions and resultant of complete incoherent averaging (as in liquids).

The theory behind each interaction is discussed separately in the following sections. The definitions of angles and internuclear distance r_{ik} (more correctly defined as the spin vector) used in the theoretical equations describing all the solid state interactions discussed in sections 3.2.1, 3.2.2 and 3.2.3 are shown in figure 3.1.

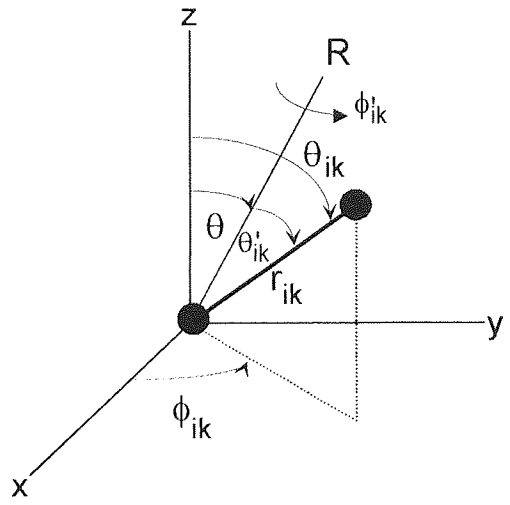

FIGURE 3.1. The description of angles for anisotropic internal rotation about an axis of rotation R, for a spin vector $\mathbf{r_{ik}}$ between two nuclear dipoles.

3.2.1 The Dipolar Interaction

The dipolar interaction Hamiltonian $\hbar\mathcal{H}_d$ for dipole - dipole interactions between magnetic moments $\gamma_i\hbar I^i$ and $\gamma_k\hbar I^k$ separated by a distance r_{ik} is defined as:

$$\hbar\mathcal{H}_D = \frac{\mu_o}{4\pi}\frac{\gamma_i\gamma_k\hbar^2}{r_{ik}^3}[\mathbf{I}^i\mathbf{I}^k - 3(\mathbf{I}^i\mathbf{r}_{ik})(\mathbf{I}^k\mathbf{r}_{ik})] \qquad \text{- (3.3)}$$

In order to calculate lineshapes in solids the above expression is manipulated to yield the secular dipolar Hamiltonian $\mathcal{H}_d^{sec}$. A secular trend is a concept in time series analysis that refers to a movement or trend in a series over a very long time

period. Non secular terms in the Hamiltonian are negligible in the calculation of energy levels since the low amplitude of thermal motions makes the probability of induced transitions small.

In the homonuclear case ($\gamma_i = \gamma_k = \gamma_I$) the secular Hamiltonian is:

$$\mathcal{H}_{D,II}^{SEC} = \frac{\gamma_I^2 \hbar^2 \mu_o}{4\pi r_{ik}^3} \frac{1}{2}(1 - 3\cos^2\theta_{ik})(3I_z^i I_z^k - \mathbf{I}^i \mathbf{I}^k) \qquad \text{- (3.4)}$$

or in the heteronuclear case ($\gamma_I \neq \gamma_k$, $\gamma_i = \gamma_I$, $\gamma_k = \gamma_S$)

$$\mathcal{H}_{D,IS}^{SEC} = \frac{\gamma_I \gamma_S \hbar^2 \mu_o}{4\pi r_{is}^3}(1 - 3\cos^2\theta) I_z S_z \qquad \text{- (3.5)}$$

S_Z is the notation used for the spin of the second nucleus in a heteronuclear system. Equations (3.4 and 3.5) show that:

1. The dipolar interaction will vary according to the sample because of gyromagnetic ratios. The dipolar interaction will be largest with large gyromagnetic ratio nuclei.

2. The internuclear distance between i and k will affect the dipolar interaction. The closer the nuclei, the stronger the interaction.

3. For single crystals, the magnitude of the dipolar interaction will depend on the orientation of a crystal to the magnetic field. The reason for this is explained below.

A single crystal can be thought of as an ensemble of identical magnetic moments that are arranged in pairs on fixed points of a lattice. Neglecting the influence of more distant neighbours, for a given pair i,k the above equations predict that an NMR spectrum will show a doublet with resonant frequencies:

$$\nu = \nu_o \pm \Delta\nu(1 - 3\cos^2\theta) \qquad \text{- (3.6)}$$

where $\Delta\nu = \frac{1}{2\pi} \frac{3\gamma_I^2 \hbar}{4r_{ik}^3} \frac{\mu_o}{4\pi}$ - (3.7)

Here, υ_O denotes the isotropic shift position.

Such an effect can be observed for single crystals having only isolated nuclear pairs present. The resultant spectrum is known as a Pake doublet, the lines of which are broadened by intermolecular interactions. Their lineshape is approximately Gaussian and the splittings change with orientation of the single crystal.

This effect can also be observed in heteronuclear systems where γ_I^2 is replaced by $\gamma_I\gamma_S$ and a fraction in equation (3.7). It is found for a directly bound C-H pair, that $2\Delta\nu$ is approximately 30kHz. Hence the ^{13}C - ^{1}H dipolar interaction can constitute a dominating line broadening influence of the ^{13}C NMR spectrum of a solid, although ^{13}C is only 1.1% abundant.

3.2.2 The Chemical Shift Interaction

The Chemical Shift Hamiltonian is of the form

$$\hbar\mathcal{H}_{CS} = -\gamma\,\hbar\,\mathbf{I}\,.\,\hat{\sigma}\,\mathbf{B_o} \qquad \text{- (3.8)}$$

where $\hat{\sigma}$ is the chemical shift screening tensor, which can be represented by the tensor matrix:

$$\hat{\sigma} = \begin{pmatrix} \sigma_{xx} & \sigma_{xy} & \sigma_{xz} \\ \sigma_{yx} & \sigma_{yy} & \sigma_{yz} \\ \sigma_{zx} & \sigma_{zy} & \sigma_{zz} \end{pmatrix} \qquad \text{- (3.9)}$$

or in the principal axis system:

$$\hat{\sigma} = \begin{pmatrix} \sigma_{XX} & 0 & 0 \\ 0 & \sigma_{YY} & 0 \\ 0 & 0 & \sigma_{ZZ} \end{pmatrix} \qquad \text{- (3.10)}$$

The form of the tensor matrix is described in appendix one. If one considers a typical carbon shape such as:

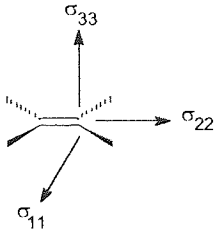

The characteristic tensor orientations are shown as σ_{11}, σ_{22} and σ_{33}. If this molecule was in the presence of a magnetic field B_o, then the tensors would be defined as the principal axes. The nomenclature (as σ_{XX}, σ_{YY} and σ_{ZZ}) would depend on the molecular orientation in the magnetic field.

For a single crystal, $\hat{\sigma}$ would have only a single value determined by the principal values σ_{XX}, σ_{YY} and σ_{ZZ} and the orientation of the principal axes to B_o. The spectrum should consist only of a single line (considering only the chemical shift interaction involved), the position being determined by σ.

If instead, a poly crystalline specimen or a powdered crystalline sample is used, then a distribution of resonance frequencies is observed. This is due to different crystallite orientations within the sample and is referred to as a chemical shift anisotropy (CSA) powder pattern. The isotropic shift is a resultant of all the $\sigma_{NN'}$ values and is the true chemical shift position:

$$\sigma_{\text{isotropic}} = \frac{1}{3}(\sigma_{XX} + \sigma_{YY} + \sigma_{ZZ}) \qquad \text{- (3.11)}$$

There are two cases to consider here. Firstly, consider a molecule with axial symmetry so $\sigma_{XX} = \sigma_{YY} \neq \sigma_{ZZ}$. The classic CSA powder pattern for such a system is shown in figure 3.2. It can be seen that statistically it is expected to find more molecules perpendicular than parallel to the applied field. It is this that gives rise to the CSA axially symmetric shape.

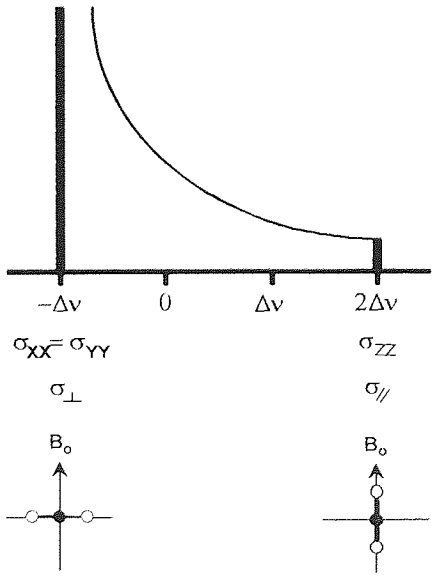

FIGURE 3.2. Axial Symmetry CSA Powder Pattern. The zero position corresponds to the isotropic shift.

If there is no axial symmetry, the spectrum is of the form shown in figure 3.3(a) with figure 3.3(b) showing how three different sets of $\sigma_{NN'}$ values can produce the same isotropic shift.

It is important to remember the maximum intensity at σ_{YY} is not the isotropic shift value. The isotropic shift must be obtained via equation (3.11). One final point on the chemical shift and CSA interactions is that equation (3.8) shows these interactions are field and gyromagnetic ratio dependant. Thus CSA line shapes become easier to detect and broader with higher frequency spectrometers.

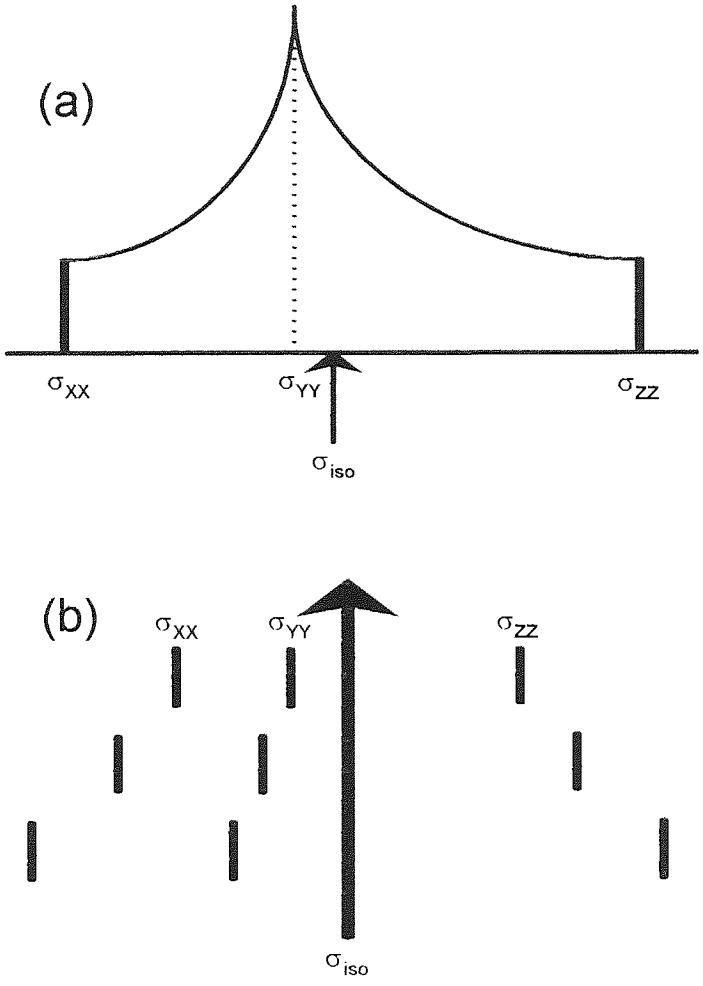

FIGURE 3.3. CSA Powder Pattern for No Axial Symmetry (a) and three different sets of $\sigma_{NN'}$ values producing the same isotropic shift (b).

3.2.3 Quadrupolar Interaction

The quadrupolar interaction is complex and the following discussion is simplified to include the areas of the theory which are relevant to the understanding of later topics. The quadrupolar Hamiltonian has the form:

$$\hbar\mathcal{H}_q = \sum \mathbf{I}_{\alpha,\beta} Q_{\beta,\alpha} \mathbf{I}_{\alpha,\beta} \qquad \text{- (3.12)}$$

$$\text{where } Q_{\beta,\alpha} = \frac{eQ}{2I(2I-1)h}.V \qquad \text{- (3.13)}$$

The nuclear electric quadrupolar interaction for nuclear magnetic moments with spin I>½ may be represented as in equation (3.12) where $Q_{\beta,\alpha}$ the nuclear quadrupole coupling tensor and $I_{\alpha,\beta}$ is the nuclear spin. $Q_{\beta,\alpha}$ is defined in equation (3.13) where Q, V and e are the electric quadrupole moment at a nucleus, the electric field gradient tensor and the elementary charge respectively. It is common to use an asymmetry parameter in the understanding of the quadrupolar interaction. The asymmetry parameter η_Q, is defined as

$$\eta_Q = \frac{V_{11} - V_{22}}{V_{33}} \qquad \text{- (3.14)}$$

where V_{11}, V_{22} and V_{33} are the principal axes of the electric field gradient tensor from equation (3.13) which are produced by the quadrupolar nucleus and the general environment. The value of this parameter can alter the appearance of solid-state quadrupolar powder patterns, as described by Amoureux *et al*[51].

The quadrupolar interaction is considered to exist in a situation where the Zeeman splitting predominates over the quadrupolar splitting, and thus contributions of the quadrupolar interaction can be deduced using perturbation theory[52] with the Zeeman interaction.

The various energy levels of $\hbar(\mathcal{H}_Z + \mathcal{H}_Q)$ can be written as:

$$E = E_n^{(0)} + E_n^{(1)} + E_n^{(2)} + E_n^{(3)} + \ldots\ldots\ldots \qquad \text{- (3.15)}$$

where $E_n^{(p)}$ represents the contribution to E_n of order p. The part $E_n^{(0)}$ includes the Zeeman energy. It is usual to discuss only the 1st and 2nd order quadrupolar terms.

The first order contribution in energy includes the secular part of the quadrupole Hamiltonian and is written as:

$$\hbar\mathcal{H}_q^{sec} = \frac{1}{12} h\nu_Q [3I_z^2 - I(I+1)]\sqrt{\frac{8}{3}} f_o \qquad \text{- (3.16)}$$

where $\sqrt{\frac{8}{3}}f_o = (3\cos^2\theta - 1) + \eta_Q \sin^2\theta \cos 2\phi$ - (3.17)

and $\nu_Q = \frac{3e^2qQ}{2I(2I-1)h}$ - (3.18)

where υ_Q is the frequency difference from the Larmor frequency υ_L, at which the nuclear quadrupolar transitions occur (see figure 3.4), e is the elementary charge and q is the electric field gradient from adjacent bonds.

and the 1st order interaction energy is given by:

$$E_n^{(1)} = \frac{1}{4}h\nu_o\left[n^2 - \frac{1}{3}I(I+1)\right]\sqrt{\frac{8}{3}}f_o \quad \text{- (3.19)}$$

The second order contribution is given by:

$$E_n^{(2)} = \frac{-h\nu_Q}{32\nu_L}n\left\{[-4I(I+1)+8n^2+1]|f_1^2|[2I(I+1)-2n^2-1]|f_2^2|\right\} \quad \text{- (3.20)}$$

where n is the transition in question and f_m are expressions of Wigner rotation matrices[53] which give the interactions in terms of Eulerian angles (α,β,γ) for the quadrupolar nucleus with respect to B_o.

For example, for axial symmetry of the electric field gradient, where η_Q = 0 then in equation (3.20):

$$f_1 = -\frac{3}{4}\sin 2\beta \text{ and } f_2 = \frac{3}{4}\sin^2\beta \quad \text{- (3.21)}$$

As a result of the above expressions, it can be seen, that in polycrystalline samples, since β (the Eulerian angle) has a range of values, the transition energy is spread, resulting in further broadening.

Quadrupolar solid state NMR spectra for nuclei with I=3/2 consist of a central transition due to ±½ energy levels superimposed on the broad pattern for additional transitions, *i.e.* in the case of I=3/2, these are -3/2, -1/2 and 1/2, 3/2 as shown in figure 3.4. Also the centre of the spectrum is shifted from the isotropic (true) point by the quadrupolar shift. For the case where the electric field gradient is axially symmetric (η_Q=0) the expressions for the frequency shift take the following form:

$$\upsilon^{1}_{(n)} = \nu_Q \frac{3\cos^2\theta - 1}{2}\left[n - \frac{1}{2}\right] \qquad \text{- (3.22)}$$

and for the central transition -1/2, 1/2, the second order frequency shift is given by:

$$\upsilon^{(2)}_{\frac{1}{2}} = \frac{I(I+1) - \frac{3}{4}}{16}\frac{\upsilon_Q^2}{\upsilon_L}(\cos^2\theta - 1)(9\cos^2\theta - 1) \qquad \text{- (3.23)}$$

In summary, the quadrupolar interaction is produced *via* an interaction between the nuclear quadrupole moment and electric field gradient in the vicinity of a nucleus. First and second order interactions are produced which broaden and shift the resonance from its isotropic (true) value. Further reading on the quadrupolar interaction can be found in an overview of the NMR of quadrupolar nuclei in the solid state which has been written by Taulelle[54].

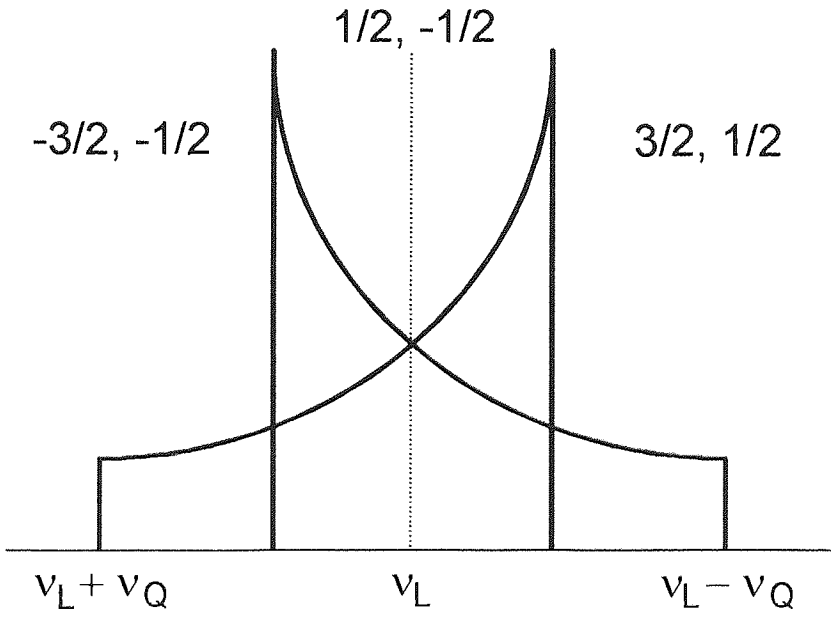

FIGURE 3.4. Quadrupolar Powder Pattern for the case I = 3/2 showing the central transition -1/2, 1/2 superimposed on the broad pattern for the other two transitions: --3/2, -1/2 and 1/2, 3/2.

3.3 TECHNIQUES AVAILABLE TO REMOVE BROADENING INTERACTIONS

The most relevant points from the discussion of the interactions described in section 3.2 have been summarised in table 3.2

INTERACTION	ANGULAR DEPENDENCE
Dipolar	$(3\cos^2\theta - 1)$
Chemical Shift	*via* the orientation of σ_{XX}, σ_{YY}, σ_{ZZ} to the applied field
Quadrupolar	
1st Order broadening	$(3\cos^2\theta - 1) + (\eta_Q \sin^2\theta \cos 2\phi)$
2nd Order broadening	$(-3/4 \sin 2\beta)$ $(-3/4 \sin^2\beta)$ for axial symmetry
1st Order Shift	$(3\cos^2\theta - 1)$
2nd Order Shift	$(\cos^2\theta - 1)(9\cos^2\theta - 1)$

TABLE 3.2. Summary of the angular dependence for selected solid state interactions. All angles are defined in figure 3.1.

The majority of techniques described in this section, with the exception of Brownian motional averaging discussed in section 3.3.4, which are availiable to reduce solid state NMR line broadening, rely on coherent averaging of the NMR solid state interactions. That is, such methods require the ability to reduce or remove a certain theoretically defined parameter which is generally the angular denpendence of the interactions to the applied field.

3.3.1 Magic Angle Spinning (MAS NMR)

The rapid rotation of solid specimens at a particularly defined angle to the magnetic field was first used independently by Andrew, Bradbury and Eades[2], and Lowe[55]. MAS NMR involves rapid rotation of a sample tilted at the so called magic angle ($54^o44'$) to the magnetic field B_O. This is so that any interaction described by an equation involving the term $(3\cos^2\theta - 1)$ or $(1 - 3\cos^2\theta)$ will reduce to zero and thus remove the interaction to which the term is attached. These terms are simply related by equation (3.24) and figure 3.5.

$$\left\langle 1 - 3\cos^2\theta_{jk} \right\rangle = (1 - 3\cos^2\theta')\frac{(3\cos^2\gamma_{ik} - 1)}{2} \qquad \text{- (3.24)}$$

It can be seen from the previous section that the dipolar interactions will be removed by such a process. However, the quadrupolar interaction is more complex. All 1st order quadrupolar shifts and interactions will be reduced by MAS NMR, but 2nd and higher orders will not be removed.

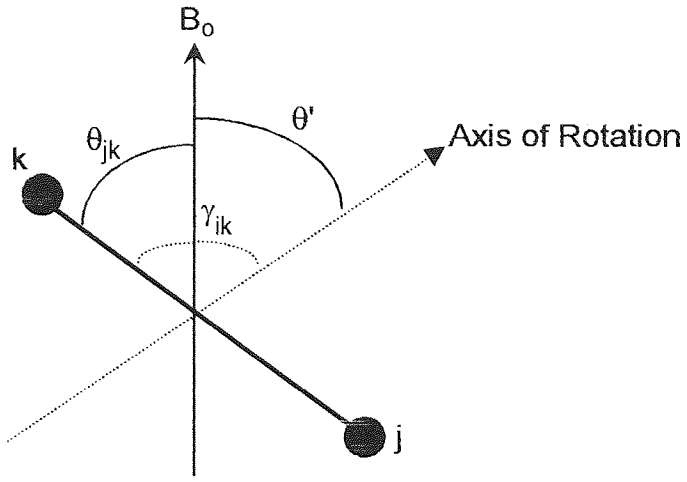

FIGURE 3.5. The relationship of angles in Magic Angle Spinning NMR showing two nuclei j and k.

MAS NMR causes a reduction in the Chemical Shift anisotropy interaction, and if spinning is sufficiently rapid (of the order $\omega/2\pi >> \Delta\upsilon$ (the powder spectrum width)) then the chemical shift screening tensor is reduced to σ_{iso}.

Lowe achieved high-speed rotation by supporting the rotor on an axle, but Andrew used a single air bearing. These systems were reported to produce rotational rates beyond 8 kHz and 4 kHz respectively[56]. The commercialisation of MAS NMR preferentially chose the use of single or multiple air bearings, the original rotors being based on designs by Beams[57], Henroit and Hugenard[58] and more recently by Zilm *et al*[59]. The most recent specialised MAS NMR rotors can spin up to 30 kHz but, in earlier models, the maximum rotation was much less. If the sample is not spun quickly enough, *i.e.* with a frequency larger than the solid spectrum width, the pattern breaks up into an array of spinning sidebands which, if observed, follow the general shape of the CSA interaction.

The MAS NMR experiment has been much improved with the advent of cross-polarisation (in the form of CPMAS) which was first experimentally realised by Schaefer, Stejskal and Buchdahl[60]. A general review of CPMAS has been written by Yannoni[61] and the advancement of complete spectral editing CPMAS has been reported by Wu and Zilm[62]. CPMAS NMR has enabled the detection of low magnetogyric ratio nuclei in the solid state, which was recently emphasised, by the report of the first examples of ^{109}Ag CP MAS spectra[63]. The apparent problem of measuring ^{13}C chemical shifts in solids by MAS NMR was addressed with solutions being achieved by Earl and Vanderhart[64].

Problems with MAS NMR include:

1. Nuclei with large gyromagnetic ratios such as ^{1}H and ^{19}F will require very high spinning speeds to remove the dipolar interactions. Rotation should at least be the frequency of the solid spectral width.

2. MAS NMR requires careful calibration of the magic angle. Andrew deduced that deviation of less than one half a degree from the magic angle would result only in a 1% reduction of the original line width[56].

3. Spinning sidebands occur from incorrect setting of the magic angle, but also can be produced from the normalised harmonics set up within the MAS experiment. Intensity anomalies produced by cross-polarisation[65] can also complicate the spinning sideband patterns[66]. The theory behind the occurrence of spinning sidebands can be found in an MAS NMR article by Andrew[56] or in a text by Schlicter[67]. There have been several methods developed to interpret spectra with spinning sideband anomalies such as iterative fitting[68] and two-dimensional separation[69].

4. MAS NMR will remove 1st order quadrupolar interactions, but not 2nd order interactions (which include the quadrupolar shift). This can be understood with reference to table 3.2 where the factor $(3\cos^2\theta - 1)$ is not present in the definition of these interactions. Spinning at the magic angle in these cases will not reduce the interactions to zero. The resultant MAS NMR spectrum can be broadened by the 2nd and higher order quadrupolar interactions with any resonances offset from their true chemical shifts. The magnitude of these effects will depend heavily on the environment of the quadrupolar nucleus. The quadrupolar effect can also be indirect, where nuclei with large quadrupolar coupling constants can affect the dipolar and scalar couplings in the MAS NMR of spin 1/2 nuclei[70].

3.3.2 Dynamic Angle Spinning (DAS NMR) and Double Rotation (DOR NMR)

The inability to remove all quadrupolar interactions by MAS NMR lead to the development of Dynamic angle spinning[3] and Double Rotation NMR[4,71,72] (DAS NMR and DOR NMR). The theoretical work of Llor and Virlet[73] in conjunction with Pines *et al*[4] showed that there was a rotational dependence of the quadrupolar interaction on the magnetic field which was due to 2nd and 4th order Legendre polynomials (P_2 and P_4 respectively):

$$P_2(\cos\theta) = \frac{1}{2}(3\cos^2\theta - 1) \qquad \text{- (3.25)}$$

$$P_4(\cos\theta) = \frac{1}{8}(35\cos^4\theta - 30\cos^2\theta + 3) \qquad \text{- (3.26)}$$

These equations show that in MAS NMR $P_2(\cos\theta) = 0$ (due to elimination of [3 $\cos^2\theta$ - 1]) but $P_4(\cos\theta) \neq 0$. The 4th order polynomial can be used to deduce different pairs of angles for which $P_4(\cos\theta) = 0$. Some solutions are shown in table 3.3 (from Mueller *et al*[3]).

DAS NMR uses a single rotor as in MAS NMR, but the angle to the applied field is made time dependant. The sample is spun at two different angles corresponding to one of the solution pairs for the 4th order polynomial. When the two spectra are superimposed, the point at which they cross is the isotropic shift position[3].

θ_1 / ^{o}	0	30.56	37.38	39.23
θ_2 / ^{o}	63.43	70.12	79.19	90.00

TABLE 3.3 Solution pairs (θ_1 and θ_2) to the angles required to solve the 4th order Legendre polynomial for $P_4(\cos\theta) = 0$.

DOR NMR uses a double rotor (one rotor inside another) with the outer rotor set at 54.7^o and the inner set at 30.56^o to the magnetic field. The inner rotor spins five times faster that the outer rotor to minimise the torque on the rotor housing yet produce optimum NMR sensitivity conditions. The resultant DOR NMR spectrum is averaged for dipolar interactions (by the 54.7^o rotor) and quadrupolar interactions (by the 30.56^o rotor). More recently, it has been reported that DOR NMR has been combined with cross-polarisation to produce the techniques equivalent to CPMAS[74].

Problems with DAS & DOR NMR

1. The complicated and expensive equipment compared to standard MAS NMR.

2. DAS NMR requires careful calibration of the rotor angles, and Mueller and co-workers[3] used a computer controller pulley system to achieve an angle resolution of better than 0.36^o.

3. DOR NMR produces spinning sidebands as in MAS NMR. However they are produced because the inner rotor spins at approximately 4000 Hz but the outer only spins up to 900 Hz. The analysis of DOR NMR spinning sidebands has been

tackled by Sun *et al*[75] and DAS NMR spinning sidebands by Grandinetti *et al*[76].

3.3.3 Multiple Pulse Experiments

A crude definition of the multiple pulse methods is to consider that MAS NMR involves spinning the sample and acquiring the mechanically averaged result. In multiple pulse methods, the NMR magnetization is rotated within a static sample to average the interactions.
Consider the NMR frame; if the magnetization is pulsed thus:

{ 90(-y) - 2t - 90(y) - t - 90(x) - 2t - 90(-x) - t -} 90(-y) - 2t - etc...
x z y z x -Magnetization

so that within a cycle (in curly brackets{ }) the magnetization has spent an equal amount of time on each axis, then the average position is along the diagonal of a cube. The diagonal has an angle to B_0 (which is along the z axis) of $54^o44'$, and dipolar interactions will be reduced towards zero. The averaging of the magnetization is in reality governed by equation (3.3) containing the spin vectors and not the reducing factor. The time period t is a constant, and acquisition is during the 2t periods. This experiment is the WHH-4 or WAHUHA[77] experiment which will remove the dipolar interactions but will maintain any chemical shift anisotropy (because the sample is stationary within the field).

Other cycles with greater numbers of pulses such as the widely used MREV-8[78] sequence have been developed. The greater number of pulses enables the sequence to use other frame quadrants unlike the WHH-4 sequence which uses the +z, +y and +x quadrant. This has the advantage of removing pulse imperfection problems which are inherent to the WHH-4 sequence[79].

Multiple pulse sequences are useful for the study of nuclei with large gyromagnetic ratios, such as ^1H and ^{19}F as there is no mechanical limitation as in MAS NMR. It is because of this point that CRAMPS[80] was developed which is Combined Rotation and Multiple Pulse Spectroscopy. This technique uses a pulse sequence (initially WHH-4 or MREV-8, more recently BR-24[81] and TREV-8[82,83]) in combination with magic angle spinning. The resulting spectra can have much reduced dipolar interactions and CSA for high gyromagnetic ratio nuclei. This technique has been very successful with nuclei such as ^1H and ^{19}F. A general review of CRAMPS has been written by Burum[84].

Disadvantages with the multiple pulse sequences are:

1. Only specialised spectrometers (which are generally expensive compared to a standard spectrometer) can cope with the short times requires to undertake a sequence. e.g. One cycle of WHH-4 needs to been done in *c.a.* 10μs in order to facilitate sufficient averaging of the magnetization. That necessitates four 90^{o} pulses and six time slices in 10μs, including two acquisition periods.

2. The CSA interaction is not removed by multipulse sequences and in fact, this was the reason for its development. These sequences are used extensively in polymers to determine proportions of amorphous and crystalline regions; see *e.g.* Vega and English[85].

Two texts on solid state NMR, with the emphasis placed on multiple pulse sequences, have been published by Mehring and Haeberlen[79].

3.3.4 Other Averaging Techniques

1. It has been reported that high resolution NMR can be obtained for solids in colloidal suspension. The procedure was demonstrated by Yesinowski[86,87] (who obtained high resolution ^{31}P NMR spectra from calcium hydroxyapatite) and Kimura and Satoh[88,89] (using ^{27}Al of AlF_3)with the latter authors calling the technique Ultrafine Particle (UFP) NMR. Yesinowski stated the particle sizes he produced were of the order of 125 x 125 x 500Å and Kimura and Satoh state 1 - 3 nm which must only be a few molecules in size. The averaging in this technique is produced by the Brownian motion of the particles in a suitable support medium facillitating incoherent particle motion. However, it must be noted, that certain studies[90] attempting to repeat the work of Yesinowski[87], have indicated that the relatively sharp resonance that he attributed to the solid was in fact derived from solution.

2. Andrew proposed that instead of rotating the sample in a magnetic field as in MASNMR, the specimen could remain at rest and the magnetic field should be rotated around it whilst inclined at the magic angle[91]. The magnetic field can be rotated electrically and this method has the advantage that there is in principal no difficulty in surpassing those rotational speeds obtained mechanically in MAS NMR. In practice the technique is hampered by the difficulty in generating and maintaining a large and uniform rotating magnetic field. However, there is one report in the literature stating that resonances have been detected by this method[92].

CHAPTER FOUR

ULTRASONICS

4.1 INTRODUCTION

Ultrasound is defined as any sound which is of a frequency beyond that which the human ear can respond[93], the upper limit of human hearing being in the region of 16 kHz. There are, however, two distinctly different uses to which ultrasound can be applied and these are identified in terms of their frequency ranges and applications as:

(a) high frequency or diagnostic ultrasound (2 - 10 MHz)

(b) low frequency or power ultrasound (20 - 100 kHz)

This sub-chapter is intended to familiarise the reader with basic acoustic theory. A more comprehensive account can be found in any standard textbook on acoustics *e.g.* Stephens and Bate[94].

4.1.1 Vibrations and Waves

The only distinction between audible sound and ultrasound is that the latter cannot be detected by the human ear. The theory of ultrasonic propagation is, therefore, exactly the same as for audible sound.

Sound is generated within a medium as a result of some mechanical disturbance taking place within it. Whatever the sound source is, it can be shown that the source is in a state of vibration. Vibrations are characterised by their frequencies, *i.e.* the number of complete periodic cycles undergone in unit time, *e.g.* one second. Thus frequencies are depicted as number of cycles per second, or more correctly, in terms of S.I. units, hertz (Hz).

Disturbances produce sound waves over continuous ranges or bands of frequencies, the widths of which depend on the nature of the source and the manner of its mounting. Continuous vibrations produce bandwidths which are narrow and centred at a number of discrete frequencies, the values of which bear a simple numerical relationship to each other. The lowest frequency is the fundamental, and all frequencies higher are harmonics or partials. The second harmonic has a frequency which is twice that of the fundamental, the third harmonic has a frequency which is three times that of the fundamental, and so on. For most ultrasonic applications, the source consists essentially of a plane surface oscillating with simple harmonic motion at a single frequency in a manner similar

to that of a piston in the cylinder of an engine but with a much smaller amplitude and at a very much higher frequency.

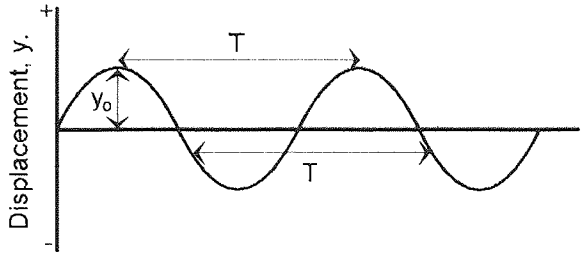

FIGURE 4.1. Variation of displacement y with time t for an ultrasonic source

Figure 4.1 shows the variation of displacement of a sound source from rest with time. The time taken for the source to execute one complete vibration is called the period T. It can be readily seen that the reciprocal of the time period T, measured in seconds, is equal to the frequency f, measured in hertz. The shape of the curve is sinusoidal and can be expressed mathematically as follows:

$$y = y_o \sin\left(\frac{2\pi t}{T}\right) = y_o \sin 2\pi ft = y_o \sin \omega t \qquad \text{- (4.1)}$$

where y represents the displacement (amplitude) at any time t, and ω is the angular frequency defined as $\omega = 2\pi f$. Every half-cycle, the source is displaced alternatively in opposite directions by a maximum amount y_o called the displacement amplitude. The angle expressed alternatively as $2\pi t/T$, $2\pi ft$ or ωt in equation 4.1 is called the phase angle and indicates the phase of vibration at a given time t.

The source transmits vibrational energy to the particles of the medium (*e.g.* atoms or molecules) which are in immediate contact with it. The energy then passes progressively through the medium as follows. Figure 4.2 illustrates two parallel plates separated by the medium of propagation.

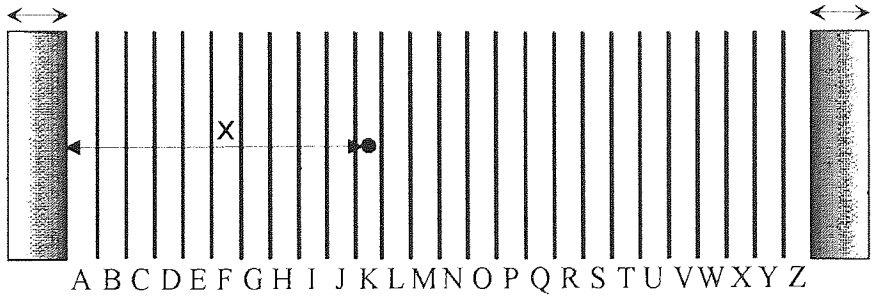

FIGURE 4.2. Division into layers of a material through which ultrasound is propagated.

The plate on the left can be considered as the source which vibrates with simple harmonic motion and the medium is thought of as a large number of thin parallel layers (A - Z), each of equal thickness. When the phase of vibrations of the source are such that displacement occurs in the right-hand direction, the first layer A is pushed in the same direction to suffer a similar displacement. The layer B is then in turn displaced , and thus the displacements are progressively transmitted from each layer to its neighbour until the final layer Z is reached. As the phase of vibration of the source varies, the magnitude of the displacement varies as in figure 4.1, taking both positive and negative values, which are experienced by all layers and the receiver.

As it takes a small but finite time for the energy to pass from one layer to the next, the phase of vibration of each layer differs from that of its neighbours by a small but finite amount. The sound waves thus take a given time to pass from the source to the receiver. The velocity of the waves is constant for a particular medium under specified physical conditions (*e.g.* constant temperature); this value depends on the elastic modulus and density of the material. If one considers a layer on figure 4.2 such as K situated at a distance x from the source, the time taken for the sound to reach this layer is equal to x/c, where c is the velocity of sound in the medium. Thus the phase of vibration of K at any time t is identical to that of the sound source at a previous time [(t - x)/c], and the value y of the displacement is obtained by substituting the quantity t in equation 4.1 thus:

$$y = y_o \sin\omega\left(t - \frac{x}{c}\right) \qquad \text{- (4.2)}$$

This description is of the propagation of longitudinal waves, sometimes referred to as compressional waves, because the imaginary layers in the medium of propagation are subjected to alternate compressional and tensile stresses by the waves. At any given time, the layers can be considered as having the appearance to those in figure 4.3, where centres of neighbouring compressed or expanded regions are separated, respectively, by distances of one wavelength.

Another form of propagation is that of transverse waves, for which the vibrations of the particles in the medium occur at right angles to the direction of the wave motion. The imaginary layers shown in figure 4.2 are then subjected to alternating shear stresses, and the resulting strains are directed parallel to their surfaces. The term shear wave is often used to describe this kind of transverse wave propagation. Shear waves are generally only passed through solids, because liquids and gases do not usually support shear stresses. An exception to this rule

is the propagation of shear waves in highly viscous liquids, such as heavy lubricating oils.

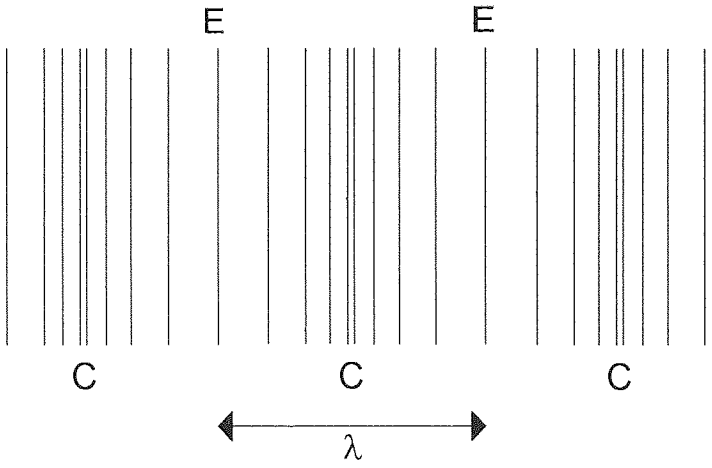

FIGURE 4.3. Appearance (exaggerated) of layers of a material in which longitudinal waves are propagated, showing compression at 'C' and expansion at 'E'. At point C the displacement (amplitude) y is at a positive maximum and at E, a negative maximum.

The principal characteristics of acoustic waves are: (a) particle displacement y, (b) particle velocity u, and (c) acoustic pressure (or stress) p. A particle is defined here as a fundamental unit of the propagating medium which is displaced by the sound wave. The particle displacement has already been defined in equations 4.1 and 4.2.

However, it is often more convenient to consider the particle velocity u, which is defined as the velocity of a vibrating particle in the medium (not of the waves) at a given time and location, *i.e.*:

$$u = u_o \sin\omega\left(t - \frac{x}{c}\right) \qquad \text{- (4.3)}$$

where u_O is called the particle velocity amplitude. Now the material carrying the sound waves is subjected to an alternating excess pressure or stress called the acoustic pressure (or stress) p, which varies as follows:

$$p = p_o \sin\omega\left(t - \frac{x}{c}\right) \qquad \text{- (4.4)}$$

here p_O is the acoustic pressure (or stress) amplitude.

4.1.2 Attenuation of Plane Waves

Ideally, and as assumed in the simple explanation of wave propagation above; the intensity of a parallel beam of plane waves should remain constant at all distances from the source. In practice this is not the case because of the attenuation of ultrasound as it progresses through the medium. Assuming that there are no major discontinuities producing regular reflections, *e.g.* cracks in solids; three causes of attenuation exist, namely diffraction, scattering, and absorption. For present purposes adsorption must be discussed.

Assuming that diffraction effects are constant, *i.e.* considering either the near field or far field, the amplitude A is found to decrease by absorption in an exponential manner as the distance x in a direction away from the source is increased, *i.e.*:

$$A = A_o \exp(-\alpha x) \qquad \text{- (4.5)}$$

where A_O is the amplitude when x = 0, and α is defined as the attenuation or absorption coefficient and may be expressed in nepers per unit distance (*e.g.* Np mm^{-1}). The neper (also known as the napier) is a physical unit used for expressing the ratio of two analogous quantities; the number of nepers being the natural logarithm of this ratio. It is often more convenient to consider attenuation with wavelength, *i.e.* $\alpha\lambda$. This is the same as the attenuation per cycle, defined as the logarithmic decrement δ, for free vibrations, thus:

$$\alpha\lambda = \delta = \frac{\pi}{Q} \qquad \text{- (4.6)}$$

where Q is known as the quality factor and is discussed in section 4.1.4. It is also common to express attenuation in decibels per millimetre ($dBmm^{-1}$) or decibels per wavelength, where the conversion is 1 neper is equivalent to 8.686 dB.

The subject of acoustic attenuation is discussed in more detail in sections 4.3.1 and 4.3.5.

4.1.3 Specific Acoustic Impedance

There is a similarity between the variations of sound wave characteristics and those of certain quantities used in electrical alternating current theory. Thus acoustic pressure may be regarded as being analogous to electrical voltage, particle velocity to electrical current, and particle displacement to electrical charge.

Using the acoustic equivalent of Ohm's law, a quantity known as the specific acoustic impedance Z_a, equivalent to electrical impedance, may be defined as:

$$Z_a = \frac{p\ (\text{acoustic pressure})}{u\ (\text{particle velocity})} \qquad \text{- (4.7)}$$

Like electrical impedance, Z_a is, in general, a complex quantity. However for plane progressive waves, *i.e.* plane waves not reflected to form stationary waves (see section 4.1.5), the imaginary component disappears leaving a real quantity (*c.f.* electrical resistance). This real quantity can be shown to be equal to the product of the density ρ, and the velocity c, of sound for different propagating media and is called the characteristic impedance R_a:

$$R_a = \rho c \qquad \text{- (4.8)}$$

The value of R_a for a given material is seen only to depend on its physical properties and thus to be independent of the wave characteristics and the sound frequency. Table 4.1 given in section 4.2.14 lists values of R_a for certain materials.

4.1.4 Reflection and Transmission at a Plane Boundary and the Quality of Resonance.

When a beam of plane waves strikes a plane boundary separating two materials, some of the sound energy is transmitted forward and the remainder reflected backward as shown in figure 4.4

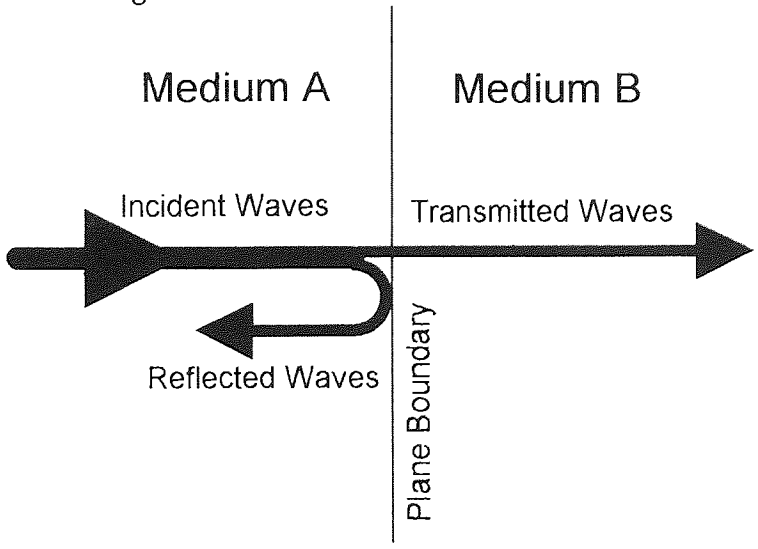

FIGURE 4.4. Reflection and Transmission for normal incidence at a plane boundary.

The relative amounts of reflected and transmitted intensities are expressed by the reflection and transmittion coefficients:

$$\text{Reflection Coefficient} = \frac{\text{Intensity of Reflected Waves at the Boundary}}{\text{Intensity of Incident Waves at the Boundary}} \quad \text{- (4.9)}$$

$$\text{Transmission Coefficient} = \frac{\text{Intensity of Transmitted Waves at the Boundary}}{\text{Intensity of Incident Waves at the Boundary}} \quad \text{- (4.10)}$$

The coefficients may be expressed either as percentages or as decreases in the number of decibels. It can be shown[95] that both coefficients can be expressed in terms of characteristic impedances R_1 and R_2 for the two media A and B, as defined by equation (4.8).

$$\text{Reflection Coefficient} = \frac{(R_1 - R_2)^2}{(R_1 + R_2)^2} \quad \text{- (4.11)}$$

$$\text{Transmission Coefficient} = \frac{4R_1R_2}{(R_1 + R_2)^2} \quad \text{- (4.12)}$$

The equations show that the transmission coefficient approaches unity and the reflection coefficient tends to zero when R_1 and R_2 have similar values. The materials are then said to be well matched or coupled. Alternatively, when the two materials have substantially dissimilar characteristic impedances, *e.g.* for a solid or liquid in contact with a gas, the transmission and reflection coefficients tend to zero and 100% respectively.

It can be seen when reflection coefficients are high and the absorption coefficient (section 4.1.2) low, the amplitude builds up to a high value within a medium. Alternatively, with high absorption and low reflection coefficients, the amplitude during oscillations is comparatively low.

The degree of resonance produced by an ultrasonic source is indicated by a dimensionless number, called the Q (or Quality) factor, a term familiar to electrical technologists, and is defined as follows:

$$Q = \frac{\text{Energy Supplied per Cycle}}{\text{Energy Dissipated per Cycle}} \quad \text{- (4.13)}$$

Here the energy is dissipated as a result of losses at the boundary, absorption, and losses due to the method of mounting the source. When the frequency is

increased above or reduced below the source value at resonance, a decrease in amplitude takes place. Figure 4.5 shows frequency response curves, which represent variations of velocity amplitude with frequency for a constant value of acoustic pressure amplitude.

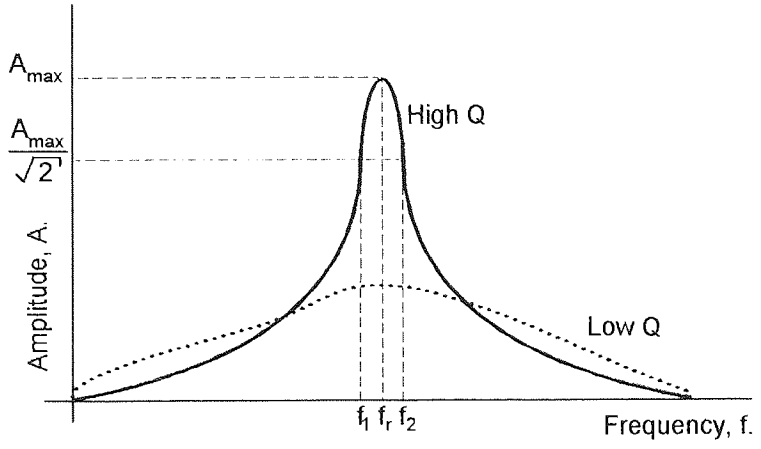

FIGURE 4.5. Frequency response curves showing relationships between amplitude A and frequency f.

The narrower and higher curve indicates a high Q, and the broader and lower curve a low Q.

An approximate value of Q can be obtained by reading off, from the curve, the values of the frequencies f_1 and f_2, on either side of the resonance frequency f_r, where the amplitude is reduced to $1/\sqrt{2}$ of its maximum value, then:

$$Q \approx \frac{f_r}{f_2 - f_1} \qquad \text{- (4.14)}$$

This approximation is only valid where Q is greater than 3. The frequency difference $f_2 - f_1$ is known as the frequency bandwidth.

4.1.5 Stationary Waves

When sound waves are reflected by plane boundaries as described in the previous section, the incident and reflected beams interfere with one another and a stationary (or standing) wave pattern may be observed. If, after a single reflection, the acoustic pressure or particle velocity amplitudes at various distances from the reflecting surfaces are measured, an amplitude variation is obtained. It is observed that the neighbouring amplitude maxima are one half-wavelength apart and that the distance between a maximum and its neighbouring minium is a quarter-wavelength. The ratio of the amplitude at the maximum to that

at the minimum is called the stationary (or standing) wave ratio (s.w.r), a quantity dependant on the reflection coefficient at the boundary and the attenuation coefficient for the material.

4.2 THE GENERATION OF ULTRASOUND

The history of the generation of ultrasound dates back over 100 years to the work of Galton who was interested in establishing the threshold frequencies of hearing for both animals and humans[96]. He produced a whistle with an adjustable resonance cavity which was capable of generating sound of known frequencies. With such an instrument he was able to determine the limit of human hearing as approximately 16 kHz. The whistle he produced was an example of a transducer - a device which converts energy from one form to that of another, which in this case was the conversion of gas motion into sound. A transducer can convert energy in one direction or be reversible whereupon the conversion in both directions is with equal efficiency.

4.2.1 Piezoelectric Oscillators

4.2.1.1 Naturally Occurring Piezoelectric Oscillators

Piezoelectric transducers are produced from materials displaying the piezoelectric effect, which was discovered by Pierre and Jacques Curie in 1880[97]. The effect occurs naturally in certain single crystals possessing polar axes, such as quartz, tourmaline, lithium sulphate, cadmium sulphide and zinc oxide.

Materials of this nature can be cut into a disc or slab, and the plane faces coated with a thin metallic film to enable electrical contact. If a mechanical stress is applied to the coated surfaces, equal and opposite electric charges will be induced on the faces which can be detected as a voltage. This is the direct piezoelectric effect, and the material's crystalline axis perpendicular to the coated face is the relevant polar axis. The converse effect is observed when a voltage is applied across the electrodes to produce an electric field which causes the crystal to suffer a mechanical strain - a method of oscillation.

The oscillation can be either compressional or shear, depending on how the crystal is cut. In quartz, for example, the principal polar axes are called the X and Y axes, of which there are three of each due to the symmetry of the crystal. The Z

axis is known as the optic axis and is non-polar for which the piezoelectric effect is not observed. X-cut quartz crystals (as shown in figure 4.6), for which the electrodes lie perpendicular to an X-axis, are associated with compressions and Y-cut crystals with shears. When an alternating voltage is applied across the faces of an cut piezoelectric transducer, it oscillates at the frequency of the applied voltage with an amplitude of the order of 10^{-6} times its thickness. If, however, the transducer is excited at one of its resonance frequencies, the amplitude is considerably increased to around 10^{-4} times the thickness. The oscillations will either be compressional or shear (as shown in figure 4.7), depending on the method of cut for the crystal.

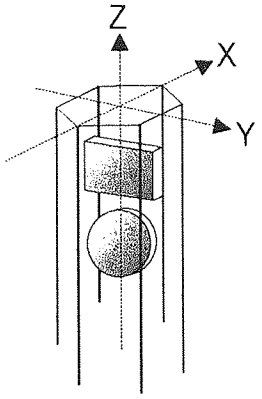

FIGURE 4.6. Axes of a quartz crystal, indicating X-cut retangular (❒) and circular (O) transducers.

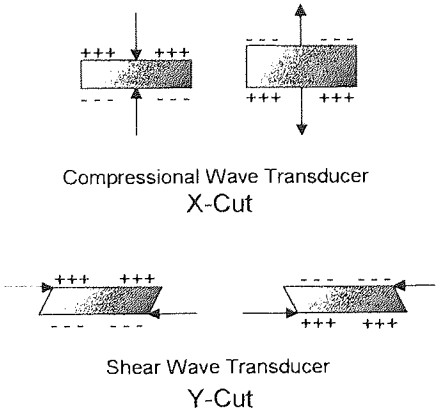

FIGURE 4.7. The Piezoelectric effect for compressional and shear wave transducers showing charges required on faces for oscillatory effects.

In practice these crystals are operated at a resonant frequency for either 'thickness' or 'length' vibrations, depending on whether resonance occurs for the direction perpendicular to or parallel with the radiating faces. The natural (fundamental) frequency for mechanical vibrations varies inversely with the

dimension along which the oscillations occur. That is, the thickness of a compressional piezoelectric transducer with a fundamental frequency f is $\lambda/2$, half the wavelength of sound through the crystal.

To generate frequencies of 20 MHz an X-cut quartz crystal plate would need to be 0.15 mm thick to be able to operate in fundamental thickness mode which corresponds to a sound velocity in quartz of *ca.* 3000 ms^{-1}. Such a plate would be extremely brittle, and for too high an applied voltage, may suffer from dielectric breakdown. It is therefore advisable when working at high frequencies to use thicker crystals but oscillating at one of the upper harmonics. Bergmann[98] has described the generation of ultrasound with a frequency around 55 MHz by oscillation of a quartz crystal 1 cm thick at its 191st harmonic. The piezoelectric effect can only occur when opposite charges appear on the electrodes, therefore only odd harmonics of the applied voltage can generate ultrasound. This can be explained with reference to figure 4.8. When a crystal is excited at its nth harmonic its thickness is divided into n equal parts with compressions and expansions taking place in adjoining sections. When n is even, compressions occur in n/2 of the sections and expansions occur in the remaining sections; thus there is no net strain in the crystal. Where n is odd, however, there is always an unequal number of compressions and expansions, leaving a compression or expansion to produce a net strain and thus oscillation.

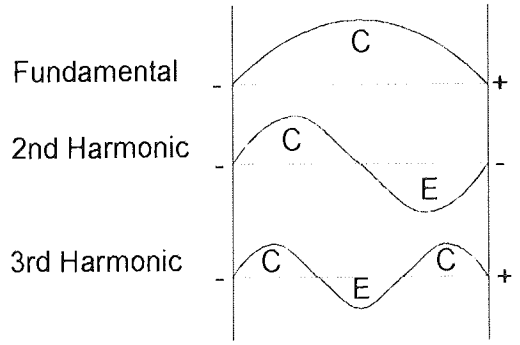

FIGURE 4.8. Distribution of pressure and charge for a piezoelectric crystal oscillating at the fundamental frequency and at the second and third harmonics.

4.2.1.2 Ceramic Transducers

The piezoelectric effect can be induced artificially in certain materials which display a phenomenon known as electrostriction, which is the elongation of a material when placed in an electric field. This effect can be observed in all dielectric materials, but its magnitude is negligible except in certain substances called ferroelectrics, which include barium titanate, lead zirconate titanate (PZT),

lead niobate and sodium meta-niobate. The ferroelectrics are generally referred to as ceramic transducers.

If one of these materials has a voltage applied across it, a mechanical strain, proportional to the applied voltage, is produced. When an alternating voltage of sinusoidal form is applied, the frequency of vibrations is double the frequency of the voltage and the form of oscillations are not smooth. To obtain a pure sinusiodal vibration at the frequency of the applied voltage as obtained with natural piezoelectric materials, the transducer must be polarised by providing the faces with steady equal and opposite charges of a sufficiently high magnitude.

A permanent polarisation can be obtained by heating the material to a temperature above the Curie point, where the electrostrictive effect disappears, and the allowing it to cool in a strong direct electric field, typically several hundred volts per millimetre. The direction of the electric field in relation to the material faces will determine its use in transverse or longitudinal strains or oscillations. Providing the exciting voltage is small compared to the initial polarising voltage, the oscillations will be purely sinusoidal and the produced transducer is effectively piezoelectric. Care must be taken to ensure the ceramic transducer is used in applications below its Curie temperature: if it is taken beyond the Curie point the piezoelectric characteristics will be lost, even on cooling. It is important to note that even naturally occurring piezoelectric materials have a Curie point and consequently an upper temperature limit.

4.2.1.3 Measurement of the Piezoelectric Effect

The piezoelectric effect is usually measured by the piezoelectric strain constant, sometimes called the d coefficient (see table 4.2). As the effect is reversible, this quantity may be expressed in one of two equivalent ways. The first definition is the amount of charge q, which flows when the crystal is subjected to a mechanical stress F:

$$d = \frac{q}{F} \quad (C\,N^{-1}) \qquad -(4.15)$$

The second definition depends on the voltage V, applied across the crystal without an applied load (*i.e.* supported freely in a vacuum) that produces a resultant strain and thus a displacement s, of the surface so that:

$$d = \frac{V}{s} \quad (V\ m^{-1}) \qquad \text{- (4.16)}$$

(*N.b.* Coulombs per Newton is dimensionally equivalent to volts per metre.)

Ceramic transducers generally have much higher d coefficients and electromechanical coupling coefficients than quartz crystals and because in addition, they have considerably lower electrical impedances, they can be operated at much lower voltages.

4.2.1.4 Practical Considerations when using Piezoelectric Transducers

The commonly used ceramic transducers are barium titanate ($BaTiO_3$) and lead zirconate titanate - PZT ($Pb[Ti,Zr]O_3$). Small amounts of various elements are added such as the substitution of Ba^{2+} in $BaTiO_3$ by Ca^{2+} and / or Pb^{2+} [99] in order to increase the operating temperature range. In PZT, the Ti/Zr ratio can be varied to provide a range of properties[100] and further modifications can occur by substitution of Pb^{2+} for Sr^{2+} or Ca^{2+} [101]. Such modifications are produced to assist in a particular application for the ceramic transducers. One formulation which is marketed as PZT-4 is especially suited for ultrasonic power generation, while another formulation PZT-5, has properties best suited as a pressure sensor. Piezoelectric transducers are reversible in operation and can produce oscillations or pick up stresses. The reason for this can be seen with the aid of table 4.1 showing the piezoelectric properties of quartz, PZT-4, PZT-5 and $BaTiO_3$.

The Quality factor Q, as defined in section 4.1.4 and equation (4.14), shows the approximate frequency band width about the resonant frequency centre. In an application such as ultrasonic power generation, the bandwidth needs to be small to produce intense ultrasound over a very small frequency range. This would correspond to a high quality factor Q. A transducer as a detector will be required to pick up over a wide frequency range, so in this case, a low Q transducer should be employed. Although the quality factor was discussed in the context of the generation of sound, it also explains which transducer properties are required for detection and transmission.

If one face of a transducer is kept rigid and the other face left free to vibrate, a condition is produced called quarter wave resonance for which the thickness l of the transducer is equal to $\lambda'/4$ where λ is the wavelength of sound in the material of the transducer. The effect of this is to cause a node at the rigid end which produces a maximum amplitude from the transducer at the resonating end.

Odd harmonics can be produced. However there is a decrease in amplitude as the order of the harmonic increases.

	Quartz	PZT-4	PZT-5	$BaTiO_3$
COMPRESSIONAL	X-cut			
Q	>25000	<500	<75	<400
Z_o / 10^6 Kg m^{-2} s^{-1}	15	30	29	25
SHEAR	Y-cut			
Q	>25000	<500	<75	<300
Z_o / 10^6 Kg m^{-2} s^{-1}	10.2	14	12.6	13.3
GENERAL				
d coefficient / C N^{-1} x 10^{12}	2.3	289 - 496	374 - 584	190 - 260
ρ / Kgm^{-3}	2650	7600	7500	5700
Maximum Operating Temperature / ^oC	550	250	290	70 - 90
Curie Temperature ^oC	575	320	365	115

TABLE 4.1 Compressional, Shear and General Properties for Various Piezoelectric Materials.

A transducer, when mounted symmetrically in a fluid having a low characteristic impedance, can be made effectively 'air-backed' by an arrangement known as quarter-wavelength backing[102]. If a solid reflector is placed parallel with the rear surface of the crystal and at a distance from it of exactly a quarter-wavelength (in the fluid), the amount of energy reflected from the surface back through the transducer into the fluid is very high; for gases it approaches 100% reflection and for non-viscous liquids such as water, 95%.

A crystal transducer must be provided with electrodes before it can be used for ultrasonic propagation. The electrodes should be as light as possible, so as not to affect the vibrational characteristics of the transducer, and they should also be durable. Commercially available transducers are usually supplied with a thin film coating of a metal, usually aluminium, gold or silver which is plated by electrolytic methods or by cathode sputtering.

The next consideration is a suitable mechanical support combined with good electrical contact to the transducer faces. The method of mounting will depend on the type of application, as mounting itself affects the quality factor Q. At a frequency of 1 MHz, the bandwidth of a nodally mounted quartz crystal in hydrogen is only 0.5 kHz, whereas for a ceramic transducer coupled to a solid it may be as high as 300 kHz[103]. Nodal mounting is considered the most ideal method of transducer mounting and involves clamping the transducer by two or three screws or pegs along its edge. The contact between mounting and transducer is at the nodal point which occurs at half the transducer's thickness.

It is for the above reasons that ceramic transducers are recommended for short pulse ultrasound work, and quartz crystals for continuous frequency stable work. The high absorption coefficients of the ceramic transducers also render them liable to overheating, with the consequent variation or even disappearance of piezoelectric characteristics.

Finally, efficient coupling is needed between the transducer and the medium it is irradiating. A suitable liquid is strongly recommended if coupling a transducer with a solid to avoid an air gap which would give rise to very high attenuation or even zero transmission. A film of oil or another suitable liquid is usually sufficient but, at low temperatures where most liquids solidify, it may be necessary to use high-vacuum grease to prevent loss of continuity of characteristic impedance.

4.2.3 Magnetostrictive Transducers

Magnetostrictive transducers are made of ferromagnetic materials such as nickel, cobalt or iron, which can be easily magnetised and display magnetostriction or the Joule effect. When a bar or rod of one of these materials is placed in a magnetic field, it suffers a change in length, either an increase or decrease, depending on the nature of the material and the strength of the field, not the field direction.

In practice, nickel is found to be the most suitable material for magnetostrictive transducers, as it has an electromechanical coupling coefficient of 31% and a Curie temperature of 358^{o}C. Permadur, an alloy of 2% vanadium and 49% each of copper and iron, has a Curie point of 980^{o}C but has a low electromechanical coupling coefficient. Magnetostrictive transducers are often made in the form of a rod surrounded by coil windings as can be seen in figure 4.9.

An alternating current through the coil induces an alternating magnetic field of the same frequency which gives rise to longitudinal oscillations of the rod. The strain in the rod depends only on the magnitude of the applied field (analogous to the mechanical strain proportional to the applied voltage in ceramic transducers) and hence the rod oscillates at twice the frequency of the field. As with ceramic transducers, without polarisation the vibrations are of low amplitude and contain unwanted frequencies.

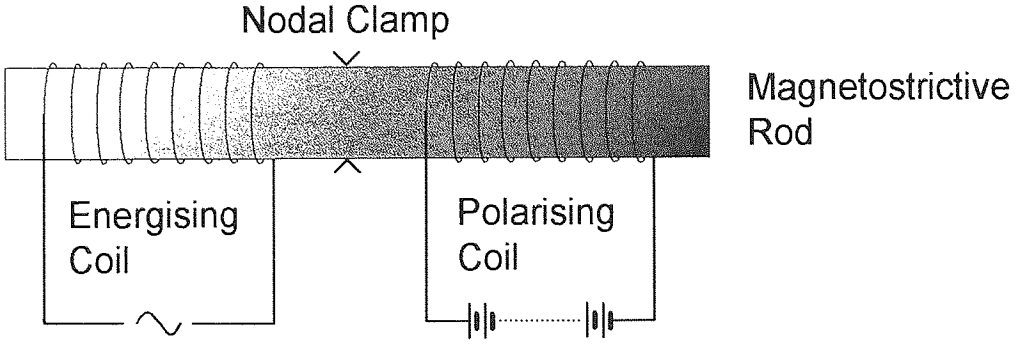

FIGURE 4.9. A method of exciting a magnetostrictive transducer in the form of a rod.

The resonance frequency varies inversely with length of the transducer rod, for example, a nickel rod 125 mm long has a fundamental resonance frequency of 20 kHz. The frequency is increased by decreasing the length, but at the same time, there is a lowering of intensity for a rod of given cross-sectional dimensions resulting from the reduction in size of the vibrating mass. The output from this type of transducer becomes vanishingly small at frequencies higher that 100 kHz and is rarely used in high intensity applications above 20 kHz.

4.2.4 Mechanical Transducers

Mechanical (only) ultrasonic generators are now used almost exclusively for high-intensity propagation in liquids and gases at frequencies of up to about 25 kHz and exist mainly in the form of whistles and sirens. They are generally more powerful and less expensive that piezoelectric and magnetostrictive transducers but are more limited in application.

Ultrasonic whistles come in two types, namely the cavity resonator, used mainly for gases, and the wedge resonator, employed for both gases and liquids. There are two forms of cavity resonator, the Galton whistle[104] and Hartmann generator[105] shown in figure 4.10.

The Galton whistle consists of a cylinder terminated by the end-surface of a piston which can be adjusted in position to provide resonance at the required frequency; for which the length of the cavity l, is one quarter-wavelength. The fluid flows through an annular slit at high speed and strikes the rim of the tube where vortices appear and produce edge tones. The frequency of the edge tones depend on the velocity of fluid which can be adjusted until the cavity resonates.

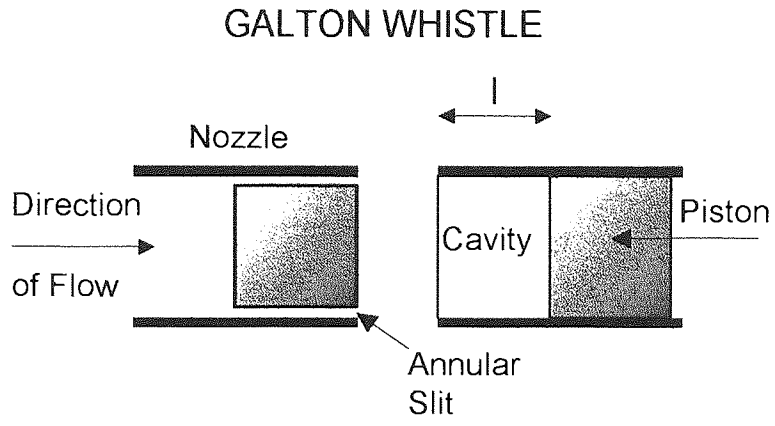

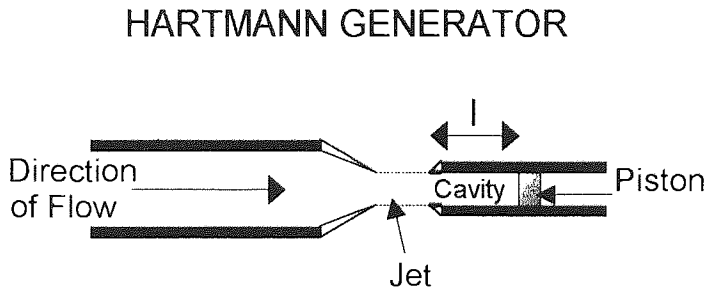

FIGURE 4.10. The Galton Whistle and Hartmann Generator. Ultrasound is emitted spherically from the centre of the space between the two sides of the equipment.

The Hartmann generator is similar to the Galton whistle, except that the annular slit is replaced by a conical nozzle. The fluid is forced through the nozzle and emerges at a supersonic velocity to produce shock waves which cause the cavity to be excited at a high intensity. Resonance is achieved by adjusting the fluid velocity and it is found that this device is more powerful than the Galton whistle. It is possible to produce up to 50 W of acoustical energy .

The wedge resonator consists of a rectangular plate with wedge-shaped edges, mounted on nodal supports and placed in a fluid jet stream as shown in figure 4.11.

The wedge is set up into flexural vibrations having an intensity comparable to the Hartmann generator. This type of transducer is especially suitable for use with liquids and is employed extensively to produce emulsions. Operating frequencies are again in the order of 20 kHz.

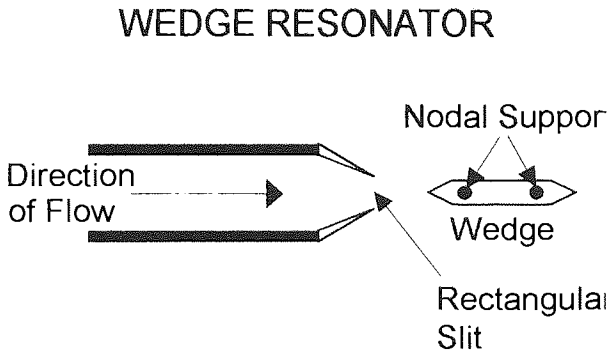

FIGURE 4.11. Side view arrangement for a wedge resonator.

Sirens are also used for generating high energy ultrasound in fluids. They consist of a disc (the rotor) in which are cut a number of identical holes spaced evenly around just inside the circumference of it. The rotor turns concentrically in front of a similar disc (the stator), which is kept at rest whilst fluid jets are directed through the holes. The frequency of the emitted ultrasound is equal to the frequency of interruption of the jet flow as the holes on the rotor and stator move relative to each other. Thus a siren with a rotor having 100 perforations and revolving at 200 rev. s^{-1} emits a sound wave of 20 kHz. The tone emitted by the siren is not pure, but it suits certain applications. One advantage of this instrument is that the frequency can be varied in a continuous manner simply by altering the speed of rotation.

4.2.5 Miscellaneous Transducers

Electromagnetic types of transducers are commonly used at audible frequencies in the form of loudspeakers and microphones but their application to ultrasonic frequencies are somewhat limited because of the rapid increase of inertial effects with frequency above the audible range. However, with the now routine techniques of thin film deposition, such disadvantages have been overcome, and lightweight electromagnetic transducers have been used in a variety of low intensity applications[106, 107].

Electrostatic transducers consist essentially of two parallel plates of conducting material close to one another to form an electrical capacitor. One plate is fixed and the other plate is free to vibrate in a direction perpendicular to the surface of

the plates. A high resistance is placed in series with the plates and a direct potential difference of several hundred volts maintains steady charges on the plates. Such a device can be used for frequencies up to 300 kHz and is capable of acting as both a receiver and a transmitter. Operation as a transmitter is obtained by an output voltage not exceeding the direct potential difference, being fed to the plates. The resultant periodic variation of the charges induces vibrations of the moveable plate.

4.2.6 The Mechanical Amplification of Ultrasound

Solid horns (sometimes referred to as probes, concentrators, rods, tools and amplitude or velocity transformers) can be used on either piezoelectric or magnetostrictive transducers to amplify the displacement or particle velocity of the transducer. They can also provide a more suitable impedance match between the transducer and the load to which it is to be coupled. Ultrasonic intensity is generally defined in terms of the power density at the radiating face of the ultrasonic transducer. Power density is defined as the electrical power into the transducer divided by the surface area of the transducer (or in the case of a mechanical horn, the end area of the probe tip). Sometimes, the power is described as the peak-to-peak amplitude of the transducer radiating face or horn tip, and is usually given in μm.

Figure 4.12 shows the profile, velocity and stress within five designs of ultrasonic horn; the stepped, the conical (or linear taper), the exponential, the catenoidal and the Fourier horn. It can be seen immediately that the stress experienced at the step of the stepped horn is the drawback in this design.

The conical horn has limitations on its design which only offers magnification by approximately fourfold. The exponential horn offers a much higher magnification (by a factor of 150 W power). However, its shape make it more difficult to manufacture but its narrow length and small tip area makes it suitable for the irradiation of small samples.

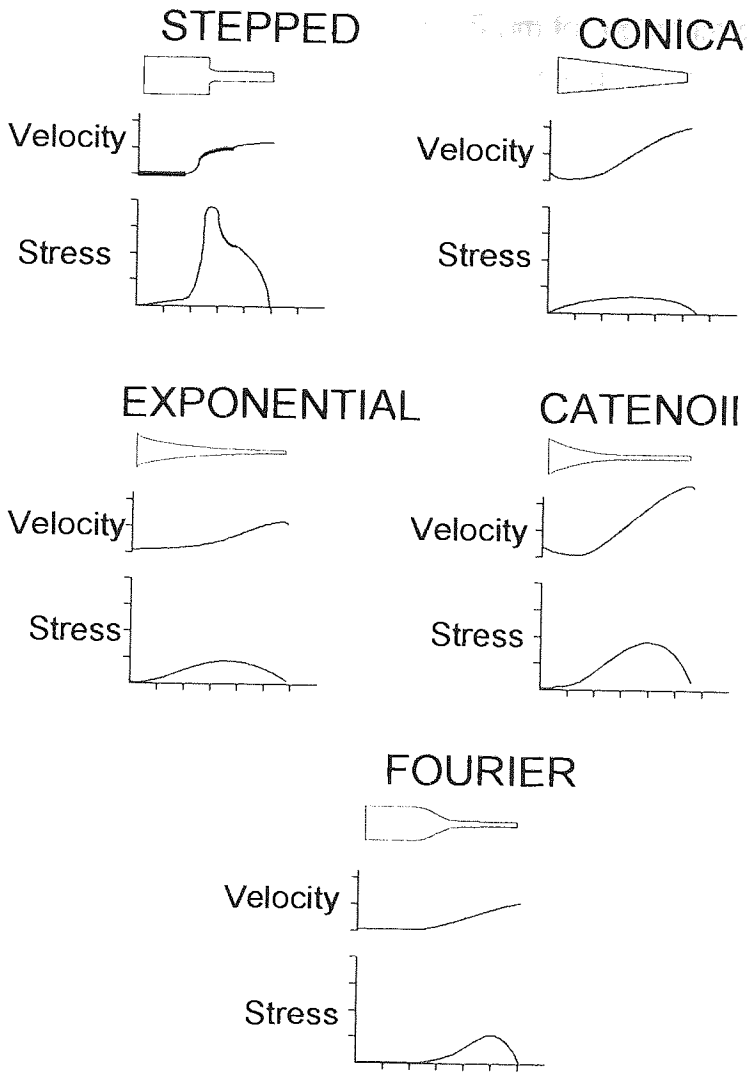

FIGURE 4.12. The profiles of horns for amplifying the output of transducers. The plots underneath each horn correspond to the velocity (top) and stress (bottom) profiles. The scales are in arbitrary but identical units for comparison of horn characteristics.

The zone of high ultrasonic intensity at the probe tip appears to be very small, *e.g.* for a horn with a tip diameter of 5 mm, the zone is approximately 7 mm wide and 100 mm long[108]. A horn must be designed to resonate at the same frequency as the transducer which is driving it. If it resonates at a slightly different frequency, there is a loss in efficiency of the horn as an amplifier. Better horns are produced by including resonant cylindrical sections on a tapered horn, *i.e.* such as a cylinder of length l_1 coupled with an exponential, catenoidal or Fourier length l_2.

It is not practical to have the large diameter section of a horn longer than a quarter of the wavelength. This is due to the excitation of shear (transverse) modes within the horn which will absorb energy from the driving element and reduce amplification. The horn should preferably be made from a material with an acoustic impedance close to that of the transducer with the face of the horn which

couples with the transducer ground to within 2.5 μm for optimum coupling. A thin film of oil or grease will provide improved coupling at the horn-transducer interface.

Disadvantages with ultrasonic amplification horns include the generation of unwanted free radicals at the tip (for example, *via* sonolysis of the solvent) and prolonged use generally results in tip erosion and fatigue in the horn, even when using metals such as titanium.

4.3 THE EFFECTS OF ULTRASOUND ON LIQUIDS AND SOLIDS

4.3.1 The Passage and Attenuation of Ultrasound Through Liquids and Solids.

As outlined in section 4.1.2, ultrasonic waves are in reality attenuated and the intensity tends to decay exponentially with distance from the source. This behaviour was described by equation (4.5). As the ultrasound passes through a liquid or solid, it can induce oscillations of the molecules about their mean rest positions. Although in principle, the translational energy produced can be transferred by elastic collisions to other molecules, in reality energy losses occur.

The observed acoustic losses depend on the medium used where physical properties such as density, viscosity and sample temperature dictate the extent of attenuation. In liquids, the two major effects causing acoustic loss are the viscous and thermal effects. Absorption of sound increases with viscosity and the extent of thermal energy transfer within the liquid.

The attenuation of sound in solids may be caused by a number of factors. Losses can occur due to the nature of the solid, *i.e.* if it is polycrystalline or non-homogeneous; or if there are lattice imperfections or dislocations in a crystalline solid. Sound travelling through such systems would be scattered in all directions and thus attenuated. The intensity of ultrasound can also be reduced by the absorption of sound by the lattice: electrons, nuclei and by the atoms or molecules themselves.

The attenuation of ultrasound also occurs at the boundary between states of matter, *e.g.* between a liquid and a solid. If a solid boundary in contact with a liquid has many surface imperfections, ultrasound is attenuated and lost at this boundary.

4.3.2 Streaming

Streaming is the term given to the bulk flow of fluid that results whenever a sound wave is present in the medium and was first observed by Faraday[109]. Under certain circumstances (high intensity ultrasound and the presence of surfaces) the effects of streaming can be quite marked.

4.3.3 Chemical Reactivity

The use of power ultrasound to accelerate and influence chemical reactions has expanded to the point that 'Sonochemistry' has become a complete subject in its own right. Many reactions utilise ultrasound for the production of radicals such as H· and OH· in water. In solid / liquid systems cavitation can act to remove inert layers on the solid or produce pitting of the surface to induce greater reactivity by increasing surface area. Examples of Sonochemistry can be found in texts edited by G.J. Price[110] and T.J. Mason[111].

4.3.4 Cavitation

The chemical effects of ultrasound (see above) largely derive from the physical phenomenon of acoustic cavitation: the creation, growth, and implosive collapse of bubbles in liquids. If the sound field in a liquid is sufficiently intense, bubbles will form in the liquid (in the presence of nucleation centres) during the expansion cycle. The oscillations of the sound field make these bubbles grow and contract. At a certain size, the bubbles can be driven into an implosive collapse. As the compression of a gas creates heat, this implosion is believed to generate an intense, but short lived, hot-spot.

In order to observe cavitation, the sound field must overcome the liquid's tensile strength, the attractive forces between molecules which hold the liquid together[112]. Simple theory predicts that more than 1000 atmospheres of negative acoustic pressure would be necessary to cavitate pure liquids. In practice, most liquids will cavitate with an applied ultrasonic negative pressure of a few atmospheres. The reduction in the necessary acoustic pressure, is due to the existence of small solid particles (*e.g.* dust) that have gas trapped in surface crevices; referred to as the Harvey model of microbubble stabilisation[113].

A microbubble cavity released from a small solid particle will oscillate at the natural resonant frequency in phase with the expansion and compression ultrasound waves. The surface area of the bubble will naturally be a little larger during expansion than in the compression cycle. Since the amount of gas that would diffuse into or out of the cavity depends on the surface area, diffusion into the cavity during the expansion cycle will be slightly greater than diffusion out of the cavity during the compression cycle. Therefore, with each cycle of sound, the bubble expands slightly more than it shrinks and over many cycles it will slowly grow. This growing cavity can eventually reach a resonant size where the gas inside the cavity efficiently absorbs energy from the ultrasound field. This critical size depends on the frequency of ultrasound through[114]:

$$R_r = \frac{1}{2\pi\upsilon}\left(\frac{3\kappa P_o}{\rho}\right)^{\frac{1}{2}} \qquad \text{- (4.16)}$$

where R_r is the resonant cavity radius (in m), υ is the ultrasound frequency (in Hz), P_o is the liquid ambient pressure (in Pa), ρ is the liquid density (in kgm^{-3}) and κ is the polytropic constant which varies between the ratio of specific heats and unity, these being the limits for adiabatic and isothermal conditions, respectively.

At this point, the bubble can grow rapidly over a single cycle of sound. High-intensity ultrasound can expand the bubble so rapidly during the negative pressure cycle that it is unable to shrink again during the positive cycle. Once the cavity has experienced very rapid growth, it can no longer absorb energy efficiently from the sound waves. Without this energy input, the cavity can no longer sustain itself, the liquid rushes in and the cavity implodes. On collapse, the peak gas phase temperature and the surrounding liquid shell temperatures have been deduced to be *ca.* 5200 K and 1900 K respectively by comparative rate thermometry[115]. It is also thought the instantaneous pressures produced on collapse could be of the order of 1000 atmospheres[116]. The origin of this 'hot-spot' hypothesis of cavitational collapse comes from the sonochemical fraternity. There have been several proposals for an alternative mechanism of electrical discharge[117]. These proposals are considered to have not been well developed on a molecular level and recently have been throughly rebutted as inconsistent with observed sonochemical reactivities and sonoluminescent behaviour[118].

When cavitation occurs in a liquid near an extended solid surface, the bubble collapse differs from the spherically symmetric implosion observed in homogeneous liquids[119]. The presence of the surface distorts the pressure form

of the sound field, and cavitational collapse generates a moving jet of liquid travelling faster than 100 ms^{-1} and directed at the surface as in figure 4.13.

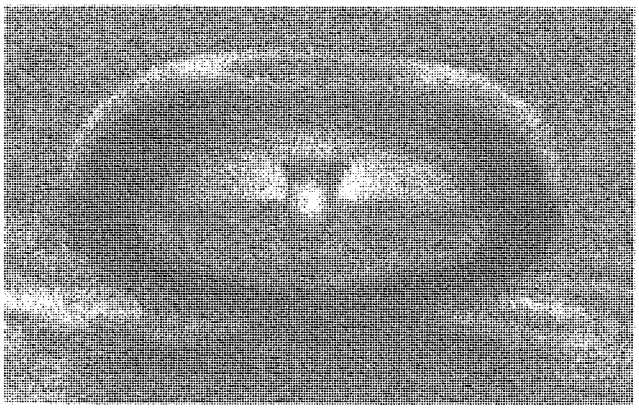

FIGURE 4.13. A collapsing cavitation bubble showing a microjet directed at a solid surface.

The impingement of this jet can create localised surface damage and is responsible for cavitation erosion, surface pitting and ultrasonic cleaning. A second contribution to cavitational erosion is the impact of shockwaves generated by bubble collapse, which can be large enough to deform metals. This microjet formation requires an extended surface[119,120] and it has been found[121] that metal powders with particle sizes comparable or larger than collapsing bubbles can be made to agglomerate; whereas those smaller do not. It is thought the shock waves produced from microjet formation combined with local turbulent flow cause metal particles such as zinc to travel at such high velocities that when the particles collide inelastically, melting occurs at the point of impact.

There are six major factors which affect the production of cavitation; which are as follows:

(a) **Ultrasonic power**. Cavitation increases with the intensity of ultrasound administered. However, with all liquids, there appears to be a minimum required ultrasonic power input to facilitate cavitation. This is known as the cavitation threshold and many of the factors listed below affect cavitation in such a way as to increase or decrease the threshold. Cavitation thresholds are generally obtained from experimental data.

(b) **Physical properties of the liquid**. Liquids with large intermolecular forces have higher cavitation thresholds than those with small intermolecular forces.

(c) **Temperature**. Cavitation threshold drops as temperature is increased towards the liquid boiling point.

(d) **The presence of dissolved gases**. Dissolved gases lower the cavitation threshold as the expansion cycle acts to release the gas by causing a reduction in pressure in the system and thus a decrease in gas solubility.

(e) **The presence of particulate matter**. Particles act as seeds to cavitation due to the presence of gases or air pockets in cavities surrounding the solid.

(f) **Ultrasound frequency**. Cavitation becomes more difficult to achieve as frequency is increased. This is due to the shorter periods between compression and expansion which inhibits the production and collapse of cavities. At frequencies above a few megahertz cavitation ceases and sonochemical reactions are not observable[122].

4.3.5 Emulsification, agglomeration and aggregate dispersal

The use of ultrasound to emulsify or disperse solid / liquid systems is widespread in the paint and dyes industries. Unfortunately, the bulk of equipment used is rather specialised and uses focusing apparatus to concentrate ultrasonic waves to a point where the systems to be emulsified or dispersed are passed[123,124]. Emulsification can also be achieved using standard ultrasonics equipment. Special care has to be taken in order to produce a stable emulsion system by the addition of stabilising agents such as surfactants.

In the same way that ultrasound can produce stable dispersions of solids in liquids, it can also produce aggregation of particles suspended in a fluid medium. Wood reported in 1939[125] the aggregation of finely powdered anthracite coal in water by ultrasound, which did not occur when the water was boiled to remove dissolved gases.

It has been proposed by Blitz[126] that a suspension of particles is likely to coalesce at low ultrasound powers due to an acoustic pressure drop between the particles. However, if the ultrasound intensity is sufficiently high, the suspended aggregates are broken up and kept apart by cavitation and thus form an emulsion.

4.4 THE ACOUSTIC MANIPULATION OF OBJECTS

The non-linear effect of the interaction of the sound field with an object within an acoustic field provides an experimenter with a unique possibility of manipulating

an object in a host medium using only the acoustic field. The first study on a spherical bubble was by Bjerknes[127] which was closely followed by King[128] and was extended for compressible objects by Yosioka and Kawasima[129]. The work of Dysthe[130] with corrections as noted by Crum[131] is a comprehensive treatment of the force exerted on solid, liquid and gas inclusions in a stationary (standing) sound field and is discussed in section 4.4.1. Other studies in this area includes the derivation of the radiation force for an arbitrary shape by Westervelt[132] and further extensions to the work of King[128] by Embleton[133]. Nyborg[134] calculated the force exerted by a sound field on a small rigid sphere and Hasegawa[135] derived theory for and conducted experiments on the radiation force on a sphere in a quasi-stationary field.

4.4.1 Interaction of a Sound Field with an Object

Dysthe[130] considered single particles with dimensions much smaller than the acoustic wavelength, in a standing acoustic wave. He showed that a small anisotropic body, subject to a vertical acoustic wave, will have three equilibrium orientations of differing stability, corresponding to each of the three principal axes of the body's induced mass tensor each being parallel to the direction of propagation of the acoustic wave. The most stable of the orientations is when the major principal axis is parallel to the direction of the wave. The particle will rapidly find the most stable equilibrium orientation and then the motion of the particle should be purely translational. In any other than the three stable orientations there is a force perpendicular to the direction of propagation of the acoustic wave that necessarily causes rotation of the particle to a stable orientation. Consequently, if any perturbation of the system moves the body from one of its stable orientations it will rapidly reorientate to its most stable equilibrium orientation.

It is known[136] that small rigid bodies can be trapped in the neighbourhood of some horizontal planes when a standing plane sound wave is applied vertically in a liquid. In addition to acoustic forces, Dysthe[130] identifies the forces due to gravity, buoyancy and viscous drag as factors in determining the trapping of particles. This suggests that through suitable choices of ultrasonic power, particle size and density of support liquid in relation to that of the solid it should be possible to manipulate particles to almost any vertical position. This can be seen with the aid of figure 4.14.

The particle of volume V_p in figure 4.14 is of a density ρ_p and has been placed in a liquid of density ρ_f, where $\rho_p < \rho_f$, so that normally the solid is able to float on

the liquid. If ultrasound is applied from the surface of the liquid, the particle will experience a downward force, submersing it in the fluid. The particle will be forced to a depth where the buoyancy (upthrust) force from the liquid F_b is identical in magnitude but opposite in direction to the ultrasonic force F_u. The force due to buoyancy is constant for any fully submerged position; however, the ultrasonic force becomes attenuated with distance. The result is that the particle reaches an equilibrium distance from the ultrasonic source where the attenuated ultrasound produces a force equal but opposite to the buoyancy on the particle.

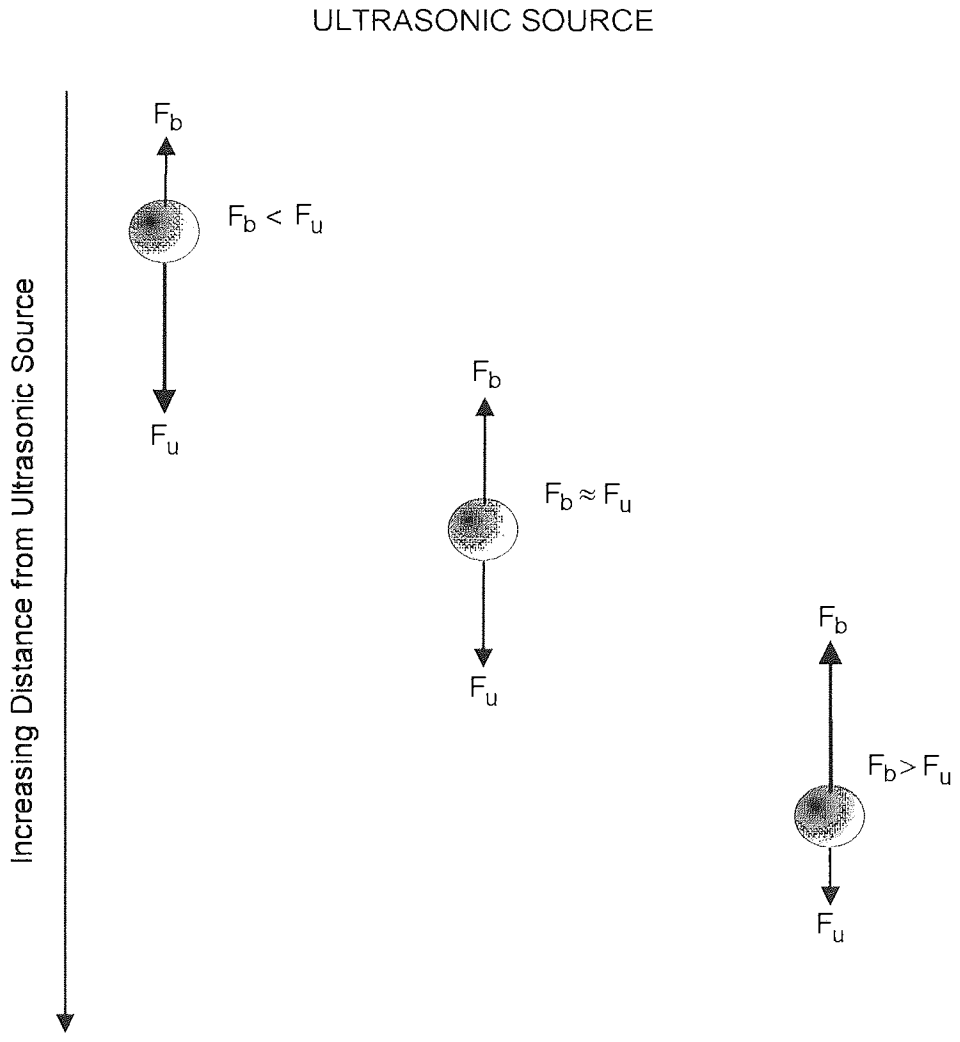

FIGURE 4.14. The balancing of ultrasonic and bouyancy forces on a single particle at different distances from an ultrasonic source. The supporting medium is considered to be more dense than the particle in this example and the effect of gravity on the particle is ignored.

CHAPTER FIVE

INTRODUCTION TO THE SONICALLY INDUCED NARROWING OF THE NUCLEAR MAGNETIC RESONANCE SPECTRA OF SOLIDS

5.1 INTRODUCTION

The first report of apparently successful experiments on the sonically induced narrowing of solid-state NMR spectra (SINNMR)[1] emphasised both the irreproducibility of the technique and the uncertainty regarding its true origin. If such a technique can be made reproducible and the effect definitively attributed to the sonically induced incoherent motional averaging of particles, the technique could offer a simple alternative to magic-angle spinning (MAS NMR)[2] and even dynamic angle spinning and double-rotation (DAS and DOR NMR)[3,4]. These methods for reducing solid state NMR line broadening involve coherent motional averaging. SINNMR attempts to average out the solid state NMR interactions by incoherent motional averaging, as the Brownian motional averaing and UFP NMR techniques do, but by a much simplified experimental method.

5.2 THE UNDERLYING HYPOTHESIS AND PRINCIPLES OF SINNMR

The principles underlying the narrowing of the NMR spectra of solids by inducing incoherent motion of particles are similar to those that result in the narrowing of the spectra of liquids due to natural incoherent molecular motion.

The exhaustive theory from chapter 3 describing the solid-state NMR interactions can be simplified by following the approach of McCall[137] for polymer solutions. Consideration of the liquid-state NMR spectra of large molecules appears to be a perfect system for analogy to SINNMR. The approach defines the proportion of NMR line broadening due to insufficient averaging in terms of a time-averaged local field (B_{loc}). The dipolar broadening component of such a field is given by:

$$B_{loc} \approx \left(\frac{\mu}{r^3}\right)\left(\frac{1}{T_2}\right)\int_0^{T_2}[3\cos^2\theta(t)-1]dt \qquad \text{- (5.1)}$$

where θ is the angle between the radial vector joining two interacting dipolar nuclei of moment μ, separated by a distance r, and the direction of the polarising magnetic field. If $\theta(t)$ varies over its range of values in a time much shorter than T_2, equation (5.1) can be replaced by the space-averaged equation (5.2):

$$B_{loc} \approx \left(\frac{\mu}{r^3}\right)\int_0^{\pi}(3\cos^2\theta-1)f(\theta)\sin\theta d\theta \qquad \text{- (5.2)}$$

where $f(\theta)$ describes any restrictions on the angular momentum of the molecule. If all angles are equally accessible, the dipolar-field line broadening will be zero, and resonances within the extreme narrowing limit will be observed. If, however, spatial averaging is restricted, some line broadening will be observed, to an extent that depends on the range of inaccessible angles.

Simple computer simulations based on equation (5.2)[138] using appropriate values of T_2 revealed that in the case of unrestricted incoherent particle motion the requirements of equation (5.2) may be largely met by the adoption of a relatively small number of random values of θ. The mean number of θ values necessary to effect the required averaging was found to be 6 for a run of 10000 samples[138] with *ca.* 66% of the samples requiring less than 20 values. This information implies that the requirement of accessing sufficient random angles in a time of the order of T_2 to effect spectral line narrowing through induced incoherent motion should be relatively easy to fulfil.

A basis for the use of ultrasound to induce the necessary incoherent particle motion may be deduced form the theoretical work of Dysthe[130] outlined in section 4.4.1. At low ultrasound intensities, it is intended that the effect of the acoustic wave on particles suspended in a liquid is to cause the particles to move so that if many are present, (tangential) interparticle collisions can occur and result in particle rotation. At higher acoustic intensities, irradiation of liquids produces cavitation bubbles in the liquids, and unstable cavity collapse. The collapse of cavities can produce microjets (as described in section 4.3.4) which can impose high energy densities at the site of impact with a solid surface. If such a jet strikes a solid particle asymmetrically with respect to its centre of mass, such an impact will facilitate rotational motion. However, as discussed in section 4.3.4, for effective interaction between collapsing cavity microjets and a solid surface, the surface must not be less than the resonance bubble size (which is defined *via* equation (4.16)).

In principle, therefore, both inter-particle collisions and microjet-particle interactions can cause the incoherent particle motion that is necessary for SINNMR. However, as implied above, the rate of particle rotation is not simply related to the frequency of ultrasound used. The latter does, nevertheless, become important if reliance is placed on microjet action to cause particle rotation because the relationship between the sizes of the resonance bubble cavities and the particles will impose a lower limit on the size of particles that can be studied using a particular ultrasonic frequency.

CHAPTER SIX

EQUIPMENT AND EXPERIMENTAL METHODS

6.1 THE JEOL FX-90Q FT-NMR SPECTROMETER

A JEOL FX-90Q iron magnet FT-NMR spectrometer was the instrument used for carrying out the research reported within this thesis. Whilst it has a proton (^{1}H) resonance frequency of 89.56 MHz, the instrument is capable of detecting all NMR active nuclei (except ^{3}H). The nuclei observed by NMR spectroscopy during the course of this thesis are shown in table 6.1, together with resonant frequencies, nuclear spin and relative receptivities (to ^{13}C).

Nuclear Isotope Observed	Resonance Frequency on FX-90Q / MHz	Nuclear Spin Quantum Number	Relative Receptivity (to ^{13}C = 1.0)
^{1}H	89.564477	1/2	5700
^{11}B	28.724671	3/2	754
^{13}C	22.523062	1/2	1.0
^{19}F	84.267756	1/2	4700
^{23}Na	23.691500	3/2	525
^{27}Al	23.337630	5/2	1200
^{29}Si	17.793860	1/2	2.1
^{31}P	36.256318	1/2	377

TABLE 6.1 General NMR Information for the nuclei observed during the course of SINNMR studies reported within this thesis.

The NMR parameters discussed within this thesis have been introduced within section 2.2.1, and the specific parameters for each nucleus observed, can be found in appendix two. Wherever comparisons were made between static solid and SINNMR spectra, identical spectral acquisition parameters were used.

In order to improve the stability of the static field B_0 generated by the iron core electromagnet of the FX-90Q, the spectrometer is equipped with an electronic device termed the field-frequency lock. While the FT experiment on the nuclei being observed is performed, a time sharing pulse experiment runs concurrently in which a dispersion mode signal of a lock substance is monitored. If any fluctuations in the polarising field or the resonant frequency occur, the off-resonance lock signal will correspond with either a positive or negative voltage depending on which way the resonance has moved. Feed-back signals can be derived from these changes to enable exact resonance for the lock material to be reachieved. The FX-90Q uses either an external ^{7}Li lock or internal ^{2}H lock. The internal lock is placed in the NMR tube of the sample under investigation.

The external lock is placed in a second probe within the magnet of the NMR spectrometer. The disruptive nature of the ultrasound within SINNMR experiments lead to the use of the external ^{7}Li lock.

The NMR spectrometer used enables Fourier transformation of detected FIDs based on up to 32 K data points but only 8 K data points during acquisition when using the foreground - background unit. The FID can be transformed with and without exponential weighting (with variable line broadening) and the resultant spectra improved by a smoothing function. The computer also enables the integration of peak intensities, external referencing in Hz or ppm, as well as the measurement of FWHM to the nearest data point. All NMR spectra were recorded using an integral flat bed plotter.

6.1.1 The NMR Variable Temperature Apparatus

The FX-90Q NMR spectrometer is equipped with a variable temperature (VT) system for the regulation of sample temperature within the machine between -100^{o}C and +180^{o}C by use of (heated) air or liquid nitrogen. When the VT is not in use, the NMR magnet operates at a temperature of 28^{o}C which is held constant by cycling deionised water around the magnet *via* a cooling system.

The VT unit was calibrated using a NORMA D1401 digital temperature meter with a COMARK NiCr / NiAl (BS 4937K) probe 300mm long, 3mm in diameter and active only at the tip. A sample of silicone oil was placed in a standard glass 10mm o.d. NMR tube and heated by the VT within the magnet for 20 minutes to obtain thermal equilibrium before probe readings were taken. All temperatures quoted are for the NMR probe coil region and are accurate well within ±0.5^{o}C when compared to the readings of a calibrated mercury thermometer.

6.1.2 The NMR Probe

The NMR probe insert used throughout the research conducted in this thesis is shown in figure 6.1.

The NMR probe coil region contains two coils, each spanning an active length of 14mm, which are responsible for the generation of the r.f. pulse, detection and decoupling.

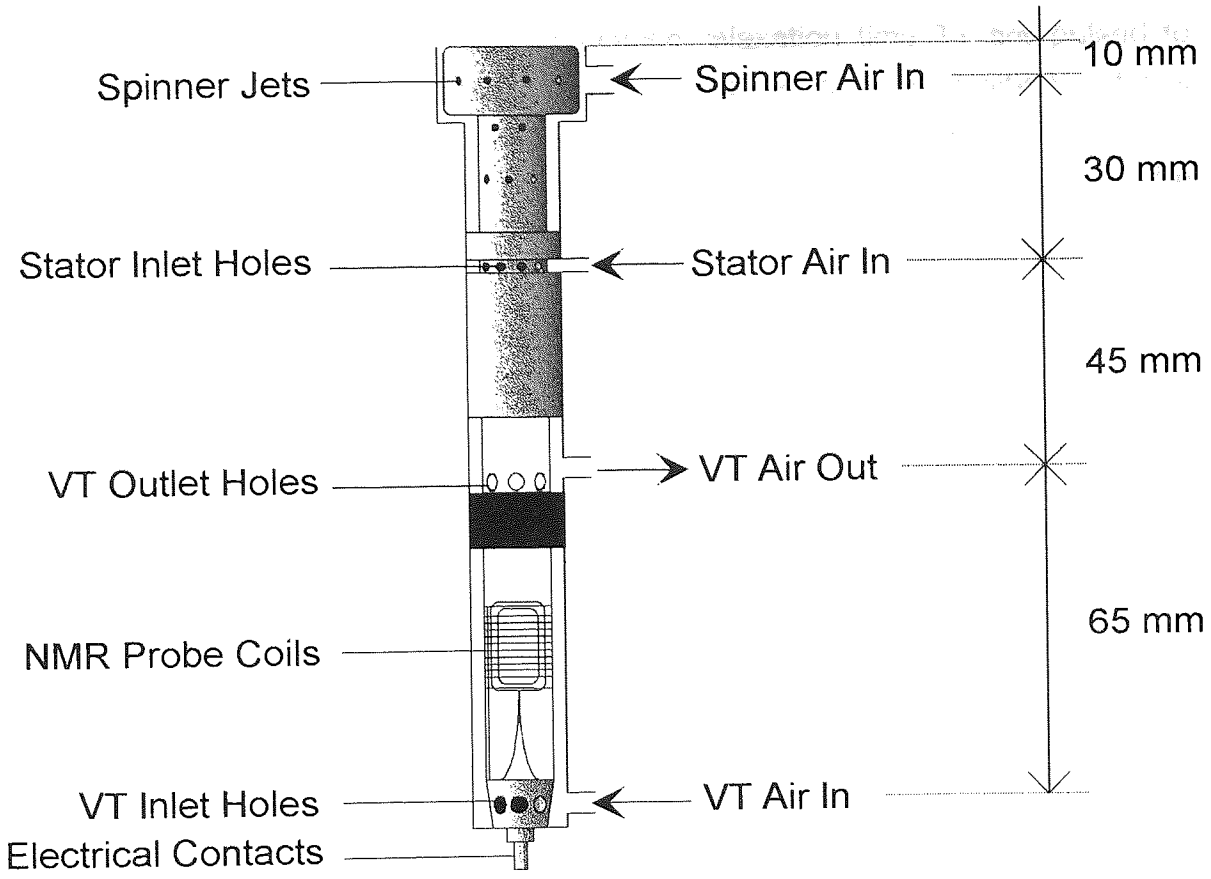

FIGURE 6.1. The Jeol FX-90Q Multinuclear NMR Probe showing air supplies, coils and seating within the permabody.

6.1.3 The Measurement of Spin-lattice Relaxation Times

There are certain arguments within this thesis which rely on the interpretation of spin-lattice relaxation times (T_1's). These were obtained by a number of methods, each being described briefly below. The particular method used is clearly stated with its associated T_1 result in the relevant results sections.

(a) Driven Equilibrium Single Pulse Observation of T_1 - DESPOT[45]

This technique relies on the rapid multipulsing of the magnetization to achieve a steady state situation. As shown in section 2.2.3 the equilibrium magnetization is governed by the nutation angle, the pulse delay and the T_1 which is related ultimately by the equation:

$$\frac{I_{eq}}{\sin\theta} = \frac{I_{eq}\cos\theta.\exp\left(-\frac{t}{T_1}\right)}{\sin\theta} + M_o\left(1-\exp\left(-\frac{t}{T_1}\right)\right) \qquad \text{- (6.1)}$$

where equivalent NMR nuclei with spin-lattice relaxation time T_1 are pulsed to reach a steady state magnetization producing a signal of intensity I_{eq} for a nutation angle θ with time between pulses t. If t is kept constant and θ varied, it is possible to obtain T_1 from a plot of (I_{eq} / sin θ) vs (I_{eq} cos θ / sin θ), with the gradient being ($\exp(-t/T_1)$).

There are three important points to consider with the DESPOT sequence. Firstly, there is the need to produce the steady state condition before acquiring. This is achieved by the application of dummy pulses (which are full pulse sequences without an acquisition period) before obtaining data. Secondly, the nutation angle requires very careful calibration, correction for pulse offset effects and elimination of off-resonance effects. Thirdly, t defined above is not simply the pulse delay (PD) alone, but PD plus the acquisition time.

This method was chosen initially over the more classical techniques due to the time saving advantage available by DESPOT[45] over sequences such as inversion-recovery[139].

(b) SATURATION RECOVERY[140]

Equation 2.4 in section 2.2.3 shows how nuclear magnetization recovers with different relaxation rates as a function of the spin-lattice relaxation time T_1. It was deduced that for 99.5% of the magnetization to recover, it is necessary to wait $5.3T_1$ after a 90^o pulse. Consider a pulse sequence such as that shown below:

$$[\ 90^o - \text{Acquire (A)} - \text{Field Spoil (FS)} - \text{Pulse Delay (PD)}\ ]_n \qquad - (6.2)$$

where the number of scans n, the acquisition period and the field spoil are kept constant between runs so only the pulse delay is altered. If the pulse delay is initially set so PD $\approx T_1$ and then lengthened by increments, the measured intensity will increase and then plateau. The point at which the plateau begins can be considered to occur at (A + FS +PD) $\approx 5.3T_1$. However, as with the DESPOT sequence, there can be deviations caused by inaccurate pulse width calibration, offset and off-resonance effects.

(c) MODIFIED SATURATION RECOVERY

This sequence was designed specifically for use when obtaining T_1 data for SINNMR samples. As will emerge later (section 7.6), a problem encountered in the SINNMR experiment is that the SINNMR signal intensity is not constant with

time for constant NMR parameters. This is due to the violent action within the NMR tubes causing particle break-up which, as explained later, alters the amounts of detectable nuclei in the NMR probe region. Naturally, this complicates the determination of T_1.

The problem was overcome by using a sequence identical to that shown in equation (6.2) but to account for the degradation of the sample in the results. Essentially, the method relies on the fact that as the relaxation delay is progressively increased the measured signal intensity increases and, as in the saturation recovery method, should become effectively constant when the delay exceeds $5.3T_1$.

If for a 90^o pulse, the pulse delay is systematically increased, the signal intensity from a degrading sample will pass through a maximum and then decrease with increasing pulse delay. Once the delay exceeds $5.3T_1$, the subsequent decrease in intensity will depend on the order of the decay process and the sonication time.

If a function of the intensity appropriate to the order of the rate of sample degredation is plotted against sonication time (not the pulse delay), the plot will have two distinct areas. There will be an area of the plot where the pulse delay exceeds $5.3T_1$ which will be linear, the only factor being the decay process. Where the delay is less than $5.3T_1$ the plot will deviate from this linear region. The point at which the two regions meet is where the delay is approximately $5.3T_1$. On such a plot, each point represents a different pulse delay and the point corresponding to $5.3T_1$ can be said to lie between the last non-linear point for x seconds delay and the first linear point for y seconds delay. Therefore, a careful systematic increase in the pulse delay is essential for an accurate result.

6.1.4 The Operation of a High-resolution Spectrometer to Facilitate Solid-State Detection.

The adaptations of the Jeol FX-90Q NMR spectrometer to observe solid state NMR spectra have been outlined within chapter 2. There are two approaches used in the research described within this thesis.

The first method is to shorten the deadtime (DEADT) and delay (DELAY) parameters for each NMR experiment. This will enable the detection of the short-lived FIDs which are characteristic of solids.

The second method, used in some of the high frequency SINNMR investigations involves using the spin-echo pulse sequence, outlined in section 2.3.7. This will also enable the detection of FIDs without pulse breakthrough.

The detection of broad solid NMR resonances also required the window on the FX-90Q to opened to its maximum width of 30030 Hz. Although such a window can be considered wide for the observation of liquid spectra, it is quite narrow by solid state NMR standards. This did result in some difficulty in detecting solid state NMR resonances with a FWHM exceeding one-third of the window size.

6.2 THE KERRY ULTRASONICS 20 kHz ULTRASONIC APPARATUS

The equipment used for the generation of 20 kHz ultrasound was the commercially available Kerry Ultrasonics Apparatus. This comprises a generator connected to a quartz piezoelectric unit to which ultrasonic horns are attached.

Two horns were used in the course of this research; a short horn 27.5 cm long and a long horn 77 cm long. Each horn has a 19 mm diameter coupling surface and is machined exponentially to provide amplification at a 5 mm diameter probe tip. The measurement of power output is *via* a meter on the generator which presents the ultrasonic horn tip displacement; this can be varied between 1 and 20 μm. Using commercial equipment, this apparatus was calibrated calorimetrically so that a 1 μm displacement of the probe tip was shown to deliver 6.5 Wcm^{-2} to water.

6.3 THE YAESU HIGH FREQUENCY ULTRASOUND APPARATUS

The equipment used to generate ultrasound between 1 and 10 MHz was the commercially available, yet modified, Yaesu apparatus. This comprises a Yaesu FP757AD power supply, FT-757GX transceiver, YS-60 standing wave ratio (SWR) and power meter and a Cap Co. Electronics SPC 300 ATU tuner; shown with connections in figure 6.2.

The combined equipment produces a.c. voltages between 0.5 and 30 MHz which can be placed across the faces of suitable transducers, to drive them. The SWR / power meter and SPC 300 tuner enable the fine tuning and matching of the transducer circuit to ensure maximum transmitted power and minimum reflected power. The measurement of power output is also monitored by the meter in terms of watts (W) which can be varied between <0.5W to above 50 W which is the point the transducer and circuit will blow (*via* a 10 A fuse placed in the power supply).

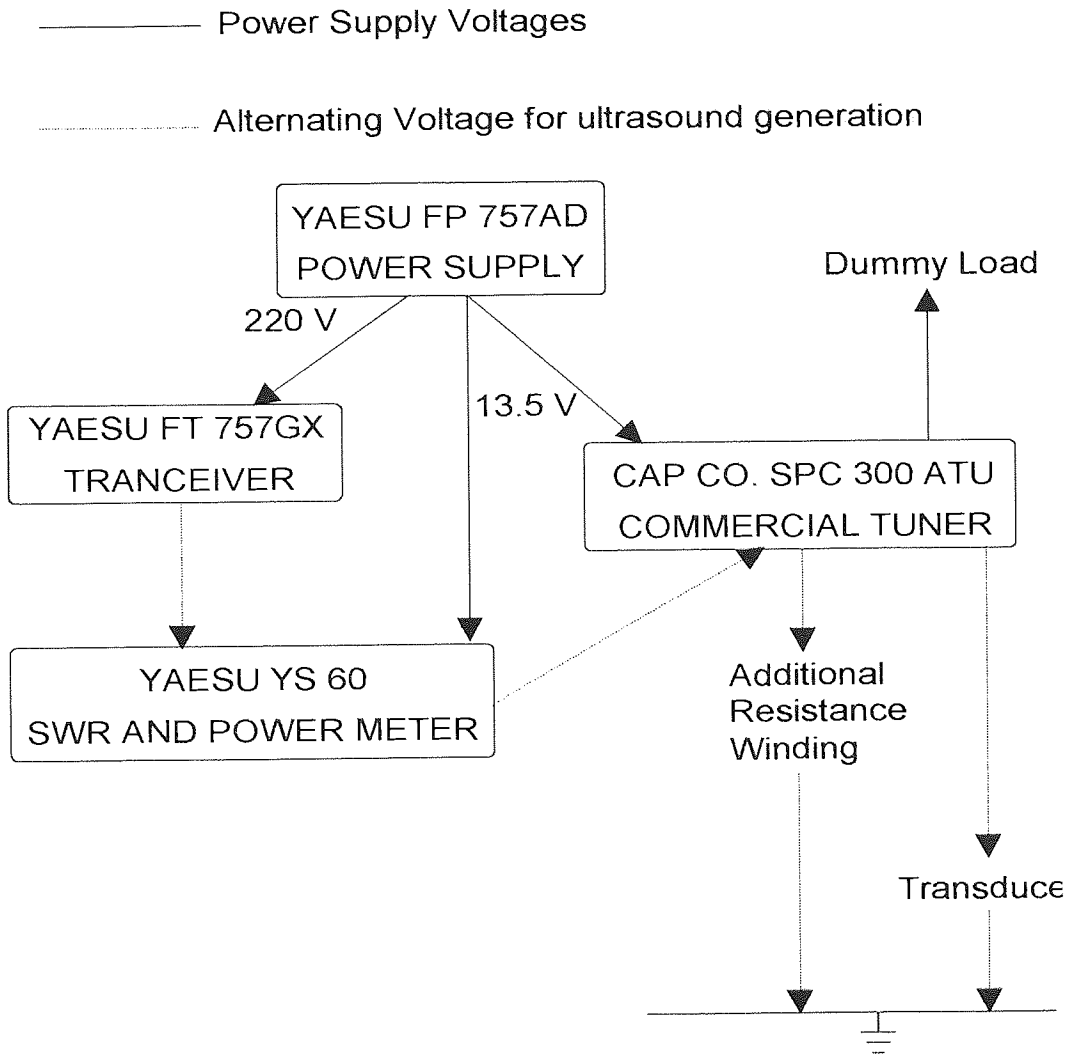

FIGURE 6.2. Schematic of the High-Frequency Ultrasound Yaesu Apparatus.

The transducers used in conjunction with this apparatus were disc lead zirconate titanate (PZT - 5A) available from Morgan Matroc, Southampton. PZT - 5A transducers have a Q value of 75 and a Curie temperature of 365^{o}C. For this research PZT - 5A transducers driven at 1, 1.5, 2, 3, 5 and 10 MHz were used.

6.4 THE COUPLING OF THE NMR SPECTROMETER AND ULTRASOUND

6.4.1 NMR Tubes and Samples

Samples are prepared for SINNMR experiments in 10mm o.d. glass or specially machined PTFE NMR sample tubes. PTFE sample tubes were preferred over glass because of the tendency of the latter to develop stresses and finally shatter when repeatedly subjected to ultrasound. It is for this reason that glass tubes were used only when PTFE was not suitable. Such instances include conducting ^{19}F SINNMR experiments. For the same reason, the PTFE tubes were valuable

in the observation of ^{29}Si and ^{23}Na. For both the SINNMR and static solid experiments the sample tubes were not spun.

The preparation of a sample for SINNMR experiments requires a definite depth of liquid which corresponds to *ca.* 2 ml for PTFE tubes and *ca.* 2.5 ml for glass tubes due to the different internal diameters of *ca.* 8 mm and 8.9 mm respectively. Unless otherwise stated, all experiments used a cotton or glass wool plug to be placed in the bottom of the tube to prevent reflection of the ultrasonic waves introduced from above. It was found useful to retain the absorbing plug in glass tubes by use of a cut PTFE 'O' ring to prevent it sliding or riding up the tube as the experiment progressed. This problem did not manifest itself in the PTFE tubes.

Unless otherwise stated, the ultrasound in a SINNMR experiment is administered from just below the surface of the liquid to produce an ultrasonic force that acts the on particles under investigation. Therefore, all SINNMR experiments were conducted with solids of lower density than the support liquid medium. Unless otherwise stated, support liquids with densities in the range of 1.48 to 2.88 cm^{-3} are conveniently produced from mixtures of chloroform and bromoform. The chloroform (ρ = 1.48 cm^{-3}) used was 99.8% A.C.S. reagent stabilised with 0.5 - 1% ethanol. The bromoform (ρ = 2.88 cm^{-3}) used was 96% stabilised with 1 - 3% ethanol. Figure 6.3 shows the ratio of the volume of bromoform to chloroform (at 25°C) to produce particular densities; the latter were measured by weighing a known volume of liquid within a tared syringe. Densities are then calculated from the relationship ρ (density) = mass / volume.

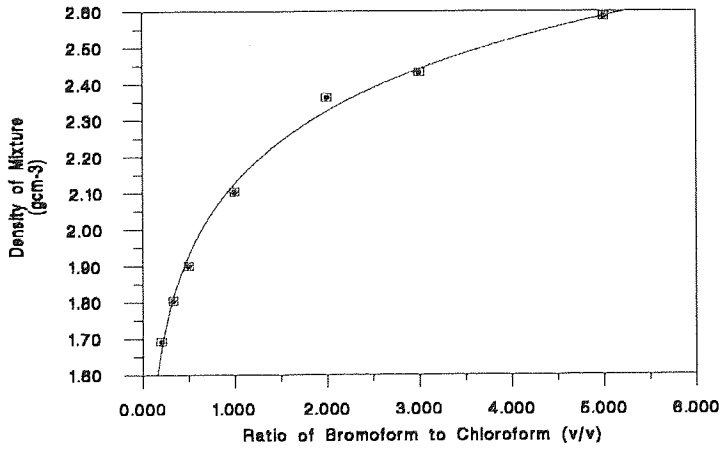

FIGURE 6.3. The relationship between the ratio of bromoform to chloroform and the density of support liquid produced.

6.4.2 NMR and 20 kHz Ultrasound

The ultrasonic transducer and horn unit is mounted on a rig that permits its complete orientational adjustment in the laboratory frame. The rig is held in position above the iron magnet unit of the spectrometer by an aluminium scaffold arrangement. The whole rig area is enclosed by acrylic perspex with an extractor fan and vent located at the rear to remove any unwanted vapours and gases. Access to the rig and magnet is *via* doors located at the front and rear of the enclosed area.

Samples prepared for SINNMR were placed in the spectrometer and the ultrasonic horn lowered to the position shown in figure 6.4, and the ultrasound was switched on throughout the duration of the experiment.

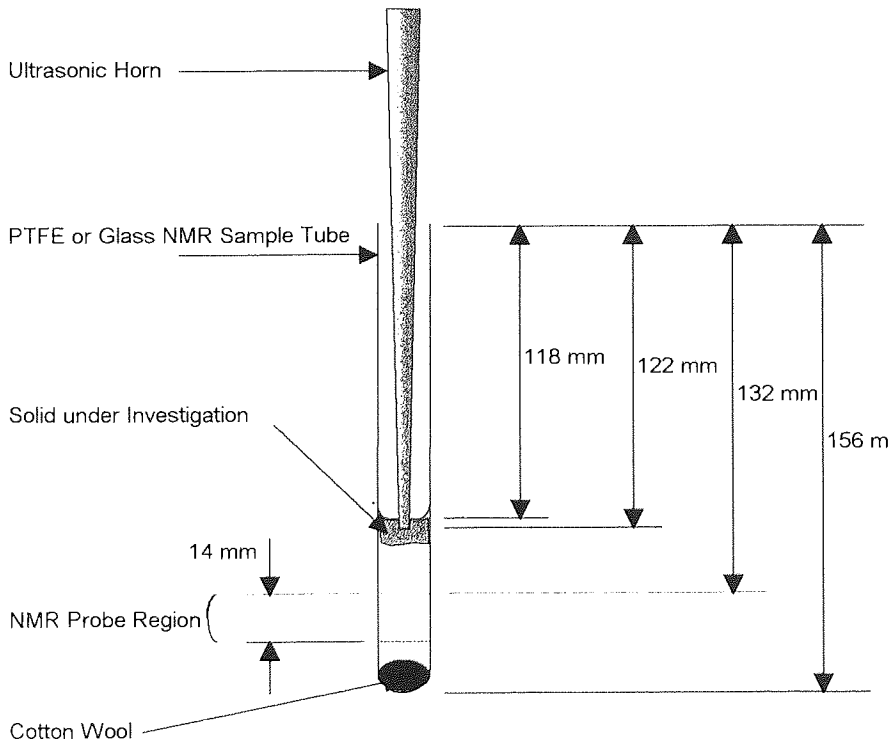

FIGURE 6.4. The position of the 20 kHz ultrasonic horn within a prepared sample tube for SINNMR experiments.

6.4.3 NMR and High Frequency Ultrasound

The PZT - 5A disc transducers used with the high frequency apparatus had first to be prepared before conducting any experiments. This entailed soldering wires to the silvered surfaces to deliver the driving alternating voltage. In order to prevent destroying the transducers by soldering at temperatures approaching the Curie

point, attaching the wires was achieved by use of a variable temperature soldering iron set to melt 18 s.w.g. low melting point solder (composition 62% Sn, 36% Pb and 2% Ag; which flows at a temperature of 179^{o}C). The copper wires used were originally of the glass ceramic screened fine transformer coil type, but after initial difficulties due to the wires tangling, twin oval overlapped screened cables are used. The electrical contact of the transducer wires to the Yaesu high-frequency unit was made *via* crocodile clips.

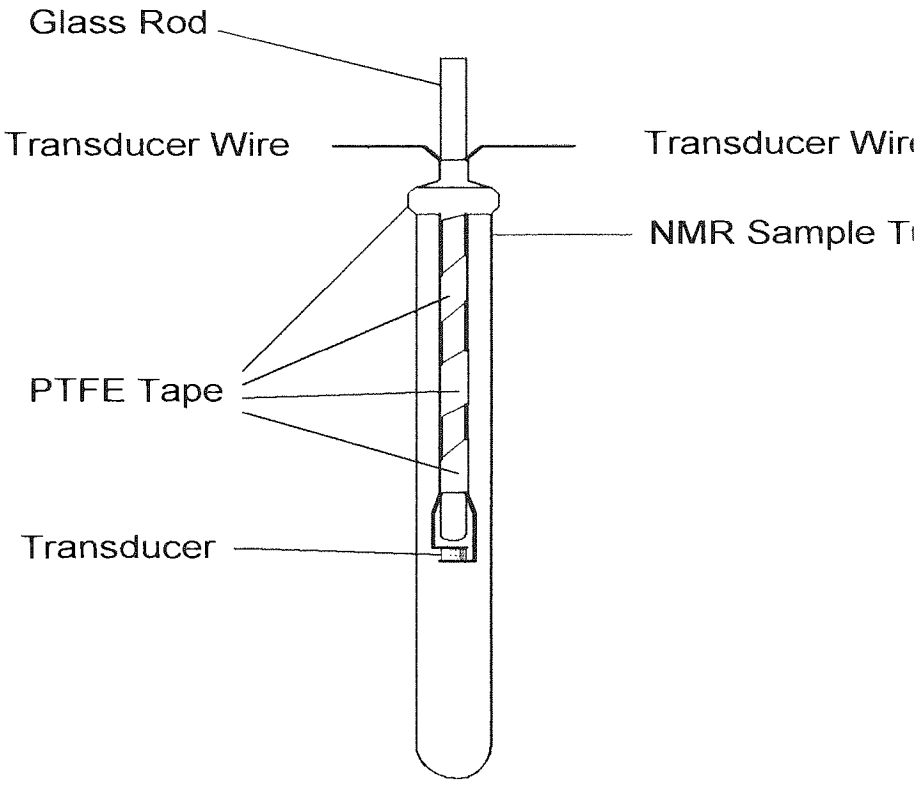

FIGURE 6.5. High frequency ultrasound using a transducer directly bound to a glass rod by PTFE tape.

Initially, the positioning of the transducers in a prepared SINNMR sample was made using a glass rod as shown in figure 6.5: as with the 20 kHz experiments, the ultrasound was applied throughout the experiment.

Due to the permanent nature of soldering wires to the transducer faces, a unit, made from brass, was designed to clamp the transducer between two terminals which could be placed within a glass NMR tube: glass tubes were used because the internal diameter of PTFE tubes were too narrow to design a unit with adequate clearance. The unit was designed to enable the depth to which the transducer was introduced into the tube to be adjusted by means of a threaded rod

and knurled nut. Figure 6.6 shows the unit and how it and the transducer rest within an NMR sample tube.

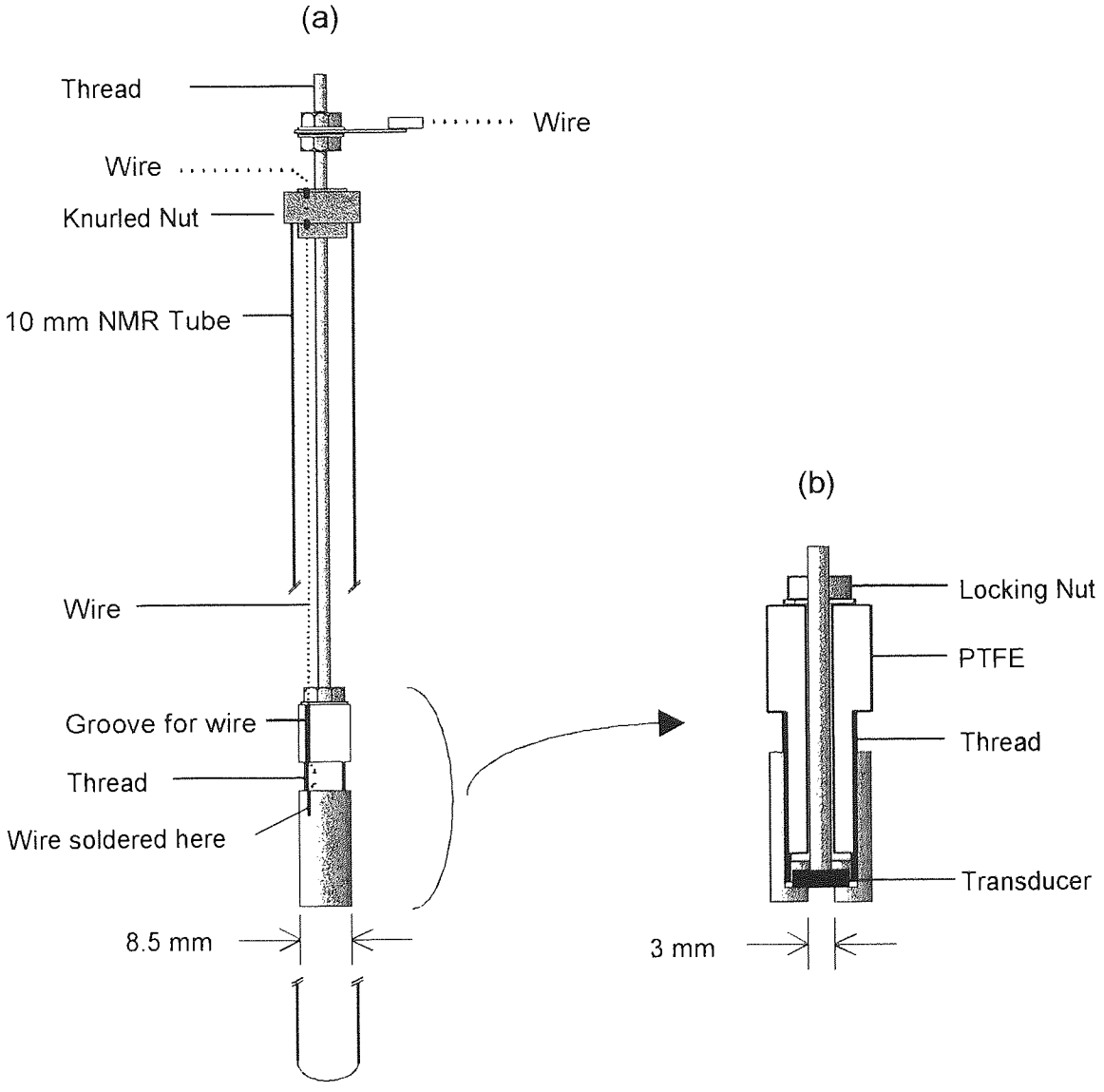

FIGURE 6.6. Transducer unit, designed and built for SINNMR experiments. The main unit (a) is shown together with a cross-section of the transducer housing (b). All shaded areas are construced from brass.

For all high-frequency ultrasound experiments, the transducer was placed within the NMR tube at the same position as the 20 kHz ultrasonic horn tip (10 mm above the NMR detector colis).

CHAPTER SEVEN

SINNMR EXPERIMENTS USING TRISODIUM PHOSPHATE

N.b. A complete list of NMR acquisition parameters for each experiment described in this chapter can be found in Appendix Two.

7.1 INTRODUCTION

All experimental results reported in this chapter and chapter eight involved the SINNMR studies of sodium phosphate, tribasic dodecahydrate, 98+% A.C. reagent (chemical formula $Na_3PO_4.12H_2O$), hereafter referred to as TSP. The appearance of TSP is a translucent colourless crystalline solid with a density of 1.62 gcm^{-3}. The ultrasound applied to all TSP experiments was *via* the Kerry 20 kHz apparatus. To date there have been no high frequency SINNMR studies on this compound.

The solid state structure of TSP was first published by Tillmans and Baur[141] which showed that it has a hexagonal sheet arrangement of $[Na(H_2O)_6]^+$ ions with PO_4^{3-} groups situated between the sheets. The sheets are held together by hydrogen bonds between the water of crystallisation and the phosphate groups. TSP is also known to have free alkali in the form of NaOH which is held in the lattice. The amount of alkali, which is produced during of the manufacture of TSP, has been reported[142,143] to correspond to $Na_3PO_4.12H_2O$. 1/11 and 2/9 NaOH.

The phase diagram is complex[144] and shows phase changes to $Na_3PO_4.8H_2O$ at 55°C and then $Na_3PO_4.6H_2O$ at 65°C which remains until the melting point at 100°C. It has been reported that the octahydrate is very similar in structure to TSP[145] but the hexahydrate is completely distinguishable.

7.2 INITIAL EXPERIMENTS

Initial investigations by Tilstone[146] on TSP concerned the sonically induced narrowing of the ^{31}P resonance of TSP with 20 kHz ultrasound. The experiments were conducted over 2000 accumulations using 1g of TSP with 10-12μm ultrasonic tip displacement (65-78 Wcm^{-2} power density). The TSP sample was not graded and used directly from the supplier's (Aldrich) container. The support liquid used was 3:1 (v/v) chloroform / bromoform corresponding to a density of 1.82 gcm^{-3}, and the liquor after each experiment showed no ^{31}P resonances. If a static sample of TSP is just wetted with the support medium, the ^{31}P FWHM is *ca.* 6500 Hz.

Repeating the experiments of Tilstone on ^{31}P SINNMR of TSP produced a narrow resonance with FWHM of 50 Hz, with variations in ultrasound power showing that SINNMR did not occur with an ultrasonic tip displacement of less than 3μm (19.5 Wcm^{-2}).

This is thought to be due to the necessity of inducing cavitation to facilitate SINNMR. The cavitation thresholds for chloroform / bromoform mixtures are considered to be similar to those obtained experimentally for most haloalkanes[147]. A common value quoted for these liquids is *ca.* 16 Wcm^{-2}[147].

As with Tilstone's experiments, the liquor (obtained by centrifugation or gravity filtering) showed no ^{31}P resonances using identical NMR parameters as used in the production of the SINNMR spectra. An example of the SINNMR spectra produced under these preliminary conditions is shown in figure 7.1. The SINNMR peak with FWHM = 50 Hz can be seen on top of a solid broad resonance with FWHM *ca.* 4950 Hz.

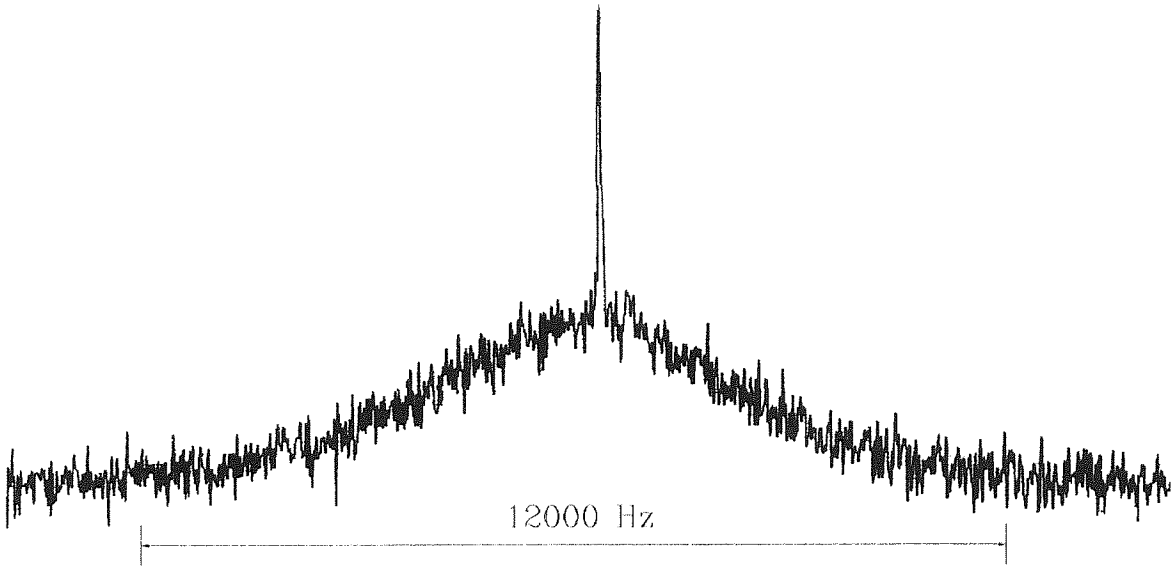

FIGURE 7.1. ^{31}P SINNMR spectrum of TSP under preliminary conditions.

7.3 THE DEPENDENCE OF THE SIGNAL TO NOISE RATIO (S/N) OF ^{31}P SINNMR WITH PARTICLE SIZE RANGE AND MASS OF SAMPLE USED.

While using the minimum ultrasonic tip displacement of 3 μm to produce sonically induced narrowing and with the support liquid density constant as in the initial experiments, the mass of TSP was systematically varied and the S/N recorded for constant NMR acquisition parameters.

Prior to this experiment, TSP was graded into particle size fractions of 1000 - 500μm, 1000 - 210μm, 500 - 210μm, 210 - 105μm, 105 - 90μm, 90 - 75μm, 75 - 53μm, 53 - 38μm and <38μm. The separation of the fractions was completed using Endecott's Test Sieves complying to BS410 mounted in 200mm brass frames with stainless steel meshes.

In ^{31}P SINNMR experiments on certain fractions, the mass of TSP used in 0.2g steps was varied between 0.4 and 1.4g; the S/N results are shown in table 7.1.

	Signal to Noise Ratio (S/N)		
Mass of Solid / g	**1000 - 210μm**	**210 - 105μm**	**105 - 90μm**
0.4	2	2	2
0.6	2	3	1
0.8	2	3	-
1.0	3	1	-
1.2	10	-	-
1.4	8	-	-

TABLE 7.1. The S/N ratio of the ^{31}P SINNMR resonance of TSP for varying particle size range and mass.

The data in table 7.1 appear to show that interparticle collisions affect the optimisation of SINNMR experiments. If the signal to noise ratio was varying purely a function of the number of nuclei present (and hence particle mass), the S/N would not appear to go through a maximum at a particular mass for each particle range: as the mass is increased, the S/N ratio would increase until a point is reached where further increases in mass would result in constant S/N due to maximum amount of sample in the NMR detector probe region being reached. It can be seen from table 7.1 that each particle range appears to have a different mass for which S/N in a SINNMR experiment was optimum. The optimum mass indicates the maximum number of particles of a particular range which can be used for SINNMR investigations of TSP.

There were no SINNMR resonances observed for the particle size ranges below 105 - 90μm. This initial strange observation is thought to be due to the dependence of SINNMR on cavitation. As outlined in section 4.3.4 each experiment with a particular medium and ultrasound frequency will produce cavitation bubbles of a particular size. Whether the cavitation will interact *via* a microjet action on the solid particles present will depend what size the bubble is in relation to the particles. The resonant bubble radii for cavities produced by 20 kHz ultrasound in chloroform / bromoform mixtures varies between 85 - 95 μm. It is known that the radius of a bubble must be comparable to the solid surface for interaction. As a result, particles which are smaller than 85 - 95 μm will not be subjected to microjet interactions. As SINNMR is not observed for particles smaller than *ca.* 90 μm, then it could be concluded that the SINNMR line narrowing mechnaism, involves microjet-particle interactions.

7.4 THE DEPENDENCE OF THE SIGNAL TO NOISE RATIO (S/N) OF SINNMR EXPERIMENTS WITH VARYING DENSITY OF THE LIQUID SUPPORT MEDIUM.

Using the optimum SINNMR conditions giving the greatest observed S/N for experiments described in section 7.3 (constant support liquid density), for 1.2 g of a particle fraction of 1000 - 210μm and 3μm ultrasound, the S/N ratio of the ^{31}P resonance was observed for varying liquid support medium density. As discussed earlier, the necessity of initially floating the solid under investigation on the support liquid was important to the SINNMR experiment and therefore must rely on the buoyancy forces depending on the density difference between the solid and support media. The liquid medium density was varied from its maximum (using bromoform only) to a minimum which was slightly greater than that stated for TSP (1.62 gcm^{-3}). The S/N ratios observed are shown in table 7.2.

Mixture (v/v)	Density of Support Liquid / gcm^{-3}	^{31}P SINNMR S/N Ratio
$CHBr_3$ only	2.60	11:1
5:1 $CHBr_3$ / $CHCl_3$	2.59	13:1
3:1	2.43	26:1
2:1	2.36	33:1
1:1	2.10	16:1
1:2	1.90	9:1
1:3	1.80	8:1
1:5	1.70	3:1

TABLE 7.2. The variation in TSP ^{31}P SINNMR S/N ratio with liquid medium density.

It can be seen immediately that the initial conditions of 3:1 $CHCl_3$ / $CHBr_3$ (as used by Tilstone) were nowhere near the optimum support liquid density. Apart from the increase in S/N as liquid density is increased, the appearance of the spectra change as well. The broad solid resonance, evident in figure 7.1, is reduced with higher support liquid densities. However the increase in the SINNMR line intensity appears to be insufficient to explain the phenomenon simply as narrowing of more of the solid line.

It is believed that the variation in the S/N ratio with support medium density is related to the Dysthe model described in section 4.4.1 (for particle manipulation by ultrasound). All particles will reach an equilibrium situation where the ultrasonic

force equals the buoyancy force, so a sample containing a distribution of particle sizes when subjected to the SINNMR experiment will have smaller particles moving further from the source (the ultrasonic horn tip) than larger particles.

As the ultrasonic power and the particle size and distribution are constant, the only variable is the support liquid density. If the support liquid density ρ_F is chosen so that particles at the centre of a size distribution lie in the NMR probe region, particles at the higher end of the distribution fall short of the region, and those at the lower end pass through, as shown by the hypothetical data in figure 7.2.

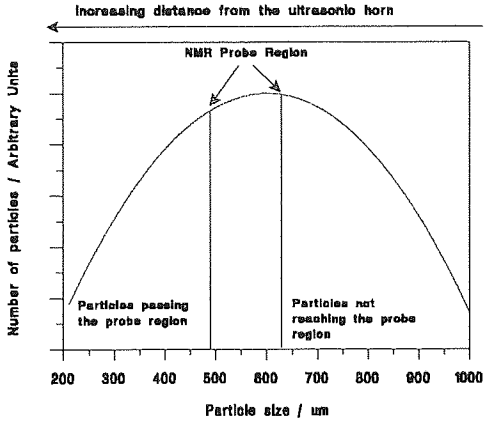

FIGURE 7.2. Particle size distribution and displacement from the ultrasonic horn tip for a particular liquid density. The particle size distribution is calculated by the method shown in appendix three.

As described in section 4.4.1, particles will come to equilibrium at a point where the upthrust force is equal to the ultrasonic force. Strictly, this point is defined by:

$$F_{us} = -F_{ut} - m_p g \qquad \text{- (7.1)}$$

where F_{us} and F_{ut} are the respective forces due to ultrasound and upthrust and $m_p g$ is the weight of the particle defined as the product of the particle mass m_p and acceleration due to gravity g. The force of the upthrust depends upon the weight of the mass m_F of fluid displaced, and is equal to $m_F g$. The masses of the particle and fluid can defined by:

$$m_p = V.\rho_p \quad , \quad m_F = V.\rho_F \qquad \text{- (7.2)}$$

where V is the volume of the particle (and hence fluid displaced). This enables equation (7.1) to be re-written as:

$$F_{us(at\ equ^n)} = -m_f g - m_p g = -V\rho_F g - V\rho_p g = -Vg(\rho_F - \rho_p) \qquad \text{- (7.3)}$$

Equation 7.3 shows that the equilibrium position where all forces cancel is dependent on the volume (and hence the dimensions) of the solid, and the density difference between the support medium and solid. The equilibrium position occurs at the point where the ultrasound is attenuated until the magnitude of the ultrasonic force is equal to $[Vg(\rho_f - \rho_p)]$.

If, (see figure 7.2) ρ_F is high, only the smaller particles in the distribution will come to equilibrium in the NMR probe region. Only the larger particles will come to equilbrium in the NMR probe region if ρ_F is made smaller. As all experiments were conducted with a constant mass of TSP, the ^{31}P intensity and hence the measured S/N ratio will depend on the portion of the distribution that reaches equilibrium within the NMR probe region.

In order to assist in this visualisation, figure 7.3 shows the dependence of TSP particle displacement from the ultrasonic horn tip (operating at 20 kHz and 3 µm tip displacement), on the support liquid density and particle size. The data were obtained from visual observations described later in chaper 8 and tabulated in table 8.1. In Figure 7.3 the inflections in the banded plots show the maximum displacement of the smallest particles in each of several samples containing the specified range of particle sizes when suspended in a variety of support media of different densities. For example, in the case of the 500 - 1000 µm particle size range with a liquid density of 2.36 gcm^{-3} the 500 µm particles were displaced *ca.* 24 mm from the ultrasonic horn tip with the larger particles distributed between that location and the horn tip. As the effective region of the NMR detector coil lay between 10 and 24 mm below the ultrasonic horn tip it can be deduced, from figure 7.3, that particles with sizes in the range 500 - 1000 µm and with a support medium density some 0.74 gcm^{-3} greater than that of the solid are likely to produce the optimum SINNMR effect, as observed: this situation is depicted by the schematic representation of the behavior of particles in an NMR sample tube at the right of this figure.

Table 7.3 shows the ^{23}Na S/N ratio for four different particle size ranges where the support liquid density was optimised to ensure the bulk of the particle displacement was between the limits of the NMR probe region. Such optimization can be achieved *via* use of diagrams such as that shown in figure 7.3. The S/N in table 7.3 falls with smaller particles due to the relationship between particle size and cavitation bubble size as outlined in section 7.3. The FWHM increases as the particle size falls showing the efficiency of line narrowing reduces and this may also be related to the cavitation bubble size.

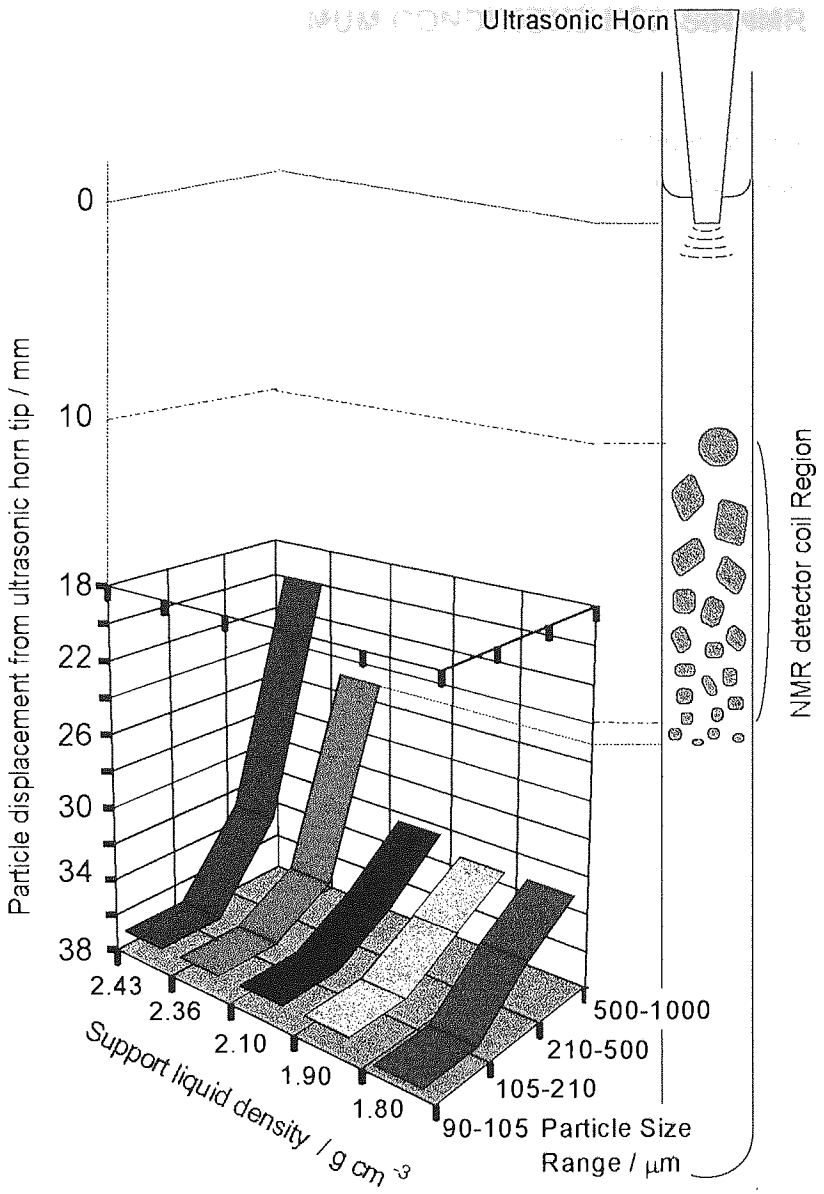

FIGURE 7.3. Dependence of TSP particle displacement, from the tip of an ultrasonic horn operating at 20 kHz and 20 Wcm^{-2} (3 µm horn tip displacement), on support liquid density and particle size.

Particle Size Range / µm	^{23}Na S/N	^{23}Na FWHM / Hz
1000 - 500	110:1	88
500 - 210	110:1	103
210 - 105	102:1	121
105 - 90	20:1	161

TABLE 7.3. ^{23}Na SINNMR S/N ratio and FWHM for different particle size ranges of TSP. All acquisition parameters were identical.
The digital resolution was ± 7 Hz

7.5 THE REFINEMENT OF OPTIMUM CONDITIONS FOR SINNMR EXPERIMENTS

The previous sections 7.2, 7.3 and 7.4 described the preliminary experiments and results which enabled a more thorough study of SINNMR using TSP. The comprehensive treatise of SINNMR is described in the remainder of this chapter.

The experiments outlined in sections 7.3 and 7.4 have indicated that the optimum ^{31}P SINNMR conditions for TSP require 1.2g of 1000 - 210 µm graded solid with a 2:1 $CHBr_3$ / $CHCl_3$ support medium. However, it appeared from the data in tables 7.1 and 7.2 that further increases in particle size could yield even higher S/N ratios. This was indeed found, when the largest TSP graded fraction of 1000 - 500 µm was used. The ^{31}P SINNMR S/N produced with the same experimental parameters (for both NMR and ultrasound) as those described in sections 7.2 and 7.3 but using a graded fraction of 1000 - 500 µm TSP in 2:1 $CHBr_3$ / $CHCl_3$ was 50:1. In addition to this increased NMR S/N, the FWHM of the ^{31}P resonance had fallen from 37 to 31 Hz. Using these conditions the SINNMR spectra shown in figure 7.4 with static solids for both ^{31}P and ^{23}Na were produced.

Although both spectra in figure 7.3 appear to be at the isotropic shift positions, it was found, quite expectedly, that there is a measurable shift between the SINNMR and solution resonances. The shift for ^{31}P SINNMR is found to vary between +1.55 and +1.92 ppm (*i.e.* deshielded) from the solution (in H_2O) resonance. Similarly, the ^{23}Na SINNMR resonance was found to be 1.81 ppm deshielded relative to the solution. However, a solution irradiated with 20 kHz, 3 µm ultrasound produced a ^{23}Na deshielded shift of 9.1 ppm compared to the non-sonicated solution. In all of these experiments, with the ultrasound on or off, the titanium ultrasonic horn was within the NMR tube and the digital resolution set to 0.0336 ppm. These shift differences between SINNMR and solution spectra are most probably due to a combination of environmental differences between solid and solution states and a susceptibility effect due to the different bulk sample environments. The large shift observed for the sonicated solution compared to the non-sonicated solution is thought to be due to a van der Waals pressure shift. Although within one cycle of ultrasound, the overall pressure change in the mixture should be zero, complications by pressure and density phase lags of the ultrasound may not make this the case and results in the observed shift.

In order to check the consistency of the optimum conditions for ^{31}P and ^{23}Na SINNMR, the dependence of ^{23}Na SINNMR S/N with mass of solid was obtained. The results are shown in figure 7.5(a) and indicate that for the 1000 - 500µm particle size range, a slightly higher optimum mass of 1.4g is preferred. The

passing of the S/N ratio through an optimum mass of solid used was also outlined in table 7.1 for ^{31}P S/N. The results in figure 7.5(b) also reveal that the SINNMR line width and hence the extent of narrowing also depended on the amount of solid used. Studies of the ^{13}C linewidths of the support liquids revealed some, but not exceptional broadening and established the SINNMR FWHM minima to be genuine (88 Hz for ^{23}Na and 31 Hz for ^{31}P) being significantly greater than the spectrometer resolution under the conditions used. These findings indicate that SINNMR may rely on interparticle collisions.

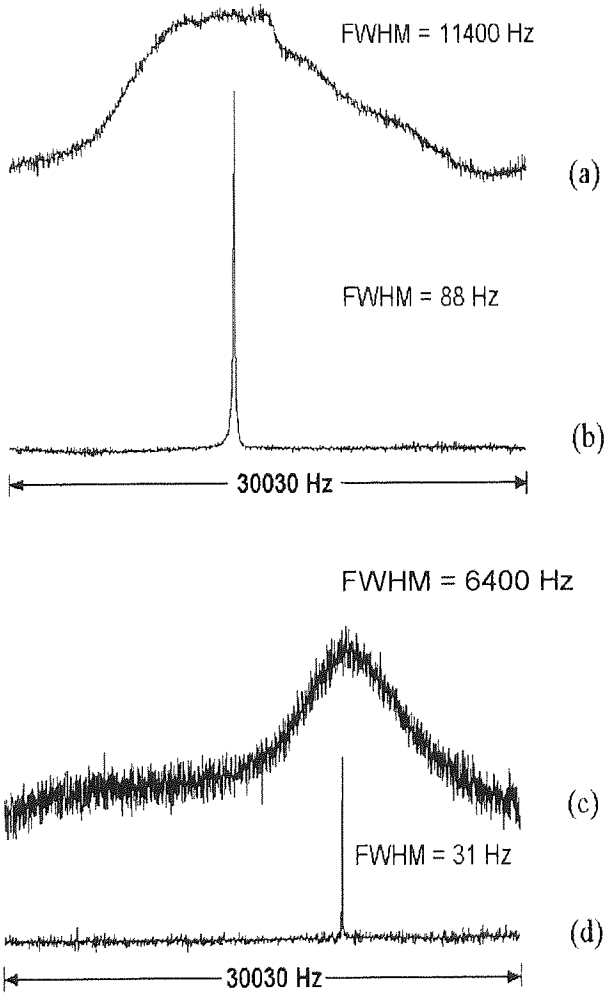

FIGURE 7.4. ^{23}Na spectra (23.64 MHz) of TSP (a) static and (b) SINNMR with 20 kHz ultrasound and 3μm tip displacement: (c) and (d) are the corresponding ^{31}P spectra (36.20 MHz).

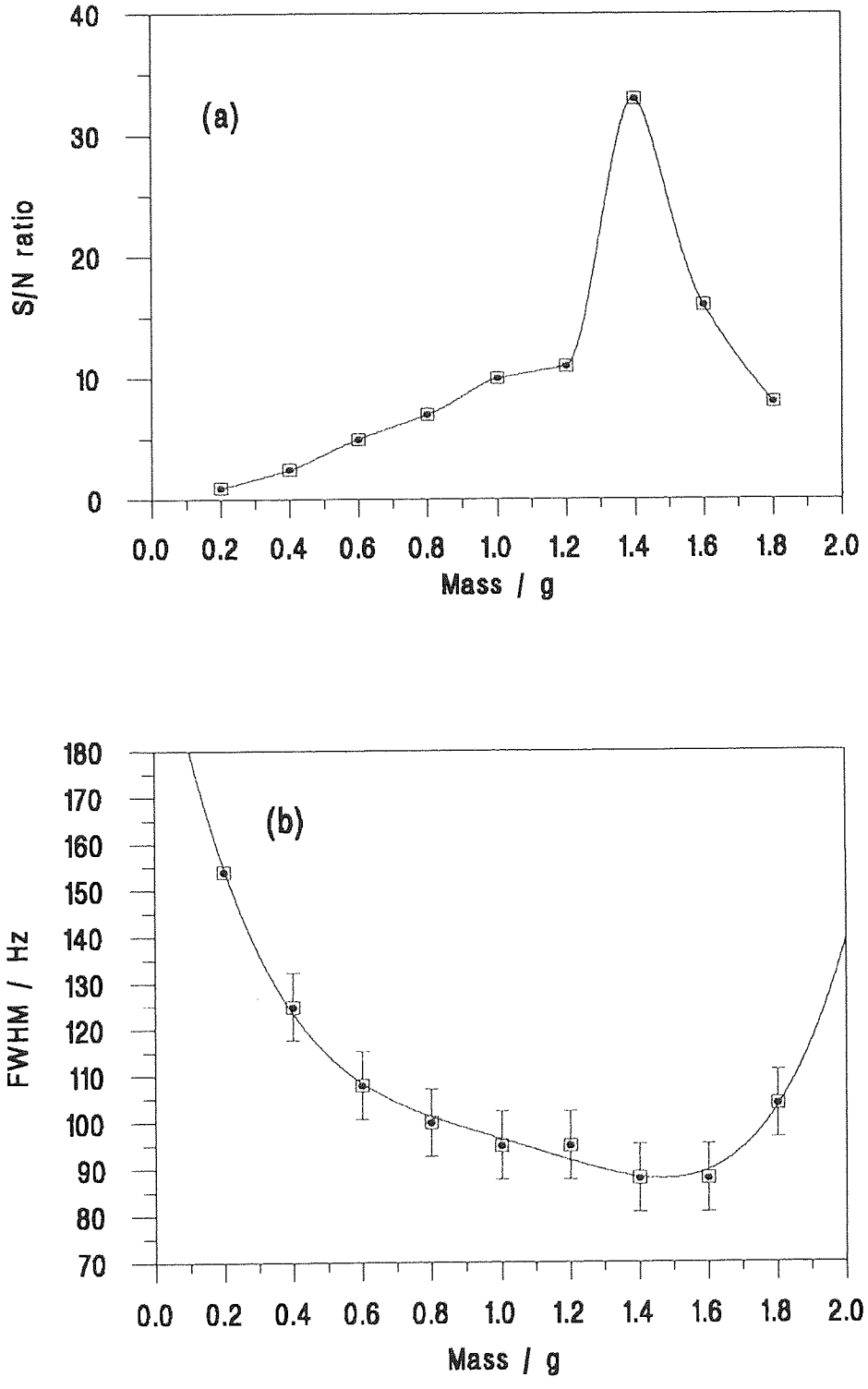

FIGURE 7.5. Effect of mass of solid TSP on (a) the S/N and (b) the FWHM of the ^{23}Na SINNMR spectra obtained using optimum particle size and support liquid. The error bars in (b) reflect the digital resolution.

7.6 OBSERVATIONS MADE AFTER SINNMR EXPERIMENTS

Three important observations were made at the end of the SINNMR experiments.

First, some degradation in particle size was found. Samples of 1000 - 500μm fractions of TSP were sonicated with 3μm tip displacement ultrasound within a PTFE sample tube, as for a SINNMR experiment, for 5 minutes. The resulting solid was gravity filtered, allowed to dry on the bench, then passed through sieves. The proportions of the fractions obtained are shown in figure 7.6.

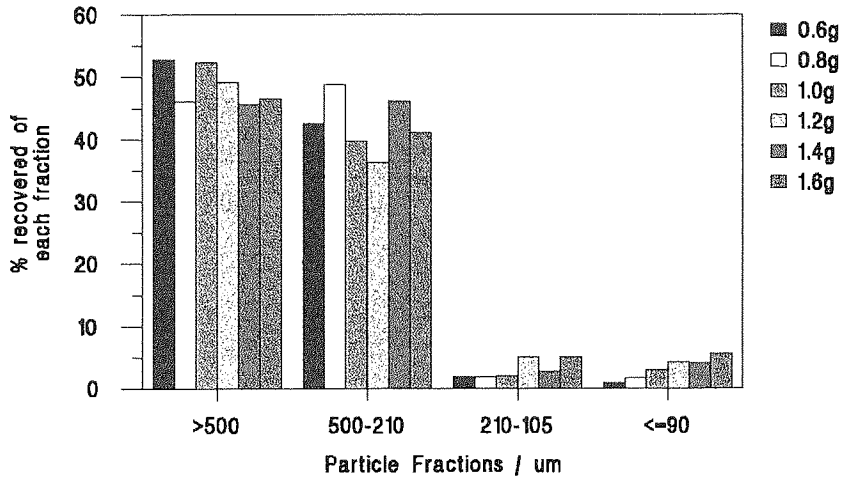

FIGURE 7.6. The proportions (w/w) of 1000 - 500 μm fraction TSP recovered (w/w) after 5 minutes sonication with 20 kHz ultrasound at *ca.* 20 Wcm^{-2}. Different masses of TSP used are shown in the legend.

Figure 7.6 shows the surprising extent of particle size degradation after 5 minutes sonication with approximately half the sample being reduced in size to yield particles with smaller than the initial lower particle size limit. The relative proportions of fractions produced as a result of degradation do not vary dramatically with the mass of sample used. This suggests that degradation occurs as a result of cavitation (*via* direct microjet impingement and shock waves) rather than *via* interparticle collisions. The smallest particles produced are found by filtration to be larger than 25 μm. Suspensions of different particle size ranges between 25 and 1000 μm produced no narrow ^{23}Na or ^{31}P resonances. Therefore, the observed SINNMR line narrowing is not a result of Brownian motional averaging of the small particles produced from sample degradation.

Second, the final temperature of the support liquid following a SINNMR experiment was in the range 40 - 45°C, and as this decreased with time it has to be concluded that the solid is initially most probably at the higher of the specified temperatures.

Third, when the sonicated solid was concentrated in the NMR detector coil region, a sharp narrow line of much reduced intensity compared to the SINNMR resonance was observed and the intensity of this decayed with time. The last observation suggests the possibility of the line narrowing *via* a mechanism other than that of incoherent motion.

7.7 INVESTIGATIONS INTO THE ORIGIN OF SINNMR IN TSP

7.7.1 Possible Mechanisms for Increasing Lattice Motion

The molecular constituents of solid lattices undergo restricted motion that, for many compounds at normal temperatures, is inadequate to result in line narrowing of the NMR spectra. However, it is known that some compounds undergo thermally induced changes, at characteristic temperatures, that result in increased molecular motion. Two theories have been advanced to explain these changes, one by Frenkel (and by Landau)[148] and the other by Pauling (and by Fowler)[149].

Frenkel proposed that, below the transition temperature, the molecules undergo low-amplitude vibrations about a single equilibrium orientation. Above the transition temperature, his model requires that similar vibrations occur about a limited number of different equilibrium orientations. Pauling, on the other hand, proposed that the transition takes place from a lower temperature state, similar to that invoked by Frenkel, to one in which the molecules are thermally excited to rotational states in which they undergo effectively free rotation.

Through studies of the temperature dependence of NMR linewidths for a selection of solids, Alpert[150] showed that the Frenkel and Pauling models could be used to explain individually the line narrowings observed at the transition temperatures for appropriate compounds. The most rapid narrowing with temperature was attributed to the Pauling model. The Frenkel model necessitates that above the transition temperature, only a few limited angles would apply to the dipolar and quadrupolar Hamiltonians so that only minor narrowing may be observed, and then possibly with an apparent change in chemical shift. The Pauling model would result in the reduction of both dipolar and quadrupolar line broadenings due to the onset of free rotation. The extent of line narrowing will depend on the correlation time in the excited rotational states, and the non-uniformity of the rotational motion due to interactions with other molecular species[149]. It must be recognised, therefore, that if the mechanism at the heart of the Pauling model can be stimulated it might, under certain conditions, and for certain compounds, contribute to SINNMR line narrowing.

The phase changes outlined in section 7.1 indicate that a phase change from TSP to the octahydrate can occur at 55°C with the possibility of dissolution in the released water of crystallisation occurring. The evidence suggests this temperature cannot be reached during the course of SINNMR experiments under the observations employed. Bench experiments[151] reveal that the mixture equilibrates at less that 60°C after prolonged sonication. Interestingly, the corresponding experiments in the NMR spectrometer show that the equilibrium temperature is significantly less than that achieved on the bench. Superficially, this observation may be attributed to the cooling effect of the spinner, stator and VT air supplies within the NMR probe, although the effect of the magnetic field has been questioned[152].

TSP has also been investigated by differential scanning calorimetry (DSC) which failed to detect any major changes in phase between 0 and 60°C. The DSC spectrum detected a small change in phase between 60 and 70°C but it was not until the temperature was over 80°C that major changes were taking place. DSC results were identical for sonicated and non-sonicated samples. The dependence on temperature of the ^{23}Na resonance of TSP wetted with the liquid support medium used for optimum SINNMR experiments was investigated. The S/N ratio showed a single maximum at 70°C and the FWHM a single maximum at 62°C that was some 15 Hz larger than that achieved through SINNMR (see figure 7.7).

The increase in S/N and decrease in FWHM as the temperature is raised are both consistent with the mechanisms central to the Pauling model. Changes in phase to the octahydrate and then the hexahydrate could disrupt the progressive enhancement of the consequences of the Pauling mechanism, and lead to the observed S/N maximum and FWHM minimum. Similarly, the observed maximum and minimum are inconsistent with the possibility of dissolution in the water of crystallisation, because this should further increase the S/N and reduce the FWHM with the increase in temperature.

7.7.2 Decay of SINNMR and Thermally Induced Narrow Resonances

The time dependence of the S/N of the SINNMR narrowed ^{23}Na resonance of TSP was followed, after switching off the ultrasound. Similar experiments were performed on a sample that was preheated to 55°C and allowed to cool naturally to the NMR probe temperature of 28°C. In both cases regressions of the ln(S/N) on the time paralleled each other as in figure 7.8, showing the similarity of the mechanism of decay.

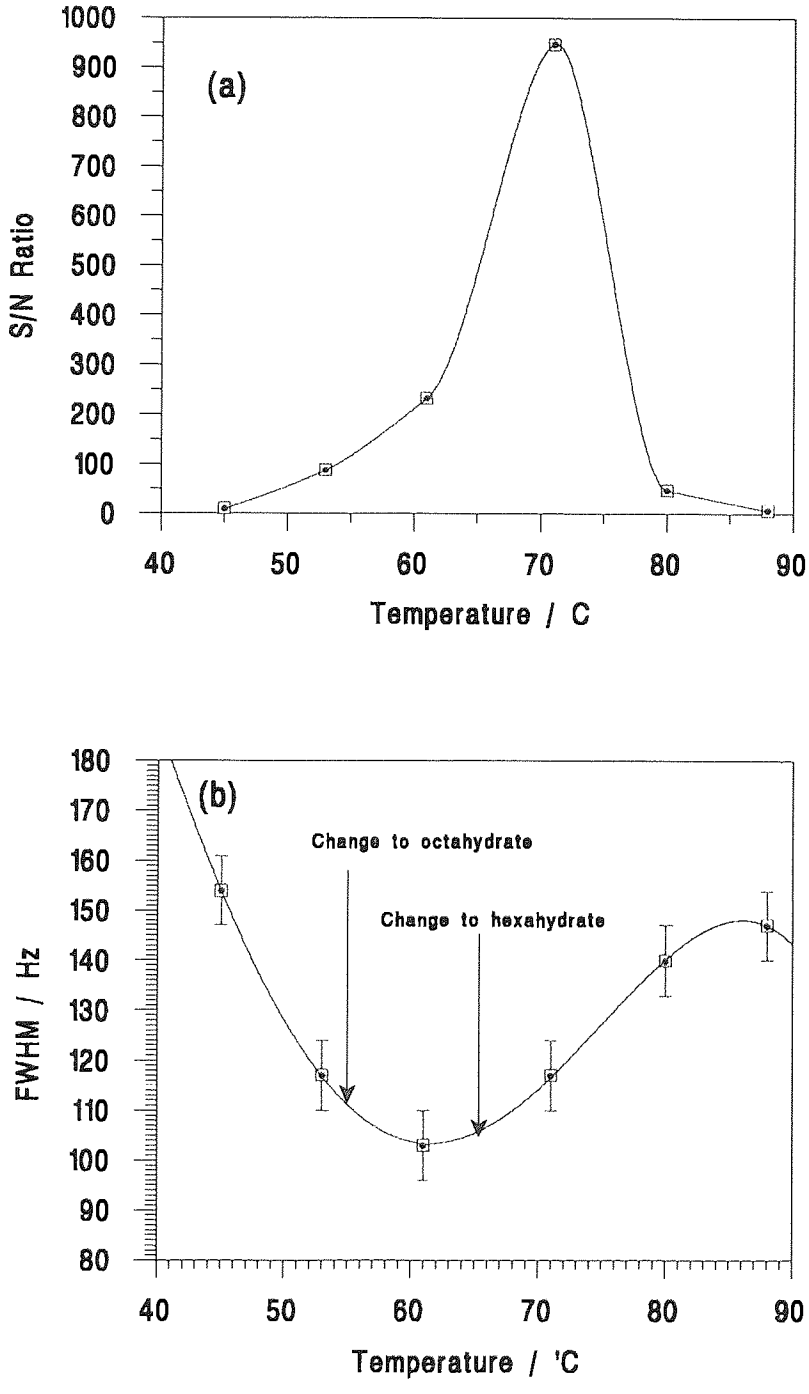

FIGURE 7.7. The temperature dependence of (a) the S/N and (b) the FWHM of the thermally narrowed ^{23}Na resonance of a wetted solid sample of TSP. The error bars in (b) reflect the digital resolution.

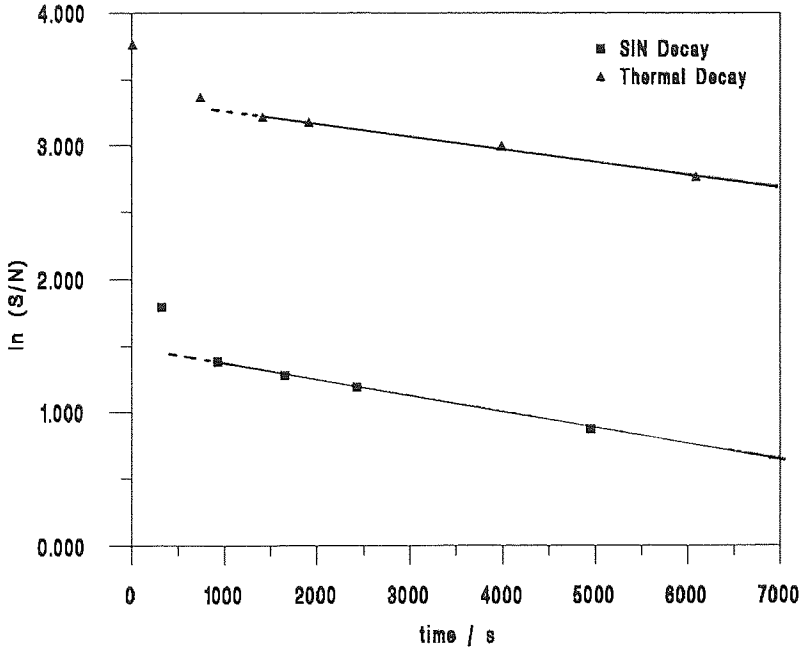

FIGURE 7.8. Decay of the ^{23}Na S/N from TSP with time after (a) thermal and (b) acoustic perturbations of approximately equal masses of solid.

Over the first 16 minutes the S/N decays were both non-linear: this period corresponds to the time taken for the samples to regain thermal equilibrium at the NMR probe temperature. Thereafter, the two plots were linear.

Of particular interest is the fact that the S/N of the SINNMR resonance decreased dramatically immediately after the ultrasound was switched off: additionally, the SINNMR S/N was considerably larger than that of the thermally narrowed resonance, by a factor of 80, as shown in table 7.4, (corrected for equal masses) for the ^{23}Na resonance at 45°C.

Sample	^{23}Na S/N[a]	^{23}Na FWHM / Hz	^{31}P FWHM / Hz
non-sonicated (at 45°C)	10:1	153	No Narrowing
restricted and sonicated	65:1	125	51
SINNMR	800:1	88	31

TABLE 7.4. ^{23}Na S/N ratio and FWHM and ^{31}P FWHM for samples of TSP.
[a] S/N for equal masses and identical acquisition parameters.

The sonicated and constrained sample involved TSP being placed in a nylon mesh bag to restrict particle motion. These observations are, at least in part, consistent with the activation of the Pauling free rotor mechanism - to a limited extent.

Whereas promotion of molecules in a solid lattice to free rotor states is normally considered to be a thermally controlled process, it is possible that ultrasound could produce a similar effect. Although speculative, an explanation may be advanced for this proposal in conjunction with the fact that neither SINNMR or sonically induced lattice motion can be induced in ground samples of TSP. If a sample of solid TSP is finely ground it has been found that electrical heating of the sample does not produce narrowed NMR spectral resonances, as are seen for the unground material. Grinding may reduce the number of lattice dislocation sites in the ground material. If this is the case, the presence of lattice dislocation sites is a prerequisite for the thermal promotion of molecules to free rotor behaviour in TSP. It is well known[150] that when crystalline materials are subjected to ultrasonically induced cyclic stress variations, the accompanying dislocation oscillation variations result in absorption of acoustic energy by the solid lattice. This is then available for promotion of constituent molecules to free rotor states.

An important point to note is that when thermally controlled, the S/N ratio attributable to the Pauling mechanism must be governed by a normal Boltzmann distribution between accessible rotational states. However, if ultrasound were to activate the mechanism and the excited state had a sufficiently low rate of relaxation to the ground state, the state populations may no longer be Boltzmann in nature. More molecules could be rotationally excited than normal to give the much higher S/N for the sonicated rather than thermally narrowed resonance, as observed.

However, the large decrease in S/N after switching off the ultrasound following the SINNMR experiment appears more likely to be due to cessation of incoherent particle motion rather than due to the required slow restoration of a Boltzmann distribution between rotor and non-rotor states. This contention is supported by the appearance of the S/N observed after the SINNMR experiment being higher than that for the heated sample and this is consistent with a lower temperature (40 - 45^{o}C) being reached by sonication than that induced electrically (55^{o}C).

7.7.3 Line Narrowing due to Incoherent Particle Motion

The evidence presented in sections 7.7.1 and 7.7.2 suggests strongly that some line narrowing may result from the ultrasound activation of the Pauling free-rotor

mechanism. The investigation of possible line narrowing due to ultrasound-induced incoherent particle motion presented particular problems. The approach adopted was to compare experiments conducted under normal SINNMR conditions with those on a sample of TSP that was constrained within the NMR coil region by an open mesh nylon bag and irradiated with ultrasound coupled by the same medium as used for the SINNMR experiments.

Initially, spin-lattice relaxation time measurements on 1000 - 500μm graded TSP samples were made to assess the correlation times and hence the effect of incoherent particle motion on the line widths. ^{31}P T_1 values were obtained because the theoretical values for this dipolar nucleus can be analysed readily. The T_1 of a solid sample of TSP was measured by MAS NMR using the saturation recovery technique[140]. Although a value of 80 s was obtained at 121.441 MHz and 303 K, this was adjusted to 7.2 s at the Larmor frequency of 36.20 MHz used in SINNMR through the known proportionality between dipolar T_1 and the square of the Larmor Frequency. This value is, as are all the T_1 values discussed in this section, shown in table 7.5 and also in figure 7.9, the latter representing the variation of T_1 and T_2 with correlation time. These curves were calculated using data from the thesis of J.K. Roberts[153] and equations 1.39 and 1.41.

TSP Sample	T_1 Measurement Method	T_1 / s
Solid (corrected MAS)	Saturation Recovery	7.2
0.05 M solution	DESPOT	2.2±0.2
SINNMR	Modified Saturation Recovery	0.52±0.05
Constrained and sonicated	Saturation Recovery	2.1±0.2
Solid (heated to 50°C)	Saturation Recovery	12.25±0.25

TABLE 7.5. Spin-lattice relaxation times with experimental method used for different samples of 1000 - 500μm graded TSP.

Because of particle size degradation, the ^{31}P SINNMR measurements were made *via* the use of the modified saturation recovery technique described in section 6.1.3. The intensities produced were plotted as a function of $(\text{intensity})^{-2}$ vs sonication time to produce the graph shown in figure 7.10. The T_1 from this graph is 0.52±0.05 s.

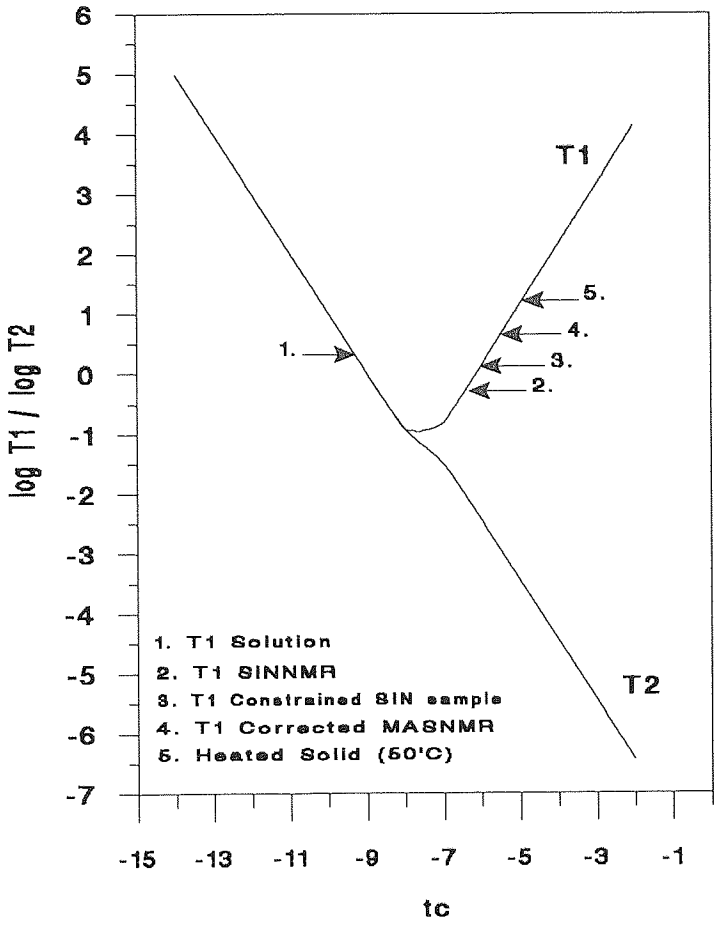

FIGURE 7.9. Theoretical dependence of relaxation times on correlation times, and T_1 values for the ^{31}P resonance (36.26 MHz) of TSP.

The ^{31}P T_1 of the solid sample heated to 50°C (323 K) and the constrained sonicated sample produced respective T_1 values of 12.25±0.25 s and 2.1±0.2 s as obtained by the saturation recovery technique. An example of the data which produced these results can be seen in figure 7.11. The constrained but sonicated sample, at the same power as for SINNMR, showed a constant signal intensity in excess of $5.3T_1$, and that no sample degradation occurred. The final ^{31}P T_1 value was obtained for the resonance from an air saturated 0.05 M aqueous solution of TSP by the DESPOT method. The resulting T_1 was 2.2±0.2 s, the DESPOT plot being shown in figure 7.12.

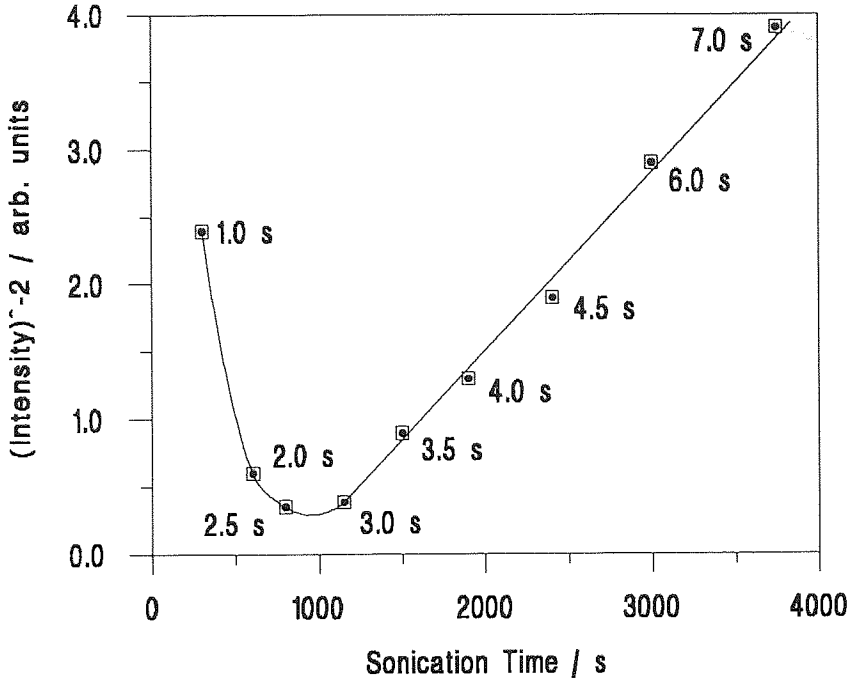

FIGURE 7.10. Variation in Saturation Recovery of ^{31}P intensities of TSP under SINNMR conditions using the modified method with sonication time and (x) relaxation delay.

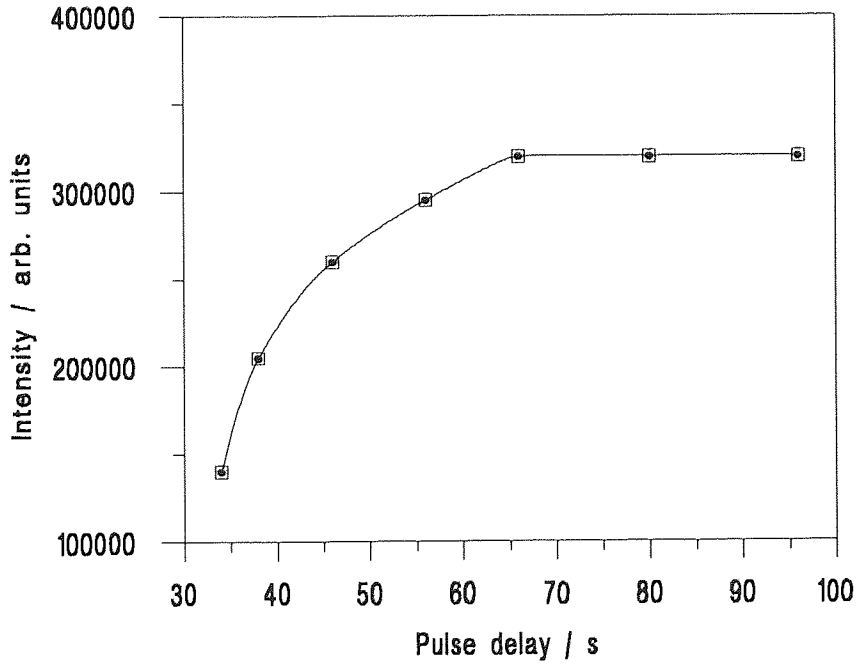

FIGURE 7.11. Variation in Saturation Recovery of ^{31}P intensities of TSP heated to 50°C.

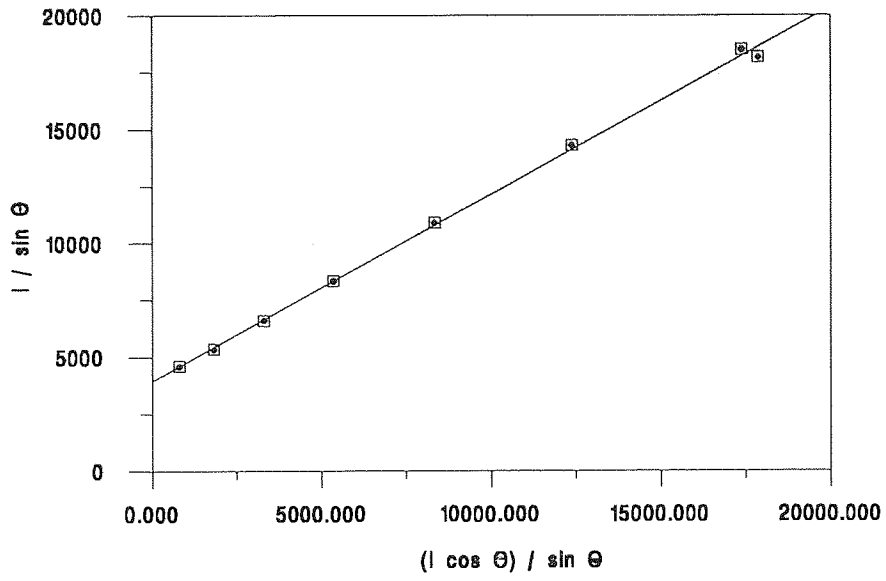

FIGURE 7.12. Despot plot of I_{eq} / sin θ against I_{eq} cos θ / sin θ of ^{31}P TSP solution (0.05 M in water).

There is little doubt that the T_1 from the SINNMR experiment is less than that obtained for the constrained sample indicating a contribution arising from incoherent particle motion. Inspection of figure 7.9 reveals that two values of T_1 just mentioned could be placed on the theoretical T_1 curve either in or outside the extreme narrowing region.

Unfortunately, T_2 measurements could not be made to resolve this ambiguity. However, to assist in this connection, the following approach was adopted. The spectrometer conditions were set so that the resonance of an air saturated 0.05 M aqueous solution of TSP showed convolution due to truncation of the FID. This was achieved by setting a short acquisition period. The same spectrometer conditions were used to produce resonances from the sonicated solid TSP and SINNMR experiments. These showed no convolution and thus suggest that the T_2's for these samples are much shorter than that for solution and that the T_1's obtained lie outside the extreme narrowing region. This requires that the correlation time for the SINNMR sample to be less than that for the constrained sample and is consistent with sonically induced incoherent particle motion in SINNMR experiments that is impossible for the constrained sample.

Contributions to relaxation processes are additive as relaxation rates. Using this approach, the relaxation time for SINNMR T_1^{SIN} can be considered as:

$$\frac{1}{T_1^{SIN}} = \frac{1}{T_1^{CONSTR}} + \frac{1}{T_1^{IM}} \qquad -(7.1)$$

where $(T_1^{CONSTR})^{-1}$ and $(T_1^{IM})^{-1}$ are the relaxation rates for the constrained sample and that due to incoherent particle motion. T_1^{IM} from equation (7.1) is found to be 0.69 s. Substitution into equation 1.39 which produced figure 7.9 reveals a correlation time beyond the extreme narrowing region of *ca.* 4×10^{-7} s. While this is significantly different from the period of the stimulating acoustic wave (20 kHz period is 5×10^{-5} s), it is evident that the induced particle motion is sufficiently rapid to cause motional averaging of NMR spectral resonances.

7.7.4 Melting and Reaction

Although melting the TSP by sonication is a possible mechanism for line narrowing, the evidence against this hypothesis includes the results of SINNMR optimisation with liquid density and particle size. If line narrowing was produced as a consequence of melting or reaction, SINNMR experiments with varying support liquid density, mass of sample and particle size, would not be expected to produce the observed S/N optimal maxima (as in tables 7.1, 7.2 and figure 7.4). TSP crystals are long, needle like and translucent, and at the end of a SINNMR experimentcrystals with identical appearances were found. If surface melting due to cavitation hot spots occurred, the crystals would become rounded or even completely change shape as they are melted then become quenched by the support liquid.

The possibility of reaction is particularly important in view of the potential chemical reactivity of the chloroform and bromoform mixtures used. The irradiation of such liquids with 20 kHz ultrasound can produce free radicals which can react with the solid. Samples of TSP before and after SINNMR experiments have been tested by infra-red (IR) spectroscopy to determine any major structural changes or additions of carbon groups. All IR spectra, obtained by CW or FT-IR, using samples prepared as mulls or KBr discs revealed no structural changes.

The liquors from before and after SINNMR experiments were compared by gas chromatography. The results show that 15 minutes irradiation of chloroform / bromoform mixtures by 3μ 20 kHz ultrasound produces no change in composition.

7.8 DISCUSSION

Several important observations have been made during the experiments on TSP that justify collation and further attention.

1. Ultrasound is essential to the SINNMR experiment because non-sonicated samples of particles suspended in density matched liquids do not produce intense narrow absorptions.

2. The signal to noise ratio of SINNMR experiments can be optimised by correct matching of the mass and particle size range of the sample used together with an optimum support liquid density.

3. No significant SINNMR narrowing has been observed using ultrasound at less than *ca.* 20 Wcm^{-2}. As the estimated cavitation threshold for the support liquids used is *ca.* 16 Wcm^{-2}[147] , it appears that cavitation is a necessary requirement for the observation of SINNMR spectra with the present experimental conditions.

This may also be true for the acoustic excitation of lattice motion by the Pauling mechanism.

4. SINNMR narrowing has not been observed for particle sizes falling below 90μm. The reason as described earlier is due to the necessary size for effective interaction with microjets caused by implosion of the cavity bubbles. This point is further amplified by reference to table 7.3 and in chapter eight.

5. It does appear that ultrasound is capable of producing narrowing through induced lattice motion, as discussed earlier. Whether this is due simply to heating the sample during ultrasonic irradiation or through acoustic stimulation of lattice motion remains to be elucidated.

The above observations demonstrate the importance of ultrasound for the stimulation of incoherent particle motion and thereby to the process of narrowing the resonances from solid materials. However, it does appear that the conditions for the promotion of interparticle collisions, microjet formation and the perturbation of particles from the Dysthe equilibrium condition to cause particle rotation may be capable of improvement. The implication is that improvements to SINNMR are required before it may become universally applicable.

CHAPTER EIGHT

STUDIES OF ACOUSTICALLY INDUCED ROTATION OF SUSPENDED TRISODIUM PHOSPHATE PARTICLES

N.b. A complete list of NMR acquisition parameters for each experiment described in this chapter can be found in Appendix Two.

8.1 PARTICLE DISPLACEMENT

8.1.1 Introduction

The research described within this chapter involves visual observations of particle displacements and SINNMR experimental results. The combination of the two sets of experimental data obtained can lead to a greater understanding of the SINNMR experiment. The knowledge of the TSP particle size limits being detected by SINNMR can enable the deduction of correlation times for certain particle sizes. These data can be further utilised to propose mechanisms by which incoherent motion of the particles is facilitated during the course of the SINNMR experiment.

Samples of TSP were graded as described in chapter 7.3 to produce a range of particle sizes of 1000 - 500μm, 1000 - 210μm, 500 - 210μm, 210 - 105μm and 105 - 90μm. Samples of the various particle size ranges were initially floated on suitable liquid mixtures of $CHCl_3$ and $CHBr_3$ designed to produce various densities. A progressive wave 20 kHz ultrasound used to displace the particles was applied *via* the short horn for bench observations, as opposed to the long horn that was used for SINNMR experiments. Bench observations required the use of glass rather than PTFE NMR tubes.

8.1.2 Bench Observations

Bench experiments using the shorter horn enabled the displacement of particles downwards from the tip of the horn to be measured for different ranges of particle sizes in a variety of support liquid mixtures. Varying the quantity of solid used between 0.1 and 1.4g (with *ca.* 2.5 ml of support liquid) did not appear to influence the vertical displacement limit of the particles. However, the use of the larger quantities tended to make observations more difficult. Consequently, 0.2g of solid were used throughout the observation experiments, with support liquids of varying densities, and irradiated with 20 kHz ultrasound with 1, 2 and 3μm horn tip displacements. The maximum displacements of the particles in a variety of samples are presented in table 8.1.

Three main points are evident from these data. First, decreasing the density of the support liquid for a specified range of particle sizes with constant acoustic power results in increased particle displacement. Second, increasing ultrasonic power applied to a given set of particles in a particular support liquid causes an increase in particle displacement. Third, for a given ultrasonic power and support

liquid density the smaller particles are subject to the greatest displacement. The implication of this last point is that the maximum particle displacement corresponds to the positions reached by the smallest particles in each size range. The data for the 3μm experiments (see table 8.1) when interpreted according to this assumption are presented in figure 8.1 where the smallest size of each range is plotted against the displacement limit for that range.

SUPPORT MEDIUM (v/v) BROMOFORM / CHLOROFORM	ULTRASOUND TIP DISPLACEMENT / μm	DISPLACEMENT FOR 1000 - 500μm PARTICLE RANGE	DISPLACEMENT FOR 500 - 210μm PARTICLE RANGE	DISPLACEMENT FOR 210 - 105μm PARTICLE RANGE	DISPLACEMENT FOR 105 - 90μm PARTICLE RANGE
3:1	1	-	-	8.30	16.70
($2.43gcm^{-3}$)	2	9.50	25.00	32.50	35.00
	3	20.00	32.50	36.70	36.70
2:1	1	-	-	17.50	21.60
($2.32gcm^{-3}$)	2	15.00	25.80	32.50	35.00
	3	25.00	33.3	36.70	36.70
1:1	1	12.50	22.00	24.50	26.70
($2.12gcm^{-3}$)	2	21.70	26.70	33.30	35.00
	3	30.00	35.00	36.70	37.50
1:2	1	20.00	25.00	26.70	26.70
($1.93gcm^{-3}$)	2	29.20	33.30	36.70	36.70
	3	31.70	35.00	36.70	36.70
1:3	1	22.50	25.80	28.30	29.20
($1.82gcm^{-3}$)	2	30.00	33.30	36.70	36.70
	3	33.30	36.70	37.50	37.50

TABLE 8.1. Displacements (in mm) of samples of TSP with varying density of support medium and 20kHz ultrasound tip displacement. Errors are ± 0.05 mm.

Figure 8.1 reveals that irrespective of density of the support liquid a limiting displacement of *ca.* 37 mm is reached corresponding to particles of about 90μm size. The same conclusion can be reached from the data obtained with other ultrasonic powers.

The implication is that for this size of particle the imbalance of forces acting on the particles is dominated by that due to the acoustic field and this permits these particles to reach an acoustic node. This observation is important in so far that it impinges on the understanding of the mechanism of the induced incoherent particle motion that is essential to SINNMR.

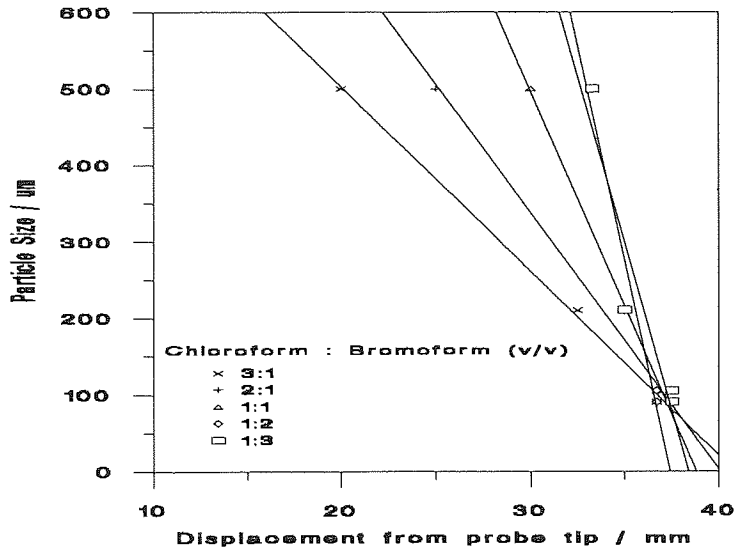

FIGURE 8.1. The displacement of the smallest TSP particles in each particle size range with 20 kHz 3μ ultrasound and varying support medium.

It has been discussed in the previous chapter that SINNMR for TSP cannot be detected with particles smaller than 90μm. As this represents the lower limit of particle size that can be subject to the action of microjets resulting from cavity collapse in the haloform mixtures used when irradiated with 20 kHz ultrasound, it was suggested that this microjet mechanism is essential for successful SINNMR experiments.

However, the data in table 8.1 and figure 8.1 could be used to reinterpret the earlier SINNMR observations and indicate that the reason why SINNMR was not observed for particles with sizes less than 90μm is simply that they are carried beyond the detector region of the NMR spectrometer (the limit of which in all 20 kHz ultrasound experiments set out as in section 6.4.2 corresponds to a particle displacement of 24 mm). Nevertheless, there is evidence that mitigates against this last interpretation. SINNMR has only been observed using probe tip displacements of 3μm or greater which correspond to being above the cavitation threshold of *ca.* 16 Wcm^{-2} for chloroform / bromoform systems. The use of lower powers to correctly position particles smaller than 90 μm in the NMR probe region gave no narrowing.

8.1.3 Using Bench Observation to Optimise Conditions for SINNMR

The upper and lower extremes of the NMR detector coil region used for SINNMR studies correspond to 10 and 24 mm particle displacements from the constantly positioned tip of the acoustic horn. If the lowest acoustic power limit for successful SINNMR studies corresponds to a 3μm tip displacement, the data in figure 8.1 can be used readily to determine the optimum particle size range for a chosen support liquid density. The appropriate data are presented in figure 8.2 and table 8.3, wherein are also shown the particle sizes that are expected to be sited at the centre of the NMR detector coil region (17 mm displacement). All of the curve fits in figure 8.2 are of the form $y = A \cdot 10^{(-B.x)}$ where y is the density (gcm^{-3}), x is the particle size (μm) and A and B for 10, 17 and 24 mm are summarised in table 8.2.

	10 mm	17 mm	24 mm
A	2.704	2.713	2.731
B	6×10^{-5}	9×10^{-5}	1.3×10^{-4}

TABLE 8.2. A and B values for the fitting equations to the data displayed in figure 8.2 for displacements of 10, 17 and 24 mm.

These fitting equations can then be generalised for use with any solid and support medium as long as the densities of both are known and the solid is less dense than the support. The generalisation is achieved *via* the knowledge that the curves in figure 8.2 are for TSP. As TSP has a density of 1.62 gcm^{-3}, a general equation for density difference between the solid and support medium can be defined. The expanded equation is shown below and is simply:

$$(\rho_f - \rho_s) = [A \times 10^{(-B.x)}] - 1.62 \qquad \text{- (8.1)}$$

where ρ_f and ρ_S are the support and solid densities respectively. The value of 1.62 corresponds to the density (in gcm^{-3}) for TSP on which the data in figure 8.2 are based. The values A and B are as those shown in table 8.2

8.2 SINNMR MEASUREMENTS

Although TSP contains both ^{23}Na and ^{31}P nuclei that are available for NMR investigation it is only the latter dipolar nucleus that provides T_1 and T_2 data that are readily amenable to theoretical analysis. Attention was, therefore focused on this nucleus and the spin-lattice relaxation times T_1 which are used are those reported in chapter seven.

DENSITY OF SUPPORT MEDIUM	10mm DISPLACEMENT	17mm DISPLACEMENT	24mm DISPLACEMENT
5:1 (2.59gcm^{-3})	346µm	223µm	177µm
3:1 (2.43gcm^{-3})	743µm	575µm	407µm
2:1 (2.32gcm^{-3})	1016µm	775µm	534µm
1:1 (2.12gcm^{-3})	1624µm	1229µm	834µm
1:2 (1.93gcm^{-3})	2244µm	1684µm	1124µm
1:3 (1.82gcm^{-3})	2706µm	2450µm	1383µm

TABLE 8.3 Prediction of TSP particle sizes reaching defined displacements within a SINNMR experiment using 3µm 20kHz ultrasonic tip displacement and the densities shown.

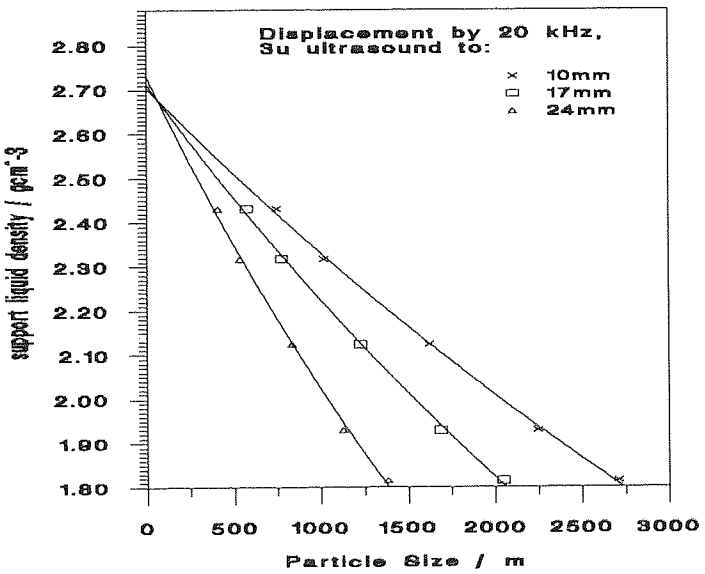

FIGURE 8.2. Support densities required for different TSP particle sizes to be displaced by 10, 17 and 24 mm from the ultrasonic horn by 20 kHz, 3µ ultrasound.

Under appropriate spectrometer operating conditions (low deadtime) ^{31}P SINNMR spectra of TSP reveal a narrowed resonance (full width at half maximum height (FWHM) in the range 30 - 50 Hz), on top of a much broader (FWHM about 6,500 Hz) resonance that arises from static or slowly moving particles. The T_1 of a solid sample of TSP was corrected to 7.2 s from the value obtained by MAS NMR (chapter seven). The FWHM of the ^{31}P SINNMR line was found to vary with change in support liquid density which suggests averaging is particle size dependant. As a result, the particle correlation time and T_1 will also be dependant on particle size.

As discussed in chapter seven there is a contribution to the SINNMR line narrowing of TSP due to sound absorption facilitating a Pauling rotor mechanism. In addition, the S/N ratio in the SINNMR experiment was shown to be a factor of 80 greater than that seen by thermal excitation of the Pauling rotor. Such a considerable enhancement leads to the conclusion that line narrowing by excitation of the Pauling rotor in the SINNMR experiment is unimportant. This latter point leads to the conclusion that the relaxation and correlation times discussed here reflect incoherent particle motion rather than lattice motion.

The observed FWHM from ^{31}P SINNMR experiments can be used to estimate T_2 and in turn the correlation time τ_c and T_1 from the equations below (which are also cited in the theoretical sections as equations 1.29, 1.39 and 1.41). The estimates are shown in table 8.4. For all experiments, the spectrometer resolution was much greater than the narrowest SINNMR resonances observed. It is for the latter reason that T_2^* can be assumed to be approximately equal to T_2.

$$FWHM = \frac{1}{\pi T_2^*} \qquad -(8.3)$$

$$\frac{1}{T_2} = K\left[3\tau_c + \left(\frac{5\tau_c}{1+\omega^2\tau_c^2}\right) + \left(\frac{2\tau_c}{1+4\omega^2\tau_c^2}\right)\right] \qquad -(8.4)$$

$$\frac{1}{T_1} = K'\left(\frac{2\tau_c}{1+\omega^2\tau_c^2}\right) \qquad -(8.5)$$

$K' = 4.68 \times 10^8$ and $K = 9.38 \times 10^7$ which are constants for the ^{31}P nucleus and the NMR spectrometer used and were obtained from the Ph.D. thesis of J.K. Roberts[153].

SUPPORT MEDIUM	Particle Size Limit in NMR Probe Region	FWHM / Hz Measured	T_2 / s	τ_c / s Estimated	T_{1DD} / s Estimated
neat $CHBr_3$	280 - 210 µm	59	5.40×10^{-3}	6.6×10^{-7}	0.92
5:1	346 - 210 µm	51	6.24×10^{-3}	5.6×10^{-7}	0.80
3:1	743 - 407 µm	44	7.23×10^{-3}	4.9×10^{-7}	0.69
2:1	1000 - 534 µm	37	8.60×10^{-3}	4.1×10^{-7}	0.58
1:1	1000 - 834 µm	37	8.60×10^{-3}	4.1×10^{-7}	0.58

Table 8.4. FWHM, estimated correlation time, τ_c and NMR spin-lattice relaxation times, T_1 for ^{31}P SINNMR spectra of 1000 - 210µm graded TSP in various support mixtures showing the detectable particle size range.

As with the spectra discussed in chapter seven, the spectra that produced the FWHM values in table 8.4 are composed of a narrow SIN resonances on top of a solid hump. The relative areas (intensities) of the two resonances and the linewidth of the SINNMR resonance can provide quantitative information about the proportions of particles having different rotational rates. However, before measured intensities can be used with quantitative rigour they must be obtained using intersequence pulse intervals that are not less than 5.3 times the longest of the T_1's for the species involved.

In the case of TSP the ^{31}P T_1 for the static solid would dictate an intersequence delay of *ca.* 38 s which would be impractical considering the effects of particle degradation (measured to be approximately 50% of a 1000 - 500μm particle range of TSP which degrades to below 500μm after 300 s of 20 kHz ultrasound with 3μ tip displacement). Consequently, the relative SINNMR and solid peak intensities were measured for individual SINNMR experiments under conditions of rapid multipulsing and corrected using equation 2.7. A specimen calculation of the correction is shown below for the solid and SINNMR peak areas (with bromoform support liquid). As M_0 is directly related to the number of nuclei giving rise to an NMR signal, and hence in a SINNMR experiment related to the proportions of sample producing the static solid and SINNMR resonances, equation 2.7 is rearranged so that

$$M_o \propto I_{eq} \frac{\left(1-\cos\theta\exp\left(\frac{-t}{T_1}\right)\right)}{\sin\theta\left(1-\exp\left(\frac{-t}{T_1}\right)\right)} \qquad \text{- (8.6)}$$

where I_{eq} is the observed intensity of a resonance detected from nuclei with a spin-lattice relaxation time T_1. The NMR experiment is conducted with a pulse angle θ and a delay between pulses t. The specimen calculation data is shown in table 8.5 and the complete corrected data set are shown in table 8.7.

	I_{eq}	θ / deg	t / s	T_1 / s	exp $(-t/T_1)$	cos θ	sin θ	M_0
Solid	0.201	46.5	1	0.92	0.3372	0.6884	0.7554	0.3209
SINNMR	0.502	46.5	1	7.2	0.8703	0.6884	0.7254	2.138

TABLE 8.5. Specimen calculation data and M_0 obtained for the correction of NMR peak intensities using equation 8.6.

In table 8.5, the observed intensities I_{eq} are measured in arbitrary units from a SINNMR experiment with bromoform as the support liquid. The resultant M_o values in table 8.5 then indicate that 13.1% of the detected sample participated in SINNMR line narrowing from:

$$\frac{\%\text{ of sample participation}}{\text{in SINNMR line narrowing}} = \frac{\text{SINNMR } M_o \text{ Value}}{\text{Sum of SINNMR and Solid } M_o \text{ values}} \times 100 \qquad \text{- (8.7)}$$

The intensities corrected in this way provide the detected proportion of the solid sample that are rotating rapidly or effectively static. The corrected intensities and thus proportions of SINNMR and static contributions are shown in table 8.7.

It must be appreciated that the NMR signals obtained are proportional to the mass of solid within the NMR detector coils which is not constant with changing support liquid density. The is because the Dysthe relationship between ultrasonic and bouyancy forces affects particle displacement.

It is for the last reason above that certain results are shown corrected for unit mass within the detector coil region. To estimate the amounts of a sample by mass in certain regions of an nmr tube, a mass distribution curve (shown in figure 8.3) with particle size was calculated by the multiplication of defined particle size masses with a theoretically estimated Gaussian distribution for the 1000 - 210 μm particle range. The calculation of the mass distribution curve is shown in appendix three. For the calculation of particle masses, it is assumed that the TSP particles are cubic.

The SINNMR experiments under scrutiny in this chapter were obtained using 1 g of TSP with a particle size range of 1000-210 μm. Application of these particle size limits to equation 8.2 produces a maximum area of the curve in figure 8.3 corresponding to 1 g of solid. The integral of the equation of the line from figure 8.3, shown as equation 8.8, can be used to deduce the of mass of material between particle size limits x_1 and x_2.

$$y = \int_{x_1}^{x_2} A - Bx + Cx^2 + Dx^3 \qquad \text{- (8.8)}$$

$$y = \left[Ax - \frac{B}{2}x^2 + \frac{C}{3}x^3 + \frac{D}{4}x^4 \right]_{x_1}^{x_2} \qquad \text{- (8.9)}$$

where $A = 2.7 \times 10^{-4}$, $B = 1.7 \times 10^{-6}$, $C = 3.3 \times 10^{-9}$ and $D = 3.3 \times 10^{-10}$.

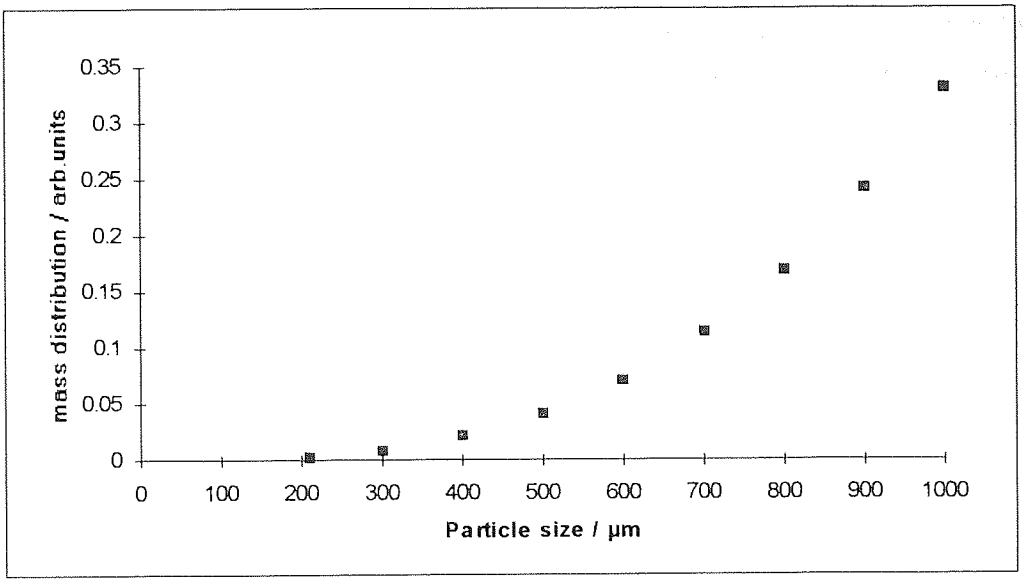

FIGURE 8.3. Theoretically derived mass distribution curve for 1000 - 210 µm particle range of TSP. The equation of line for this distribution is given as equation (8.9).

Using the known particle size limits which are manipulated to the NMR probe region (from table 8.4), equation 8.9 can produce a reasonable estimate of the proportion of the sample (by mass) present in the NMR probe for SINNMR experiments using different support liquid densities. This is shown as data in table 8.7 under the heading of '% of 1g of sample in the NMR probe region' and is shown in table 8.6. These data is then utilised to produce S/N per unit mass, as shown in table 8.7.

Support Medium Ratio of $CHBr_3$ to $CHCl_3$	Particle size limits within NMR probe / µm	Integral result from equation (8.9)	% of total mass in NMR probe region
n/a	1000 - 210	82.83	100
neat $CHBr_3$	280 - 210	0.35	0.42
5:1	346 - 210	1.03	1.24
3:1	743 - 407	23.02	27.79
2:1	1000 - 534	76.24	92.05
1:1	1000 - 834	42.83	51.71

TABLE 8.6. The calculated integrals of the mass distribution curve for different particle size limits present in the NMR detector coils.

It can be seen from table 8.7 that only between 13 and 2% of the detected sample is induced by ultrasound to undergo sufficiently ultrasonically induced incoherent

rotation to cause effective line narrowing (as reflected by the corrected % SIN peak total area). As the S/N per unit mass increases with decreasing particle size, the proportion of sample participation in SINNMR appears to be at its greatest with small particles. In contrast however, the efficiency of SINNMR is greatest with large particles. This is reflected in table 8.4 where FWHM, τ_C and T_1 all reduce as the particle size increases. Explanations for these observations are forwarded later. Evidently, the receptivity of SINNMR is, at present, significantly worse than that of MASNMR for which all of the sample used contributes to spectral intensity (except where skin depth is important).

8.3 PROPOSED MECHANISMS FOR SINNMR LINE NARROWING

Reference to table 8.4 reveals the superficially surprising fact that ultrasonic induced particle correlation times decrease with increasing particle size. A tentative explanation for this is now offered.

It has been stated that no narrowed resonances of TSP occur with 20 kHz ultrasound intensities below the cavitation threshold for the support liquids used or with particles having dimensions less than 90 μm. This implies that narrowing by incoherent motion and the Pauling rotor require cavitation. Analysis of the change in correlation time with particle size in table 8.4 shows the mechanism for particle motion (and hence line narrowing) is not a straight function of rotational kinetic energy. The rotational kinetic energy of a particle is $1/2\ I\omega^2$, where I is the moment of inertia and ω the angular frequency.

Although the definition of I varies with particle shape, it is always proportional to r^2; which is proportional to particle size. The energy imparted to each particle can be considered as constant for a particular ultrasound power. This would imply that smaller particles, with smaller moments of inertia, would have greater angular velocities. The latter would produce greater averaging of the smaller particles by incoherent motion, but this is contrary to that observed.

For effective interaction between microjets, produced on cavity collapse, and a solid surface, the surface dimensions must be no less than the resonance bubble size, as given by equation 4.16. It can be deduced that support liquids used in this work produce resonant cavitation bubble radii between 85 and 95 μm.

Support Liquid (ratio of CHBr3 to CHCl3)	Pulse Angle / °	T1 /s	Intersequence Delay / s	SIN peak total observed area / arb units	Solid peak total observed area / arb units
Solid State (ref. only)	90	7.2	1	0	1.301
(SINNMR) CHBr3 only	46.5	0.92	1	0.201	0.502
(SINNMR) 05:01	46.5	0.80	1	0.168	1.387
(SINNMR) 03:01	46.5	0.69	1	0.149	1.412
(SINNMR) 02:01	46.5	0.58	1	0.142	1.345
(SINNMR) 01:01	46.5	0.58	1	0.138	2.239

Support Liquid (ratio of CHBr3 to CHCl3)	Particle Size Limits in NMR Probe Region	Corrected SIN peak total area / arb units (%age)	Corrected solid peak total area / arb units (%age)	Observed S/N ratio of SINNMR peak	% of 1g sample in NMR probe	S/N per unit mass
Solid State	N/A	0	10.033 (100%)	-	-	-
(SINNMR) CHBr3 only	280 - 210 µm	0.321 (13.0%)	2.140 (87.0%)	11	0.4	2750
(SINNMR) 05:01	346 - 210 µm	0.261 (4.2%)	5.912 (95.8%)	13	1.2	1083
(SINNMR) 03:01	743 - 407 µm	0.225 (3.6%)	6.018 (96.4%)	26	27.8	94
(SINNMR) 02:01	1000 - 534 µm	0.209 (3.5%)	5.733 (96.5%)	33	92	36
(SINNMR) 01:01	1000 - 834 µm	0.203 (2.1%)	9.543 (97.9%)	16	51.7	31

Table 8.5. SINNMR acquisition parameters and observed and correceted signal to noise ratio and relative peak areas for various support mixtures used.

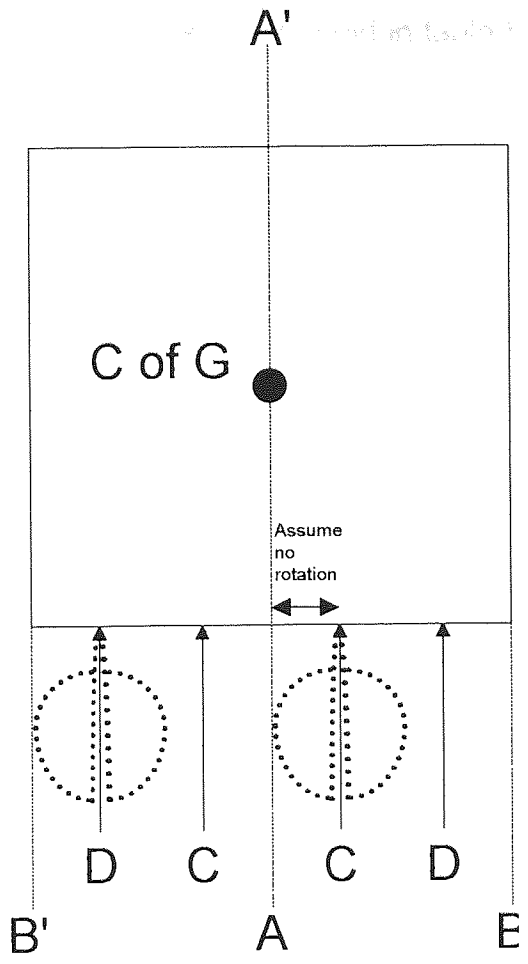

Figure 8.4. Two dimensional slice through a hypothetical cubic particle used to discuss microjet interactions. To assist with the definitions, micro-jets are drawn at points C and D.

Figure 8.4 shows a schematic two dimensional view of a cubic particle upon which a microjet impinges on face B'AB. A line AA' passes through the centre of mass, so that the distances AB and AB' are the same. A microjet can be considered to impact the solid surface at any point along AB (or the identical AB'). Points C and D can be considered as the limits within which impact can result in particle rotational motion. C can be defined as a point such that the distance AC must be at least the bubble radius for two reasons. (i) The incident length of the solid surface must not be less than two times the resonance bubble radius (CAC in figure 8.4) and (ii) a jet impinging within the distance AC will facilitate a high degree of translational motion due to the impact proximity to the line through the centre of mass (C of G between AA'). Point D is also defined by distance BD being equal to the bubble radius and allows for the whole of the bubble to be incident to the particle face in order to facilitate collapse.

Using this approach, an estimate of the percentage area of a particle face upon which microjet impact could produce incoherent motion can be calculated, and is

shown for varying particle size and support liquid in table 8.8. The effective limits for which microjet interaction could facilitate incoherent motion of the particle is between points C and D. As the resonant bubble radius is dependant on the support liquid density, there will be a corresponding dependence of the percentage area on the mixture considered.

	Percentage Areas of a particle face upon which microjet impact could produce Incoherent motion with different support liquids. (Based on Figure 8.4)					
Particle Size / μm	**$CHBr_3$ neat (86 μm)**	**5:1 (86 μm)**	**3:1 (89 μm)**	**2:1 (90 μm)**	**1:1 (96 μm)**	**Inverse of 3:1 data**
1000	66	66	64	64	62	0.0156
900	62	62	60	60	58	0.0167
800	58	57	56	55	53	0.0179
700	51	51	49	48	46	0.0204
600	43	43	41	39	37	0.0244
500	32	31	29	27	24	0.0345
400	15	14	11	9	5	0.0909

Table 8.8. Estimated percentage area of different size particle faces upon which microjet impact could facilitate incoherent particle motion. The figures beneath the support liquid ratios (in parentheses) are the calculated radii of acoustically induced cavitation bubbles in that particular support medium.

These percentages can be thought of as probabilities of microjet impact facilitating incoherent motional averaging. Ignoring the losses of microjet energy transfer on impact with a particle, the energy dissipated on microjet impact must be proportional to the angular velocity of a particle which is inversely proportional to its correlation time τ_C. If microjet interactions produce incoherent motion, then the implication is that the higher the probability of effective microjet impact, the smaller the correlation time τ_C. The ^{31}P linewidths obtained for TSP with varying support liquid density reflect the dependence of the correlation time on the particle size, as shown in table 8.4. These data can be used to corroborate the hypothesis of microjet impact causing incoherent motion in the following way.

The inverse of the probabilities of effective microjet impact (shown as data in the far right column of table 8.8) is plotted against particle size and shown in figure 8.5. Onto the same graph is superimposed a plot of estimated correlation time (from table 8.4) with particle size. A similar degree of linearity can be seen for the two curves at particle sizes above 600μm indicating that particle motion is facilitated *via* a microjet interaction mechanism. It appears that particles with sizes below 600 - 500μm undergo motional averaging by another mechanism or even an additional mechanism to that based on the considerations of microjet probability.

It must be appreciated that this proposed model is based on the defined C-D limits in figure 8.4 through a one dimensional slice of assumed cubic particles.

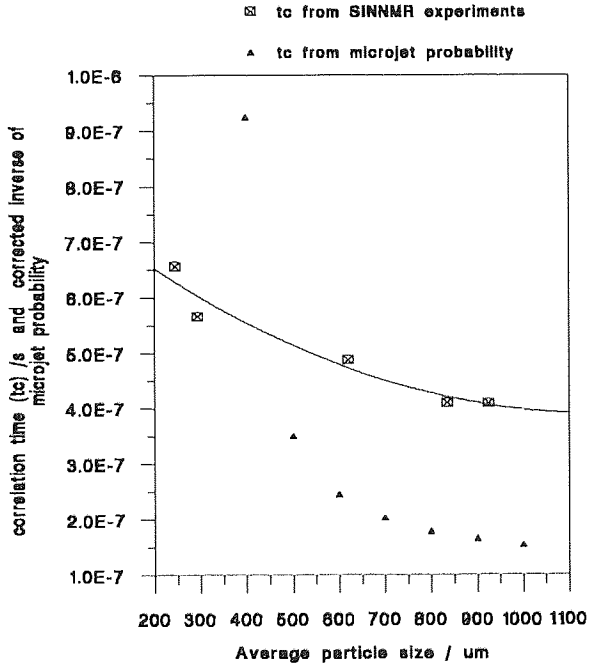

Figure 8.5. Correlation time obtained from SINNMR experiments compared with a corrected inverse of microjet probability of facilitating incoherent motion. The correction of the inverse microjet probability was divided by 10^5 so both data sets could be plotted on the same y axis scale.

Unfortunately, it has been very difficult to prove quantitatively a particular mechanism for the averaging of particles smaller than 500μm. It may be the case that the definitions of the length CAC in figure 8.4 may be different for smaller particles. This may be due to inaccuracies in the assumption that a high degree of translational motion would occur if microjet impact occurs within the limits CAC. The following are some qualitative arguments for other mechanisms which could facilitate incoherent motion of the smaller particles in SINNMR experiments.

Certain aspects of results presented in chapter seven indicate that a particle size mechanism was apparently occurring to facilitate incoherent motion in SINNMR experiments. The results of particular interest, within section 7.3, involved the study of the dependence of ^{31}P SINNMR S/N of TSP for different particle size ranges with mass of solid used. The observation of an optimum mass which varied for different particle size ranges suggests that particle collisions are important to the SINNMR experiment.

Another suggested mechanism for incoherent averaging in SINNMR experiments is one of interparticle collisions which can derive from particle interactions with the pressure wave or particle streaming. Although not strictly correct, a simple model which can be used to consider this mechanism is one based on chemical kinetic collision theory[154]. For N particles in a SINNMR experiment, each particle with diameter σ, (collision diameter 2σ), and number of particles N, will on the basis of kinetic theory have a mean free volume and consequential mean free path equal to :

$$L = \frac{1}{\sqrt{2\pi\sigma^2 N}} \qquad \text{-(8.10)}$$

Inspection of equation 8.10 in relation to the SINNMR results discussed earlier leads to the following points:

1. As mean free path is essentially unit length per collision, its reciprocal is collisions per unit length and the mean free path is inversely proportional to the square root of number of particles and the particle diameter (and therefore particle size).

2. As the number of particles within each SINNMR experiment is constant then the only variable is the collision diameter. As a result the mean free path would be inversely proportional to particle size. Therefore, large particles have smaller (relative) mean free paths than smaller particles.

The observations of (a) the increase in S/N per unit mass as particle size is decreased and (b) the increase in the efficiency of SINNMR line narrowing (reduction of FWHM) as particle size is increased could be explained with reference to point 2 above.

First, it is proposed that the proportion of particles participating to produce SINNMR line narrowing is a function of the mean free path of those particles. This

implies that smaller particles with longer mean free paths have a higher proportion of sample participation in the SINNMR experiment. This is observed *via* the results of S/N per unit mass in table 8.7. Second, and in a similar context, particles with shorter mean free paths experience greater incoherent motion and hence line narrowing. This is observed *via* the reduction in FWHM as particle size is increased. As a result, particle collisions operate to assist and hinder the SINNMR experiment. If this proposal is accurate, the implication is that increased S/N per unit mass could be achieved at the expense of optimum narrowing.

It is entirely possible that the dependence of the SINNMR experiment on the mean free path is present even for larger particles (> 500 μm). Although it has been shown that incoherent motion appears to be dependent upon the microjet impact probability with a particular particle size, the observed S/N per unit mass may be dependant on the mean free path as explained above.

It is appreciated that the treatment of solid particle interactions *via* a theory designed specifically for gases is far from perfect. However, for the arguments involving mean free paths, it is considered adequate for the adopted empirical viewpoint . At this stage it is unclear as to the mechanism by which the mean free path could inhibit or enhance the SINNMR experiment.

An alternative mechanism for induced incoherent motion of particles is *via* the acoustic pressure difference across a particle during the SINNMR experiment. If a particle is at a Dysthe equilibrium position, at any one point in time, as shown in figure 8.6, a pressure difference (p_1 - p_2), due to the acoustic wave, acts across the two faces A and B. This pressure difference will depend on the ultrasonic frequency and particle size, the greatest difference being when the particle size is half the ultrasonic wavelength. The pressure difference necessitates that different forces act on the extremes of the particle which is then induced to rotate.

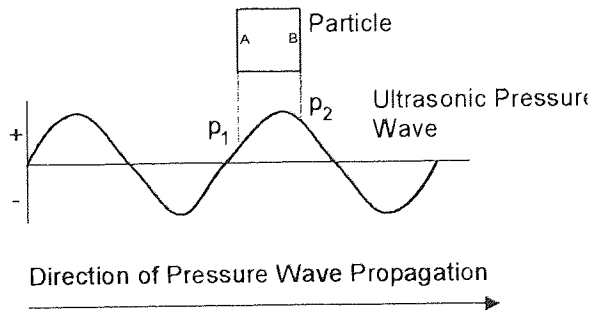

FIGURE 8.6. The interaction of an ultrasonic pressure wave with a particle showing the difference in pressure placed on faces A and B. The relative sizes of the particle and wavelength of ultrasound are exaggerated.

It has also been considered that streaming cavitation[155] could contribute to incoherent motion, especially of smaller particles. A line of bubbles along a path in a sound field is referred to as a cavitation streamer, which results when bubbles smaller than the resonant size move towards pressure maxima in a standing wave. Such bubbles coalesce to produce a resonant size bubble which moves from the pressure maxima and collapses into microcavities. The collapse into micro cavities is thought to be due to sub division of the bubble by liquid crests projecting into the bubble airspace.

A large particle in the vicinity of such a collapse will not be perturbed to a great extent. However as the particle size approaches that of the bubble, turbulence by such a mechanism could easily perturb the particle. It is, however, unlikely for such a mechanism to play an important role in SINNMR because of the failure to explain why particles smaller than 90μm appear not to motionally average.

8.4 DISCUSSION

The weight of evidence presented strongly suggests that the theory outlined by Dysthe showing the displacements of single particles suspended in fluids by ultrasound can be used to optimise the SINNMR experiment. Equations have been derived to show that the displacements observed by visual inspection for TSP can be generalised for use with other suitable support liquids and solids, so long as their densities are known.

It is also proposed that the sonically induced narrowing of the NMR spectra of particles in the systems studied here larger than *ca.* 500μm is *via* an interaction between a microjet from a collapsing bubble and a particle surface. Contrary to the superficial expectation, it is the larger particles (*ca.* 1000μm) which undergo the most rapid averaging. It is still unclear as to the origin of incoherent motion in particles below 500μm although possible suggestions for particle induced rotational mechanisms have been advanced.

Particles below 350μm which equilibrate in the NMR probe show the largest S/N per unit mass. In principle, this could be due to a skin depth effect problem with the larger sized particles, although this latter point is unlikely. It is also proposed that S/N per unit mass may be dependent on the mean free path of particles which may enhance or inhibit certain conditions of the SINNMR experiment.

CHAPTER NINE

SINNMR EXPERIMENTS ON POLYTETRAFLUOROETHYLENE (PTFE)

N.b. A complete list of NMR acquisition parameters for each experiment described in this chapter can be found in Appendix Two.

9.1 INTRODUCTION

PTFE was discovered much by accident by R.J. Plunkett and J. Rebok[156] in 1938 when it was formed inside a pressurised cylinder containing tetrafluoroethylene that was being used in experiments to develop new refrigerants. PTFE is a non-polar polymer containing two fluorine substituents on each main chain carbon atom and has a density of 2.20 gcm^{-3}. There is considerable evidence to suggest that molecules of PTFE are linear and unbranched[157]. PTFE usually has a high degree of crystallinity (93 - 98%) a crystalline melting point of 327°C and a low coefficient of friction. PTFE was considered to be an ideal solid to study using SINNMR because of its inert nature.

The crystal structure shows two distinct changes at 19 and 30°C. Between these temperatures the packing of molecules on the hexagonal lattice is somewhat disordered owing to small angular displacements of chain segments about the chain axis. Above 30°C the preferred crystallographic orientation is lost and the molecular segments oscillate about their long axes with a random angular orientation in the lattice[158].

The ^{19}F NMR spectrum of PTFE has been the subject of extensive investigations. The spectra of static samples reveal significant anisotropy in the screening tensors, so that absorption covers a wide spectral range[159]: absorptions from both amorphous and crystalline regions of appropriate samples may be distinguished. In view of the strong dipolar coupling between ^{19}F nuclei in this sample, MREV-8 pulse sequences rather than MAS NMR have been used to reduce ^{19}F line widths in PTFE samples. PTFE, therefore, offers a severe challenge for the production of definitive SINNMR spectra.

All SINNMR experiments on PTFE were conducted using the 20 kHz Kerry Ultrasonics apparatus, but obviously, conducted using glass NMR sample tubes.

9.2 ^{19}F SINNMR STUDIES OF PTFE

The investigations were conducted on 'particles' cut as 0.5, 1 and 2 mm squares from a 0.75 mm thick sheet of highly crystalline PTFE, and suspended in mixtures of bromoform and chloroform. Significantly, the experimental conditions were initially set using the data obtained for the optimum SINNMR experiments for TSP. This extrapolated to a 7:1 (v/v) chloroform / bromoform support liquid for the 1 mm^2 and 2 mm^2 PTFE and neat bromoform for the 0.5 mm^2 PTFE. 1.0g of solid was used throughout the SINNMR PTFE investigations.

Preliminary investigations showed that if each size of particles of PTFE was studied separately, the maximum narrowing that could be achieved was only to a FWHM of *ca.* 2500 Hz. More efficient narrowing was achieved by mixing equal proportions (w/w) of the 0.5, 1 and 2 mm particle squares and this system was used to obtain the results discussed below. This preferred use of a mixture of particle sizes indicates that SINNMR experiments benefit from the use of a range of particle sizes.

An observation during the investigation of PTFE was that the commercial bromoform used was contaminated with a fluorine containing impurity that produces a sharp resonance (not attributable to sonication) on the lower screening side of the major PTFE ^{19}F absorption. It is necessary to have a combined spectrometer deadtime (DEADT) and delay time (DELAY) of at least 100μs, to eliminate baseline roll and pulse artefacts. Unfortunately, such parameters cause the elimination of much of the broad anisotropic base of the solid state ^{19}F resonance of PTFE. However, as can be seen in figure 9.1, SINNMR was still able to narrow the major absorption from a FWHM of *ca.* 3750 Hz to *ca.* 1650 Hz.

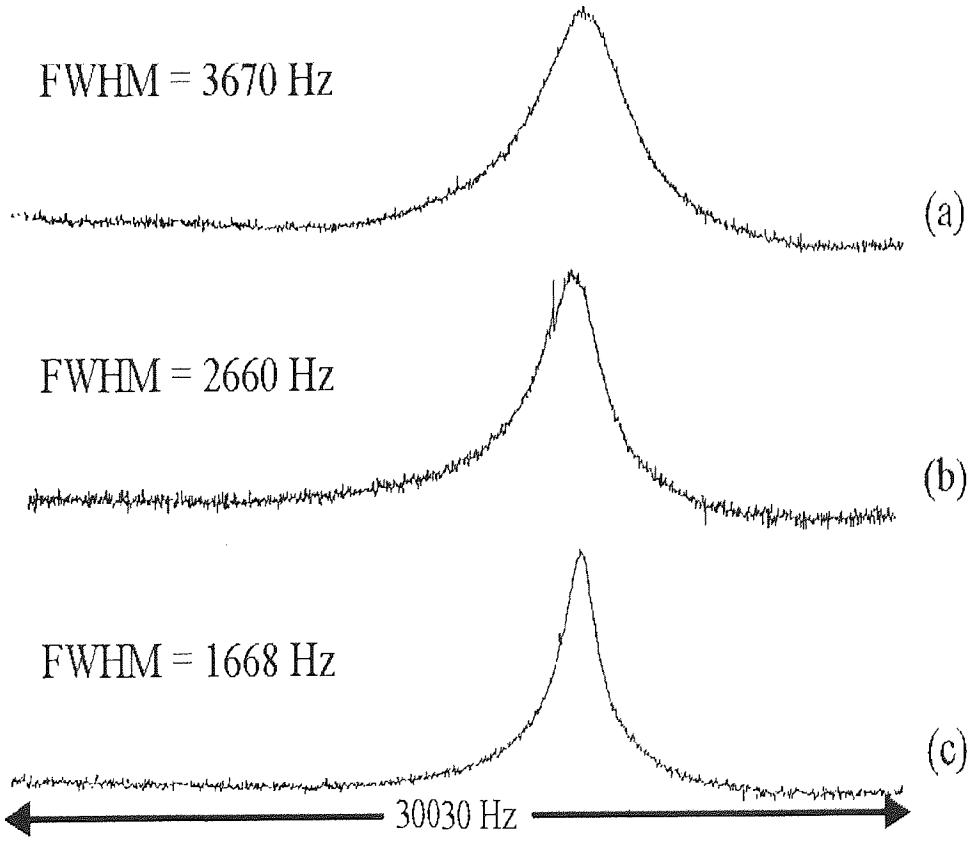

FIGURE 9.1. The Static solid (a), and progressive narrowing by SINNMR (b) and (c), of the ^{19}F resonance in PTFE. Acquisition parameters were identical for all three experiments.

Unlike the SINNMR observations with TSP, the ^{19}F PTFE resonance could be narrowed gradually by altering the ultrasonic horn tip displacement (and hence the power density). This is seen by reference to table 9.1. There is no obvious explanation for the increase in FWHM for ultrasonic tip displacements higher than 4.5 μm.

Ultrasonic Tip Displacement / μm	FWHM / Hz	Temperature of Sample after SINNMR Experiment / ^{o}C
0.0 (standard solid)	3750	28
2.0	2836	29.5
2.5	2256	29.5
3.0	2085	29.5
3.5	2043	30.0
4.0	2335	30.0
4.5	1668	30.0
5.0	1835	30.0
6.0	2168	30.0

TABLE 9.1. The FWHM and final sample temperature measured for ^{19}F SINNMR spectra of PTFE. All acquisition parameters were identical.

9.3 THE ORIGIN OF SINNMR LINE NARROWING IN PTFE

The analysis of the support medium before and liquor (obtained by gravity filtration) after SINNMR experiments by ^{19}F NMR show no change, indicating that PTFE does not melt or dissolve in the course of a SINNMR experiment. The fact that no PTFE resonances are present after gravity filtering indicates the narrowing is not *via* ultra-fine particles.

It must be acknowledged that the material does exhibit phase changes and consequently molecular chain motion which could be induced by direct heating during the SINNMR expeirment. To eliminate this possibility, electrically induced temperature studies of PTFE were undertaken. The results are presented graphically in figure 9.2.

It can be seen that for the alleged SINNMR linewidths to have been achieved the particle temperature would have been required to reach 90^{o}C during the course of the experiment. This cannot be the case from the evidence in table 9.1.

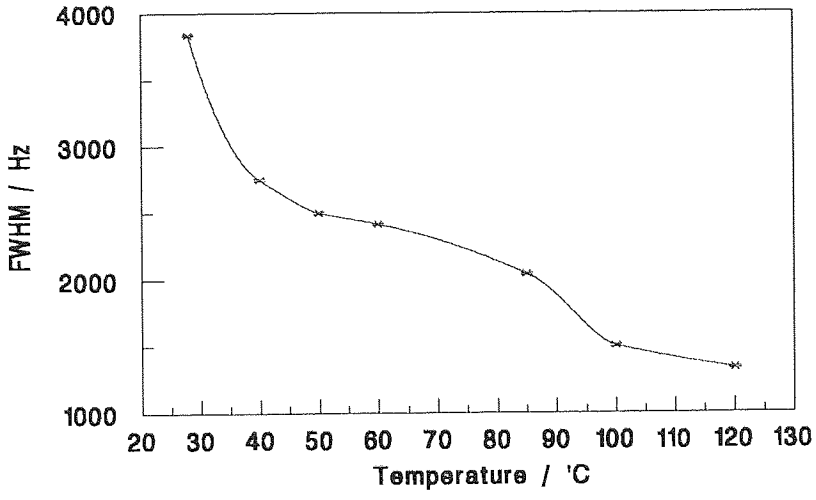

FIGURE 9.2. Variation with temperature of the FWHM of the major ^{19}F resonance (84.26 MHz) of a static sample of PTFE.

9.4 DISCUSSION

The study of the ^{19}F PTFE resonance by SINNMR proves that the displacement results for TSP can be extrapolated to other systems for 20 kHz ultrasound. It is also important to note that a mixture of particle sizes can produce better averaging of PTFE than if a single particle size is used. The use of various particle sizes may indicate that SINNMR requires particle collisions and corroborates the evidence in chapters seven and eight that there is a necessity for this interaction for SINNMR experiments.

Although the above results appear to be definitive proof of a genuine demonstration of the SINNMR effect, (that is to say averaging of the broad NMR resonance occurs as a result of incoherent particle motion), it is noted that the Young's modulus of PTFE is relatively low. This could facillitate averaging of the NMR resonance by subjection of the solid to ultrasound when the decompression cycle could increase the free volume and facilitate adequate motion of the polymer chain. However, McCall[137] has pointed out that for PTFE two T_2 values are evident over a wide range of temperature, with the change near 20°C being attributed by Schlicter[160] to main-chain rotation. Above 20°C the constancy of T_2 up to 50°C and the small increase thereafter are unlikely to result in the ^{19}F line narrowing seen in figure 9.1. Although induced lattice motion may produce some of the narrowing in PTFE by SINNMR, it is unlikely. This is supported by the fact that the ^{19}F resonance can be narrowed progressively to a minimum FWHM of *ca.* 1650 Hz compared to *ca.* 3750 Hz for the static solid through optimisation of the SINNMR conditions.

CHAPTER TEN

SINNMR INVESTIGATIONS OF KNIGHT SHIFTED NMR SIGNALS

N.b. A complete list of NMR acquisition parameters for each experiment described in this chapter can be found in Appendix Two.

10.1 INTRODUCTION

Knight shifts are due to the interaction of nuclei with the electrons in electrically conducting materials, especially metals. They are usually a large deshielding compared to the normal chemical shift range for compounds of the relevant isotope. If it proves possible to obtain Knight shifted signals for metallic species, these can only be attributed to the metallic state and must provide definitive proof for the validity of the SINNMR experiment.

A particular attraction of studying metals by SINNMR is that because of strong metallic bonding, there is a low probability of invoking Frenkel or Pauling rotational mechanisms by sonication well below the melting point.

This chapter reports the 20 kHz ultrasound SINNMR study of certain alloys and pure aluminium as well as doped silicon.

10.2 SINNMR INVESTIGATIONS INTO ALUMINIUM AND SOME OF ITS ALLOYS

Several metallic samples containing aluminium [lithium (3%) - aluminium alloy, Dural® (95% Al, 4% Cu and 1% Mg), 99% aluminium and aluminium foil (99.9%)] were studied by SINNMR. As the densities of these materials are in the region of 2.70 - 2.80 gcm^{-3}, all experiments were conducted within a PTFE NMR sample tube using a bromoform support medium . The samples of metal were cut into strips of varying sizes but no larger than 3mm x 1.5 mm x 0.5 mm.

It is known[161] that the support liquid will readily react (particularly in the presence of ultrasound) to produce aluminium alkyls by the scheme shown as equation (10.1) below:

$$4\,Al + 6RX \Leftrightarrow 2R_3Al_2X_3 \qquad -(10.1)$$

This reaction had to be avoided and two procedures were adopted for this purpose. First, the experimental time was reduced to a minimum by rapid multipulsing. Second, all samples were coated in a Cascamite® resin matrix and allowed to set for 48 hours before conducting experiments. The time allowed for the resin to set was found to be important to the success of the experiment. Allowing too short a setting period left the cascamite too flexible and liable to tear under sonication. If the setting time was 72 hours or more, the cascamite appeared too brittle and would shatter in a matter of seconds under sonication. If

the correct setting time was allowed, it was possible to recover 100% of the coated metal samples at the end of a SINNMR experiment.

All experiments used 1.0g of the coated metal sample with 20 kHz ultrasound at varying power ratings. However only a 4μm tip displacement of the ultrasonic horn produced ^{27}Al SINNMR spectra. The ^{27}Al SINNMR Knight shift obtained for each material is shown in table 10.1, referenced to 0.004M aqueous aluminium chloride.

Material	Chemical Shift δ / ppm	Average Chemical Shift / ppm	FWHM / Hz	Average FWHM / Hz
Li(3%) - Al Alloy	1368,1367, 1371,1369	1369	350,380,350, 350	358
Dural®	1372, 1375, 1368, 1371	1372	350,350,350, 380	358
99% Al	1373, 1372, 1374, 1373	1373	350,350,350, 350	350
Al Foil	1379,1373, 1377,1375	1376	500,480,500, 450	483

TABLE 10.1. ^{27}Al SINNMR Knight Shifts and line widths for a variety of metallic aluminium solids. *N.b.* Digital resolution throughout was set at 7 Hz (0.3 ppm).

An example of the spectra produced by SINNMR is shown in figure 10.1 which is a typical ^{27}Al SINNMR spectrum of lithium (3%) - aluminium alloy with the aluminium chloride reference (separate sample). As the window of the NMR spectrometer is too small to produce a sufficiently wide spectrum, figure 10.1 is the result of two superimposed spectra (one SINNMR and one reference) which were recorded separately. Such spectra were achieved by using two separate frequency offset values of 82 kHz for the Knight shift and 47.68 kHz for the reference. The FWHM of the static solid for Dural® was found to be *ca.* 17000 Hz on the FX-90Q NMR spectrometer. It is likely, due to the limits of the observation window, that this figure is inaccurate and is amplified by the baseline roll present.

Figure 10.2 illustrates the different average chemical shift positions obtained for each aluminium alloy. It is possible that these average chemical shifts reflect the different compositions of each alloy.

The Knight shifted ^{27}Al SINNMR resonance may be considered as having a poor S/N ratio, however, this is considered to be a consequence of the skin depth and the use of large particles in a sample having an overall small surface area.

However, chapter eight table 8.7 shows that only between 2 to 13 % of a TSP sample contributes to the SINNMR experiment. It is possible that the efficiency of SINNMR with aluminium and its alloys is also of this order.

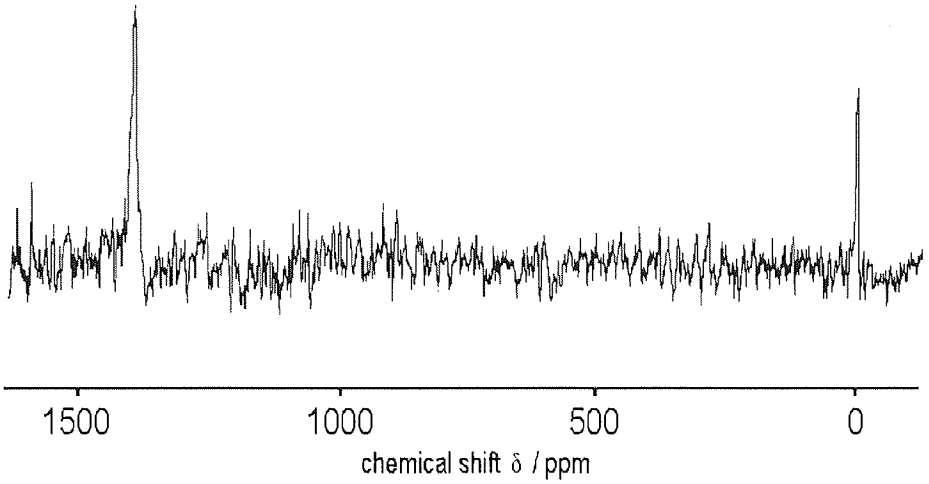

FIGURE 10.1. Superimposed ^{27}Al SINNMR spectra at 23.3 MHz of a metallic lithium (3%) / aluminium alloy and aqueous aluminium chloride (0.004 M) reference.

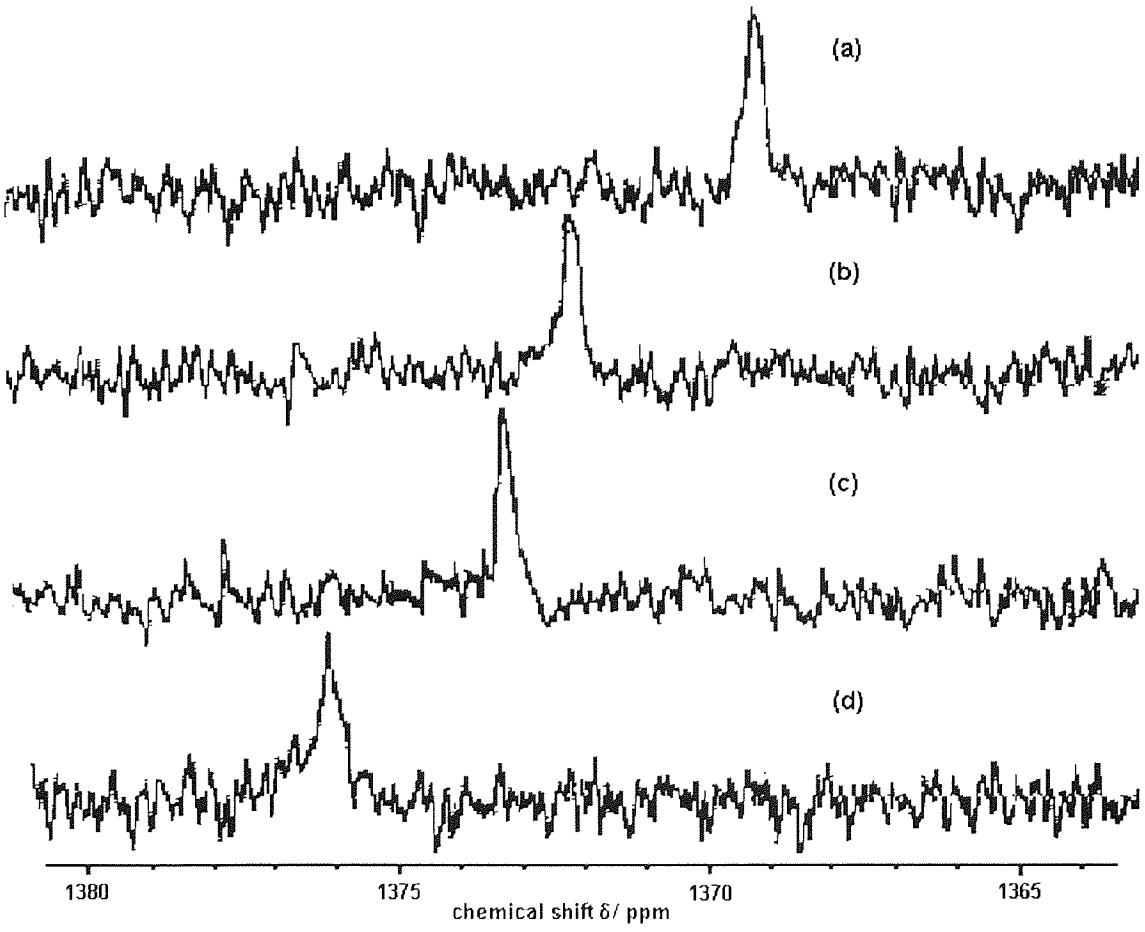

FIGURE 10.2. Average ^{27}Al chemical shift positions (relative to aqueous aluminium chloride) obtained for (a) Li (3%) - Al alloy, (b) Dural®, (c) 99 % Al and (d) Al foil.

It can be seen immediately from table 10.1 (which contains several data sets for each sample to indicate the reproducibility of the SINNMR experiment) that SINNMR is capable of extensive narrowing to 500 Hz and below. This contrasts with the corresponding MAS NMR Knight shifted resonance shown in table 10.2 obtained by Andrew and that at 78.172 MHz using a Bruker AC 300 NMR spectrometer at Aston University. The Aston University measured MAS NMR line widths recorded in table 10.2 are undoubtedly large as a consequence of the difficulty experienced in packing the rotor.

Material	Method of Analysis	FWHM / Hz	δ / ppm
Aluminium (Andrew[162])	Static Solid	9000	1650
	MAS NMR	700	1650
Aluminium Foil (At Aston)	MAS NMR	14500	1638
	SINNMR	483	1376
Li (3%) - Al Alloy (At Aston)	MAS NMR	14895	1390
	SIN NMR	352	1369

TABLE 10.2 Some ^{27}Al Knight shift results for various experiments.

In MAS NMR it is general practice to dilute metallic samples with gypsum[163] to a ratio of 1:5. This procedure was neglected for the MAS NMR experiments reported in table 10.2. The purpose of packing with gypsum is to reduce eddy current effects which can severely broaden a spectrum by causing inhomogeneity and decreasing spinning efficiency. The ^{27}Al MAS NMR Knight shift measured by Andrew[162] involved machining a rotor from the metal to ensure eddy current effects were kept to a minimum.

Investigation of the support medium liquors and solids (both obtained by gravity filtration) after each SINNMR experiment showed no Knight shifted aluminium resonances. In the few cases where a reaction had occurred, (which was apparent by the colour change of the support from a translucent straw colour to a deep brown or black), no Knight shifted resonances were detected from these liquors, but a ^{27}Al NMR signal with FWHM *ca.* 150 Hz could be detected at 4 ppm deshielded from the reference. This was thought to be from aluminium bromide which sublimed and condensed to produce ultrafine particles in the liquor. It is known that aluminium bromide is produced as a breakdown component of the

aluminium alkyls. If aluminium alkyls had been produced and detected by NMR, their chemical shift limits occur between 110 and 290 ppm[164] deshielded from the reference.

The Knight shifts obtained by MAS NMR and SINNMR do not correlate for the Al foil sample but do reasonably well for the Li (3%) - Al alloy. It is suggested that in the case of the SINNMR determined Knight shifts, their differences from the expected position of *ca.* 1600 ppm are due to varying amounts of iron impurities. It is known[165] that iron impurities can move the Knight shift upfield from its expected position by up to 400 ppm. The iron is introduced into the sample from the steel tools used to work the metal into fragments. This latter approach was used for all the SINNMR samples and Aston MAS NMR samples reported in table 10.2.

Another possible reason for the difference between the SINNMR and MAS NMR Knight shifts may have its origin in the pressure dependence of Knight shifts[28,166]. The interaction of phonons with Fermi electrons[166] might modify the observed Knight shift when a sample is irradiated with ultrasound. The phonon - Fermi electron interaction may reduce the Knight shift and cause differences between the values obtained from different SINNMR experiments (due to the ultrasonic absorption by different particle shapes).

10.3 SINNMR INVESTIGATIONS ON SINGLE CRYSTAL DOPED SILICON

The samples used in ^{29}Si experiments were obtained from silicon wafers which were 76.2 mm in diameter and 0.36 mm thick. The wafers were from a single crystal grown for integrated circuit manufacture and were of the N type, doped with 0.005ppm phosphorus. The wafers were ground in a pestle and mortar then graded using test sieves so only 1000 - 500μm particle sizes were used. The experiments were conducted in a PTFE sample tube with bromoform as the support liquid, using 1.0g of graded solid and 20 kHz ultrasound operating with 3μm horn tip displacement.

On only one occasion was a ^{29}Si SINNMR resonance recorded. This was due largely to 'pick-up' problems with the NMR spectrometer. It was found that NMR observation at the ^{29}Si frequency of 17.79 MHz, produced large spikes at 5 kHz intervals across the observation window. The magnitude of the spikes would vary and were present to the same extent with or without ultrasound, and whether the ultrasonic horn was present or not. Increasing the deadtime / delay time did not remove or reduce the 'pick-up'. A second reason for the observation of the ^{29}Si

Knight shift on only one occasion is the inadequate prepolarization time allowed for the material. When the material is placed in the NMR magnet spin states lose their degeneracy and achieve states by α and β (as ^{29}Si has I = 1/2). At this initial point in time the populations of the spin states are identical and a situation equivalent to saturation is apparent. It is therefore necessary to allow a time period for bulk magnetization to be established, ideally equal to $5.3T_1$, called the prepolarization time. It is thought, in hindsight, that for subsequent attempts to reproduce the ^{29}Si Knight shift, an inadequate prepolarization time was allowed for these experiments, whereas, an adequately long prepolarization time was fortuitously used for the initial experimental run.

The only resonance observed by ^{29}Si SINNMR was found at 239 ppm (deshielded relative to the tetramethylsilane external reference) with a FWHM of 32 Hz. As with the ^{27}Al static solid studies, the limits of the FX-90Q NMR spectrometer produced extensive baseline roll which prevented a quantitative analysis of the solid FWHM. There were no ^{29}Si resonances detected in the liquor or solid after the experiment.

Rahilly[167] investigated the ^{29}Si Knight shift in lithium doped single crystals of silicon and came to the conclusion that shifts were no larger than 10 ppm deshielded from TMS unless high concentrations of dopants are present. Similarly Sasaki *et al*[168] showed the ^{29}Si Knight shift of phosphorus doped silicon crystals even when doped to high concentration (0.68 ppm) gave shifts no larger than 80 - 90 ppm deshielded from TMS. It is, therefore, concluded that if the resonance reported here is genuine, there must be some perturbation of the Fermi electrons by ultrasound, to cause a larger deshielding of the ^{29}Si Knight shift than usually observed.

10.4 DISCUSSION

As the Knight shift is a characteristic of the metallic state, there can be few explanations for the observation of such shifted resonances.

The acoustically induced motion of metallic particles in a magnetic field introduces possible differences of the particle behaviour from the situation where non-metallic species are used. Small eddy currents could enhance the particle motion within the SINNMR experiment. Whenever a conductor moves within a magnetic field, EMFs are induced within in. These give rise to induced eddy currents which circulate within the body of the material. According to Lenz's law[169], if particles studied by SINNMR have induced eddy currents, there will be forces present

which would enhance the effect of incoherent motion by perturbation of an assembly of particles suspended at Dysthe equilibrium positions, and hence enhance the SINNMR experiment.

There is another consequence of eddy currents. As these currents follow low resistance paths they can reach high magnitudes and result in significant heating effects, sometimes great enough to melt the sample. Several factors rule this possibility out in the present work. First, the general appearance of the solid after sonication does not indicate any melting which would degrade the resin coating. Second, if the eddy currents were large enough to facilitate melting of the metal, the inhomogeneity of the NMR applied field would be so great that resonances of 500 Hz and less could not be resolved.

There is also the remote possibility that solid state line narrowing could be produced *via* the action of ultrasonic cavitation on the solid producing metal clusters. These clusters could become mobile and produce high resolution spectra due to averaging *via* Brownian motion. However, there are no Knight shifted resonances found in the liquor after SINNMR experiments on the aluminium alloy and, after successful experiments, the solid was recovered intact. Also, it must be realised, that small clusters do not have similar properties to the bulk metallic solid. If Knight shifted SINNMR spectra were produced through the production of clusters, it would be unlikely that MAS and SINNMR data would be in such agreement.

The internal rotation of species would be most unlikely within the metallic lattice. Additionally, if there had been any reaction, melting or particle breakdown, the results would have been clearly different; either the Knight shift would not be present, or Knight shifted species would have been detected in the liquor. It is important to note that the poor S/N produced by the ^{27}Al SINNMR Knight shifts shows there is much room for improvement of SINNMR. Although this observation may be due in part to a skin depth problem, the poor signal must also be due the use of non-optimum SINNMR conditions.

The specificity in origin of Knight shifts allows the SINNMR experimental results to be used to demonstrate definitively that solid state NMR broadening interactions can indeed be reduced by incoherent particle motion induced by ultrasound. There is, in addition, preliminary evidence that SINNMR line narrowing of a metallic sample, yields a Knight shifted resonance, which reflects the composition of that sample.

CHAPTER ELEVEN

SINNMR EXPERIMENTS ON OTHER SYSTEMS

N.b. A complete list of NMR acquisition parameters for each experiment described in this chapter can be found in Appendix Two.

11.1 SINNMR INVESTIGATIONS OF AMBERLITE

Amberlite MB-3 monobed resin is a mixture of Amberlite IR-120 and IRA-410. IR-120 is a polystyrene - divinylbenzene cross linked thermoset polymer with 8% cross linking and an active sulphite group. IRA-410 is identical to IR-120 except it has an active ammonium group. Amberlite MB-3 particles are essentially spherical with diameters between 0.3 and 1.2 mm and have varying densities between 0.9 and 1.2 gcm^{-3}.

All SINNMR experiments involving amberlite MB-3 used 1.0g of ungraded solid suspended in carbon tetrachloride (CCl_4) and irradiated using 20 kHz ultrasound with a 3μm horn tip displacement. The volume of support liquid was identical to all other 20 kHz experiments, outlined in section 6.4.2.

The SINNMR experiments enabled the study of ^1H and ^{13}C resonances, being conducted in PTFE and glass sample tubes respectively. The advantage of using CCl_4 as the support liquid is the ability to suppress the ^{13}C signal because of its long T_1 and the absence of ^1H resonances. The last point is not strictly true because of the presence of ethanol stabiliser, but it was found, that its low concentration did not complicate the ^1H SINNMR results. The density of CCl_4 of 1.59 gcm^{-3} falls conveniently close to the recommended optimum density of support required from the trisodium phosphate (TSP) data (chapter eight).

A static wetted (with CCl_4) solid spectrum and a ^1H SINNMR spectrum for Amberlite MB-3 are shown in figure 11.1.

The narrowing of three distinct regions of the solid spectrum is very apparent in figure 11.1(a). It is believed the three ^1H SINNMR regions correspond to the aromatic, vinylic and aliphatic protons of the resin. However, the ^{13}C SINNMR spectra showed at best modest averaging compared to the solid. Investigation of the liquor after SINNMR experiments showed no resonances which could be associated with the amberlite narrowing.

The interpretation of the results was complicated by the observation that it was possible to follow the SINNMR narrowed spectrum for some time after the end of a SINNMR experiment. Although this phenomenon appears similar to that observed in TSP, narrowing could be due to induced chain mobility caused by CCl_4 swelling the polymer matrix. Amberlite samples allowed to stand in CCl_4 did not show any narrowing unless the sample was simultaneously sonicated, which suggests, that if swelling occurred during the SINNMR experiment, it was ultrasonically induced.

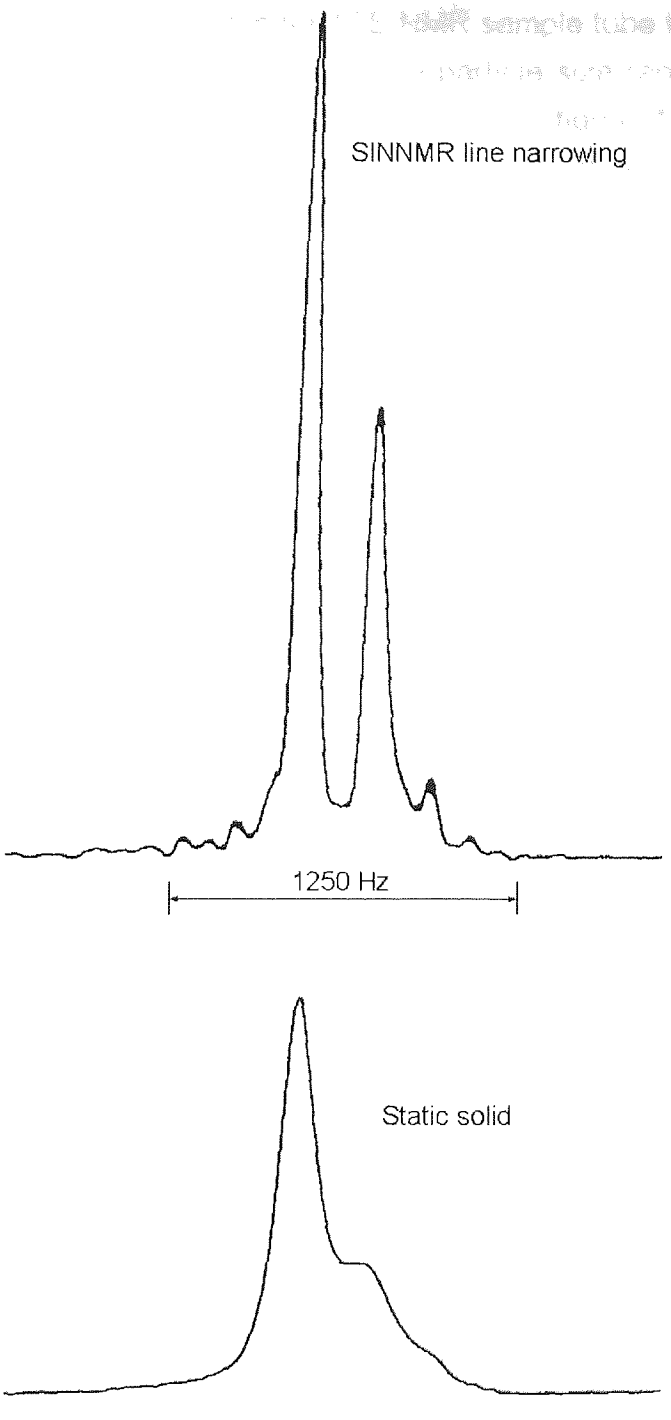

FIGURE 11.1. ^{1}H NMR spectra (89.56 MHz) of Amberlite showing narrowing from the static solid by 20 kHz SINNMR with 3μm tip displacement.

11.2 SINNMR INVESTIGATIONS ON SILYLATED COAL

A single sample of silylated coal with an estimated density of *ca.*1.30 gcm^{-3} was prepared for ^{29}Si SINNMR investigation. This sample density was used to estimate an optimum support liquid density of 1.895 gcm^{-3} *via* the TSP data in chapter eight. This corresponded to a 2.5:1 chloroform / bromoform mixture (v/v).

The experiment was accomplished in a PTFE NMR sample tube that was set up as for all 20 kHz experiments: 1.0g of solid with a particle size range of *ca.* 200 µm was used. The ^{29}Si SINNMR spectrum presented in figure 11.2 was acquired using gated decoupling (nOe suppressed) with 20 kHz ultrasound running with 3 µm tip displacement. As the nOe interaction of ^{1}H with ^{29}Si produces a decrease in intensity, gated decoupling was used. This enables spectra to be decoupled (in this case ^{1}H decoupled ^{29}Si) without enhancement by the nuclear Overhauser effect (nOe).

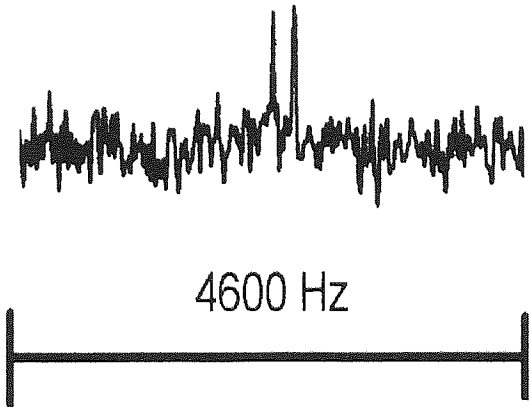

FIGURE 11.2. ^{29}Si SINNMR resonances obtained using gated decoupling and 20 kHz ultrasound (3µm tip displacement) for silylated coal.

The resulting ^{29}Si SINNMR spectrum shows two resonances at 16.5 and 7 ppm from external TMS. Analysis of the filtered liquor showed no ^{29}Si NMR resonances. A sample of silylated coal from the same production batch was analysed using ^{29}Si MAS NMR on a Brüker AC-300 spectrometer which detected ^{29}SI resonances at 19.8 ppm and 6.9 ppm.

There appears to be good correlation between MAS NMR and SINNMR. The possibility of solubility of silylated groups in the organic liquid medium does not appear to be justified. Unfortunately, due to instrumental difficulties with ^{29}Si observation (as outlined in chapter 10), this experiment has never been repeated and as a consequence it is unreasonable to draw firm conclusions from the results.

11.3 MATERIALS WHICH HAVE ELUDED SINNMR

Attempts to produce SINNMR line narrowing using 20 kHz ultrasound on many compounds did not produce any line narrowing. Some of the compounds for which it was not possible to produce narrowing are listed in table 11.1.

Compound and NMR Nuclei Investigated	Structure	Particle Size Range in form available
Aluminium Phosphate ^{27}Al , ^{31}P	Amorphous	< 35 μm
Lithium Sulphate Monohydrate ^{7}Li	Crystalline	0.2 to 1.5 mm
Potassium Hexafluorophosphate ^{31}P, ^{19}F	Crystalline	0.5 mm to 0.1 mm
Muscovite Mica ^{27}Al	Amorphous	> 2 mm to 0.2 mm
Sodium Oxalate ^{23}Na, ^{13}C	Polycrystalline	< 0.1 mm

TABLE 11.1. List of compounds investigated by SINNMR which have failed to show narrowing of resonances compared with the solid-state.

All 20 kHz experiments were conducted using identical conditions to those which produced the TSP, PTFE, Knight shift and Amberlite SINNMR spectra. Aluminium phosphate and other similar solids which were of the fine powdery type, tended to aggregate under sonication and clog the NMR sample tube, even when amounts as small as 0.1 g were used. Sodium oxalate can be readily recrystallised from the available fine powder to produce particles with dimensions in excess of 1 mm. However, the recrystallised sodium oxalate particles break up very easily in the 20 kHz sound field and as with the aluminium phosphate particles, they aggregate. The break-up of large particles to produce an aggregating mass was also found with muscovite mica.

The two crystalline samples investigated, potassium hexafluorophosphate and lithium sulphate produce a worrying result. The densities of these compounds, both *ca.* 2.0 gcm^{-3}, are not too high and enabled the prediction of an accessible optimum support liquid density for displacement to the NMR probe region. The reason for the absence of SINNMR line narrowing with these compounds remains a mystery.

Lithium sulphate monohydrate and potassium hexafluorophosphate have melting points far higher than TSP and therefore they can be considered to have greater lattice energies. Consequently, barriers to rotation will be larger than for TSP and sonication is insufficient to induce molecular rotation in these solids. Thus the production of sonically induced narrowing *via* lattice site mobility is inhibited and as a consequence, no narrowing is observed at all.

11.4 DISCUSSION

It appears that averaging by incoherent particle motion is again evident in the experiments involving silylated coal. The ^{29}Si SINNMR study of silylated coal gave no evidence of reaction or dissolution and produced two peaks which were in general agreement to those obtained by MAS NMR.

The production of SINNMR line narrowing by methods other than incoherent particle motion may take place in Amberlite MB-3 because narrowed resonances were obtained which decayed with time after the conclusion of the SINNMR experiment. Such observations together with the indications that SINNMR can be difficult to achieve with other materials, (especially by those which are not too dissimilar to TSP), could throw some doubt on the value of the technique. However, in the defence of SINNMR, it must be pointed out that, at present, SINNMR is a very complicated technique and its basis requires even more thorough investigation than reported in this thesis.

Problems occurring from particle break-up and aggregation are discussed further in chapter twelve where SINNMR takes a new dimension by the application of high frequency ultrasound.

CHAPTER TWELVE

PRELIMINARY SINNMR STUDIES USING HIGH FREQUENCY ULTRASOUND

N.b. A complete list of NMR acquisition parameters for each experiment described in this chapter can be found in Appendix Two.

12.1 INTRODUCTION

The application of SINNMR using high frequency ultrasound was stimulated by the implications of the 20 kHz ultrasound experiments involving TSP, and the difficulty in obtaining results with very small particle sizes. If the proposed mechanism for incoherent motion *via* particle interaction with bubble cavities is correct, it will be necessary to produce smaller resonant cavities to induce incoherent motion in smaller particles. The production of smaller resonant cavities is possible using higher frequency ultrasound.

Equation 4.16 for the resonant cavitation bubble radius can be used to produce data as in table 12.1 which show the approximate frequencies required to produce particular bubble radii.

Bubble Radius / μm	Required Frequency
90	21 kHz
80	23 kHz
70	27 kHz
60	31 kHz
50	37 kHz
40	47 kHz
30	62 kHz
20	94 kHz
10	187 kHz
1	1.9 MHz
0.5	3.7 MHz
0.2	9.4 MHz
0.1	18.7 MHz

TABLE 12.1. The required ultrasound frequency to produce selected cavitation bubble radii under isothermal conditions in a support liquid with a nominal density of 2.20 gcm^{-3}.

Table 12.1 suggests that the problems previously encountered with SINNMR in application to powders could be resolved by increasing the frequency of applied ultrasound. The samples which gave negative results with 20 kHz ultrasound mainly had particle sizes below 35μm. Such particles require an ultrasound frequency of at least 60 kHz for interaction with cavitation micro-jets.

The problem with using such small particles, as evident through the 20 kHz investigations, is that ultrasound generally aggregates the particles. Initial

investigations were undertaken therefore using a bromoform support mixture with a stabilising surfactant on a variety of readily available materials with 1 and 2 MHz ultrasound. Using the glass rod set-up (described in chapter 6.4.3) visual observations on certain systems were made and are recorded in table 12.2.

The compostion of the samples, unless otherwise stated, used throughout the high frequency investigations were 0.5 g of finely ground solid, 5 ml of bromoform and 0.5 ml of octan-1-ol surfactant. The solid was always ground in the presence of an 'inert' lubricant such as ethanol or acetone. Samples ground in octan-1-ol did not show any extra stability over the normally ground samples. Once the samples were prepared, they were placed in a 20 kHz ultrasonic bath for 30 minutes to ensure thorough mixing and dispersion before the application of high frequency ultrasound.

Compound	Observations	
	1 MHz Ultrasound	2 MHz Ultrasound
Lithium Phosphate	Coagulation with restricted motion at powers beyond 10 W	Coagulation with restricted motion at powers beyond 10 W
Sodium Phosphate Anhydrous	As Lithium Phosphate but coagulation not as extensive	As Lithium Phosphate but coagulation not as extensive
Lithium Iodide	Immediately fused below the transducer	Immediately fused below the transducer
Silicon Oxide	Produces a very fine suspension at all powers.	Produces a very fine suspension at all powers.
Sodium, Boron, Aluminium Glass	Produces a very fine suspension at all powers.	Produces a very fine suspension at all powers.
Aluminium Phosphate	Extensive coagulation at all powers.	Extensive coagulation at all powers.

TABLE 12.2. Visual observations using high frequency ultrasound on different compounds.

On the basis of the information in table 11.2, it was decided to study silicon dioxide and the sodium-boron-aluminium glasses. It was found that for these systems, the fine suspensions produced were stable for at least 1 hour.

The problem with finely grinding materials is knowing what particle size limits are present within such powders. It has been stated[170] that stable colloidal suspensions produced are expected to have a maximum particle size of *ca.* 10 μm and a minimum just below 1 μm. Using these suspensions creates the problem that gravity filtration is insufficient to remove all particulates from SINNMR samples after each experiment. It was common practice to analyse the liquor after each SINNMR experiment by NMR to see whether any narrowed resonances were present. Particles present in the liquor would complicate the analysis of the support media for evidence of reaction or solvation after SINNMR experiments. Consequently, two other techniques were employed to remove the particles as gravity filtration was not reliable. First, centrifugation at 5000 revolutions per second was used. This produces the equivalent force of *ca.* 250 g and is only sufficient to force the sedimentation of particles down to *ca.* 5 μm. The second, and preferred technique, was microfiltration, using micropore filter units with pore sizes down to 0.2 μm. The support media used, being organic in origin, necessitated the use of PTFE micro-filter membranes.

Due to the small particle sizes present in the colloidal suspensions prepared for SINNMR investigations, it was expected, that there would be a contribution to line narrowing due to Brownian motion not unlike that described by UFP NMR and related techniques. The extent of SINNMR line narrowing would therefore be shown as a reduction in the line width from the Brownian averaged line. Glasstone[171] states that relatively large suspended particles show a rotational, in addition to a translational, Brownian movement. This indicates that Brownian motional averaging will in the main be due to the larger of the small particles in a distribution producing a colloidal suspension.

12.2 HIGH FREQUENCY SINNMR INVESTIGATIONS OF SILICON DIOXIDE

The SINNMR experiments on SiO_2 with high frequency transducers at the end of a glass rod set up involved the use of fused silica powder with the ^{29}Si nucleus being investigated. The ^{29}Si MAS NMR spectrum of the material showed a single resonance at 107 ppm (shielded from TMS external reference) with a FWHM of *ca.* 92 Hz. A ^{29}Si SINNMR spectrum for silicon dioxide is shown in figure 12.1 and selected results for the ^{29}Si colloidal suspension and SINNMR spectra are shown in table 12.3. Microfiltration of the suspension after SINNMR experiments yielded the liquor from which no ^{29}Si resonances were detected.

The FWHM and chemical shift were observed for each colloidal sample before SINNMR because it was feared that sample preparation (involving sonication) would alter the observed values. It is suggested that for this reason, the observed

FWHM was found to vary for each SINNMR experiment. SINNMR does produce narrowing in addition to Brownian motion for 2MHz ultrasound applied with 10 W power.

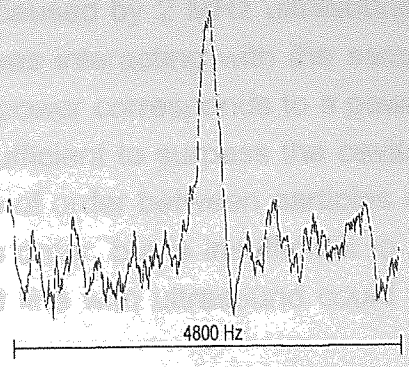

FIGURE 12.1. ^{29}Si SINNMR spectrum of silicon dioxide obtained with 2 MHz ultrasound at 10 W power.

The narrowing observed is of the order of 10 to 15 % in relation to the colloidal sample. There is a chemical shift difference between the colloidal suspension and SINNMR experiments, however, according to the digital resolution, the difference is only one or two data points and may be insignificant. However, the chemical shift difference between the observed ^{29}Si MAS NMR and those in table 11.3 is most likely due to a susceptibility shift difference as both samples used an external reference sample.

SINNMR Conditions	Colloidal Suspension FWHM / Hz	Colloidal Suspension δ / ppm	SINNMR FWHM / Hz	SINNMR δ / ppm
2 MHz US @ 10 W	286	-116.1	242	-116.9
2 MHz US @ 10 W	330	-116.1	293	-116.5
2 MHz US @ 5 W	300	-116.1	367	-115.7
1 MHz US @ 10 W	300	-116.1	330	-116.9
1 MHz US @ 5 W	340	-116.1	360	-116.5

TABLE 12.3. FWHM and chemical shift values (all relative and shielded to TMS) for the ^{29}Si NMR observation of SiO_2 in colloidal suspension and SINNMR experiments. The digital resolution in all experiments is 7.33 Hz (0.4 ppm).

It is surprising that 2 MHz ultrasound with 5 W power and all the 1 MHz experiments produced a broadening of the line compared to that obtained by Brownian averaging. The inability of 1 MHz ultrasound to produce narrowing could have been due to the extremely small particle size range of the sample. However, the broadening caused by 2 MHz ultrasound with 5 W power suggests that although ultrasound was interacting with the sample, incoherent motion was not being produced. This power corresponds to a power density of *ca.* 6.4 Wcm^{-2} and may not have been sufficient to surpass the cavitation threshold. Within the suspension, a high degree of order between particles could exist. If ultrasound is applied which disrupts this order, but is insufficient to produce incoherent particle motion, then the observed line with ultrasound could indeed be broader than for the suspension.

12.3 HIGH FREQUENCY SINNMR INVESTIGATIONS INTO GLASSES

Two specially prepared glasses, both containing sodium oxide, boron oxide and aluminium oxide were used for high acoustic frequency SINNMR investigations. The first sample was Na_2O-B_2O_3-Al_2O_3 with a nominal composition of 15/70/15 mole-% and the second being 20/70/10 mole-%. The glasses were kindly supplied by Dr. C. Jäger, Max-Planck-Institut für Polymerforschung. The 20/70/10 sample has only tetrahedral aluminium sites and BO_3 and BO_4 sites in the ratio of 80:20. The 15/70/10 sample contains 4, 5 and 6 coordinated aluminium with most of the boron in BO_3 sites.

It was initially attempted to grind these samples and react them with a silylating agent to coat the surface to inhibit aggregation. The silylating method (using a siloxane) required acid catalysis which unfortunately was found to attack the glass samples rendering them soluble. Thus all experiments were conducted with samples prepared identically to those experiments in which silicon dioxide was studied. All investigations by NMR were of the ^{27}Al and ^{11}B nuclei. As with SiO_2, microfiltration of the colloidal suspension after SINNMR experiments yielded the translucent liquor which showed no ^{27}Al or ^{11}B resonances.

Selected results for the ^{27}Al and ^{11}B colloidal suspension and SINNMR spectra for the 20/70/10 glass are shown in table 12.4. All ^{11}B experiments were conducted using a PTFE sample tube with the high frequency (glass rod) experimental setup. All ^{27}Al experiments used the purpose built high frequency unit in a glass tube.

The narrowing of the ^{11}B resonance appears to be much more dramatic than that observed for the ^{27}Al resonance. The reason for this does not appear to be clear.

There could be three explanations for the difference in the narrowing of the ^{11}B and ^{27}Al SINNMR glass spectra.

SINNMR Conditions	Colloidal Suspension (^{11}B / ^{27}Al) FWHM / Hz	^{11}B SINNMR FWHM / Hz	^{27}Al SINNMR FWHM / Hz
2 MHz @ 7 W	254 / 7700	293	5960
3 MHz @ 6 W	261 / 7700	88	6356
5 MHz @ 5 W	254 / 7700	87	not measured
5 MHz @ 10 W	254 / 7700	73	6300
6 MHz @ 10 W *	254/ 7700	95	not measured

TABLE 12.4. FWHM for the ^{11}B and ^{27}Al NMR observation of 20/70/10 glass in colloidal suspension and SINNMR experiments.

First, the correlation time for the ^{27}Al species may be much longer than for the ^{11}B species. Second, and related to the previous point, the chemical shift anisotropy for the ^{27}Al site could be much greater than that observed for the ^{11}B site. Third, the FWHM of the static solid ^{27}Al resonance could be much broader than for the ^{11}B resonance. The high-frequency SINNMR experiment may produce sufficient particle averaging to reduce a relatively short ^{11}B correlation time but not a relatively long ^{27}Al correlation time. The argument of producing sufficient averaging to affect ^{11}B to a greater extent than the much larger ^{27}Al interactions also applies to chemical shift anisotropy and FWHM.

The ^{11}B SINNMR resonance was obtained for the 15/70/15 sample, with maximum narrowing to 102 Hz being achieved with 5 MHz ultrasound with 7 W power. ^{11}B MAS NMR and SINNMR spectra of the 15/70/15 glass are shown in figure 12.2.

All of the 20/70/10 glass spectra produced, either from colloidal suspension or SINNMR possess a narrowed resonance sitting on a broad hump. Although this glass has boron in two sites, two distinct narrow resonances were not observed. An example of a 20/70/10 sample SINNMR spectrum is shown in figure 12.3.

It is proposed that the broad hump evident in figure 12.3 is the signal from the BO_3 site and the narrow resonance from the BO_4 site. This is concluded because the ratio of BO_3 to BO_4 obtained by ^{11}B MAS NMR experiments is 80:20 in the 20/70/10 glass sample, which appears to be reflected in the intensities in figure 12.3. In contrast, the 15/70/15 glass sample produces a single sharp resonance and contains only the BO_3 site. It is unclear why the BO_3 site is averaged by

SINNMR in the 15/70/15 glass sample, but remains broad in the 20/70/10 glass sample. It can only be concluded that the broadening interactions acting on the ^{11}B nucleus in BO_3 sites are greater in the 20/70/10 sample compared to the 15/70/15 sample.

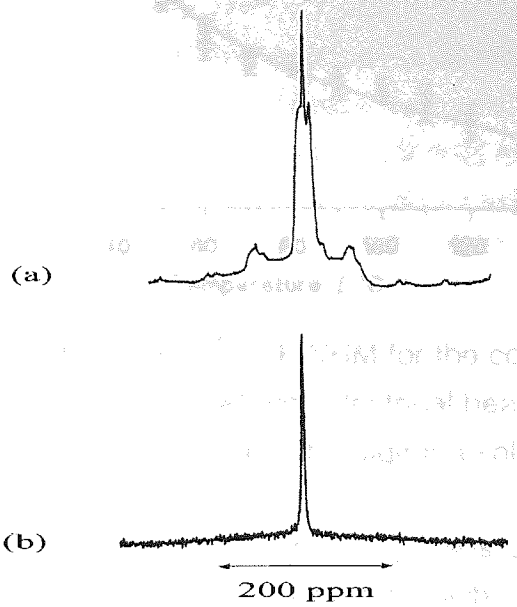

FIGURE 12.2. ^{11}B NMR spectra of a $Na_2O/B_2O_3/Al_2O_3$ (15/70/15 mole %) glass with a density of 2.15 gcm^{-3}: (a) 96.3 MHz MAS NMR spectrum and (b) 28.75 MHz SINNMR resonance with FWHM 88 Hz in a suspension of bromoform with 2 MHz ultrasound from a PZT-5A transducer running at 10 W.

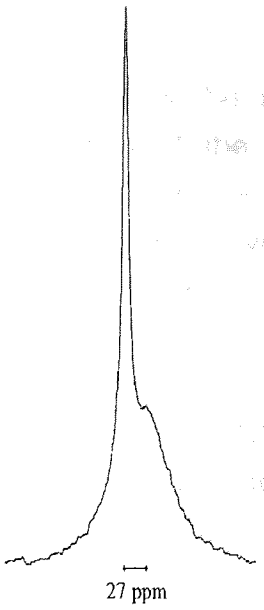

FIGURE 12.3. ^{11}B SINNMR spectrum (28.75 MHz) of a $Na_2O/B_2O_3/Al_2O_3$ (20/70/10 mole %) glass from a suspension of bromoform irradiated with 2 MHz ultrasound at 10 W.

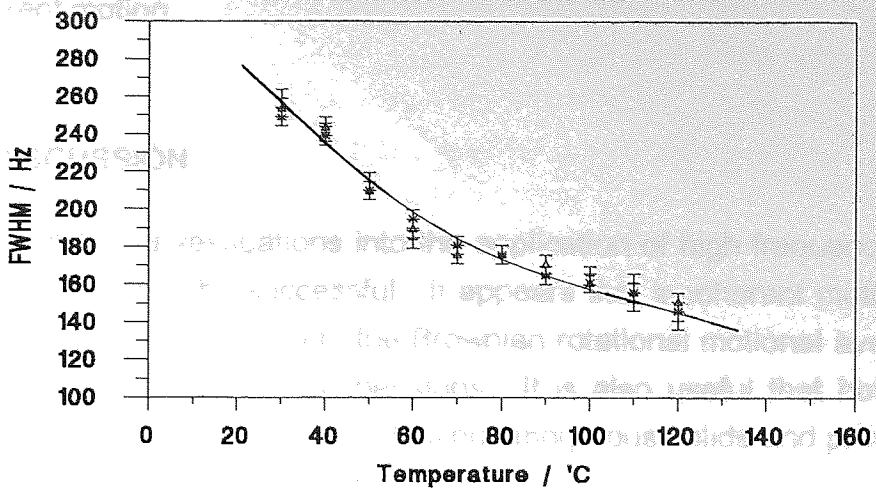

FIGURE 12.4. Variation in the ^{11}B FWHM for the colloidal suspension of $Na_2O/B_2O_3/Al_2O_3$ (20/70/10 mole %) with electrical heating of the sample. The y axis error bars reflect the digital resolution.

The narrowing of the ^{11}B resonance in these glasses could be attributed to the temperature rise during the SINNMR experiment which could cause more efficient Brownian averaging. To test this hypothesis, the ^{11}B colloidal NMR spectrum was followed with increasing temperature. The result of the change in FWHM with temperature is shown in figure 12.4. The rate of Brownian motion is directly affected by the diffusion coefficient D for a fluid given by:

$$D = \frac{k_b T}{6\pi\eta r} \qquad \text{- (12.1)}$$

Here, k_b is the Boltzmann constant, T is the absolute temperature, η is the viscosity of the fluid and r the radius of the molecule diffusing. Thus, as temperature increases, D increases and so does the rate of Brownian motion. Although the diffusion coefficent is primarily involved with translational motion, Glasstone[171] states that rotational Brownian effects can be quantitatively defined from analogous equations to those derived for translational Brownian movement. It is the rotational Brownian motion which will lead to the averaging of NMR broadening interactions. From figure 12.4 it can be projected that a temperature in excess of *ca.* 200°C are required to produce the equivalent FWHM to that obtained from optimum ^{11}B SINNMR narrowing of the 20/70/10 glass. Such a temperature is unlikely to be achieved during the course of the experiment for various reasons, the most important being the boiling point of the support medium which was found by fractional distillation to be *ca.* 150°C. Obviously the support medium would be vapourized before a line width approaching that obtained by SINNMR could be achieved. The only possibility for producing

narrowing is by interaction of the ultrasound with the particles producing incoherent motion.

12.4 DISCUSSION

The preliminary investigations into the application of high frequency ultrasound in SINNMR appear to be successful. It appears that incoherent motional averaging can be achieved in addition to the Brownian rotational motional averaging already present in stable colloidal suspensions. It is also useful that both examples of SINNMR narrowing were obtained using amorphous solids and proves SINNMR is not restricted to crystalline solids.

The modest narrowing in the ^{27}Al SINNMR and the inability to completely resolve the two boron sites in the 20/70/10 glass indicate that averaging in both the colloidal suspension and SINNMR systems is not complete and selective towards a singular boron site. Reasons for this selectivity are not clear. This implies there is much still to be investigated through the use of high frequency ultrasound.

CHAPTER THIRTEEN

INVESTIGATIONS INTO OTHER SINNMR SYSTEM CONFIGURATIONS

13.1 INTRODUCTION

This chapter contains a brief summary of other experimental configurations investigated for the application of ultrasound to NMR. Each system listed either did not work or was not able to be applied for the reasons given. This is not to say that these systems could not be modified and re-applied to SINNMR.

13.2 THE SIDE TRANSDUCER

The side transducer involved mounting a 5mm diameter PZT-5A transducer at a point down the NMR sample tube with its oscillating faces perpendicular to the applied field. It was intended for use with the 20 kHz ultrasound horn so a combined and addititve effect could be utilized.

The prototype unit is shown in figure 13.1 and involved a soldered transducer being held in place by PTFE rings.

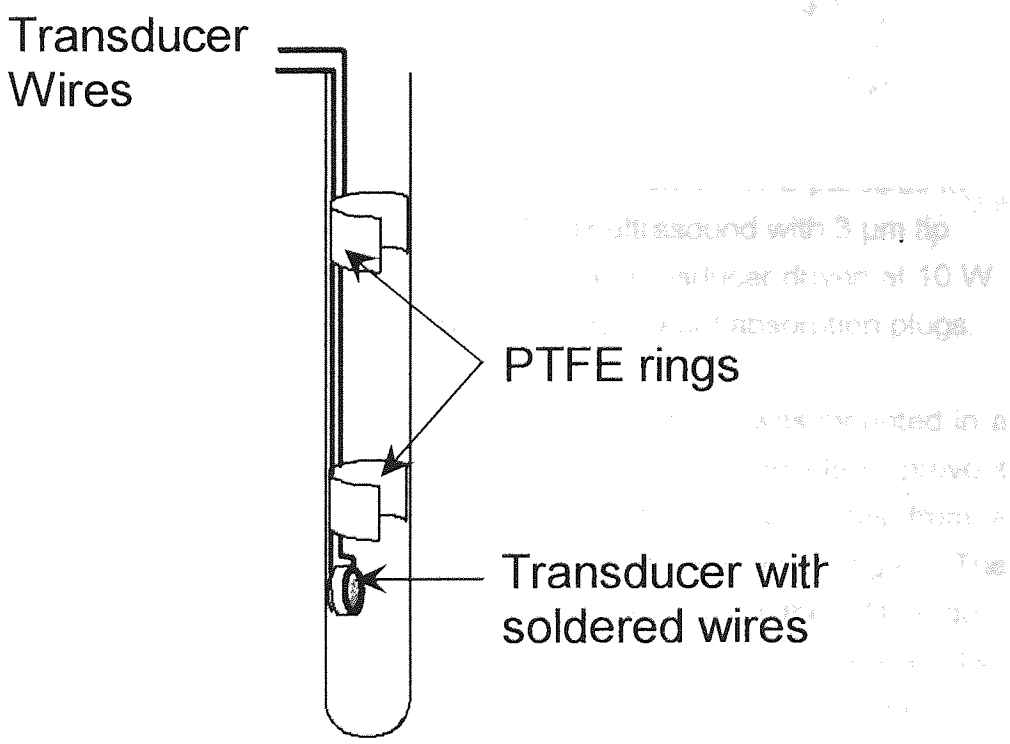

FIGURE 13.1. Prototype side transducer unit within a 10 mm o.d. glass NMR sample tube.

Experiments using 1mm square PTFE particles suspended in bromoform produced some interesting qualitative results obtained by visual inspection. The 20 kHz ultrasound was set to give 3 μm tip displacement and a 2 MHz side transducer driven by 5 W. The observations are shown diagramatically in figure 13.2.

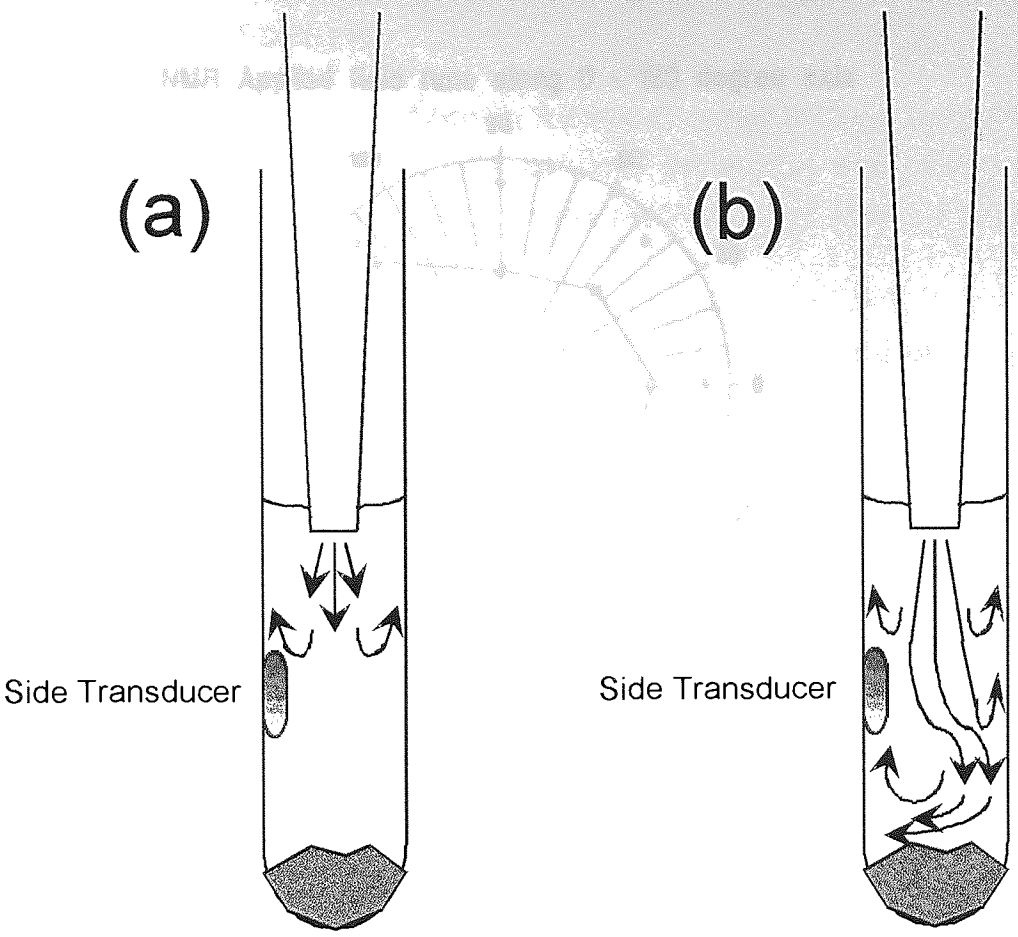

FIGURE 13.2. The observed manipulation of 1 mm square PTFE particles in bromoform under (a) the action of only the 20 kHz ultrasound with 3 μm tip displacement and (b) with the addition of a 2 MHz side transducer driven at 10 W. The shaded areas in the bottom of the tubes are cotton wool absorption plugs.

After the success of the observations, a 2 MHz side transducer was mounted in a specially prepared PVC NMR sample tube with the wires glued inside to prevent ringing. Ringing is the unwanted pick-up by the NMR receiver coils from a conductor placed within the magnetic field with insufficient anchorage. The spurious ringing signals produced can be large enough to obscure the FID. Figure 6.1 in the experimental section shows the NMR probe assembly. There are two detector coils, one wound around the probe and the other of the saddle variety in which the coils are wound parallel with the applied field. The effect of the transducer on the NMR detector probe region was ascertained by measurement of the ^{1}H NMR signal intensity of water within the tube. The transducer was rotated to be in different orientations with respect to the saddles: 2 MHz ultrasound at 5W was delivered to a water sample. The results are shown in figure 13.3.

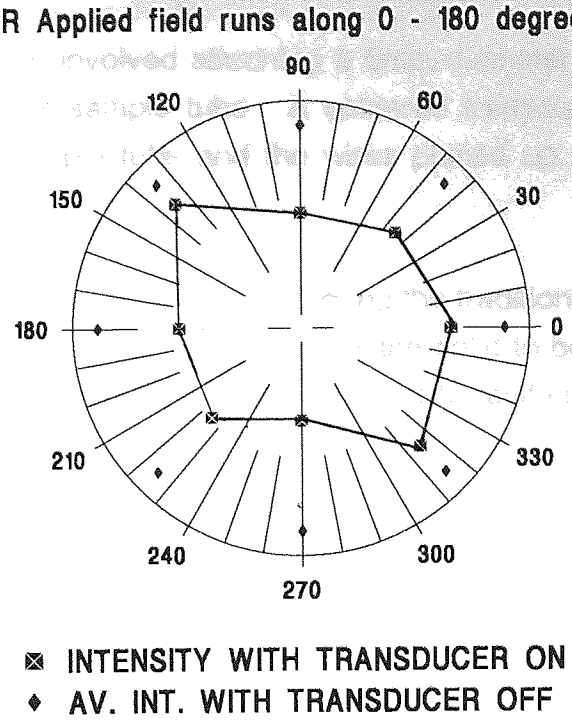

FIGURE 13.3. Variation in intensity of ^{1}H NMR signal from water with orientation of a side transducer at the NMR probe region depth. The intensity scale is in arbitrary units.

The intensity was at the highest when the transducer was at 315 or 135^{o} to the applied field direction, although all intensities were reduced compared to when the ultrasound is switch off.

The intention was to use the unit for SINNMR experiments on PTFE particles in bromoform. The unit suffered irreparable damage at a point opposite and just above the side transducer after only 2 minutes operation. It is thought the hole produced was due to a contribution of sound wave intensity from both the 20 kHz and 2 MHz transducers. Excessive heating could not have caused the hole because heating is at its greatest at the coupling surface and the hole would have appeared next to the 20 kHz horn tip or the 2 MHz transducer and did not occur near the transducer wires.

Although no attempt was made to produce a new unit it is felt that further investigations into multiple transducer units could be utilised in the future of SINNMR. Such a unit as the one described above could be rebuilt, but using a more durable polymer such as polyetheretherketone (PEEK) or polyamide / imide (Torlon®).

13.3 BOTTOM TRANSDUCER

The bottom transducer involved attaching a 5mm diameter PZT-5A transducer to the bottom of an NMR sample tube. A soldered transducer was placed in the bottom of an NMR sample tube and the wires placed up the inside and held in place by PTFE rings.

This configuration has the advantage of turning the traditional SINNMR experiment through 180^{o}. Experiments would now allow the solid to be more dense than the support liquid and the ultrasound could be used to levitate the solid sample into the NMR detector coil region.

All experiments involving this unit produced large noise spikes on the NMR spectrum which suppressed and in many cases obscured a NMR signals. This was due to 'ringing' of the transducer wires which pass through the NMR detector coil region. Attempts to fix the wires by gluing or PTFE rings did not curb the ringing. It is for this reason that this unit could not be applied to SINNMR.

The ideal unit based on this design is to have the transducer wires trailing down from the bottom of the NMR sample tube and thus not entering the NMR probe region. This configuration is very difficult to achieve with the iron magnet system of the FX-90Q. It could only be possible by passing the transducer wires through the VT inlet holes of the probe and out through the VT air in pipe in the probe permabody (see figure 6.1 in section 6.1.2). However, the configuration is entirely possible in a superconducting magnet system.

CHAPTER FOURTEEN

CONCLUSIONS AND SUGGESTIONS FOR FUTURE WORK

14.1 CONCLUSIONS

The objectives of the research outlined within this thesis are to expand upon the initial observations of the sonically induced narrowing of the NMR spectra of solids (SINNMR) as reported in 1991 by Homer *et al*[1]. The study of SINNMR over the last three years has produced an invaluable contribution and insight into this novel technique.

The investigation of trisodium phosphate (TSP) by 20 kHz ultrasound SINNMR has shown that experimental conditions can be optimised by careful choice of physical parameters. These parameters include the mass and particle size distribution of the solid under investigation, and the density difference between the solid and support liquid. Further studies using TSP have also proved that solid state line narrowing is achieved by incoherent particle motion in addition to ultrasonic induced lattice motion. It has been estimated experimentally that the correlation time for incoherent motion of TSP particles within a SINNMR experiment is *ca.* 4 x 10^{-7} s.

Visual observations in conjunction with SINNMR experimental data for TSP have enabled a greater understanding of the optimisation of experiments. It has been shown that Dysthe's theory of particle displacements using ultrasound can be applied to 20 kHz ultrasound SINNMR experiments. Data have also been interpreted to suggest that incoherent motion is facilitated *via* micro-jet interactions for particles larger than 500 μm. There is also evidence that indicates that the present efficiency of SINNMR is such that only between 2 to 13 % of the total sample is subject to line narrowing.

The ^{27}Al SINNMR line narrowing achieved with aluminium and its alloys enabled the detection of the characteristic Knight shift. The observation of these shifts which are due to the metallic nature of these materials indicates a definitive proof for SINNMR line narrowing by incoherent particle motion. The resultant ^{27}Al SINNMR spectra contained resonances with frequency widths at half maximum height (FWHM) between *ca.* 350 and 500 Hz. This resolution enabled the measurement of individual Knight shifts for each alloy investigated.

Further examples of SINNMR line narrowing are reported for polytetrafluoroethylene (PTFE), amberlite, silylated coal and silicon. In each of these systems there may be an alternative mechanism rather than incoherent particle motion that results in line narrowing.

In order to obtain SINNMR spectra from particles having maximum dimensions below 100 μm, initial investigations have proved the necessity of increasing the frequency of ultrasound above the 20 kHz that was initially used. It has been shown that high-frequency SINNMR experiments require the solid to be in a (relatively) stable inert colloidal suspension with a suitable support liquid. High-frequency SINNMR line narrowing has been reported for stable suspensions of silicon dioxide and some sodium-boron-aluminium glasses. High-frequency sonication of these colloidal suspensions have been shown to produce SINNMR narrowed lines in which the averaging is greater than that achievable from Brownian motion, even at high temperature.

The weight of evidence presently to hand strongly suggests that those spectra purported to arise from the SINNMR technique may be interpreted to indicate that they do have their origin in ultrasonically induced effects. In some materials effectively free rotation of species in the solid lattice may be induced by ultrasound. However, the evidence suggests strongly that sonically induced incoherent rotational motion of solids provide the major mechanism for line narrowing. An initial understanding of the relationships between particle size, support liquid density, ultrasound frequency, cavitation microjets and induced incoherent particle motion can enable a more precise planning of SINNMR experiments in the future.

Undoubtedly SINNMR is still in its infancy, but shows sufficient promise to warrant undertaking the considerable further work needed to optimise the technique for general use. The complexity of the results and discussions presented in this thesis indicate that what can be described as a simplistic technique, can in practice produce in some respects quite baffling, yet interesting results. It is hoped that the work described in this thesis can at least make those who may originally have been sceptical aware of the complications produced by the marriage of ultrasound and NMR spectroscopy. There are many parameters to be considered and it is felt by the author that only the surface of the study of these has been scratched during the last three years.

14.2 FUTURE WORK

The future work described within this section has been broken down into two sub-sections. First, further studies using the ultrasound and samples described in this thesis. Second, the description of novel experiments which mainly involve new experimental set-ups not described within this thesis.

14.2.1 Further Studies from experiments described in this thesis

There appear to be certain areas of the 20 kHz SINNMR study which could benefit from further investigation. Although several possible mechanisms for the averaging of TSP particles smaller than 500 μm were proposed in chapter eight, further investigations are needed to ascertain whether one or a combination of these mechanisms dominate the incoherent motion of these particles. Extensive T_1 measurements for these smaller particle sizes could yield the correlation time which can be used to see if these experimental observations can fit the theory for one or more of the proposed mechanisms.

Experiments reported in chapter seven also showed that 20 kHz ultrasound SINNMR reduces the overall sample particle size. It could be useful to ascertain how the particle size range is altered for different compounds when subject to identical experimental conditions of irradiation by 20 kHz ultrasound. Each compound studied should be graded so that the initial particle size limits are the same, and are irradiated in support media with 20 kHz ultrasound of constant power for an equal length of time. The support media densities should be chosen such that the density difference (between support and solid) is constant for all compounds. This ensures that all particles will be displaced an equal distance from the ultrasonic horn. It is quite possible that this could lead to an explanation for the limited success of 20 kHz SINNMR with some of compounds.

Other experiments to be included in the further investigations of the SINNMR technique should involve attempts to observe the high frequency ultrasound SINNMR spectra of all the samples previously investigated with 20 kHz ultrasound. It should be important to ascertain whether the SINNMR spectra produced are identical or different. This could produce further information about the possibility of sonically induced narrowing by mechanisms other than incoherent particle motion.

The experiments using high frequency ultrasound on silicon dioxide and the sodium, boron, aluminium oxide glasses need to be further investigated. Further investigations are necessary to obtain more knowledge about the required optimum frequency of ultrasound and ultrasonic power. The line narrowing by Brownian motion and additional narrowing by sonication can be quantitatively assessed by the measurement of spin-lattice relaxation times. In view of the fact that the sodium-boron-aluminium glass samples contain only quadrupolar nuclei, spin-lattice relaxation results would be easier to interpret by studying the ^{29}Si resonance in silicon dioxide.

It is also considered important to pursue the possibility of a side transducer mounting in addition to the ultrasound administered from above the sample. The experiments reported in this thesis show that NMR signals can still be detected whilst a transducer is oscillating next to the NMR probe coils.

14.2.2 Proposed Novel SINNMR Experiments

It must be appreciated that certain areas covered in this sub-section are currently being investigated by other members of the SINNMR research group.

The application of high frequency ultrasound by PZT-5A disc transducers produces a wide band of frequencies which is dictated by the quality factor Q which is *ca.* 75. A 1 MHz PZT-5A transducer will produce a frequency spread at half the r.m.s maximum amplitude output of *ca.* 13000 Hz. If a 1 MHz PZT-4 transducer, which has a Q of *ca.* 500, is used; the frequency spread is only 2000 Hz at half r.m.s maximum amplitude. This can produce a more intense ultrasonic wave for an identical driving power compared to PZT-5A which was used for all investigations reported in this thesis. It has therefore, been recommended that high frequency SINNMR investigations use a PZT-4 rather than a PZT-5A transducer.

Transducers are also available as a focusing bowl rather than a disc. It is recommended that SINNMR studies using a focusing bowl could produce the required perturbations discussed in the conclusions. This is due to the ultrasonic waves no longer being parallel but converging to a point. Other methods which produce similar effects of focusing plane ultrasonic waves involve lenses of Plexiglas[172] or using reflecting surfaces[123,124].

SINNMR has only been involved with ultrasound produced by piezoelectric transducers. It is proposed here that the use of mechanical transducers could also facilitate incoherent particle motion in one of two ways. The use of a Galton whistle or Hartmann generator, as discussed in section 4.2.5, placed in a modified NMR sample tube would produce ultrasound around 20 kHz which would perturb a suspension of particles. A continuous loop of support liquid and suspended solid would be circulated through the whistle. Unfortunately, such a method would require a wide bore superconducting NMR magnet because of the equipment required to pump the support liquid through the whistle.

REFERENCES

1. J. Homer, P.McKeown, W.R. McWhinnie, S.U. Patel and G.J. Tilstone, 'Sonically Induced Narrowing of Solid-state Nuclear Magnetic Resonance Spectra: A Possible Alternative to Magic Angle Spinning Nuclear Magnetic Resonance', J. Chem. Soc., Faraday Trans., 1991, **87**, 2253.

2. E.R. Andrew, A. Bradbury and R.G. Eades, 'Nuclear Magnetic Resonance Spectra from a Crystal rotated at High Speed', Nature, 1958, **182**, 1659.

3. K.T. Mueller, B.Q. Sun, G.C. Chingas, J.W. Zwanziger, T. Terao and A. Pines, 'Dynamic-Angle Spinning of Quadrupolar Nuclei', J. Magn. Reson, 1990, **86**, 470.

4. A. Samosen, E. Lippmaa and A. Pines, 'High resolution solid state NMR. Averaging of the second order effects by means of a double rotor.', Mol. Phys., 1988, **65**, 1013.

5. McGraw-Hill Dictionary of Physics and Mathematics, 2nd Ed., Ed. D.N. Lapedes, McGraw-Hill, New York, 1978.

6. S. Tolansky, High Resolution Spectroscopy, Methuen, London, 1947.

7. W. Pauli, 'Zuschriften und varläufige Mitteilungen', Naturwisschaften, 1924, **12**, 741.

8. F. Bloch, W.W. Hansen and M. Packard, 'The Nuclear Induction Experiment', Phys. Rev., 1946, **69**, 127.

9. E.M. Purcell, H.C. Torrey and R.V. Pound, 'Resonance Absorption by Nuclear Magnetic Moments in a Solid', Phys. Rev., 1946, **69**, 37.

10. R.R. Ernst, 'Sensitivity Enhancement in Magnetic Resonance', Adv. Mag. Reson., 1966, **2**, 1.

11. M.P. Klein and G.W. Barton, 'Enhancement of signal-tonoise ratio by continuous Averaging: Application to magnetic resonance', Rev. Sci. Instrum., 1963, **34**, 754.

P. Laszio and P.R. Schleyer, 'Ring size effect on cis-olefinic coupling constants of cycloalkanes. Use of ^{13}C patterns', J. Am. Chem. Soc., 1963, **85**, 2017.

L.C. Allen and L.F. Johnson, 'Chemical applications of sensitivity enhancement in nuclear magnetic resonance and electron spin resonance', J. Am. Chem. Soc., 1963, **85**, 2668.

O. Jardetsky, N.G. Wade and J.J. Fisher, 'Proton magnetic resonance investigations of enzyme -coenzyme complexes', Nature, 1963, **197**, 183.

R.R. Ernst, 'Sensitivity Enhancement in Magnetic Resonance I. Analysis of the Method of Time Averaging', Rev. Sci. Instrum., 1965, **36**, 1689.

12. J. Jeener, Ampère Summer School, Basko Polje, Yugoslavia, 1971. - cited in R.R. Ernst, G. Bodenhausen and A. Wokaun, 'Principles of Nuclear Magnetic Resonance in One and Two Dimensions' - Ch. 1, pg. 6, 1990, Oxford Univ. Press, Oxford.

for general introduction: D.D. Traficante, 'The Nature of the Second Dimention in 2D NMR', Concepts Magn. Reson., 1989, **1**, 7.

13. R.J. Blin-Stoyle, 'Nuclear and Particle Physics', Ch. **4** - 'Models of Nuclear Structure', Chapman and Hall, London, 1991.]

14. F.A. Bovey, Nuclear Magnetic Resonance Spectroscopy, 2nd Ed., pg. 3, Academic Press, London, 1988.

15. F. Bloch, 'Nuclear Induction', Phys. Rev., 1946, **70**, 460.

16. A.W. Overhauser, 'Polarization of Nuclei in Metals', Phys. Rev., 1955, **92**, 411.

17. J.H. Noggle and R.E. Schirmer, The Nuclear Overhauser Effect, Chemical Applications., Academic Press, New York, 1971.

18. R. Freeman, A Handbook of Nuclear Magnetic Resonance, pg. 28 - 32, Longman Scientific, Harlow, England, 1987.

19. C.C. Hinckley, 'Paramagnetic shifts in solution of cholesterol and the dipyridine adduct of trisdipivalomethanatoeuropium (III). A shift reagent.', J. Am. Chem. Soc., 1969, **91**, 5160.

20. H. Friebolin, Basic One- and Two-Dimensional NMR Spectroscopy, Ch. 12 - Shift Reagents, VCH, New York, 1991.

21. J.W. Emsley, J. Feeney and L.H. Sutcliffe, High Resolution Nuclear Magnetic Resonance Spectroscopy, Vol. 1, pg. 4, Pergamon Press, Oxford, 1965.

22. G. Lindström, 'An experimental investigation of the nuclear magnetic moments of deuterium and hydrogen', Phys. Rev., 1950, **78**, 817.

23. H.A. Thomas, 'The diamagnetic correction for protons in water and mineral oil', Phys. Rev., 1950, **80**, 910.

24. F.A.L Anet and D.J. O'Leary, 'The Shielding Tensor. Part 1: Understanding its symmetry Properties', Concepts Magn. Reson. 1991, **3**, 193.

F.A.L Anet and D.J. O'Leary, 'The Shielding Tensor. Part 2: Understanding its Strange Effects on Relaxation', Concepts Magn. Reson. 1992, **4**, 35.

25. I.U.P.A.C., 'Recommendations for the presentation of NMR data for publications in chemical journals', 1972, **29**, 627.

I.U.P.A.C., 'Presentation of NMR data for publication in chemical journals - B. Cnventions relating to spectra from nuclei other than protons.', Pure Appl. Chem., 1976, **45**, 217.

26. C. Brevard and P. Granger, Handbook of High Resolution Multinuclear NMR, Wiley, New York, 1981.

27. for *e.g.* see: D.H. Williams and I. Flemming, Spectroscopic Methods in Organic Chemistry, 4th Ed., McGraw-Hill, London, 1989.

28. W.D. Knight, 'Electron paramagnetism and nuclear magnetic resonance in metals', Solid State Phys., 1956, **2**, 93.

29. C.P. Schlicter, Principles of Magnetic Resonance, 3rd Ed., Ch. 4.7 pg. 113 - 127, Springer-Verlag, 1990.

30. J. Winter, Magnetic Resonance In Metals, Oxford, London, 1971.

31. W.G. Procter and F.C. Yu, 'Nuclear Magnetic Moments of Several Stable Isotopes', Phys. Rev., 1951, **81**, 20.

32. H.S. Gutowsky and D.W. McCall, 'Nuclear magnetic resonance fine structure in liquids', Phys. Rev., 1951, **82**, 748.

33. J. Homer and M.S. Mohomaadi, 'A simple , general method for predicting the relative intensities of first order NMR spin-spin coupled multiplets', J. Chem. Ed., 1983, **60**, 932.

34. M. Karplus, 'Contact electron spin coupling of nuclear magnetic moments', J. Chem. Phys., 1959, **30**, 11.

M. Karplus, 'Vicinal proton couplings in nuclear magnetic resonance', J. Am. Chem. Soc., 1963, **85**, 2870.

35. J. Keeler, D. Neuhaus and J.J. Titman, 'A convenient tehnique for the measurement and assignment of long range carbon-13 proton coupling constants', Chem. Phys. Lett., 1988, **146**, 545.

J.J. Titman, D. Neuhaus and J. Keeler, 'Measurement of long range heteronuclear coupling constants', J. Magn. Reson., 1989, **85**, 111.

J. M. Richardson, J.J. Titman and J. Keeler, 'Assessment of a method for the measurment of long-range heteronuclear coupling constants', J. Magn. Reson., 1991, **93**, 533.

36. N. Bloembergen, E.M. Purcell and R.V. Pound, 'Relaxation effects in nuclear magnetic resonance absorption', Phys. Rev., 1948, **73**, 679.

37. M. Goldman, T. Tabti, C. Ferman, J.F. Jacquinot and G. Saux, 'A model for the influence of motion on the NMR lineshape', J. Magn. Reson., 1993, **103**, 288.

38. J.W. Emsley, J. Feeney and L.H. Sutcliffe, High Resolution Nuclear Magnetic Resonance Spectroscopy, Vol. 1, Ch. 2.5 pg. 20 - 33, Pergamon Press, Oxford, 1965.

39. C. Brevard and P. Granger, Handbook of High Resolution Multinuclear NMR, Ch. 1.6 pg. 12 - 19, Wiley, New York, 1981.

40. N. Bloembergen, Nuclear Magnetic Relaxation, W.A. Benjamin, New York, 1961.

41. M.L. Martin, J.J. Delpuech and G.J. Martin, Practical NMR Spectroscopy, Ch. 4.1 pg. 231, Heydon, London, 1979.

42. R. Bracewell, 'The Fourier Transform and Its Applications', 2nd Edn., 1978, McGraw-Hill, New York.

43. W. Heisenberg, 'Uber den anschaulichen Inhalt der quantentheoretischen Kinematik und Mechanik', Z. Phys., 1927, **43**, 172.

W. Heisenberg, 'The Physical Principles of Quantum Theory', 1930, Dover, New York.

P.W. Atkins, 'Quanta: A Handbook of Concepts', 2nd ed., 1991, Oxford Univ. Press, Oxford.

44. R.R. Ernst, G. Bodenhausen and A. Wokaun, 'Principles of Nuclear Magnetic Resonance in One and Two Dimensions' - Ch. 4.3.1.5, pg. 153, 1990, Oxford Univ. Press, Oxford.

45. J. Homer and M.S. Beevers, 'Driven equilibrium single-pulse observation of T_1 relaxation. A reevaluation of a rapid "new" method for determining NMR spin-lattice relaxation times', J. Magn. Reson., 1985, **63**, 287.

46. J. Homer and J. K. Roberts, 'Routine Evaluation of M_0 Ratios and T_1 Values from Driven-Equilibrium NMR Spectra', J. Magn. Reson., 1990, **89**, 265.

47. R.R. Ernst, G. Bodenhausen and A. Wokaun, 'Principles of Nuclear Magnetic Resonance in One and Two Dimensions' - Ch. 4.2.3, pg. 121, 1990, Oxford Univ. Press, Oxford.

48. R. Freeman, S. Kempsell and M.H. Levitt, 'Radiofrequency pulse sequences which compensate their own imperfections', J. Magn. Reson., 1980, **38**, 453.

49. E.L. Hahn, 'Spin-Echoes', Phys. Rev., 1950, **80**, 580.

H.Y. Carr and E.M. Purcell, 'Effect of diffusion on free precession in nuclear magnetic resonance experiments', Phys. Rev., 1954, **94**, 630.

50. S.A. Smith, W.E. Palke and J.T. Gerig, 'The Hamiltonians of NMR: Part 1', Concepts Magn. Reson., 1992, **4**, 107.

S.A. Smith, W.E. Palke and J.T. Gerig, 'The Hamiltonians of NMR: Part 2', Concepts Magn. Reson., 1992, **4**, 181.

51. J.P. Amoureux, C. Fernandez and P. Granger,'Interpretation of Quadrupolar Powder Spectra: Static and MAS Experiments', Multinuclear Magnetic Resonance in Liquids and Solids - Chemical Applications, eds. P. Granger and R.K. Harris, 1990, pg. 409 Kluwer Academic Publishers, Netherlands.

52. J.O. Hirschfelder, W. Byers Brown and S.T. Epstein, 'Recent developments in perturbation theory', Adv. Quantum Chem., 1964, **1**, 256.

P.W. Langhoff, S.T. Epstein and M. Karplus, 'Aspects of time-dependent perturbation theory', Rev. Mod. Phys., 1972, **44**, 602.

P.W. Atkins, 'Quanta: A Handbook of Concepts', 2nd ed., 1991, Oxford Univ. Press, Oxford.

53. D.M. Brink and G.R. Satchler, 'Angular Momentum', 1968, Clarrendon Press, Oxford.

R.N. Zare, 'Angular Momentum: Understanding Spacial Aspects in Chemistry and Physics', 1987, Wiley, New York.

54. F. Taulelle, 'NMR of Quadrupolar Nuclei in the Solid State', Multinuclear Magnetic Resonance in Liquids and Solids - Chemical Applications, eds. P. Granger and R.K. Harris, 1990, pg. 393, Kluwer Academic Publishers, Netherlands.

55. I.J. Lowe, 'Free Induction Decays of Rotating Solids', Phys. Rev. Lett., 1959, **2**, 285.

56. E.R. Andrew, 'The Narrowing of NMR Spectra of Solids by High-speed Specimen Rotation and the Resolution of Chemical Shift and Spin Multiplet Structures for Solids', Prog. NMR Spectry., 1971, **8**, 1.

57. J.W. Beams, 'An Apparatus for Obtaining High Speeds of Rotation', Rev. Sci. Instrum., 1930, **1**, 667.

J.W. Beams and E.G. Pickels, 'The Production of High Rotational Speeds', Rev. Sci. Instrum., 1935, **6**, 299.

J.W. Beams, 'High Rotational Speeds', J. Appl. Phys., 1937, **8**, 795.

J.W. Beams, 'A Tubular Vacuum-Type Centrifuge', Rev. Sci. Instrum., 1938, **9**, 413.

58. E. Henroit and E. Huguenard, 'Sur la réalisation de trè grandes vitesses de rotation', Compte Rend., 1925, **180**, 1389.

59. K.W Zilm, D.W. Alderman and D.M. Grant, 'A High-Speed Magic Angle Spinner', J. Magn. Reson., 1978, **30**, 563.

60. J. Schaefer, E.O. Stejskal and R. Buchdahl, 'High-reolution carbon-13 nuclear magnetic resonance study of some solid, glassy polymers', Macromolecules, 1975, **8**, 291.

61. C.S. Yannoni, 'High-Resolution NMR in Solids: The CPMAS Experiment', Acc. Chem. Res., 1982, **15**, 201.

62. X. Wu and K.W. Zilm, 'Complete Spectral Editing in CPMAS', J. Magn. Reson., 1993, **102**, 205.

63. L.H. Merwin and A. Sebald, 'The First Examples of ^{109}Ag CP MAS Spectroscopy', 1992, **97**, 628.

64. W.L. Earl and D.L. Vanderhart, 'Measurement of ^{13}C Chemical Shifts in Solids', J. Magn. Reson., 1982, **48**, 35.

65. A. Pines, M.G. Gibby and J.S. Waugh, 'Proton enhansed NMR of dilute spins in solids', J. Chem. Phys., 1973, **59**, 569.

66. G. Jeschke and G. Grossmann, 'Spinning-Sideband-Pattern Deviations in Cross-Polarization MAS NMR Spectra', J. Magn., Reson., 1993, **103**, 323.

67. C.P. Schlicter, Principles of Magnetic Resonance, 3rd Ed., Ch. 8.9 pg. 392 - 406, Springer-Verlag, 1990.

68. H.J.M. De Groot, S.O. Smith, A.C. Kolbert, J.M.L. Courtin, C. Winkel, J. Lugtenburg, J. Herzfeld and R.G. Griffen, 'Iterative Fitting of Magic Angle Spinning NMR Spectra', J. Magn. Reson., 1991, **91**, 30.

69. S. Feaux De Lacroix, J.J. Titman, A. Hagemeyer and H.W. Spiess, 'Increased Resolution in MAS NMR Spectra by Two-Dimensional Separation of Sidebands by Order', J. Magn. Reson., 1992, **97**, 435.

70. A.C. Olivieri, 'Dipolar and Scalar Couplingin Magic Angle Spinning Solid-State NMR Spectra of Spin 1/2 Nuclei Affected by Quadrupolar Nuclei with Large Quadrupole Coupling Constants', J. Magn. Reson., 1993, **101**, 313.

71. A. Samosen and A. Pines, 'Double rotor for solid state NMR', Rev. Sci. Instrum., 1989, **60**, 3239.

72. A. Samosen and E. Lippmaa, 'Syncronized Double-Rotation NMR Spectroscopy', J. Magn. Reson., 1989, **84**, 410.

73. A. Llor and J. Virlet, 'Towards High-Resolution NMR of More Nuclei in Solids: Sample Spinning with Time Dependent Spinner Axis Angle', Chem. Phys. Lett., **152**, 248.

74. Y. Wu, D. Lewis, J.S. Frye, A.R. Palmer and R.A. Wind, 'Cross-Polarization Double-Rotation NMR', J. Magn. Reson., 1992, **100**, 425.

75. B.Q. Sun, J.H. Baltisberger, Y. Wu, A. Samosen and A. Pines, 'Sidebands in Dynamic Angle Spinning (DAS) and Double Rotation (DOR) NMR', Sol. State NMR, 1992, **1**, 267.

76. P.J. Grandinetti, Y.K. Lee, J.H. Baltisberger, B.Q. Sun and A. Pines, 'Sideband Patterns in Dynamic-Angle-Spinning NMR', J. Magn. Reson., 1993, **102**, 195.

77. J.S. Waugh, L.M. Huber and U. Haeberlin, 'Approach to High-Resolution NMR in Solids', Phys. Rev. Lett., 1968, **20**, 180.

85. A.D. English and A.J. Vega, 'Multiple Pulse Nuclear Magnetic Resonance of Solid Polymers: Dynamics of Poly(tetrafluoroethylene)', Macromol., 1979, **12**, 353.

A.J. Vega and A.D. English, 'Multiple-Pulse Nuclear Magnetic Resonance of Solid Polymers. Polymer Motions in Crystalline and Amorphous Poly(tertafluoroethylene)', Macromol., 1980, **13**, 1635.

86. J.P. Yesinowski, 'High-Resolution NMR of Solids and Surface-Adsorbed Species in Colloidal Susspensions: ^{31}P NMR of Hydroxyapatite and diphosphonates.', 20th Experimental NMR Conference, Asilomar, California, USA, 1979.

87. J.P. Yesinowski, 'High-Resolution NMR Spectroscopy of Solids and Surface Adsorbed Species in Colloidal Suspension: ^{31}P NMR Spectra of Hydroxyapatite and Diphosphonates.', J. Am. Chem. Soc., 1981, **103**, 6266.

88. K. Kimura and N. Satoh, 'High Resolution Solid State NMR of $^{27}AlF_3$ Particles Observed by a Conventional Fourier Transform Spectrometer.', Chem. Lett. (Jpn.), 1989, 271.

89. N. Satoh and K. Kimura, 'High Resolution Solid State NMR in Liquids. 2. ^{27}Al NMR Study of AlF_3 Ultrafine Particles.', J. Am. Chem. Soc., 1990, **112**, 4688.

90. J. Homer, S.A. Reynolds and S. Firth-Clark, unpublished results.

91. E.R. Andrew and R.G. Eades, 'Possibilities for high-resolution nuclear magnetic resonance spectra of crystals', Disc. Faraday Soc., 1962, **34**, 38.

92. A. Bradbury, R.G. Eades and J.G. McCarten, 'Nuclear magnetic resonance in a rotating magnetic field', Phys. Lett., 1968, **26A**, 405.

93. T.J. Mason, Ch.1 - 'Introduction', 'Chemistry with Ultrasound', ed. T.J. Mason, Elsevier Applied Science, 1990.

94. R.W.B. Stephens and A.E. Bate, 'Acoustics and Vibrational Physics', 2nd edition, Arnold, London, 1966.

95. J. Blitz, 'Elements of Acoustics', Butterworths, London, 1964, pg. 30.

96. F. Galton, 'Inquires into Human Faculty and Development', MacMillan, London, 1883.

97. P. Curie and J. Curie, 'Développment, par pression, de l'électricité polaire dans les cristaux hémièdres à faces inclinées', Compt. Rend., 1880, 91, 294.

78. P. Mansfield, 'Symmetrized Pulse Sequences in High Resolution NMR in Solids', J. Phys. C: Solid State Phys., 1971, **4**, 1444.

P. Mansfield, M.J. Orchard, D.C. Stalker and K.H.B. Richards, 'Symmetrized Multipulse Nuclear Magnetic Resonance Experiments in Solids: Measurement of the Chemcial Shift Shielding Tensor in some compunds.', Phys. Rev., 1973, **B7**, 90.

W.K. Rhim, D.D. Elleman, R.W. Vaughan, 'Analysis of Multiple Pulse NMR in Solids', J. Chem. Phys., 1973, **59**, 3740.

A.N. Garroway, P. Mansfield and D.C. Stalker, 'Limits to Resolution in Multiple-Pulse NMR', Phys. Rev., 1975, **B11**, 121.

W.K. Rhim, D.D. Elleman and R.W. Vaughan, 'Enhanced Resolution for Solid State NMR', J. Chem. Phys., 1973, **58**, 1772.

79. M. Mehring, 'Principles of High Resolution NMR in Solids', 2nd Ed., 1983, Springer-Verlag, Berlin.

U. Haeberlin, 'High Resolution NMR in Solids, Selective Averaging', Suppliment 1, 1976, Adv. Magn. Reson., Academic Press, New York.

80. R.E. Taylor, R.G. Pembleton, L.M. Ryan and B.C. Gerstein, 'Combined Multiple Pulse NMR and Sample Spinning: Recovery of Proton Chemical Shift Tensors', J. Chem. Phys., 1979, **71**, 4541.

81. D.P. Burum and W.K. Rhim, 'Proton anisotropic chemcial shift spectra in a single crystal of hexagonal ice', J. Chem. Phys., 1979, **71**, 3139.

D.P. Burum and W.K. Rhim, 'An improved NMR technique for homonuclear dipolar decoupling in solids. Application to polycrystaline ice', J. Chem. Phys., 1979, **70**, 3553.

D.P. Burum and W.K. Rhim, 'Proton NMR study of gypsum. $CaSO_4.2H_2O$, using an improved technique for homonuclear dipolar decoupling in solids', J. Magn. Reson., 1979, **34**, 241.

W.K. Rhim, D.P. Burum and D.D. Elleman, J. Chem. Phys., 1979, **71**, 3139.

G.E. Maciel, C.E. Bronnimann and B.L. Hawkins, 'High-resolution ^1H nuclear magnetic resonance in solids via CRAMPS', Adv. Magn. Reson., 1990, **14**, 125.

82. K. Takegoshi and C.A. McDowell, 'A 'magic echo' pulse sequence for the high-resoultion NMR spectra of abundant spins in solids', Chem. Phys. Lett., 1985, **116**, 100.

83. M.L. Buszko, C.E. Bronnimann and G.E. Maciel, '^1H CRAMPS Based on TREV', J. Magn. Reson., 1993, **103**, 183.

84. D.P. Burum, 'Combined Rotation and Multiple Pulse Spectroscopy (CRAMPS)', Concepts Magn. Reson., 1990, **2**, 213.

98. L. Bergmann, 'Ultrasonics', Wiley, New York / Bell, London, 1938.

99. W. P. Mason, 'Piezoelectro Crystals and their Applications to Ultrasonics', Van Nostrand, Princeton, New Jersey, 1950.

100. B. Jaffe, R.S. Roth and S. Marzullo; 'Piezoelectric properties of lead zirconate-lead titinate solid-solution ceramics', J. Appl. Phys., 1954, 25, 809.

101. F. Kulcsar; 'Electromechanical properties of lead titinate zirconate ceramics with lead partially repalced by calcium or strontium', J. Am. Ceram. Soc., 1959, 42, 49.

102. J. Blitz, 'Fundamentals of Ultrasonics', 2nd Edn., Butterworths, London, 53, 1967.

103. J. Blitz, 'Ultrasonics: Methods and Applications, Butterworths, London, 34, 1971.

104. F. Galton, 'Hydrogen whistles', Nature, 1883, 491, 27.

105. J. Hartmann and B. Trolle, 'A new acoustic generator. The air-jet generator', J. Sci. Instr., 1927, 4, 101.

106. W.P. Mason, 'Physical Acoustics and the Properties of Solids', Van Nostrand, Princeton, New Jersey, 1958.

107. L. Filipczynski, Proc. natn. Conf. non-destr. Test., Warsaw, 1955, 499. - cited in J. Blitz, 'Ultrasonics: Methods and Applications, Butterworths, London, pg. 53, 1971.

108. T.J. Goodwin, Ch.5 - 'Equipment', 'Chemistry with Ultrasound', ed. T.J. Mason, Elsevier Applied Science, 1990, 167.

109. M. Faraday, 'On a peculiar class of Acoustical Figures; and on certain forms assumed by groups of particles upon vibrating elastic Surfaces.', Philos. Trans., R. Soc., London, 1831, **121**, 229.

110. G. J. Price (Ed.), 'Current Trends in Sonochemistry', Royal Society of Chemistry, 1992.

111. T. J. Mason (Ed.), 'Chemistry with Ultrasound', Elsevier Applied Science, 1990.

112. A. A. Atchley and L. A. Crum, 'Acoustic Cavitation and Bubble Dynamics', in, 'Ultrasound: It's Chemical, Physical and Biological Effects.', *Ed.* K. S. Suslick, VCH Publishers, New York, 1988.

113. E. N. Harvey, K. K. Barnes, W. D. McElroy, A. H. Whitely, D. C. Pease and K. W. Cooper; 'Bubble formation in animals (I). Physical factors', J. Cell. Comp. Physiol. 1944, **24**, 1.

114. See *e.g.* R. E. Apfel, Methods of Experimental Physics, ed. P. D. Edmonds, Academic Press, New York, 1981, Vol. 19, ch. 7.

115. K. S. Suslick, R. E. Cline Jr., D. A. Hammerton; 'The sonochemical hot-spot', J. Am. Chem. Soc., 1986, **108**, 5641.

116. T.J. Mason, Ch.1 - 'Introduction', 'Chemistry with Ultrasound', ed. T.J. Mason, Elsevier Applied Science, 1990, 6.

117. E.N. Harvey, 'Sonoluminescence and sonic chemiluminescence', J. Am. Chem. Soc., 1939, **61**, 2392.

Y.I. Frenkel,'Electrical phenomena associated with cavitation due to ultrasonic vibrations in liquids', Acta Physicochim. URSS, 1940, **12**, 317.

118. C.M. Sehgal and R.E. Verrall, 'A review of the electrical hypothesis of sonoluminescence', Ultrasonics, 1982, **20**, 37.

M.A. Margulis, 'Study of electrical phenomena related to cavitation. I. Electrical theories of chemcial and physicochemical action of ultrasound', Zh. Fiz. Khim., 1981, **55**, 154.

119. M. S. Plesset and R. B. Chapman, 'Collapse of an initially spherical vapour cavity in the neighbourhod of a solid boundary', J. Fluid. Mech., 1971, **47**, 283.

120. E. A. Neppiras, 'Acoustic Cavitation', Phys. Rep., 1980, **61**, 159.

121. K. S. Suslick and S. J. Doktycz, 'The sonochemistry of Zn powder', J. Am. Chem. Soc., 1989, **111**, 2342.

122. P. Renaud, 'Hypothèse d'un Effet Réciproque de l'électrostriction produit par l'ultrasonnation des solvants hydroides', J. Chim. Phys., 1953, **50**, 135.

R. G. Busnel, D. Picard and H. Boulzigues, 'Rapports entre la Longueur D'onde et L'oxydation de L'iodure de potassium par les ultrasons', J. Chim. Phys., 1953, **50**, 97.

R. O. Prudhomme, D. Picard and R. G. Busnel, ' Sur l'utilisation Chimique de l'energie Acoustique émise par le Quartz dans les Réactions ultrasonores', J. Chim. Phys., 1953, **50**, 107.

123. T. W. Hislop, 'New Ultrasonic Emulsifying Devices', Ultrasonics, 1970, **8**, 88.

124. A. J. Last, 'Focused Ultrasonic Emulsifiers and Dispersers', Ultrasonics, 1969, **7**, 131.

125. R. W. Wood, 'Supersonics: The Science of Inaudible Sounds', Brown University, 1939, 73 - 74.

126. 7. J. Blitz, 'Fundamentals of Ultrasonics', 2nd Edn., Butterworths, London, 210, 1967.

127. V. F. K. Bjerknes, 'Fields of Force', Columbia Univ. Press, New York, 1906.

128. L. V. King, 'On the acoustic radiation pressure on spheres', Proc. R. Soc. London Ser., 1934, **A147**, 212.

129. K. Yosioka and Y. Kawasima, 'Acoustic Radiation Pressure on a Compressible Sphere', Acustica, 1955, **5**, 17.

130. J. B. Dysthe, 'Force on a Small Inclusion in a Standing Acoustic Wave', J. Sound Vib., 1969, **10**, 331.

131. L. A. Crum, 'Comments on "Force on a Small Inclusion in a Standing Acoustic Wave"', J. Acoust. Soc. Am. 1971, **50**, 157.

132. P. J. Westervelt, 'The Theory of Steady Forces Caused by Sound Waves', J. Acoust. Soc. Am., 1951, **23**, 312.

133. T. F. W. Embleton, 'Mean Force on a Sphere in a Spherical Sound Field. I. (Theoretical)', J. Acoust. Soc. Am., 1954, **26**, 40.

T. F. W. Embleton, 'Mean Force on a Sphere in a Spherical Sound Field. II. (Experimental)', J. Acoust. Soc. Am., 1954, **26**, 46.

134. W. L. Nyborg, 'Radiation Pressure on a Small Rigid Sphere', J. Acoust. Soc. Am., 1967, **42**, 947.

135. T. Hasegawa, 'Acoustic radiation force on a sphere in a quasistationary wave field - Theory', J. Acoust. Soc. Am., 1979, **65**, 32.

T. Hasegawa, 'Acoustic radiation force on a sphere in a quasistationary wave field - Experimental', J. Acoust. Soc. Am., 1979, **65**, 41.

136. W. G. Lambert, 'Solution of non-linear differential equations', Instrum. Control Syst. 1966, **39**, 177.

137. D.W. McCall, 'Nuclear Magnetic Resonance Studies of Molecular Relaxation Mechanisms in Polymers', Acc. Chem. Res., 1971, **4**, 223.

138. J. Homer and S.A. Palfreyman, unpublished results.

139. R.L. Vold, J.S. Waugh, M.P. Klein and D.E. Phelps, 'Measurement of spin-lattice relaxation in complex systems', J. Chem. Phys., 1968, **48**, 3831.

R. Freeman and H.D.W. Hill, 'High resolution studies of nuclear spin-lattice relaxation', J.Chem. Phys., 1969, **51**, 3140.

140. J.L. Markley, W.J. Horsley and P.M. Klein, 'Spin-lattice relaxation measurements in slowly relaxing complex spectra', J. Chem. Phys., 1971, **55**, 3604.

G.G. McDonald and J.S. Leigh, 'A new method for measuring londitudinal relaxation times', J. Magn. Reson., 1973, **9**, 358.

141. E. Tillmanns and W.H. Baur, 'On the Stoichiometry of Trisodium Orthophosphate Dodecahydrate', Inorg. Chem., 1970, **9**, 1957.

142. K.A. Kobe and A. Leipper, 'The system trisodium phosphate -sodium carbonate - water', Ind. End. Chem., 1940, **32**, 198.

143. O.T. Quimby, 'The chemistry of sodium phosphates', Chem. Rev., 1947, **40**, 150.

144. B. Wendrow and K.A. Kobe, 'The System Sodium Oxide-Phosphorous Pentoxide-Water', Ind. Eng. Chem., 1952, **44**, 1439.

145. R.N. Bell, 'Hydrates of Trisodium Orthophosphate', Ind. Eng. Chem., 1949, **41**, 2901.

146. G.J. Tilstone, 'Sonically Induced Narrowing of Solid State Nuclear Magnetic Resonance Spectra: A Possible Alternative to Magic Angle Spinning', Final Year Undergraduate Project Thesis, Aston University, Dept. of CEAC, April 1991.

147. B. Brown and J. E. Goodman, High-Intensity Ultrasonics', Iliffe Books, London, 1965, ch. 2.

148. J. Frenkel, 'Kinetic Theory of Liquids', ch. 1 and 2, 1955, Dover Publ., New York.

L. Landau, 'The theory of phase transitions II', Physik Zeits. Sowjetunion, 1937, **11**, 26.

149. L. Pauling, 'The Rotational Motion of Molecules in Crystals', Phys. Rev., 1930, **36**, 430.

R.H. Fowler, 'The theory of the rotations of molecules in solids and of the dielectric constants of solids and liquids', Proc. Roy. Soc. (Lond.), 1935, **A149**, 1.

150. N.L. Alpert, 'Study of Phase Transitions by Means of Nuclear Magnetic Resonance Phenomena', Phys. Rev., 1949, **75**, 398.

151. K. Mehay, Final Year Undergraduate Project Thesis, Aston University, Dept. of CEAC, April 1991.

152. J. Homer and M.J. Howard, 'Studies on the Origin of Sonically Induced Narrowing of Solid-state Nuclear Magnetic Resonance Spectra', J. Chem. Soc., Faraday Trans., 1993, **89**, 3029.

153. J.K. Roberts, 'The Use of Driven Equilibrium Conditions in the Measurement of NMR Relaxation Times', Ph.D. Thesis, University of Aston in Birmingham, 1989.

154. See e.g. G. M. Barrow, Physical Chemistry, McGraw-Hill, London, 1961, ch. 15.

155. W. L. Nyborg and D. E. Hughes, 'Bubble Annihilation in Cavitation Streamers', J. Acoust. Soc. Am. 1967, **42**, 891.

156. R.J. Plunkett, 'The History of Polytetrafluoroethylene, discovery and development', Meeting of the American Chemical Society, April 1986, New York.

157. C.A. Sperati and H.W. Storkweather, 'Fluorine containing polymers. II. Polytetrafluoroethylene', Adv. Polymer Sci., 1961, **2**, 465.

158. E.S. Clarke, Symposium on Helices in Macromolecular Systems, Polytech. Inst. Brooklyn, May 1959.

159. A. N. Garroway, D. C. Stalker and P. Mansfield, '^{19}F PTFE chemical shift anisotropy in aligned PTFE fibres', Polymer, 1975, **16**, 161.

160. W.P. Schlicter, 'Nuclear magnetic resonance in some fluorine derivatives of polyethylene', J. Polymer. Sci., 1957, **24**, 173.

161. C. Elschenbroich and A. Salzer, 'Organometallics: A Concise Introduction', 1989, pg. 75, VCH Publ., New York.

162. E.R. Andrew, W.S. Hinshaw and R.S. Tiffen, 'More Precise Determination of the Knight Shift of Aluminium', Phys. Lett., 1973, **46A**, 57.

163. D. Mueller, private communication.

164. C. Elschenbroich and A. Salzer, 'Organometallics: A Concise Introduction', 1989, pg. 84, VCH Publ., New York.

165. T. Kushida and J.C. Murphy, 'Pressure Dependence of the Knight Shift in Al and Nb Metals', Phys. Rev., 1971, **3B**, 1574.

166. R.T. Beyer and S.V. Letcher, 'Physical Ultrasonics', 1969, Academic Press, New York, Ch. 10.

167. W.P. Rahilly, 'Nuclear Magnetic Resonance of Si^{29} in Lithium Doped Single Crystal Silicon', Aero Propulsion Lab., Wright Patterson Air Force Base, Ohio, 1975.

168. W. Sakasi, S. Ikehata and S. Kobayashi, '^{29}Si NMR in Heavily Doped Silicon', Phys. Lett., 1973, **42A**, 429.

169. for *e.g.* see G.B. Arfken, D.F. Griffing, D.C. Kelly and J. Priest, 'University Physics', 2nd Ed., 1989, Harcourt Brace Jovanovich, Orlando, Florida.

170. Millipore, Laboratory Catalogue 1991, Particle size and separation techniques, pg. 7, Millipore (U.K.) Ltd., Chester, England.

171. S. Glasstone, Textbook of Physical Chemistry', Macmillan, London, 2nd ed., 1947, pg. 255 - 263.

172. D. Sette, 'Ultrasonic Lenses of Plastic Materials', J. Acoust. Soc. Am., 1949, **21**, 375.

BIBLIOGRAPHY

ULTRASONICS

R.T. Beyer and S.V. Letcher, PHYSICAL ULTRASONICS, Academic Press, New York, 1969.

R.T. Beyer, NONLINEAR ACOUSTICS, Naval Sea Systems Command (USA), 1974.

J. Blitz, ULTRASONICS: METHODS AND APPLICATIONS, Butterworths, London, 1971.

J. Blitz, FUNDAMENTALS OF ULTRASONICS, Butterworths, London, 1967.

B. Brown and J.E. Goodman, HIGH-INTENSITY ULTRASONICS, Iliffe Books, New Jersey USA, 1965.

P.D. Edmonds (Ed.), METHODS IN EXPERIMENTAL PHYSICS, VOLUME 19 - ULTRASONICS, Academic Press, New York, 1981.

J. R. Frederick, ULTRASONIC ENGINEERING, Wiley, New York, 1965.

B. Jaffe, W.R. Cook and H. Jaffe, PIEZOELECTRIC CERAMICS, Academc Press, London, 1971.

T.J. Mason and J.P. Lorimer, SONOCHEMISTRY, THEORY, APPLICATION AND USE OF ULTRASOUND, Ellis Horwood Ltd, London, 1991.

T.J. Mason, CHEMISTRY WITH ULTRASOUND, Elsevier, Essex, 1990.

W. P. Mason (Ed.), PHYSICAL ACOUSTICS, VOLUMES ONE AND TWO, Academic Press, New York, 1965.

K.S. Suslick (Ed.), ULTRASOUND - ITS CHEMICAL, PHYSICAL AND BIOLOGICAL EFFECTS, VCH Ltd, New York, 1988.

NUCLEAR MAGNETIC RESONANCE SPECTROSCOPY

A. Abragam, PRINCIPLES OF NUCLEAR MAGNETISM, Oxford, 1961.

F.A. Bovey, NUCLEAR MAGNETIC RESONANCE SPECTROSCOPY, 2nd Ed., Academic Press, New York, 1988.

C. Brevard and P. Granger, HANDBOOK OF HIGH RESOLUTION MULTINUCLEAR NMR, Wiley, New York, 1981.

A.E. Derome, MODERN NMR TECHNIQUES FOR CHEMISTRY RESEARCH, Pergammon, Oxford, 1987.

G. Engelhardt and D. Michel, HIGH-RESOLUTION SOLID-STATE NMR OF SILICATES AND ZEOLITES, Wiley, Chichester, U.K.

J.W. Emsley, J. Feeney and L.H. Sutcliffe, HIGH RESOLUTION NUCLEAR MAGNETIC RESONANCE SPECTROSCOPY - VOLUME ONE, Pergammon, Oxford, 1965.

R.R. Ernst, G. Bodenhausen and A. Wokaun, PRINCIPLES OF NUCLEAR MAGNETIC RESONANCE IN ONE AND TWO DIMENSIONS, Oxford, 1987.

R. Freeman, A HANDBOOK OF NUCLEAR MAGNETIC RESONANCE, Longman, Essex, U.K., 1987.

H. Friebolin, BASIC ONE AND TWO DIMENSIONAL NMR SPECTROSCOPY, VCH Ltd., New York, 1991.

E. Fukushima and S.B. Roeder, EXPERIMENTAL PULSE NMR, A NUTS AND BOLTS APPROACH, Addison-Wesley, Reading, Mass. USA, 1981.

C.A. Fyfe, SOLID STATE NMR FOR CHEMISTS, C.F.C Press, Ontario, Canada, 1983.

U. Haeberlen, HIGH RESOLUTION NMR IN SOLIDS, SELECTIVE AVERAGING, Suppl. 1, Adv. Magn. Reson., Academic Press, New York, 1976.

R.K. Harris, NUCLEAR MAGNETIC RESONANCE SPECTROSCOPY. A PHYSICOCHEMICAL VIEW, Pitman, London, 1983.

S.W. Homans, A DICTIONARY OF CONCEPTS IN NMR, Oxford, 1989.

M. Mehring, PRINCIPLES OF HIGH RESOLUTION NMR IN SOLIDS, 2nd Ed., Springer, New York, 1983.

J.K.M. Sanders and B.K. Hunter, MODERN NMR SPECTROSCOPY - A GUIDE FOR CHEMISTS, 2nd Ed., Oxford, 1993

C.P. Schlicter, PRINCIPLES OF MAGNETIC RESONANCE, 3rd Ed., Springer, New York, 1990.

APPENDIX ONE

INTRODUCTION TO HAMILTONIANS AND TENSOR MATHEMATICS

A1.1 A BRIEF INTRODUCTION TO HAMILTONIANS

The discussion of solid state NMR interactions usually involves the terms Hamiltonians and Tensors. This appendix intends to introduce the reader to the concept of Hamiltonians describing NMR interactions by an example of just one of those interactions. In the simplest of terms, the Hamiltonian $\mathcal{H}$ is defined as the energy involved with an interaction. To see how an energy can be used to describe NMR, consider the following:

The energy of a magnetic moment μ in a magnetic field B_0 (relative to zero field) is equal to $E = -\mu.B_0$

$$E = -\mu B_o \qquad \text{- (A1.1)}$$

In quantum mechanics, the magnetic moment of a nuclear spin I is an operator proportional to the nuclear spin operator as:

$$\mu = \gamma \hbar I \qquad \text{- (A1.2)}$$

An operator is a mathematical function which when performed on a wavefunction produces a prediction of an observation of a particular property. e.g. Schrödingers equation may be written $\mathcal{H}\ \psi = E\ \psi$. Here, ψ is the known wavefunction for a system, and $\mathcal{H}$ is the operator.

To the classical energy there corresponds a quantum mechanical Hamiltonian operator called the Zeeman Hamiltonian:

$$\hbar\mathcal{H} = -\gamma \hbar I B_o \qquad \text{- (A1.3)}$$

Thus the NMR Zeeman interaction is described as a Hamiltonian. This is not to say that all NMR interactions described in this way can be defined as simply. It is only possible to describe certain interactions *via* the use of quantum mechanics, but to consider the Hamiltonian as an energy quantity should enable readers to more comfortably follow the concepts dealt with in chapter three. The broadening interactions described as Hamiltonians can be considered simply as having a magnitude related to the Hamiltonian energy quantity. *i.e.* when the Hamiltonian is large, the broadening interaction is large, and *vice versa* when the Hamiltonian is small.

It must be stressed that this is by no means a comprehensive treatment of Hamiltonians. The author recommends texts by Hennel and Klinowski[A1] or Goldman[A2] for further reading into the quantum mechanics of NMR.

A1.2 A BRIEF INTRODUCTION TO TENSOR MATHEMATICS

As with the brief introduction to Hamiltonians, the understanding of Tensor mathematics is introduced *via* the application of tensors in terms of the nuclear magnetic moment μ.

A magnetic field B_0 causes a magnetic moment μ to be not exactly parallel to the magnetic field. The magnitudes of x,y and z components of μ to the applied field B_0 and are written $\mu_{xz}B_0$, $\mu_{yz}B_0$ and $\mu_{zz}B_0$ and are defined shown in figure A1.1. Similar expressions could describe the induced moment if the field is applied along the x and y axes, and from this there will be a total of nine expressions.

The nine μ quantities $\mu_{qq'}$ form the nine components of a second rank tensor μ as shown as equation (A1.4). Knowing μ enables the prediction of the direction of the magnetic moment when the field is applied in any direction.

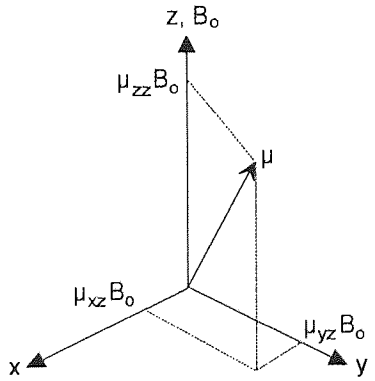

FIGURE A1.1. The components of the magnetic moment μ in a magnetic field B_0.

$$\mu = \begin{pmatrix} \mu_{xx} & \mu_{xy} & \mu_{xz} \\ \mu_{yx} & \mu_{yy} & \mu_{yz} \\ \mu_{zx} & \mu_{zy} & \mu_{zz} \end{pmatrix} \qquad \text{- (A1.4)}$$

There are three directions that the field can be applied along to result in the magnetic moment being exactly parallel to the field. These three components $\mu_{nn'}$ along these directions are known as the principal components of the tensor, shown in equation (A1.5), and the directions known as the principal axes.

$$\mu = \begin{pmatrix} \mu_{XX} & 0 & 0 \\ 0 & \mu_{YY} & 0 \\ 0 & 0 & \mu_{ZZ} \end{pmatrix} \qquad \text{- (A1.5)}$$

Within chapter three, tensors are discussed for the chemical shift interaction σ. As with the magnetic moment, the chemical shift interaction lies at an angle to the applied field and can be described in terms of the second rank tensor as for μ in the matrix (A1.4). This produces a tensor matrix of the form:

$$\hat{\sigma} = \begin{pmatrix} \sigma_{xx} & \sigma_{xy} & \sigma_{xz} \\ \sigma_{yx} & \sigma_{yy} & \sigma_{yz} \\ \sigma_{zx} & \sigma_{zy} & \sigma_{zz} \end{pmatrix} \qquad \text{- (A1.6)}$$

Knowing the components of the second rank tensor enables the definition of the chemical shift interaction within the principal axis system in the same way as that described for the magnetic moment shown in (A1.5). This produces a principal axis tensor of the form:

$$\hat{\sigma} = \begin{pmatrix} \sigma_{XX} & 0 & 0 \\ 0 & \sigma_{YY} & 0 \\ 0 & 0 & \sigma_{ZZ} \end{pmatrix} \qquad \text{- (3.10)}$$

It is the second rank and principal axis tensors in the form of these matrices which describe the shape (as axial and non-axial symmetry) and angular dependence of the chemical shift anisotropy.

REFERENCES FOR APPENDIX ONE

A1. J. W. Hennel and J. Klinowski, 'Fundamentals of Nuclear Magnetic Resonance', 1993, Longman UK, Essex, England.

A2. M. Goldman, 'Quantum Description of High-Resolution NMR in Liquids', 1988, Oxford Univ. Press, Oxford, England.

APPENDIX TWO

NMR PARAMETERS USED IN ALL EXPERIMENTS

Parameter	Value
NMR Nucleus Under Observation	^{31}P
Observation Method	Single pulse
Observation Frequency	36.20 MHz
Observe Frequency Offset	77.58 kHz
Data Points	4096
Frequency Width (Window)	30030 Hz
Delay	21.2 µs
Deadtime (DEADT)	5 µs
Acquisition Time	68.20 ms
Number of Scans	2000
Pulse Width (PW)	10 µs / 30°
Pulse Delay (PD)	500 ms

TABLE A2.1. TSP ^{31}P SINNMR Initial Parameters as for figure 7.1.

Parameter	Value
NMR Nucleus Under Observation	^{31}P
Observation Method	Single pulse
Observation Frequency	36.20 MHz
Observe Frequency Offset	77.58 kHz
Data Points	4096
Frequency Width (Window)	30030 Hz
Delay	21.2 µs
Deadtime (DEADT)	5 µs
Acquisition Time	68.20 ms
Number of Scans	2000
Pulse Width (PW)	10 µs / 30°
Pulse Delay (PD)	1.0 s

TABLE A2.2. TSP ^{31}P SINNMR parameters for measuremetns of the S/N ratio with varying particle size, mass of solid and density of support liquid.

Parameter	Value
NMR Nucleus Under Observation	^{23}Na
Observation Method	Single pulse
Observation Frequency	23.64 MHz
Observe Frequency Offset	60.15 kHz
Data Points	16384
Frequency Width (Window)	30030 Hz
Delay	21.2 µs
Deadtime (DEADT)	5 µs
Acquisition Time	272.79 ms
Number of Scans	2000
Pulse Width (PW)	25 µs / 44°
Pulse Delay (PD)	200 ms

TABLE A2.3. TSP ^{23}Na SINNMR parameters for S/N ratio and FWHM with varying mass.

Parameter		
NMR Nucleus Under Observation	^{23}Na	^{31}P
Observation Method	Single pulse	Single pulse
Observation Frequency	23.64 MHz	36.20 MHz
Observe Frequency Offset	60.15 kHz	77.58 kHz
Data Points	16384	4096
Frequency Width (Window)	30030 Hz	30030 Hz
Delay	100 µs	100 µs
Deadtime (DEADT)	5 µs	5 µs
Acquisition Time	272.79 ms	68.20 ms
Number of Scans	2000	2000
Pulse Width (PW)	25 µs / 44°	10 µs / 30°
Pulse Delay (PD)	200 ms	1.0 s

TABLE A2.4. TSP ^{23}Na and ^{31}P solid and SINNMR Parameters for Optimum SINNMR Conditions. These parameters were used for all other TSP SINNMR experiements.

Parameter	Value
NMR Nucleus Under Observation	^{31}P
Observation Method	Single pulse
Observation Frequency	36.20 MHz
Observe Frequency Offset	72.551 kHz
Data Points	4096
Frequency Width (Window)	30030 Hz
Delay	100 µs
Deadtime (DEADT)	5 µs
Acquisition Time	68.20 ms
Number of Scans	1000
Pulse Width (PW)	31 µs / 90°
Pulse Delay (PD)	34, 38, 45, 55, 65, 80, 95 s

TABLE A2.5. TSP ^{31}P solid Saturation Recovery Parameters.

Parameter	Value
NMR Nucleus Under Observation	^{31}P
Observation Method	Single pulse
Observation Frequency	36.20 MHz
Observe Frequency Offset	72.551 kHz
Data Points	4096
Frequency Width (Window)	30030 Hz
Delay	100 µs
Deadtime (DEADT)	5 µs
Acquisition Time	68.20 ms
Number of Scans	1000
Pulse Width (PW)	31 µs / 90°
Pulse Delay (PD)	1.0, 2.0, 2.5, 3.0, 3.5, 4.0, 4.5, 6.0, 7.0 s

TABLE A2.6. TSP ^{31}P SINNMR Modified Saturation Recovery Parameters.

Parameter	Value
NMR Nucleus Under Observation	^{31}P
Observation Method	Dummy pulse sequence followed by single pulse sequence.
Observation Frequency	36.20 MHz
Observe Frequency Offset	72.551 kHz
Data Points	8192
Frequency Width (Window)	1000 Hz
Delay	1.95 ms
Deadtime (DEADT)	5 µs
Acquisition Time	256 ms
Number of Scans	128
Pulse Width (PW)	variable (see table A2.8 below)
Field spoil (FS) + Pulse Delay (PD)	FS - 1 ms and PD - 1.136 s

TABLE A2.7. TSP ^{31}P solution DESPOT parameters (dummy pulses shown below).

Pulse Width	Dummy Pulses Required
3.4 µs / 10°	30
5.1 µs / 15°	31
6.8 µs / 20°	30
8.6 µs / 25°	27
10.3 µs / 30°	23
12.0 µs / 35°	20
13.7 µs / 40°	17
15.4 µs / 45°	15
17.1 µs / 50°	13
18.8 µs / 55°	11
20.5 µs / 60°	9
22.2 µs / 65°	8
24.0 µs / 70°	7
25.7 µs / 75°	5
27.4 µs / 80°	4

TABLE A2.8. TSP ^{31}P solution DESPOT number of dummy pulses estimated for $t_i/T_1 = 0.1$

Parameter	Value
NMR Nucleus Under Observation	^{19}F
Observation Method	Single Pulse
Observation Frequency	84.26 MHz
Observe Frequency Offset	77.56 kHz
Data Points	8192
Frequency Width (Window)	30030 Hz
Delay	100 µs
Deadtime (DEADT)	5 µs
Acquisition Time	31.96 ms
Number of Scans	1000
Pulse Width (PW)	10 µs / 45°
Pulse Delay (PD)	1.0 s

TABLE A2.9. PTFE ^{19}F SINNMR and solid parameters.

Parameter	Value
NMR Nucleus Under Observation	^{27}Al
Observation Method	Single pulse
Observation Frequency	23.30 MHz
Observe Frequency Offset	47.892 kHz
Data Points	8192
Frequency Width (Window)	30030 Hz
Delay	100 µs
Deadtime (DEADT)	5 µs
Acquisition Time	31.96 ms
Number of Scans	8
Pulse Width (PW)	20 µs / 30°
Pulse Delay (PD)	200 ms

TABLE A2.10. Aluminium and certain alloys, ^{27}Al NMR parameters for aqueous aluminium chloride reference.

Parameter	Value
NMR Nucleus Under Observation	^{27}Al
Observation Method	Single pulse
Observation Frequency	23.30 MHz
Observe Frequency Offset	82 kHz or 87 kHz
Data Points	8192
Frequency Width (Window)	30030 Hz
Delay	100 µs
Deadtime (DEADT)	5 µs
Acquisition Time	31.96 ms
Number of Scans	4000
Pulse Width (PW)	10 µs / 15°
Pulse Delay (PD)	10 ms

TABLE A2.11. Aluminium and its Alloys, ^{27}Al SINNMR parameters.

Parameter	Value
NMR Nucleus Under Observation	^{29}Si
Observation Method	Single pulse
Observation Frequency	17.76 MHz
Observe Frequency Offset	41.88 kHz
Data Points	8192
Frequency Width (Window)	30030 Hz
Delay	100 µs
Deadtime (DEADT)	5 µs
Acquisition Time	31.96 ms
Number of Scans	2260
Pulse Width (PW)	10 µs / 36°
Pulse Delay (PD)	1 s

TABLE A2.12. Doped Silicon ^{29}Si SINNMR Parameters.

Parameter	Value
NMR Nucleus Under Observation	^{1}H
Observation Method	Single pulse
Observation Frequency	89.56 MHz
Observe Frequency Offset	44.70 kHz
Data Points	8192
Frequency Width (Window)	30030 Hz
Delay	100 µs
Deadtime (DEADT)	5 µs
Acquisition Time	31.96 ms
Number of Scans	500
Pulse Width (PW)	15 µs / 45°
Pulse Delay (PD)	1 s

TABLE A2.13. Amberlite-MB3 ^{1}H SINNMR parameters

Parameter	Value
NMR Nucleus Under Observation	^{29}Si
Observation Method	Single pulse & ^{1}H gated decoupling
Observation Frequency	17.76 MHz
Observe Frequency Offset	41.88 kHz
Data Points	8192
Frequency Width (Window)	30030 Hz
Delay	100 µs
Deadtime (DEADT)	5 µs
Acquisition Time	31.96 ms
Number of Scans	4000
Pulse Width (PW)	10 µs / 36°
Pulse Delay (PD)	1 s

TABLE A2.14. Silylated coal ^{29}Si SINNMR Parameters

Parameter	Value
NMR Nucleus Under Observation	^{29}Si
Observation Method	Spin-echo
Observation Frequency	17.76 MHz
Observe Frequency Offset	41.88 kHz
Data Points	8192
Frequency Width (Window)	30030 Hz
Delay	150 µs
Deadtime (DEADT)	5 µs
Acquisition Time	136.3 ms
Number of Scans	3000
Pulse Width (PW)	25 µs / 90^{o} - 50 µs - 180^{o}
Pulse Delay (PD)	10 s

TABLE A2.15. Silicon dioxide ^{29}Si High frequency SINNMR parameters.

Parameter	Value
NMR Nucleus Under Observation	^{11}B
Observation Method	Single pulse
Observation Frequency	28.70 MHz
Observe Frequency Offset	49.10 kHz
Data Points	8192
Frequency Width (Window)	30030 Hz
Delay	200 µs
Deadtime (DEADT)	5 µs
Acquisition Time	136.3 ms
Number of Scans	20000
Pulse Width (PW)	20 µs / 45^{o}
Pulse Delay (PD)	200 ms

TABLE A2.16. Sodium-boron-aluminium oxide glass ^{11}B SINNMR parameters for both 20/70/10 and 15/70/15 mole % samples.

Parameter	Value
NMR Nucleus Under Observation	^{27}Al
Observation Method	Single pulse
Observation Frequency	23.30 MHz
Observe Frequency Offset	47.68 kHz
Data Points	8192
Frequency Width (Window)	30030 Hz
Delay	100 µs
Deadtime (DEADT)	5 µs
Acquisition Time	31.96 ms
Number of Scans	6550
Pulse Width (PW)	20 µs / 30°
Pulse Delay (PD)	200 ms

TABLE A2.17. Sodium-boron-aluminium oxide glass ^{27}Al SINNMR parameters for both 20/70/10 and 15/70/15 mole % samples.

Parameter	Value
NMR Nucleus Under Observation	^{1}H
Observation Method	Single pulse
Observation Frequency	89.56 MHz
Observe Frequency Offset	44.70 kHz
Data Points	8192
Frequency Width (Window)	2500 Hz
Delay	500 µs
Deadtime (DEADT)	50 µs
Acquisition Time	1.6384 s
Number of Scans	8
Pulse Width (PW)	10 µs / 45°
Pulse Delay (PD)	2 s

TABLE A2.18. ^{1}H NMR parameters for the investigation of $^{1}H_2O$ intensity with side transducer.

APPENDIX THREE

THE CALCULATION OF THEORETICAL GAUSSIAN DISTRIBUTION CURVES

The particle size ranges used in a SINNMR experiment can be considered to consist of a Gaussian distribution of particle sizes. A Gaussian distribution can be estimated for the particle ranges 1000 - 500 μm and 1000 - 210 μm from the following equation:

$$D = \frac{1}{\sigma\sqrt{2\pi}} \exp\left(\frac{-(x-\mu)^2}{2\sigma}\right) \qquad \text{- (A3.1)}$$

Here, D is the relative number of particles of size x in a distribution where the mean number of particles is μ with a standard deviation of σ.

In order to predict a Gaussian distribution, it is therefore necessary to ascertain the mean particle size and standard deviation of the distribution. Although no method to deduce these parameters was immediately available, they can be estimated in the following way.

1. Each particle size range is divided into n equal sections, *i.e.* the 1000 - 500 μm range is divided into equal sections of 50 μm so that the sections are 1000, 950, 900, 850 *etc.* down to 500 μm. The 1000 - 210 μm range is divided into equal sections of 100 μm.

2. The sum of particle sizes corresponding to each section divided by n yields the mean of the distribution μ, *i.e.*

$$\mu = \frac{\sum_{a=1}^{a=n} x_a}{n} \qquad \text{- (A3.2)}$$

3. The standard deviation is calculated as:

$$\sigma = \sqrt{\frac{\sum (x-\mu)^2}{n-1}} \qquad \text{- (A3.3)}$$

In this equation the denominator is (n-1) rather than n when the number of sample values is small (usually when $n < 100$).

The mean and standard deviations for the two particle size ranges are given in table A3.1

	mean, μ	standard deviation, σ
1000 - 500 μm range, n = 11	750 μm	168 μm
1000 - 210 μm range, n = 9	601 μm	272 μm

TABLE A3.1. Mean and standard deviation values calculated for the Gaussian distribution of 1000 - 500 μm and 1000 - 210 μm particle size ranges.

These values can be used in equation (A3.1) to produce the following distribution values shown in table A3.2:

	Gaussian Distribution	Gaussian Distribution
Particle size / μm	**1000 - 500 μm range**	**1000 - 210 μm range**
1000	2374.2148	1466.270
950	2374.3738	not calculated n/c
900	2374.4974	1466.459
850	2374.5859	n/c
800	2374.6387	1466.593
750	2374.6564	n/c
700	2374.6387	1466.673
650	2374.5859	n/c
600	2374.4974	1466.700
550	2374.3738	n/c
500	2374.2148	1466.672
400	n/a	1466.591
300	n/a	1466.455
210	n/a	1466.287

TABLE A3.2. Calculated Gaussian distributions for 1000 - 500 μm and 1000 - 210 μm particle size ranges.

These values can then be used directly to produce a Gaussian distribution curve as shown in figure 7.2 or to produce a distribution with mass curve as shown in figure 8.3.

As the mass distribution is related to the theoretical Gaussian distribution, the actual mass of each particle size present cannot be read directly from the curve. It is for this reason that the integral of the curve is used, as the total area

underneath must correspond to the total mass of the sample. The mass distribution data is calculated in the following way (see table A3.3)

Initially, the Gaussian distribution numbers are simplified by division of each distribution value by the Gaussian value for 1000 μm particles. The particle size distribution is now represented as proportions of particle sizes relative to the number of 1000 μm particles (shown in table A3.3 as the proportional distribution). The shallow distribution dictates the necessity of a large number of significant figures.

For each particle size range represented in the Gaussian distribution, the mass of one particle is calculated from:

$$\text{mass} = \text{density} \times \text{volume} \approx \text{density} \times (\textbf{particle size})^3 \qquad \text{- (A3.4)}$$

It is assumed that trisodium phosphate particles are cubic. The density of trisodium phosphate is 1.62 gcm^{-3} or 1620 kgm^{-3}.

The mass of each particle is then multiplied to its corresponding proportional distribution value: *i.e.* the mass of one 500 μm particle is multiplied by the 500 μm proportional distribution value of 1.0002739.

Particle Size / μm	Gaussian Distribution	Proportional Distribution	Mass of one Cubic Particle / kg x10^{-6}	Proportional Mass / x 10^{-6}	Mass Distribution
1000	1466.270	1	1.62	1.62	0.331
900	1466.459	1.0001283	1.18100	1.18113	0.241
800	1466.593	1.0002199	0.82944	0.82962	0.169
700	1466.673	1.0002747	0.55660	0.55581	0.113
600	1466.700	1.0002927	0.34992	0.35002	0.071
500	1466.672	1.0002739	0.20250	0.20255	0.041
400	1466.591	1.0002184	0.10368	0.10370	0.021
300	1466.455	1.0001261	0.04374	0.04375	0.009
210	1466.287	1.0000116	0.01500	0.01500	0.003

TABLE A3.3. Data used in the Calculation of the Mass Distribution.

This produces a proportional mass value, which for 500 μm particles is 2.0255×10^{-7}. To make these figures easier to work with, all proportional mass values are divided by the sum of all proportional masses which is 4.9016×10^{-6}. The resulting values are then plotted against particle size to produce the mass distribution curve shown in chapter eight.

Table A3.3 shows by comparison of the mass of one particle and the proportional mass that accounting for the distribution has a negligible effect on the estimated distribution of mass with particle size. This is due to the shallow nature of the distribution.

Although the exercise of producing a mass distribution is not completely justified in this case, it is expected that this worked example may be of use to the SINNMR research team in the future.